Ultrafast Photoprotection Mechanisms

Expediting the Molecular Design of Sunscreen Agents

Natércia das Neves Rodrigues

Thesis submitted for the qualification of

Doctor of Philosophy in Chemistry

Department of Chemistry

University of Warwick

May 2018

Contents

List of Figures

List of Tables

List of Abbreviations

1D	One-Dimension(al)
2D	Two-Dimension(al)
3D	Three-Dimension(al)
AO	Atomic Orbital
BBO	β-Barium Oxide
CAS(SCF)	Complete Active Space (Self-Consistent Field)
(cc-)pVDZ	Correlation-Consistent Polarised Valence Double Zeta
ConA	Coniferyl Alcohol
CI	Conical Intersection
DADS	Decay Associated Difference Spectrum
DFL	Disperse Fluorescence
DFT	Density Functional Theory
EADS	Evolution Associated Difference Spectrum
EF	Ethyl Ferulate
eKE	Electron Kinetic Energy
FFT	Fast Fourier Transform
Fl	Fluorescence
FWHM	Full Width at Half Maximum
fs	Femtosecond (10^{-15} s)
GVD	Group Velocity Dispersion
HB	Hole-Burning (Spectroscopy)
HOMO	Highest Occupied Molecular Orbital
IET	Intermolecular Energy Transfer
IC	Internal Conversion
IP	Ionisation Potential
IR	Infra-Red (radiation)
IRF	Instrument Response Function
ISC	Intersystem Crossing

IVR	Internal Vibrational Redistribution
KE	Kinetic Energy
LCAO	Linear Combination of Atomic Orbitals
LIF	Laser Induced Fluorescence
LUMO	Lowest Unoccupied Molecular Orbital
MA	Methyl Anthranilate
MCP	Micro-Channel Plate
MCSCF	Multiconfiguration Self-Consistent Field
MenA	Menthyl Anthranilate
MO	Molecular Orbital
m/z	Mass-to-Charge Ratio
ns	Nanosecond (10^{-9} s)
OPA	Optical Parametric Amplifier
OPO	Optical Parametric Oscillator
PAD	Photoelectron Angular Distribution
PEC	Potential Energy Curve
Ph	Phosphorescence
POP	Polar Onion Peeling
ps	Picosecond (10^{-12} s)
R2PI	Resonant Two-Photon Ionisation
REMPI	Resonance Enhanced Multi-Photon Ionisation
ROS	Reactive Oxygen Species
s	Second
SFG	Sum Frequency Generation
SHG	Second Harmonic Generation
SPM	Self-Phase Modulation
TKER	Total Kinetic Energy Release
TAS	Transient Absorption Spectrum
TEAS	Transient Electronic Absorption Spectroscopy
TOF	Time-of-Flight
TR-IY	Time-Resolved Ion Yield
(TR)PES	(Time-Resolved) Photoelectron Spectroscopy

TVAS	Transient Vibrational Absorption Spectroscopy
UV	Ultraviolet (radiation)
UVHB	Ultraviolet Hole-Burning (spectroscopy)
(v)FC	(Vertical) Franck-Condon
Vis	Visible (radiation)
VMI	Velocity Map Imaging
VR	Vibrational Relaxation
WLC	White Light Continuum

List of Symbols and Constants

c	Speed of light	2.998×10^8 ms^{-1}
λ	Wavelength	$\lambda = c/\nu$
$\tilde{\nu}$	Wavenumber	$\tilde{\nu} = 1/\lambda$
ν	Frequency	$\nu = c/\lambda$
p	Momentum	$p = mv$
v	Velocity	$v = displacement/time$
m_e	Mass of the electron	9.109×10^{-31} kg
m_p	Mass of the proton	1.672×10^{-27} kg
m_n	Mass of the neutron	1.674×10^{-27} kg
e	Elementary Charge	1.602×10^{-19} C
μ_0	Vacuum Permeability	1.256×10^{-6} NA^{-2}
ϵ_0	Vacuum Permittivity	$\epsilon_0 = \frac{1}{\mu_0 c^2} = 8.854 \times 10^{-12}$ J^{-1} C^2 m^{-1}
h	Planck's Constant	6.626×10^{-34} Js
$\hbar$	Reduced Planck's Constant	$h/2\pi = 1.054 \times 10^{-34}$ Js
R_∞	Rydberg Constant	1.097×10^5 cm^{-1}
$\tilde{R}_H$	Rydberg Unit of Energy	$hc \times R_\infty = 13.605$ eV
k_B	Boltzmann Constant	1.381×10^{-23} JK^{-1}

Acknowledgments

It is safe to say there were times in the past few months and, indeed, in the past three and a half years that I was not at all sure that I would ever get to the point of writing these words. But here I finally am, where I certainly wouldn't be without a number of people who, together, constitute an immense support network which I am incredibly blessed to have with me.

First and foremost, I want to express my thanks to my PhD supervisor, Professor Vas Stavros. His unwavering and unrivalled commitment to his work, his team and his students proved crucial in my own PhD journey as part of his research group. I am eternally grateful for the offer of a PhD position, the help, the time, the frank conversations, the tactful feedback, the strategically delivered "calls to action", the guidance for the future and, importantly, the continuous belief in my abilities, even when I doubted them myself.

I would also like to thank the dynamic duo who introduced me to the world of postgraduate research, Dr. and Dr. Young-Stabiforth. Once I deciphered what "the thing that we use to thingy the things" meant, sharing a lab with you was an absolutely delightful experience. Individually, I thank Dr. Stabiforth for sharing his love of books, reading, writing, theatre and other forms of art and culture. To Dr. Young, I am sorry that I wasted all those hours of his life (meticulously recorded on the lab board) and I am sorry I said I was not easily annoyed! But also, thank you for the patience, the guidance, the proofreading, the weekly quizzes and the banter.

Further thanks are in order to Dr. Neil "The Interrogator" Cole-Filipiak, whose teaching (or questioning?) methods were crucial to creating the scientist I am today. I hated (almost) every second of the difficult questions, but they played a major role in making me a critical thinker, able to consider the implications of my approaches and assumptions regarding a given problem and able to risk explaining what I see based on what I know. I am forever grateful for the invaluable instruction and mentorship.

Even though I started my journey as a gas-phase scientist, I ended up becoming interested in the wonderful mess that is the world of solution chemistry. My first steps in this field were taken under the supervision of Dr. "Reddit" Horbury, to whom I direct

my thanks for all the help with experiments, data analysis and write ups. Thank you also to Dr. Greenough for building our solution setup, for engaging in helpful discussion (and banter, also) and for reading my work.

The Stavros group has recently experienced a well deserved and significant "boom" (and that's not including little Sebastian!); it almost feels like the office is shrinking! Which means there are a lot of other PhD and master's students with whom I have worked and/or interacted with, who I would also like to thank. In no particular order, I thank Lewis Baker, Jack "Baymax" Wooley (and his mother's lemon cake, the only lemon cake I've ever truly enjoyed), Konstantina Marsella Krokidi, Matt Turner, Emily Holt, Daniel Coxon, Georgia Thornton, Jack Peters, Baljeet Panesar, Daniel King, Faye Monk and Heather Wainwright. Oh, and to Vic... I don't quite know what to say. Thank you for providing me with the experiential learning route to how to stand up for myself, Dr. Quan (I think).

I extend my thanks to all the members of the Stavros group I have already mentioned, to others I may have forgotten and to all past and present associates (special shout out to the Costantini group!) for being the amazing team I have been fortunate and proud to be part of. In the days when I didn't want to be in the lab, I could still drag myself to campus because I knew at least hanging out with the team would be fun. And so I kept showing up, which, the internet says, is the key to success. Thank you!

Throughout my PhD I also had the opportunity to work with some fantastic people outside the Stavros group bubble whom I'd like to thank: Dr. Russ Kitson, Dr. Dan Murdock, and the rest of the undergraduate teaching team at the Warwick chemistry department (academic and technical staff alike); the Learning and Development Centre team, in particular my good friends Sara Hattersley who sparked my passion for teaching and William Rupp who guided my first steps in non-chemistry teaching; Dr. Elena Riva and the rest of the team at IATL; and every other member of the Warwick team who has helped make the last three and a half years some of the most life-changing of my whole life.

Last, but certainly not least, I want to not only acknowledge but also dedicate the following pages to my family. To my husband, Filipe, who refuses to let me give up on myself and whose arms have been my home for the past 6 years. Thank you for listening to the science you don't understand, for celebrating my victories with me, for cheering

me up on cloudy days and wiping my tears on more difficult ones. And finally, as ever, an enormous message of gratitude to my grandparents, José and Maria, my father, Paulo, my mother, Adriana, and my brother, João, whose resolute support has always been the platform from which I have dived into the most challenging adventures of my life, and the reason of my success. There will never be enough words to express my gratitude for the unconditional love I have received from these six people in my life. I can only hope that my humble achievements make them proud.

Bones: *When I see effects and I am unable to discern a cause, my faith in reason and consequence is shaken.*

Booth: *And then, what happens?*

Bones: *Two plus two equals four. I put sugar in my coffee and it tastes sweet. The Sun comes up because the World turns. These things are beautiful to me. There are mysteries I will never understand, but everywhere I look, I see proof that for every effect there is a corresponding cause. Even if I can't see it. I find that reassuring.*

Bones, Season 5 Episode 14, *The Devil is in the Details*

Declarations

This thesis is submitted to the University of Warwick in support of my application for the degree of Doctor of Philosophy. It has been composed by myself and has not been submitted in any previous application for any degree. The work presented (including data generated and data analysis) was carried out by myself except in the cases outlined below, where details regarding the separate publication of parts of this thesis are also given.

- **Chapter 3:** the work presented has been published in two separate publications, namely:

    - Rodrigues, N. d. N. *et al.* Towards elucidating the photochemistry of the sunscreen filter ethyl ferulate using time-resolved gas-phase spectroscopy. *Faraday Discussion* **194**, 709-729 (2016).

    - Horbury, M. D. *et al.* Photoisomerization of ethyl ferulate: A solution phase transient absorption study. *Chemical Physics Letters* **673**, 62-67 (2017).

    All frequency-resolved measurements (LIF, R2PI, UVHB, DFL) presented in this chapter were carried out in collaboration with the research group led by Professor Timothy S. Zwier (Purdue University, USA). I have carried out all gas-phase time-resolved measurements and analysis, assisted Dr. Michael Horbury (University of Warwick, UK) with measurements in solution and respective data analysis, and carried out NMR and fluorescence quantum yield measurements. Computational studies were carried out by Dr. Michael Staniforth (University of Warwick, UK).

- **Chapter 4:** the work presented in section 4.1 has been published in:

    - Rodrigues, N. d. N. *et al.* Photophysics of the sunscreen ingredients methyl and menthyl anthranilate: a bottom-up approach to photoprotection. *Journal of Photochemistry and Photobiology A: Chemistry* **353**, 376-384 (2018).

    All frequency-resolved measurements (LIF, R2PI, UVHB, DFL) presented in this chapter were carried out in collaboration with the research group led by Professor Timothy S. Zwier (Purdue University, USA). I have carried out all time-resolved measurements in vacuum and in solution, and respective data analysis, in close col-

laboration with Dr. Neil Cole-Filipiak (University of Warwick, UK). Computational studies were carried out by Dr. Tolga Karsili (Temple University, USA).

- **Chapter 5:** the literature review presented has been published in:

  - Rodrigues, N. d. N. and Stavros, V. G. From fundamental science to product: a bottom-up approach to sunscreen development. *Science Progress* **101(1)**, 8-31 (2018).

I have carried out the literature search and produced the review article. The preliminary results for *meta*- and *para*-MA, presented in section 5.3.2, were obtained by Dr. Neil Cole-Filipiak, Ms. Konstantina Marsella Krokidi and Ms. Georgia Thornton; I carried out the data analysis of the data presented.

Abstract

While ultraviolet (UV) radiation is essential for sustaining life, it can also be destructive for biological systems. In humans, for example, UV radiation initiates production of vitamin D, while also being the primary external source of skin cancer. Despite the skin's melanin providing natural protection against radiative stress, and despite the wide range of commercially available photoprotective lotions, *i.e.* sunscreens, skin cancer incidence has risen in recent years. The urgent need for more effective sunscreens is, therefore, obvious. However, the sunscreen industry is currently challenged with limited availability of suitable and photostable sunscreen active ingredients.

The work presented in this thesis aims to address these challenges by presenting an innovative approach to sunscreen molecular design based on the unique insight provided by laser femtochemistry. The ideal sunscreen should dissipate excess energy *via* fast, efficient and safe relaxation mechanisms, which typically occur on ultrafast timescales. The studies presented in this thesis focus on two categories of sunscreens, the cinnamates and the anthranilates, and employ ultrafast laser spectroscopy techniques to map and understand the photoprotection mechanisms that afford these sunscreens their photoprotective capabilities. As such, this thesis constitutes a significant contribution to the field of research whose primary concern is to unveil the mechanisms of action of photoprotection in sunscreen molecules: the results reported have identified key photophysical photoprotective mechanisms and raised important questions regarding the effects of a sunscreen molecule's environment on its photodynamics.

Based on the insight provided by the research herein presented, a rationale for sunscreen molecular design may be developed for which the molecular structure of sunscreen active ingredients can be manipulated in order to either enhance the desired energy redistribution mechanisms or hinder any relaxation pathways that may lead to harmful side photochemistry. In reaching its full potential, this innovative approach to sunscreen development has the potential to create a new generation of high-performance sunscreens to be incorporated in commercial sunscreen formulations, in an attempt to disrupt the rise in skin cancer incidence.

1 Introduction

1.1 Sun, Skin and Sunscreens

Planet Earth orbits around a 4.6 billion year old star, the Sun. The crucial role of sunlight in the existence and maintenance of life on Earth has been recognised since well before the birth of modern science. Even in the earliest forms of human civilisation, the observation that crops required sunlight to thrive led ancient societies to worship the Sun and its power to bring fertility, abundance and prosperity. For centuries, solstices were celebrated and temples were raised in honour of the many versions of the Sun god. [1]

As science evolved, the powers of the Sun were demystified. It is now understood that the Sun's role in sustaining life on Earth is related to the electromagnetic radiation (light) that it emits. The Sun has an emission spectrum at its surface which resembles that of a black body radiator (that is, an idealised perfect absorber and emitter) at 5800 kelvin (K), as shown in Figure 1.1. [2] The solar spectrum thus encompasses the ultraviolet (UV, 100 – 400 nm), visible (Vis, 400 – 720 nm) and infrared (IR, 720 nm – 1 mm) regions of the electromagnetic spectrum, peaking at approximately 500 nm. [3,4] After passing through the Earth's atmosphere, a significant part of the solar radiation is either absorbed, scattered or reflected, so that the intensity of the solar spectrum at the Earth's surface is reduced overall, with marked depletions at the wavelengths corresponding to the absorption energies of key gases in the atmosphere. [5] The absorption of IR radiation by carbon dioxide and water, for example, results in well-defined absorption dips in the IR region of the solar spectrum. Ozone, on the other hand, absorbs at the highest energies of the solar spectrum, *i.e.* in the UV region. Atmospheric ozone thus prevents the highly energetic and highly destructive UVC radiation (100 – 280 nm) from reaching the Earth's surface, as well as absorbing a significant portion of UVB radiation (where UVB corresponds to the 280 – 315 nm range). [5] The UV radiation reaching the Earth's surface is, therefore,

mostly composed of UVB and UVA radiation, with UVA encompassing wavelengths of 315 – 400 nm radiation, and the combined total of these (UVB and UVA) accounting for approximately 3.4% of the total atmosphere attenuated solar spectrum (*c.f.* 8% before the atmosphere).[6,7] Despite the lower solar irradiance at the Earth's surface when compared to the pre-life era (due to the evolution of a richer atmosphere), the Sun has remained the most important source of energy on Earth since prebiotic times.[8]

The UV radiation provided by the Sun plays a crucial role in sustaining life on Earth, as it prompts a collection of chemical reactions that are fundamentally responsible for the survival of living organisms. Such radiation–induced type chemistry, otherwise termed *photochemistry*, is the trigger for photosynthesis, for example, the unique biological process which converts the energy from sunlight into the biochemical energy necessary to sustain life on Earth.[9] Photosynthesis is not exclusive to higher terrestrial plants — it is also the source of energy for many species of algae and phytoplankton which live at the surface of waterbodies (where UV radiation can reach), as well as bacteria and other living organisms.[10,11]

In humans, one of the most important UV-induced processes is the production of vitamin D in the outermost layer of skin, the epidermis, where 7–dehydrocholesterol is stored.[12,13] When skin is exposed to UVB radiation, 7–dehydrocholesterol is photoexcited, prompting chemical reactions which lead to the production of previtamin D_3. Previtamin D_3 then eventually thermally isomerises to vitamin D. In order to obtain a biologically active compound, vitamin D is then hydroxylated in the liver. The well-established relationship between vitamin D deficiency and rickets (in children) or osteomalacia (in adults) has made vitamin D best known for its ability to protect against musculoskeletal disorders.[12] However, healthy levels of vitamin D have also been shown to protect against infectious, autoimmune and cardiovascular diseases, diabetes, some types of cancer, neurocognitive dysfunction, and mental illness, amongst other health benefits.[14]

The extensive benefits of UV radiation to life — and, indeed, its crucial role in sustaining it — are heavily counterbalanced by the serious consequences of excess exposure to this type of radiation. In plants, excess UV radiation greatly disrupts photosynthetic processes, as well as reducing carbon dioxide fixation and oxygen evolution, for example.[10,15] In algae, on the other hand, excessive UV radiation inhibits growth, alters photosynthetic contents and induces damaging structural changes;[16] UV radiation has even been suggested to play a role in coral bleaching.[17] Moreover, it is now firmly established that
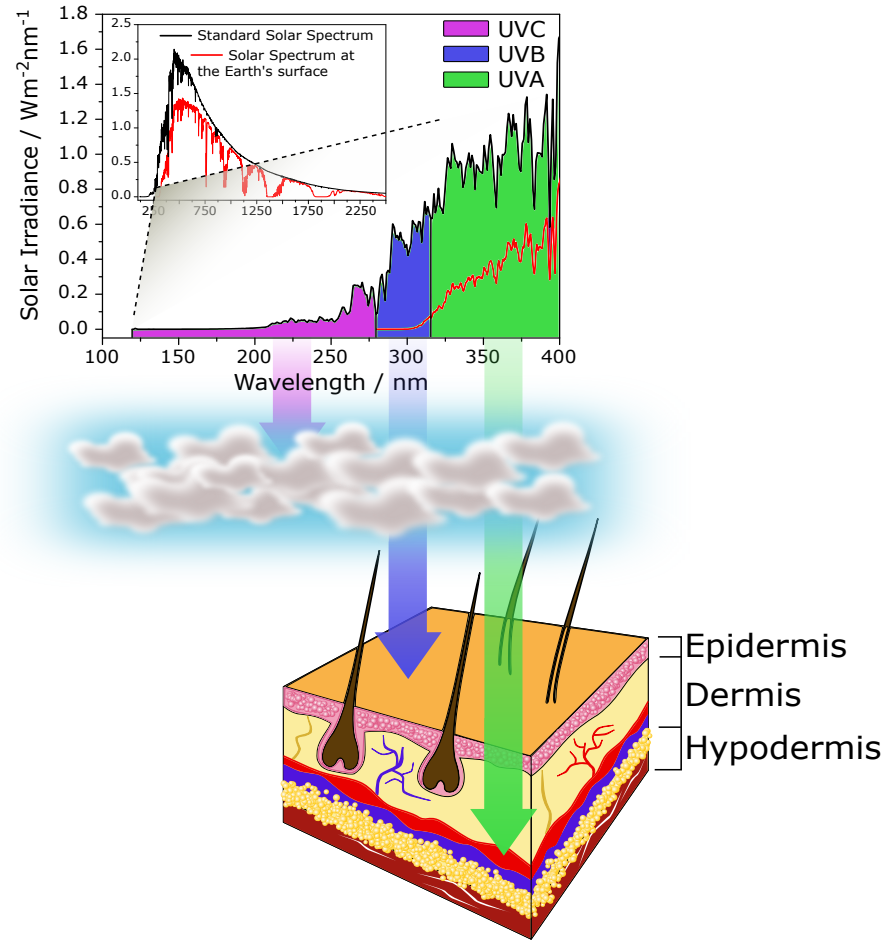
Figure 1.1: (Top) The plot of solar irradiance *vs.* wavelength shows the solar spectrum before and after the Earth's atmosphere (black and red lines, respectively). Solar spectra adapted from reference 6. (Bottom) A representation of the interaction between the different types of UV radiation and the skin: UVC (purple arrow) is mostly absorbed/scattered/reflected by the atmosphere and hence its presence at the surface of the skin is negligible; UVB (blue arrow) reaches the skin's epidermis and UVA (green arrow) penetrates deeper into the skin, reaching the dermis.

overexposure of human skin to UV radiation is related to erythema (sunburn), skin aging and carcinogenesis — namely, it is related to melanoma, one of the most aggressive of human cancers.[18,19]

The most commonly known and most readily observable effect of UV radiation on human skin is erythema, commonly referred to as sunburn: a redness of the skin which appears a few hours after sun exposure as a result of vasodilatation and increased blood volume in the skin.[20] Nevertheless, there are many other damaging effects of overexposure to UV radiation which take place at a molecular level and, in this context, the effects of UVB and UVA radiation can be quite distinct.[21] UVB radiation is readily absorbed by the

(a) Cyclobutane pyrimidine dimer   (b) Pyrimidine 6-4 photoproduct
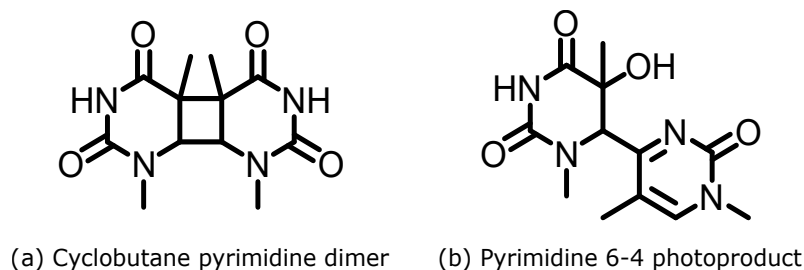
Figure 1.2: UVB signature photolesions: (a) cyclobutane pyrimidine dimers and (b) pyrimidine 6 – 4 photoproducts.

building blocks of DNA, resulting in molecular rearrangements which disrupt the DNA sequence and jeopardise the healthy functioning of the cell.[22] The main DNA photolesions caused by UVB radiation — so called UVB signature photolesions — are cyclobutane pyrimidine dimers and pyrimidine 6 – 4 photoproducts; these lesions, shown in Figure 1.2, distort the structure of DNA (the strand becomes "bent" or "kinked") such that transcription and replication are disrupted.[23–25] If the organism's natural DNA excision repair pathways fail to repair these photolesions, they may lead to DNA mutations and, potentially, cancer.[24–26] The areas of DNA most susceptible to UVB signature photolesion are the most flexible, such as the p53 gene, which was found to be a common site for UV-induced damage and whose mutation is believed to be the initial step towards non-melanoma skin cancer, *i.e.* basal cell carcinoma or squamous cell carcinoma.[21,25] Carcinomas outnumber melanoma cancer in incidence, but are relatively easier to treat. Melanoma cancer tends to metastasize quickly, decreasing the chances of long-term survival for patients diagnosed at an advanced level of the disease. UVB is considered to be the cause for nearly 65% of melanoma and 90% of non-melanoma skin cancer cases.[27]

In comparison, UVA radiation is often regarded as almost innocuous, being a lower energy type of UV radiation which does not interact directly with DNA. The idea that UVA radiation is harmless is misguided, however. UVA radiation has been extensively reported to produce harmful levels of reactive oxygen species (ROS) in the skin, which are a major factor contributing to both skin aging (uneven pigmentation, wrinkling, dryness, sagging, *etc.*) and skin cancer *via* oxidative stress pathways.[28,29] In addition to its adverse effects on the skin, UVA radiation can be more problematic than UVB since: *i)* UVA is approximately 20 times more abundant at the Earth's surface than UVB; *ii)* a significant amount of UVA is transmitted by glass and hence UVA doses are received even when indoors; and *iii)* UVA penetrates the skin much deeper than UVB, reaching far into the dermis, as shown in Figure 1.1.[28,29]

The human body defends itself against such radiative stress by producing melanin pigments to absorb harmful radiation before it reaches DNA molecules.[30] Melanin pigments are stored in keratinocytes, the main constituting cells of the epidermis. The production of melanin, or *melanogenesis*, takes place in the melanocytes. Melanogenesis occurs when the UV radiation dose exceeds a damage threshold activating response pathways in keratinocytes and leading to a cascade of hormonal interactions between keratinocytes and melanocytes.[27] The newly produced melanin is transferred to the keratinocytes, where they provide additional protection against UV radiation and result in darker skin colour, *ergo* tanning. Melanogenesis is a delayed response, however, and it may take three to five days for any significant protection to be afforded by the extra melanin being produced.[31] Any photodamage occurring before the skin is sufficiently protected may have a catastrophic effect on the skin and, at a molecular level, may initiate photochemistry that could ultimately lead to cancer, as discussed above.

The often insufficient natural photoprotection provided by melanin can be complemented by artificial photoprotection. The most effective way to protect skin against UV-induced damage is to avoid UV exposure during critical periods of the day and use protective clothing when outdoors.[32] However, the social desire for sun exposure, often seeking a "tanned look", leads the public to overlook this advice; sunscreens are, in fact, the most popular source of artificial photoprotection.[32] The history of sunscreens starts as early as 1891, when F. Hammer stated that 'materials which prevent UV radiation from reaching the skin protect it from erythema solare'.[33] At that time, the photoprotective capabilities of quinine were being investigated. Later, photoprotective mixtures containing aesculin, a natural compound extracted from chestnuts that had been used in folk medicine for some time, were being sold under the name "Zeozon". The era of modern sunscreens began in the early 20$^{\text{th}}$ century with the production of Ambre Solaire by Eugène Schueller.[33] Made commercially available in 1935, Ambre Solaire contained benzyl salicylate as its active ingredient in an oily vehicle. Since then, other sunscreen active ingredients emerged around the world. Initially, the focus of sunscreens was on avoiding sunburn, widely believed to be caused by UVB radiation, hence the active ingredients in sunscreen products were mostly strong UVB absorbers. However, the growing evidence for the detrimental effects of UVA radiation on the skin, as detailed above, generated interest in UVA protection;[34] the first UVA/UVB sunscreen was developed by Coppertone in the early 1980's.[33] Currently, sunscreens around the globe are required by the relevant regulatory agencies (such as the

United Stated Food and Drug Administration or the European Commission) to provide broad-spectrum photoprotection, *i.e.* against both UVA and UVB radiation.[32]

Modern sunscreens are skin care products whose formulations are a complex mixture of active ingredients, stabilisers, solvents, emollients, film structure enhancers and cosmetic adjuncts. The active ingredients in commercially available sunscreen formulations can be categorised as either particulate filters or organic filters.[32] Particulate filters, such as titanium dioxide (TiO_2) and zinc oxide (ZnO) nanoparticles, are part of sunscreen formulations as particle suspensions. Despite the small size of these sunscreen nanoparticles, they have been shown to remain at the surface of the skin, rather than penetrate into the body where they could have adverse effects.[32] Careful balance between particle size, dispersion, solvent and volume fraction can ensure that particulate filters act as mild, safe and effective UV blockers. Nevertheless, the currently available particulate filters cannot, on their own, provide the necessary protection against UV radiation, since their combined absorption spectra do not cover the full UVA and UVB regions as required by with sunscreen regulations. Therefore, organic filters — also referred to as chemical filters/absorbers or, simply, sunscreen molecules — need to be included in sunscreen formulations to ensure appropriate protection. The chemical absorbers currently used in the sunscreen industry can be grouped into seven broad categories, shown in Figure 1.3: (a) *para*-aminobenzoate derivatives, (b) cinnamate derivatives, (c) benzophenone derivatives, (d) anthranilate derivatives, (e) salicylate derivatives, (f) dibenzoyl methane derivatives and (g) camphor derivatives.[35] Since, as was the case for particulate filters, no single one of these molecules can provide photoprotection across the entire UVA and UVB wavelength range, sunscreen formulations typically include several chemical absorbers. Because sunscreens are seen as both cosmetic and pharmaceutical products — often referred to as *cosmeceuticals* — they are subject to strict regulations and require adequate testing before being made commercially available.[32]

The most fundamental requirement of an ideal sunscreen molecule is that it strongly absorbs UVA/UVB radiation.[36] The efficacy of sunscreens regarding absorption of UVB radiation is measured in terms of sun protecting factor (SPF). SPF values are determined using the *International Sun Protection Factor Test Method*, which measures the degree and response time of skin erythema caused by increasing UV radiation dose (administered by a solar simulator such as a xenon arc lamp) on human subjects with and without sunscreen application.[37] SPF is then defined as the ratio between the minimal erythema
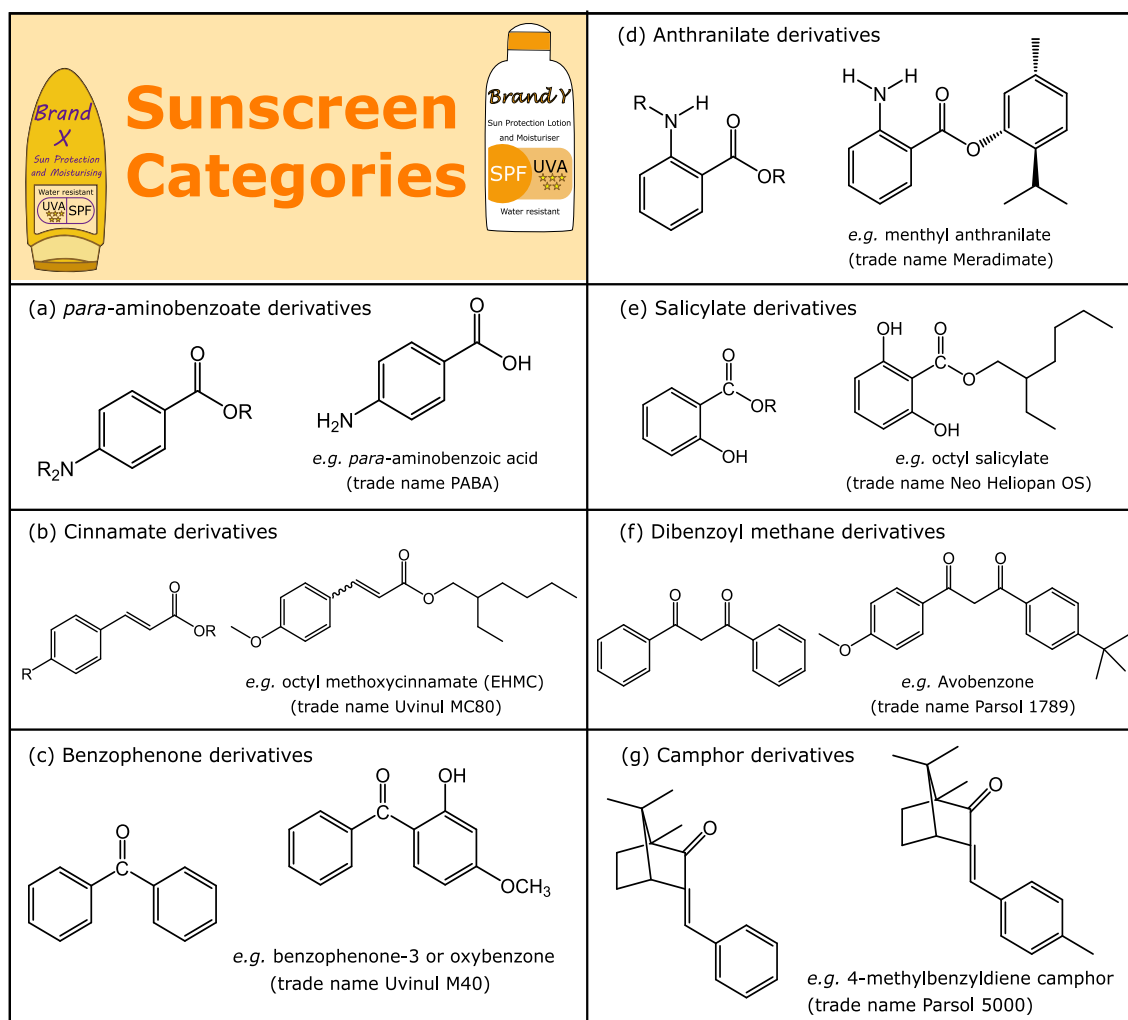
Figure 1.3: The seven main categories of sunscreen active ingredients along with representative examples.

dose (MED, the minimal UV dose required to produce perceptible erythema in human skin) for treated and untreated skin:

$$\text{SPF} = \frac{\text{MED}_{\text{protected skin}}}{\text{MED}_{\text{unprotected skin}}} \tag{1.1}$$

SPF values range from low protection (label SPF 4 – 10), medium/moderate protection (label SPF 15 – 25), high protection (label SPF 30 – 50) and very high protection (label SPF 50+). To ensure sufficient protection against UVA is also provided by sunscreen formulations, the concept of *critical wavelength* was introduced, which is defined as the wavelength at which 90% of the integrated UV absorbance is reached (from 290 nm towards 400 nm).[32] A sunscreen formulation is then said to provide appropriately

broad-spectrum protection if its *critical wavelength* is longer than 370 nm. These testing methods have their limitations, however, since they may be carried out *in vitro* and hence not accurately represent the efficacy of the sunscreen when on the skin. Importantly, most current sunscreen tests report on sunscreen performance for an application dosage of, typically, 2 mg/cm^2 when in reality consumer application doses vary between 0.5 – 1.0 mg/cm^2.[32] While sunscreens have been shown to undoubtedly reduce the risk of erythema, skin aging and skin cancer, there are reported cases of photodamage despite sunscreen application.[32]

Apart from concerns with UV absorption effectiveness, the fact that sunscreen lotions are, after all, skin care products, also raises aesthetical issues in terms of scent, feel and appearance. A sunscreen that can be applied easily, has a pleasant odour and a pleasant on-skin appearance and texture is likely to improve compliance with sunscreen application guidelines and, therefore, aesthetic considerations are extremely important for a sunscreen product.[32,36] An aesthetically pleasing sunscreen can only be achieved if all the components — including UV absorbers — are readily solvated in the sunscreen formulation and do not agglomerate to form a non-uniform lotion. Sunscreens should also not discolour, for example, and, in the case of water resistant sunscreens, the active ingredients should not be soluble in water.[32] Apart from that, sunscreens should of course be non-toxic and pose no risk to human health or the environment. Particular attention should be paid here to the photosensitisation and/or photoallergenic potential of sunscreens. Some UV absorbers may not cause an allergic or other cutaneous reaction when initially applied to the skin, but they may do so after exposure to UV radiation — these species are then called photosensitisers or said to cause photoallergy.[38]

There is one important aspect of sunscreens — and, in particular, of UV absorbers — that is not explicitly taken into account in current regulation requirements or other formulation considerations: their photodynamic behaviour, *i.e.* the molecular events which occur in sunscreens immediately after absorption of UV radiation. A sunscreen molecule's photodynamics encompass both its photochemistry and photophysics, as shall be discussed in more detail in the next section. Upon absorption of UV radiation, a sunscreen active ingredient will have excess energy, the fate of which may or may not produce a macroscopic effect (such as photosensitisation) but it may, nonetheless, cause damage at a molecular level. To avoid such damage, the photodynamics of an ideal sunscreen should allow for dissipation of excess energy without loss of molecular integrity and without generating re-

active photoproducts such as ROS; this sunscreen would then be said to be *photostable.*[39] It is also important that, if excess energy is transferred to other components of the sunscreen formulation or to the skin itself, it does not initiate harmful chemical reactions. An understanding of light–matter (sun–sunscreen) interactions and of the resulting molecular level events is, therefore, essential for a thorough assessment of the safety and efficacy of a UV absorber to be used in commercial sunscreen formulations. The next section of this chapter explores in more detail the principles governing such light–matter interactions as well as the possible fates of excess energy resulting from radiation absorption. These fundamental considerations on light–induced processes are the foundations upon which the ensuing discussion in later chapters is drawn.

1.2 Fundamentals of Quantum Mechanics and Spectroscopy

Spectroscopy is the field of science concerned with the study of the interaction between light (electromagnetic radiation) and matter (namely, atoms and molecules). Given that the photoprotective species in sunscreen formulations are molecules whose purpose is to absorb harmful radiation before it reaches vulnerable skin cells, it is relevant to consider the principles which govern interactions between molecules and radiation, as well as the molecular events which occur as a result of them. These interactions are best described and understood in terms of quantum mechanics. Therefore, a review of quantum mechanical postulates is also relevant at this stage. The following section will first cover the quantum mechanical descriptions of light and matter individually, after which the fundamental principles of spectroscopy relevant to our discussion on sunscreen photodynamics will be presented.

1.2.1 Light: Electromagnetic Radiation

Since theoretical work undergone by James Clerk Maxwell between 1861 and 1865[40] and, later, the experimental observations by Heinrich Hertz in 1887 – 1888,[41] light is described as oscillations of electric and magnetic fields perpendicular to each other.[40,41] More precisely, light can be seen as a propagating electromagnetic wave, hence "light" is sometimes referred to as electromagnetic radiation. The electromagnetic wave is characterised by its frequency (ν, the number of wave cycles completed per unit of time) and its wavelength (λ, the distance between consecutive corresponding points of the wave). These two quan-
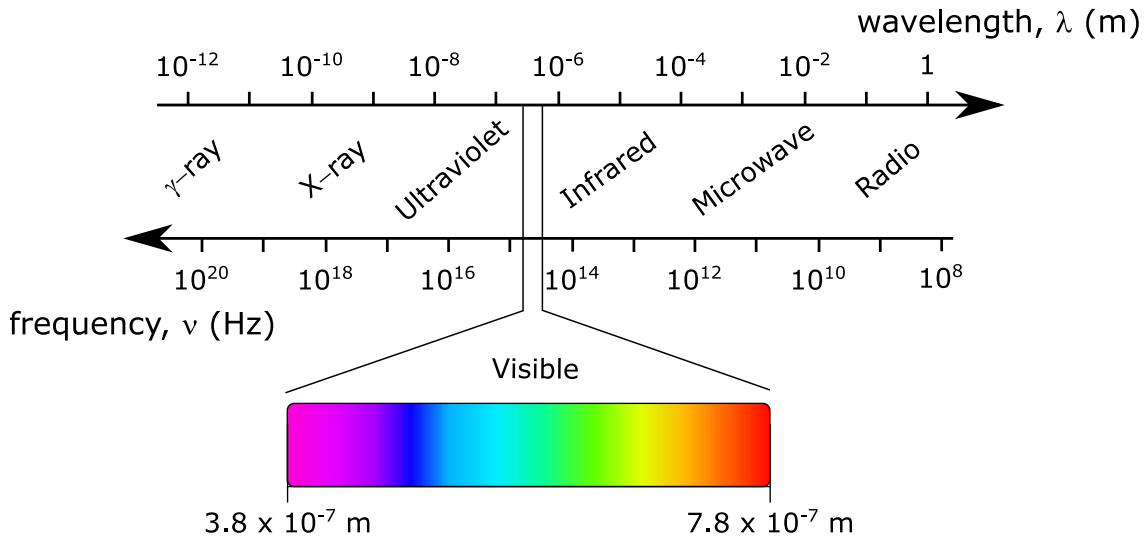
Figure 1.4: The electromagnetic spectrum with approximate wavelength, λ, and frequency, ν, values for each radiation category. The visible range of the spectrum, $\sim 380 - 780$ nanometres (nm, 10^{-9} metres), and the colours associated with these wavelengths is presented in greater detail.

tities are related to each other by the speed of light (in vacuum), $c \approx 2.998 \times 10^8$ metres per second (m $\cdot$ s^{-1}), by $c = \lambda\nu$. The electromagnetic spectrum, shown in Figure 1.4, corresponds to the range of possible frequencies of electromagnetic radiation. In order of increasing wavelength (decreasing frequency), electromagnetic radiation can be classified in seven broad categories: γ-rays, X-rays, ultraviolet (UV), visible (Vis), infrared (IR), microwaves and radio waves.[42]

Any physical object can emit electromagnetic radiation. For a black–body, *i.e.* an idealised object which is capable of absorbing and emitting all wavelengths of radiation, the peak wavelength of the emitted radiation shifts to shorter wavelengths as its temperature, T, is increased, as shown in Figure 1.5.[42,43] Drawing on classical principles, Lord Rayleigh proposed a model for black–body radiation which reasonably predicted the emission spectrum at long wavelengths but failed for shorter wavelengths (see Figure 1.5). In fact, the *Rayleigh–Jeans law* implies that even objects at room temperature would emit UV (and even higher energy) radiation. This obviously nonsensical result is famously known as the "ultraviolet catastrophe".[42,43]

In 1901, Max Planck presented an alternative description of black–body radiation for which the ultraviolet catastrophe was not a concern.[44] A constant term arose from Planck's work on black–body radiation, so that the energy of electromagnetic radiation would be
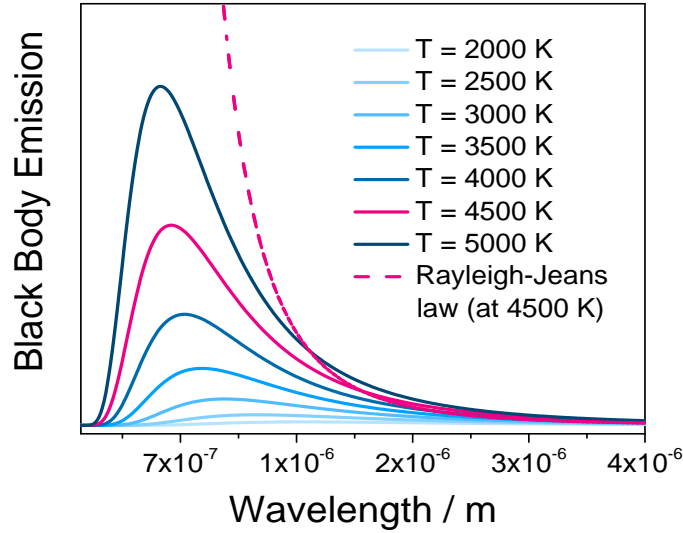
Figure 1.5: Emission spectra from an idealised black–body at different temperatures (increasingly darker blue lines for increasing temperature). The spectra were produced by employing Planck's law (closest to experimental observation), which defines black–body radiation emission as $8\pi hc/\lambda^5(e^{hc/\lambda kT} - 1)$. For comparison, the Rayleigh-Jeans law for a blackbody at 4500 K was also produced (pink dashed line, compared with its equivalent under Planck's law in the pink solid line). According to the Rayleigh-Jeans law the black–body radiation emission is modelled by $8\pi kT/\lambda^4$. Notice that the Rayleigh-Jeans law follows the same trend as Planck's law for long wavelengths but quickly deviates and thus fails to accurately predict black–body radiation emission at higher energies.

given by:

$$E = h\nu \tag{1.2}$$

where h is Planck's constant, $h = 6.626 \times 10^{-34}$ Joules $\times$ seconds (Js). The implications of this result were only fully understood in 1905, when Einstein interpreted the 'pioneering work by Mr. Lenard' on photoelectric phenomena in light of Planck's ideas.[45] These photoelectric phenomena related to the observation that, when irradiating metals with ultraviolet radiation, the ejection of an electron is independent from the light's intensity but highly dependent on the radiation's frequency.[42] Particularly, no electrons are ejected until a certain threshold frequency (characteristic to each metal) is reached, and above this threshold the kinetic energy of ejected electrons increases linearly with increasing frequency of incident radiation. To provide an explanation for these observations, Einstein reasoned that light would be composed of energy *quanta*, *i.e.* a "packet" of energy, or particle of light, now known as a *photon*.[45] Assuming a photon collides with an electron to eject it, for the energy to be conserved the kinetic energy of the electron, eKE, must be defined by:

$$\text{eKE} = \frac{1}{2}m_e v^2 = h\nu - W \tag{1.3}$$

where m_e is the mass of the electron, v its velocity, $h\nu$ is the energy of the photon and W is called the *work function*, *i.e.* the threshold energy necessary to eject an electron from a certain metal.[42,45] This relationship, now commonly referred to as the *photoelectric effect*, predicts both the proportionality between eKE and ν, and the impossibility of electron ejection when $h\nu < W$ (since this implies eKE < 0). The existence of photons — or, in other words, the *particle character of electromagnetic radiation* — was thus proven. Note, however, that the particle-like behaviour of light demonstrated by Einstein does not invalidate its wave-like characteristics: it remains true that, once directed at a set of double slits, a beam of light will produce a diffraction pattern, a characteristic behaviour of a wave.

It is important to expand on this point to mention that, in light of the aforementioned conclusions for photons, Louis de Broglie suggested in his doctoral thesis of 1924 that electrons (commonly regarded as particles) would demonstrate wave-like behaviour under certain conditions.[46] He then defined the *de Broglie wavelength*, *i.e.* the wavelength associated with the wave character of a particle, as:

$$\lambda_{deBroglie} = \frac{h}{p} = \frac{h}{mv} \tag{1.4}$$

with p being the momentum of the particle. Experimental evidence for de Broglie's theories was gathered in the Davisson–Germer experiment of 1928, where an electron beam was observed to produce a diffraction pattern akin to that observed for waves of light and with wavelengths comparable to the theoretical de Broglie wavelength.[47] It was then concluded that both matter and radiation can demonstrate either wave- or particle-like characteristics, depending on the experimental conditions; this is now known as the *wave-particle duality*.[48]

1.2.2   Matter: The Schrödinger Equation

Having established the wave-particle duality, one now needs to consider the behaviour of matter-waves, as well as attempt to extract physical meaning from them. The mathematical description of such waves was provided by Erwin Schrödinger in 1926, with the introduction of the concept of a wavefunction.[49] The wavefunction, Ψ, provides a complete description of any system of total energy E and can be found by solving the *Schrödinger*

equation, commonly presented as:[42]

$$\hat{H}\Psi = E\Psi \tag{1.5}$$

This equation is an example of an eigenvalue problem, *i.e.* one can find an eigenfunction/eigenvalue pair (Ψ/E) that verifies the above relationship. The operator $\hat{H}$ is known as the *Hamiltonian*, a linear hermitian operator whose eigenvalues correspond to the total energy of the system, the sum of kinetic and potential energies. If we write $\hat{H}$ explicitly, in a one-dimensional case the *time-independent* Schrödinger equation becomes:[42,50]

$$-\frac{\hbar^2}{2m}\frac{\mathrm{d}^2\Psi(x)}{\mathrm{d}x^2} + \hat{V}(x)\Psi(x) = E\Psi(x) \tag{1.6}$$

where m is the mass of the particle being considered and $\hat{V}$ is the potential energy operator. When one is concerned with the time evolution of the system, described by a time-dependent wavefunction Φ, the one-dimensional *time-dependent* Schrödinger equation should be evaluated instead:

$$-\frac{\hbar^2}{2m}\frac{\mathrm{d}^2\Phi(x,t)}{\mathrm{d}x^2} + \hat{V}(x,t)\Phi(x,t) = i\hbar\frac{\partial\Phi(x,t)}{\partial t} \tag{1.7}$$

While the work by Schrödinger allowed for a mathematical description of matter-waves, it was Max Born who, also in 1926, suggested a physical meaning for the wavefunction.[51] Specifically, the Born interpretation of the wavefunction is that the square of its modulus, $|\Psi|^2$, corresponds to the probability density, P, of finding a particle between x_1 and x_2 (a one-dimensional region of space), *i.e.*:

$$P = \int_{x_1}^{x_2} |\Psi(x)|^2 \mathrm{d}x \tag{1.8}$$

Born's interpretation places general constraints on what are acceptable solutions for the wavefunction: *i)* the wavefunction must not be infinite over a non-infinitesimal region (the particle must be found at some point within the defined region); *ii)* the wavefunction must be single-valued (only one probability of finding the particle at a single point x); and *iii)* the wavefunction must be continuous and have a continuous slope, due to the second-order differential character of the Schrödinger equation.[42]

Another consequence of the mathematical characteristics of Schrödinger's equation is
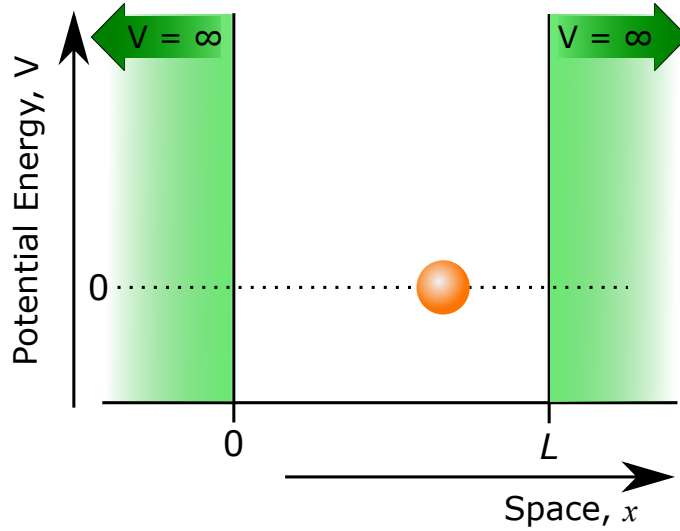
Figure 1.6: Representation of the "particle in a box" scenario, where the motion of particle (in orange) is restricted to the region between $x = 0$ and $x = L$ and at $V = 0$. The particle is surrounded by regions of infinite potential energy on each side, for which $\Psi_n = 0$ (in green). These boundaries essentially trap the particle in this "box": it cannot exist anywhere else as it is impossible to provide it with enough energy for it to be able to leave this region of space.

that it requires certain boundary conditions to be placed on the system for a solution to be found. The importance of such boundary conditions, which imply that only certain wave-functions are acceptable solutions to the Schrödinger equation, is suitably demonstrated by considering the famous problem of the "particle in a box" or "particle in an infinite potential well" (solved in Appendix 1). In this scenario, depicted in Figure 1.6, the system under consideration constitutes a particle of mass m placed in a one-dimensional region of space, from $x = 0$ to $x = L$, where the potential energy is zero; everywhere else, $V = \infty$, and thus $\Psi_n = 0$. The possible solutions to the Schrödinger equation for this system are given by:[42]

$$\Psi_n(x) = C \sin\left(\frac{n\pi x}{L}\right) \qquad\qquad n = 0, 1, 2, 3, \ldots \qquad\qquad (1.9)$$

where C is a constant and L the length of the "box". The integer n which arises from the solution to this problem, often called the *principal quantum number*, describes the energy level state of a given system. For each n, there is an associated wavefunction and its corresponding probability function, $|\Psi|^2$, as shown in Figure 1.7. At this point, it is important to note that while $n = 0$ is, strictly speaking, a mathematical solution to Equation 1.9, this solution would result in a zero-valued wavefunction, so that the probability function would also be zero, *i.e.* the particle would not exist. If one assumes that the particle must exist, $n = 0$ is not a valid solution to the problem of the particle-in-
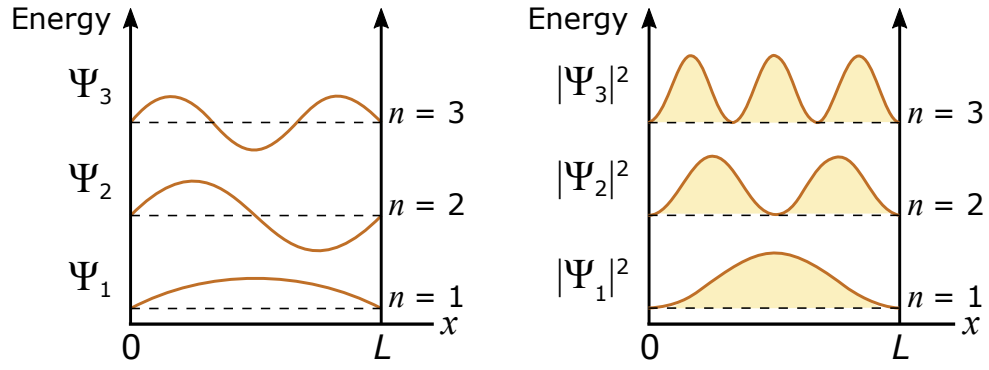
Figure 1.7: Wavefunctions (Ψ, left) and corresponding probability density functions ($|\Psi|^2$, right) for the particle in a box problem. For the particle in a box problem, at $n = 0$ the energy is zero, *i.e.* the wavefunction does not exist, hence, it is not shown in this figure. Moreover, the energy spacing between the energy levels (here shown unchanged for increasing energy) is not shown to scale: for the particle in a box problem, energy level spacing should increase with increasing energy.

a-box. The fact that only certain wavefunctions are solutions to the problem of the particle in a box means that its energy is *quantised* — in stark contrast to the classical particle, whose energy can assume any value. In other words, in the described one-dimensional "box", the particle assumes discrete energy levels, n, the energy of which, E_n, is given by:

$$E_n = \frac{n^2 h^2}{8mL^2} \qquad\qquad n = 1, 2, 3, \ldots \qquad\qquad (1.10)$$

The boundary conditions applied in order to find the wavefunction for the particle in a box system thus give rise to the quantisation of energy and to the principal quantum number n. Analogously, further quantisation arises from applying different boundary conditions to solve the Schrödinger equation. In particular, cyclic boundary conditions reveal quantisation of rotation, giving rise to the *orbital angular momentum quantum number*, l, and the *magnetic quantum number*, m_l.[42] The energy quantisation which arises from these problems is found to have physical significance, *i.e.* the energy of real systems (such as atoms and molecules) is also found to be quantised, with the form of the acceptable wavefunctions depending on the "boundary conditions" of each individual system and being described by a particular combination of quantum numbers, as we will discuss later in this section.

It is interesting to note that the idea that a particle — and, very specifically to the present discussion, an electron — can only assume certain energy levels, in fact precedes quantum physics. Already in 1913, the experimental observation that hot atomic gases

emit radiation of discrete frequencies led Niels Bohr (following on from work by Ernest Rutherford) to suggest that an atom consisted of a central nucleus of positively charged protons and neutral neutrons being orbited by negatively charged electrons (akin to planets orbiting the Sun).[52] Importantly, Bohr's atomic model suggests that the motion of electrons is confined to well defined atomic shells, also called *orbitals*. When being promoted from lower to higher lying orbitals (*i.e.* from closer to further away from the nucleus) an electron will only absorb radiation of the energy corresponding to the energy difference of the orbitals between which it transitions; it is common to refer to this as a *resonant* transition, or to say that the radiation is *resonant* with a given transition. Similarly, the electron will emit radiation resonant with the transition to lower energy orbitals (*i.e.* orbitals closer to the nucleus). These well defined transitions, Bohr suggested, would be the origin of the discrete absorption and emission spectra experimentally observed for atomic gases. We now find that Bohr's classical view that electrons can only occupy n orbitals, with increasing n corresponding to increasing energy, holds true for a quantum physical perspective on a given system, for which n describes its energy level state. However, the quantum physical descriptions of these orbitals are not concentric circles around the nucleus, as suggested in the Bohr model of the atom, nor even necessarily spheres: they may have rather complex shapes, as will be discussed later in this chapter and as can be seen in Appendix B.

1.2.2.1 Solving the Schrödinger equation: hydrogenic atom and beyond

As discussed earlier, solving the Schrödinger equation, that is, finding the eigenvalues and eigenfunctions of the Hamiltonian operator for a given system, should unveil all information regarding that system. In an attempt to understand how the Schrödinger equation may be solved and to evaluate the results that may be obtained from it, let us consider the simple case of an hydrogenic atom, *i.e.* a single electron orbiting a nucleus, described in terms of polar coordinates (r, θ, ϕ), as shown in Figure 1.8.

We recall that in the time-independent Schrödinger equation (Equation 1.6), the Hamiltonian $\hat{H}$ corresponds to the sum of the kinetic and potential energy operators of the system. To describe the motion of the electron relative to the nucleus (proton) in the hydrogen atom problem we must, therefore, consider its potential and kinetic energies.

The Coulomb potential energy for the hydrogenic system is given by:[42]

$$V(r) = -\frac{Ze^2}{4\pi\epsilon_0 r}$$ (1.11)

where Z is the number of protons in the nucleus of the hydrogenic atom, e is the elementary charge (1.602×10^{-19} coulombs, C), ϵ_0 is the vacuum permittivity (8.854×10^{-12} J⁻¹C²m⁻¹) and r is the polar coordinate corresponding to the distance of the electron from the nucleus. The kinetic energy for the hydrogenic electron also depends on the other two polar coordinates, θ and ϕ, and is described by a Laplacian operator, ∇^2, which can be explicitly written as[42]

$$\nabla^2 = \frac{1}{r^2}\frac{\partial}{\partial r}r^2\frac{\partial}{\partial r} + \frac{1}{r^2}\Lambda^2$$ (1.12)

where

$$\Lambda^2 = \frac{1}{\sin^2\theta}\frac{\partial^2}{\partial\phi^2} + \frac{1}{\sin\theta}\frac{\partial}{\partial\theta}\sin\theta\frac{\partial}{\partial\theta}$$ (1.13)

The complete Schrödinger equation for the hydrogenic atom is, then:

$$-\frac{\hbar^2}{2\mu}\nabla^2\Psi - \frac{Ze^2}{4\pi\epsilon_0 r}\Psi = E\Psi$$ (1.14)

where μ is the reduced mass, which in this case can be approximated to the mass of the electron, m_e, given that $1/\mu = 1/m_e + 1/m_n$ and the mass of the nucleus, m_n, is much larger than m_e. Because, as we have just established, the potential and kinetic energy components of the Schrödinger equation for the hydrogen atom depend on different
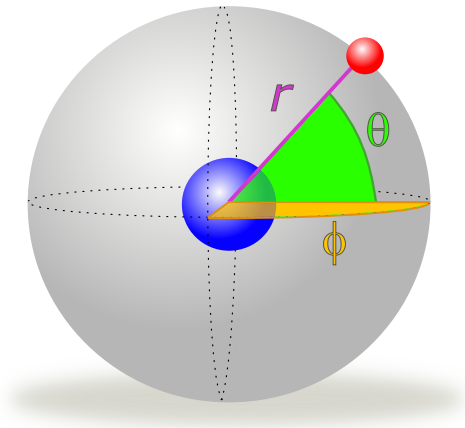
Figure 1.8: The hydrogen atom described in polar coordinates. The blue and red spheres represent the proton (nucleus) and the electron in this system, respectively. The radial coordinate r describes the radius of the atomic sphere (purple line), while θ (green angle) and ϕ (orange angle) are angular coordinates.

coordinates it is reasonable to assume that the two components can be separated. Indeed, such separation of variables is mathematically valid and it follows that the wavefunction for the hydrogenic atom may also be separated into a radial, $R(r)$, and angular, $Y(\theta, \phi)$, component; the potential energy of the system then depends solely on $R(r)$, while its kinetic energy depends on $Y(\theta, \phi)$. The wavefunction can therefore be described by:[42]

$$\Psi(r, \theta, \phi) = R(r)Y(\theta, \phi) \tag{1.15}$$

The solutions to each of these components can then be combined to yield the final wavefunctions, each of which will describe a different atomic orbital of the hydrogen atom, *i.e.* regions of space surrounding the nucleus which may be occupied by the electron. The quantum numbers n (principal), l (angular momentum) and m_l (magnetic), briefly discussed above, emerge here as descriptors of the atomic orbitals, each combination of quantum numbers describing a particular orbital (see Appendix B) and the electrons occupying it. Specifically, for the hydrogen atom, an electron occupying an orbital of quantum number n has an energy E_n of:

$$E_n = -\frac{m_e e^4}{8\epsilon_0^2 h^2 n^2}. \tag{1.16}$$

Notice that, in the equation above, if $n = 1$ then the result reduces to the Rydberg unit of energy (109 677 cm^{-1} or 13.6 eV), which unsurprisingly coincides with the ionisation energy for ground-state hydrogen, *i.e.* with the energy necessary to remove the electron from the hydrogen atom (from $n = 1$), generating H$^+$.

The hydrogenic system in our example will also have an angular momentum of magnitude $\sqrt{[l(l+1)]}\hbar$, with the quantum number $l = 0, 1, 2, \ldots, n - 1$. The direction of the electron's angular momentum is given by $m_l\hbar$, with $m_l = 0, \pm1, \pm2, \ldots, \pm l$. A full description of an electron requires an additional quantum number due to the constraints of the *Pauli exclusion principle*, which states that no more than two electrons may occupy the same orbital and, when two electrons *do* occupy a single orbital, their spins must be paired. Therefore, a *spin magnetic quantum number*, m_s, is necessary to distinguish between these two spin-paired electrons; m_s takes values of $+\frac{1}{2}$ and $-\frac{1}{2}$.[42]

The solutions to the Schrödinger equation for a hydrogen atom thus arise with no significant complications: we can solve this problem exactly and calculate wavefunctions defined by combinations of quantum numbers. However, the complexity of the problem quickly escalates with the addition of another electron, yielding a helium-like atom. For

electrons 1 and 2, at distances r_1 and r_2 from the nucleus, respectively, and at distance r_{12} from each other, we need to consider the kinetic energy of each electron (eKE_1 and eKE_2), the potential energies arising from their interactions with the nucleus (V_{n-e}^1 and V_{n-e}^2) and the interactions between the electrons themselves (V_{e-e}). The Hamiltonian thus becomes:[42,50]

$$\hat{H} = eKE_1 + V_{n-e}^1 + eKE_2 + V_{n-e}^2 + V_{e-e}$$

$$= -\frac{\hbar^2}{2\mu}\nabla_1^2 - \frac{Ze^2}{4\pi\epsilon_0 r_1} - \frac{\hbar^2}{2\mu}\nabla_2^2 - \frac{Ze^2}{4\pi\epsilon_0 r_2} + \frac{e^2}{4\pi\epsilon_0 r_{12}}.$$

(1.17)

The solution to this problem now involves a term which depends on the coordinates of both electrons, which ultimately voids the possibility for separating the variables and thus renders the Schrödinger equation unsolvable for this problem. Electron correlation, as this issue is usually referred to, further complicates for larger atoms, for which the interactions between each pair of electrons needs to be taken into account.

In 1927, Douglas Hartree suggested solving the Schrödinger equation approximately by disregarding instantaneous electron correlation and instead assuming that electrons interact with a Coulomb repulsion cloud. This approach maintains the validity of the separation of variables and, therefore, approximate wavefunctions for the system may be found. If one then describes these tentative wavefunctions as Slater determinants (to ensure that Pauli's exclusion principle is obeyed) and iteratively optimises the result, as suggested by Vladimir Fock, one may calculate reasonable solutions to the Schrödinger equation. This approach, now known as the *Hartree-Fock method*,[55] laid the foundations for the development of computational chemistry, the field of science concerned with calculating the most accurate solution possible to the Schrödinger equation for complex systems and thus modelling and predicting their characteristics and behaviour. The information provided by computational chemistry methods is extremely valuable for the understanding of chemical dynamics and particularly to inform and guide the interpretation of experimental results such as those presented in Chapters 3 and 4 of this thesis. That being the case, a brief overview of computational chemistry will be given in section 1.4.

1.2.2.2   Complicating the problem: diatomic and polyatomic molecules

As we have just discussed, electron correlation renders the Schrödinger equation for many-electron problems unsolvable, even in an atomic scenario, for which only one nucleus needs to be considered. However, most of chemistry (including our discussion on sunscreens)

is concerned with *molecules*: collections of two or more atoms (diatomic and polyatomic molecules, respectively), held together by chemical bonds. Understanding these chemical bonds, as well as the causes and behaviour of their breaking and forming — essentially, the basis of chemical reactions — is one of the most central interests of the chemical sciences.

In classical terms, a bond between two atoms can be thought of as a spring holding together two spheres. When a force is applied to the spring, the spheres will be displaced by a certain amount, x; the spring will then experience a proportional restoring force that causes the system to oscillate towards equilibrium. In one-dimension, the force applied to the system, F, can be described as $F = -dV/dx$, while the restoring force is, simply, $-kx$ (where k is the *force constant*). The potential energy of such an oscillator is given by:[42,50]

$$V(x) = \frac{1}{2}kx^2 \tag{1.18}$$

Equation 1.18 corresponds to a parabolical potential, shown in Figure 1.9(a). We can use this potential energy to define the Hamiltonian of the harmonic oscillator; the solutions to the corresponding Schrödinger equation reveal the quantised energy for the harmonic oscillator, given by:

$$E_v = \left(v + \frac{1}{2}\right)\hbar\omega \qquad\qquad \omega = \sqrt{\frac{k}{\mu}} \qquad v = 0, 1, 2, 3, \ldots \tag{1.19}$$

Each one of the quantised levels that arise from the harmonic oscillator describe a different vibration, *i.e.* a different *vibrational level* or *state*, of the system. The equation above implies that the vibrational energy levels of the harmonic oscillator are equally spaced by $\hbar\omega$. It is important to note that the energy of the harmonic oscillator at $v = 0$ is not zero: as it is clear from Equation 1.19, $E_v = \frac{1}{2}\hbar\omega$ at $v = 0$. This energy is called the *zero-point energy* of the harmonic oscillator, indicating that each bound molecular vibration has a minimum energy which cannot be removed. This can be understood in light of *Heisenberg's uncertainty principle*, which states that the position, x, and momentum, p, of a particle cannot be simultaneously known with absolute certainty.[56] If we specify a molecule's position by confining it to a given potential curve, the uncertainty in the molecule's momentum, Δp, cannot be precisely zero. Since $p = mv$ (see Equation 1.4), it follows that the particle must have non-zero kinetic energy at all times for the uncertainty principle to be valid. While Heisenberg's uncertainty principle, typically presented in the
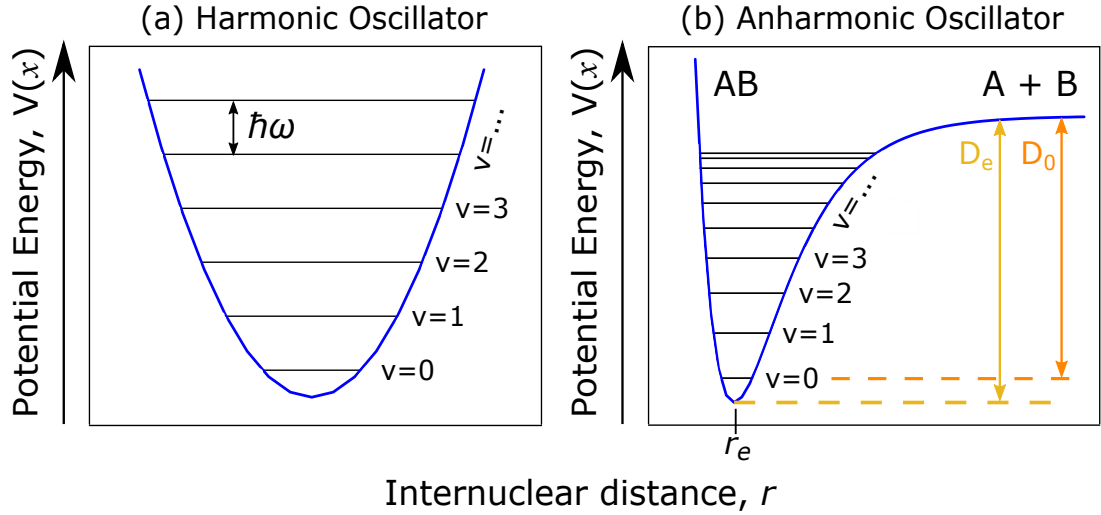
Figure 1.9: Potential energy curves for a (a) harmonic and (b) anharmonic oscillator (not to scale). In (a) the vibrational energy levels are equally spaced by $\hbar\omega$ and the potential energy increases indefinitely for both infitely small and infinitely large internuclear separation. In (b), on the other hand, increased displacement from the position of equilibrium r_e eventually leads to a potential energy plateau, corresponding to the energy of the separate atoms. D_e then defines the depth of the potential energy well and D_0 the molecule's dissociation energy. For short internuclear separations (contraction from the position of equilibrium, r_e) (b) correctly predicts a sharp increase in potential energy, arising from the close proximity of the nuclei.

form:

$$\Delta x \Delta p \geq \frac{\hbar}{2}, \tag{1.20}$$

refers to the specific case of position and momentum, there is also a *generalised uncertainty principle*, which holds valid for any pair of complementary observables, that is, any pair of observables, a and b, whose corresponding operators, $\hat{A}$ and $\hat{B}$ do not commute. Mathematically, the generalised uncertainty principle can be expressed as:

$$\Delta a \Delta b \geq \frac{1}{2}|\langle[\hat{A}, \hat{B}]\rangle| \tag{1.21}$$

where the commutator $[\hat{A}, \hat{B}] = \hat{A}\hat{B} - \hat{B}\hat{A}$. There are broader implications of the generalised uncertainty principle (herein simply referred to simply as uncertainty principle), some of which will be mentioned later, namely when discussing frequency-time uncertainty relationships in Chapter 2.

The parabolic potential of the harmonic oscillator implies that, as the displacement between the two bonded "spheres" (interpreted here as atoms) increases, the potential

energy of the system increases indefinitely. In other words, the harmonic oscillator model of the chemical bond fails to predict bond dissociation, the process by which molecule AB dissociates to generate the separate species A and B (Figure 1.9(b)). In an attempt to improve on the harmonic oscillator description of a chemical bond, let us expand on the earlier approach to the hydrogen atom and consider a system where two nuclei are made to interact. For simplicity, let us also confine motion to the x-axis and suppose the two nuclei interact with only one electron — in essence, we shall consider the case of the hydrogen molecule ion, H_2^+. The full Hamiltonian for such a system is:[50]

$$\hat{H} = -\frac{\hbar^2}{2m_e}\frac{\partial^2}{\partial x^2} - \sum_j \frac{\hbar^2}{2m_j}\frac{\partial^2}{\partial X_j^2} + V(x; X_1, X_2) \tag{1.22}$$

The first term in this Hamiltonian should be familiar from previous discussion: it describes the kinetic energy of the electron. The second term describes the kinetic energy for the two nuclei, with X_j $(j = 1, 2)$ being the location of nuclei X_1 and X_2. The last term describes the potential energy arising from the simultaneous interaction between the three particles.

In the case for an hydrogenic system, discussed above, we have found that separation of variables, made possible due to the dependence of potential and kinetic energies on different coordinates, allows for the Schrödinger equation to be solved. While such separation of variables is not strictly possible for polyatomic molecules, a similar approach can be employed in light of the *Born-Oppenheimer approximation*, which states that the motion of electrons may be considered to be independent from that of nuclei, given the large discrepancies between their masses. Under this assumption, one may separate the overall wavefunction into two terms, one which depends on all three particles and another which depends only on the nuclei. Apart from simplifying the Schrödinger equation, the Born-Oppenheimer approximation has drastic implications and allows for much of the modern understanding of spectroscopy, as we discuss later in this chapter.[42,50] Electronic motion can now be considered to take place under the influence of the potential $V(x; X_1, X_2)$, which accounts for both nuclei-nuclei and nuclei-electron interactions, and, therefore, the electronic wavefunction is given by:

$$-\frac{\hbar^2}{2m_e}\frac{\partial^2 \psi}{\partial x^2} + V(x; X_1, X_2)\psi = E(X_1, X_2)\psi. \tag{1.23}$$

It then follows from the Born-Oppenheimer approximation that nuclear motion will take

place independently from electronic motion, but under the influence of the energy potential $E(X_1, X_2)$. The nuclear wavefunction χ, corresponding to this movement of nuclei is given by:

$$-\sum_j \frac{\hbar^2}{2m_j} \frac{\partial^2 \chi}{\partial X_j^2} + E(X_1, X_2)\chi = \varepsilon(X_1, X_2)\chi. \qquad (1.24)$$

Analogously to what the harmonic oscillator aimed to do, the wavefunction given by Equation 1.24 describes the potential energy resulting from motion of the nuclei relative to each other. Given the two separate electronic and nuclear wavefunctions (Equation 1.23 and 1.24, respectively), valid under the Born-Oppenheimer approximation, instead of solving the Schrödinger equation for all three particles simultaneously, the arrangement of nuclei can be fixed and the electronic wavefunction solved for the resulting potential.[50] A potential energy curve (or surface, if we consider a polyatomic molecule with, at least, 3 atoms) can then be produced by repeatedly changing the nuclei arrangement and calculating the electronic energy contribution for each arrangement; this is, in fact, a method we have employed broadly in our computational studies of sunscreen molecules, as will be further discussed in Chapters 3 and 4.

The behaviour of a potential energy curve produced as described above is suitably modelled by, for example, a Morse potential function (shown in Figure 1.9(b)):[50]

$$V(x) = D_e(1 - e^{-ax})^2 \qquad\qquad a = \sqrt{\left(\frac{k}{2D_e}\right)} \qquad (1.25)$$

where D_e, given in Joules in Equation 1.25, is the depth of the potential energy well (see Figure 1.9(b)). This quantity is not to be confused with the dissociation energy, D_0, since D_0 is measured from the $v = 0$ vibrational level of the state of interest; recall that all molecules possess an irremovable amount of energy, their zero-point energy, E_0. Within the Morse potential description, these two quantities are related by $D_0 = D_e - E_0/hc$, where D_0 is here given in wavenumbers (cm^{-1}).

This deviation from the harmonic oscillator behaviour — called *anharmonicity* —also results in a different energy distribution of vibrational levels. The quantised energy of the anharmonic oscillator described in Equation 1.25 is given by:[42,50]

$$E_v = \left(v + \frac{1}{2}\right)\hbar\omega - \left(v + \frac{1}{2}\right)^2 \hbar\omega x_e \qquad (1.26)$$

where x_e is the *anharmonicity constant*, given by:[50]

$$\omega x_e = \frac{a^2 \hbar}{2\mu} \qquad \text{with} \qquad \omega = \sqrt{\frac{k}{\mu}} \qquad (1.27)$$

and μ is the reduced mass of the system, $1/\mu = 1/m_1 + 1/m_2$. The effects of anharmonicity become more significant for large values of v: vibrational levels are increasingly closer together with increasing v, eventually converging to what is essentially a continuum, or a "bath" of vibrational states. This aspect of the Morse potential model of the molecular bond has important implications for light–matter interactions and for the fate of the energy in excited states; these will be discuss in further detail in section 1.2.3. Quantisation is not limited to the electronic and vibrational energy of a given molecule: rotational and translational energy are also quantised, however, since these are less relevant to the systems under study in this thesis, they will not be discussed further.

Unfortunately, even with the Born-Oppenheimer approximation, the simplest case of the H_2^+ diatomic we have just considered, or any other such single-electron cationic system, is the only "many-nuclei" system for which the Schrödinger equation can be approximately solved. Nevertheless, important information can be extracted from an analysis of the *molecular orbitals* (MOs) for the H_2^+ ion in finding approximate solutions for more complex systems. The two lowest energy molecular orbitals for H_2^+ are shown in Figure 1.10(a) and (b): these MOs resemble atomic orbitals (AOs), but spread over both nuclei.[50] In fact, the most extensively employed approximation in calculating MOs (for either simple diatomic or large, complex polyatomic molecules) is that of a Linear Combination of i Atomic Orbitals (LCAO), each described by an electronic wavefunction ϕ_i and multiplied by a coefficient c_i representing the weight of its contribution to the MO. Within this approximation, the electronic wavefunction which describes the MO, ψ_{MO}, of any given molecule is given by the expansion:[50]

$$\psi_{\text{MO}} = \sum_i c_i \phi_i. \qquad (1.28)$$

The simplest MOs for the H_2^+ ion can be obtained by taking into account only the 1s orbitals of each H atom. The two possible combinations of the 1s orbital of H atom "a", ϕ_a, and that of H atom "b", ϕ_b, corresponding to MOs ψ_1 and ψ_2 are:

$$\psi_1 \approx \phi_a + \phi_b \qquad\qquad \psi_2 \approx \phi_a - \phi_b \qquad (1.29)$$

26

For ψ_1 the AOs interact constructively, so that the electron probability density in the internuclear region is enhanced, pulling the nuclei together; the resulting MO is, therefore, referred to as a *bonding orbital*. The opposite situation occurs for ψ_2: the AOs interact destructively, the electron probability density in the internuclear region decreases and the MO is thus labelled an *anti-bonding orbital*.

The extent to which AOs interact to yield a MO is described by the overlap integral, integrated over all orbital space or volume, dV:

$$S = \int \phi_a^* \, \phi_b \, dV \tag{1.30}$$

with more efficient overlaps occurring for orbitals which *i)* are of the correct size, *i.e.* neither too compact nor too diffuse; *ii)* are of similar energies; and *iii)* have the same symmetry.[50] MOs that have cylindrical symmetry about the internuclear axis, such as those resulting from the interaction from two spherical AOs, are labelled σ, while orbitals which are not symmetrical about the internuclear axis are referred to as π orbitals. Following this notation, the two lowest energy MOs of the H_2^+ ion are labelled 1σ and 2σ, as shown in Figure 1.10 (a) and (b), respectively.

The potential energy curves corresponding to each of the H_2^+ ion MOs we have discussed are shown in Figure 1.10(c). It is important to interpret these curves in terms of the bonding and anti-bonding character of the orbitals to which they correspond. For the 1σ orbital (or state), there is a well defined potential energy minimum towards which the molecule will tend to relax. The molecule will also tend to remain in this region of equilibrium, as there is a clear energy barrier to dissociation. Therefore, when in such a
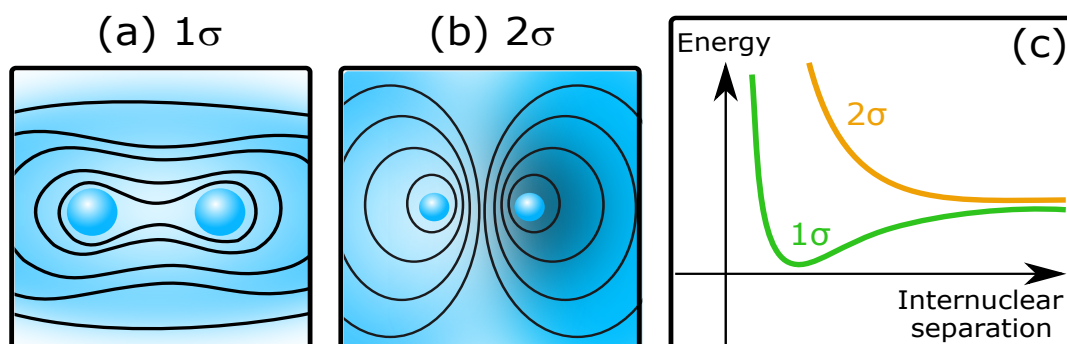
Figure 1.10: Schematic representation of the contour diagrams for the (a) bonding, 1σ and (b) anti-bonding, 2σ orbitals of the hydrogen molecule ion. Light/dark shading represents different orbital phases. (c) Schematic representation of the potential energy curves corresponding to each orbital, 1σ (green line) and 2σ (orange line).

state, a molecule will tend to remain bound unless enough energy is provided to the system to sufficiently displace it from equilibrium and dissociate it; such states are therefore referred to as *bound states*. For the 2σ state of the hydrogen molecule ion, however, no such position of equilibrium exists. The potential energy for the 2σ state tends directly towards the dissociative regime; thus, when in such an *unbound* or *dissociative state*, the molecule will spontaneously dissociate.

In real systems, such as the many-atom sunscreen molecules we are discussing, several electrons populate the available MOs. For a molecule at rest in its lowest electronic state, electrons are distributed amongst the several MOs according to the *aufbau principle*, which states that electrons occupy available orbitals in order of increasing energy. [42] Moreover, the previously mentioned Pauli's exclusion principle still applies for MOs: only two electrons of paired spins may occupy the same orbital. Note, however, that there are cases of single orbital occupancy. In such cases, *Hund's maximum spin multiplicity rule* applies, where spin multiplicity is defined as $2S+1$ and S is the molecule's total spin angular momentum; we then refer to singlet, doublet, triplet states, *etc.* for $S = 0, 1, 2$, *etc.* According to Hund's rule, electrons of parallel spins singly occupy degenerate orbitals before doubly occupying any one of them, since that would result in maximum spin multiplicity. [42,50]

The last of the occupied valence orbitals (*i.e.* the higher energy, outer-lying orbitals, as
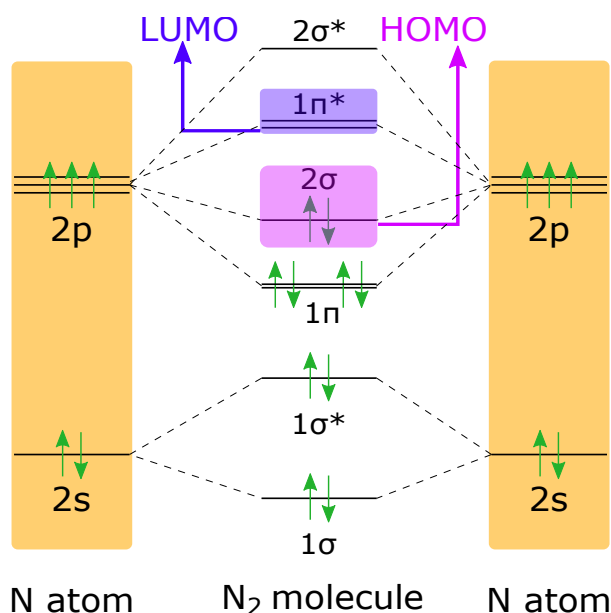
Figure 1.11: MO diagram representing how the 2s and 2p AOs of two nitrogen (N) atoms combine to give the σ and π molecular orbitals of molecular nitrogen. The * refers to anti-bonding orbitals. The HOMO and LUMO orbitals are also highlighted.

opposed to lower energy, core orbitals) is usually termed the highest occupied molecular orbital (HOMO), with the next orbital being the lowest unoccupied molecular orbital (LUMO); both are shown in the MO diagram for nitrogen presented in Figure 1.11. These are the orbitals commonly involved in the electronic transitions we will be concerned with in the ensuing discussion and throughout this thesis. In particular, we refer to LUMO $\leftarrow$ HOMO electronic transitions, $e.g.$ electronic transitions from a molecule's singlet ground-state, S_0, to its its first singlet excited state, S_1, which we shall term a $S_1 \leftarrow S_0$ transition. However, a molecule has S_n excited states ($n = 1, 2, 3, \ldots$), hence transitions to higher lying excited states are possible if enough energy is provided to the system. For a molecule with fully occupied MOs in the ground electronic state, a $S_2 \leftarrow S_0$ generally corresponds to a LUMO+1 $\leftarrow$ HOMO transition, a $S_3 \leftarrow S_0$ corresponds to a LUMO+2 $\leftarrow$ HOMO transition, $etc.$ We note, however, that other transitions are possible, such as LUMO $\leftarrow$ HOMO-1 or other such combination. When talking about the chromophores (light-absorbing units) of large molecules (particularly the sunscreen molecules under study in the work presented in this thesis) we also commonly refer to $\pi^* \leftarrow \pi$ and $\pi^* \leftarrow n$ transitions, for example. These transitions involve promotion of electrons from a bonding π orbital to an anti-bonding π orbital or from a non-bonding orbital (n) to an anti-bonding π orbital, respectively. This notation will be used in the next section, where we will explore the nature and principles governing such transitions, and throughout the following chapters.

1.2.3   The Interactions between Light and Matter

Now that we have discussed the principles by which we describe and understand light and matter individually, we may proceed to explore the principles which govern the interactions between them. In the ensuing discussion, we shall focus on the effects of UV/Vis light on matter, since this is most relevant in the context of sunscreen science.

1.2.3.1   Photoexcitation: Absorption of Radiation

As we have discussed in earlier sections, in light of quantum mechanical principles energy is said to be quantised, $i.e.$ a particle can only occupy discrete energy levels. As a result, the particle will preferentially absorb radiation whose energy coincides with the energy difference between a given initial and final states; the radiation is then said to be

resonant with the transition between these two states. An ideal sunscreen molecule should, therefore, have resonant transitions within the UVA and UVB range of the electromagnetic spectrum, so that it strongly absorbs these wavelengths. Transitions resonant with the UV/Vis region of the electromagnetic spectrum are likely to prompt the promotion of an electron from a lower energy state of the sunscreen molecule to a higher energy state — called an *electronic* transition — since the energy difference between electronic energy levels is usually on the order of $\sim 100\,\mathrm{kJmol^{-1}} \sim 1\,\mathrm{eV} \sim 8065\,\mathrm{cm^{-1}}$, approximately matching the orders of magnitude for UV/Vis energies.[42] For comparison, the analogous value for vibrational energy levels is $\Delta E_{\mathrm{vib}} \sim 10\,\mathrm{kJmol^{-1}}$.[42]

As the electron transitions between an initial (i) and a final (f) electronic state, there will be a charge redistribution across the molecule, the extent of which is described by the *transition dipole moment*, μ_{if}, given by:[42,50]

$$\mu_{if} = \int \psi_f^* \, \hat{\mu} \, \psi_i \mathrm{d}V \tag{1.31}$$

where $\hat{\mu}$ is the electric dipole moment operator, and ψ_i and ψ_f are the electronic wavefunctions for states i and f, respectively. For an electronic transition to take place, its transition dipole moment must be non-zero, which will be true if the integrand $\psi_f^* \, \hat{\mu} \, \psi_i$ is totally symmetric (*i.e.* it remains unaltered for any symmetry operation). This will be the case if the direct product of the irreducible symmetry representations for the initial state, Γ_i, transition dipole moment, $\Gamma_{\hat{\mu}}$, and final state, Γ_f, contains the totally symmetric representation, $\Gamma^{(s)}$:

$$\Gamma_i \otimes \Gamma_{\hat{\mu}} \otimes \Gamma_f \supseteq \Gamma^{(s)}. \tag{1.32}$$

This is a consequence of group theory considerations, and in particular a consequence of the orthogonality of different irreducible symmetry representations,[57,58] however, group theory will not be discussed in any great detail in this thesis. According to Equation 1.32, if photoexcitation takes place from a totally symmetric state, the symmetry product between the transition moment operator and the final state must contain the totally symmetric irreducible representation[57,58] (along at least one of the x, y, z coordinates which describe the molecule) for the transition to be formally *symmetry allowed*.[59,60] If, for the photoexcitation from a totally symmetric state, none of the three products $\mu_x\psi_i$, $\mu_y\psi_i$ or $\mu_z\psi_i$ is totally symmetric, then the transition is said to be *symmetry forbidden*.[59] Under this symmetry selection rule, $\pi^* \leftarrow \pi$ transitions are typically strong (also said to be *bright*

transitions) due the common π character of the initial and final orbitals. On the other hand, $\pi^* \leftarrow n$ transitions are commonly very weak, *dark*, transitions.[42,50] The strength of electronic transitions can be described in terms of *oscillator strength*, f: in general, $f \sim 1$ for bright transitions and $f \ll 1$ for dark transitions.

Notice however, that forbidden transitions are not *non-existent*. Symmetry rules as strict as we have just stated them are only valid for the case of pure electronic transitions and this is seldom representative of experimental observation. There is a whole manifold of vibrational levels associated with each of the molecule's electronic states (akin to what is shown in Figure 1.9(b)) which may be accessed upon photoexcitation. In fact, electronic spectra (showing either absorption to or emission from electronic energy levels) often display vibrational structure, *i.e.* electronic spectra in which finer bands (corresponding to vibrational levels) are superimposed onto the broader electronic absorption (or emission) features, due to vibrational-electronic transitions.[42] Such *vibronic transitions* are the result of coupling between vibrations and electronic transitions; this coupling may relax the aforementioned symmetry selection rules so that "symmetry forbidden" transitions are, in fact, observed in experimental spectra. To account for the effects of vibronic coupling to the intensity the vibronic transition between states i and f, a vibrational term should be added to the transition dipole moment integrand:[50]

$$\mu_{if} = \int \psi_f^* \psi_{f,vib}^* \; \hat{\mu} \; \psi_i \psi_{i,vib} \; \mathrm{d}V. \tag{1.33}$$

The symmetry of the vibrational levels thus plays a role in the overall vibronic transition, which often results in a change of symmetry for the relevant products and thus attenuates the selection rules for the transition.

Apart from symmetry, a number of other selection rules related to the conservation of momentum and spin govern vibronic transitions. The selection rules which ensure conservation of momentum for a given electronic transition are related to the fact that a photon is considered to carry a spin angular momentum of 1.[42] Hence, a change in orbital or electronic angular momentum ($\Delta\Lambda$ and $\Delta\Omega$, respectively) must take place for a photon-induced transition, in order to compensate for the angular momentum carried by the photon and thus conserve momentum. Thus, the selection rules for orbital and electronic angular momentum are $\Delta\Lambda = 0, \pm 1$ and $\Delta\Omega = 0, \pm 1$, respectively. Conversely, photon characteristics do not influence electronic spin, so that the selection rules in this

case are that both an electron's individual spin (Σ) and the system's overall spin multiplicity (S) must remain the same upon electronic transition; these selection rules are often represented as $\Delta\Sigma = 0$ and $\Delta S = 0$, respectively.[42,50] These spin selection rules are of particular relevance to the studies herein presented, namely the spin multiplicity selection rule, which implies that only singlet-singlet or triplet-triplet transitions are formally *spin allowed* (even though, as we shall discuss at a later stage, singlet-triplet transitions do take place in real systems).

Finally, we discuss a crucial factor which contributes to the intensity of a given vibronic transition and stems directly from the Born-Oppenheimer approximation, that is, the assumption that the motion of an electron as it undergoes vibronic transitions is independent from nuclear motion. In a potential energy curve (such as the one in Figure 1.9(b), for example) such transition could be represented as a vertical line (such as the green arrows in Figure 1.12), *i.e.* increased energy with no changes in internuclear separation, hence why electronic transitions are sometimes said to be "vertical". In quantum mechanical terms, it can analogously be said that upon vibronic transitions nuclei retain their dynamical state, so that preferred electronic transitions are those for which there is minimal or no change in nuclear configuration — this statement is the basis of the *Franck-Condon*
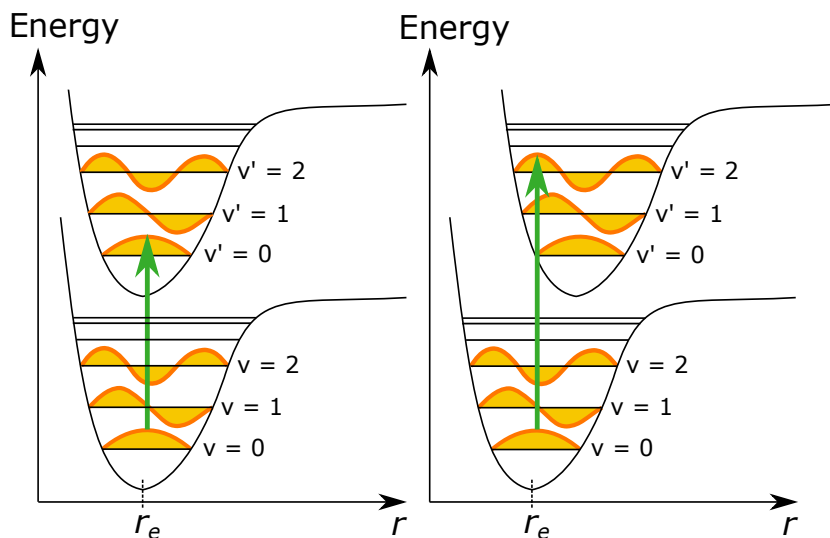
Figure 1.12: Pictorial representation of the Franck-Condon principle. A vibronic transition (represented by the green arrows) will occur to the excited state whose wavefunction best overlaps with the initial state; if the potential energy curves for the two states are displaced (as shown on the right), the vibronic transition may preferentially occur to a higher lying vibrational state. As per common notation, the vibrational states of the ground electronic state are labelled with v, while those of the first electronic excited states are labelled v' (those of the second electronic excited state would be v'', of the third v''', *etc.*).

Principle, which guides much of the current understanding of vibronic transitions.[42,50,61] Assuming, for a given sunscreen molecule under study, for example, that the molecule is initially in the ground vibrational level (v = 0) of its ground electronic state, the vibronic transition will take place to the vibrational level in the excited state whose nuclear wavefunction most closely resembles the nuclear wavefunction of the initial state, as shown in Figure 1.12. This "resemblance" is best referred to as an overlap between the nuclear wavefunctions of the initial and final vibronic states, the extent of which is measured in terms of *Franck-Condon factor*:[42,50]

$$|S(v_f, v_i)|^2 = \left| \int \chi^*_{v,f} \chi_{v,i} \; \mathrm{d}V \right|^2 \tag{1.34}$$

In considering the vibronic state to which photoexcitation will most likely occur (in terms of its Franck-Condon factor), we refer to a "Franck-Condon state" or speak of a "vertical excitation region". If the potential energy curves for the two vibronic states involved in the transition are aligned, *i.e.* their equilibrium nuclear arrangements are similar, the most likely transition will be $S_n(v = 0) \leftarrow S_0(v = 0)$; however if there is a considerable geometry change upon photoexcitation a $S_n(v = v') \leftarrow S_0(v = 0)$ transition is likely to take place instead, as depicted in Figure 1.12. For each of these cases the system would be said to have a Franck-Condon propensity of $\Delta v = 0$ (aligned potentials) or $\Delta v \neq 0$ (misaligned potentials).

1.2.3.2   Decay of Excited States: the Fate of Excess Energy

We have just described how vibronic transitions to higher energy vibronic states occur as a result of absorption of a photon — these are the events taking place when a sunscreen molecule absorbs UV/Vis radiation. As we have briefly mentioned earlier in this chapter, an ideal sunscreen molecule should be able to dissipate excess energy without detriment to its molecular integrity and without generating reactive photoproducts or initiating undesirable side reactions. If the molecule is able to dissipate the excess energy relatively fast and thus return to its ground electronic state, it is less likely that this excess energy will be available to prompt any of the aforementioned undesirable processes.

The rates at which molecules dissipate energy, or the rates of photochemical and photophysical reactions, can be described in terms of chemical kinetics.[62] The decay of excited states can be said to be *unimolecular*: taking the example of fluorescence, the reaction can

be written $A^* \rightarrow A + h\nu$, with $h\nu$ representing the energy of the emitted photon; species A therefore does not need to collide or react for the reaction to take place. Instead, the rate of the unimolecular reaction depends only on the "concentration" of species A^*, $[A^*]$, and the reaction *rate constant*, k. The reaction is therefore said to be *first-order*, and the corresponding *differential rate law*, describing the rate of the process, is given by:[62]

$$\frac{d[A^*]}{dt} = -k[A^*] \tag{1.35}$$

where the rate constant k accounts for all sources of excited state population decay, radiative and non-radiative, which we will describe in greater detail in the ensuing discussion. Note, however, that this equation would apply only in the case of instantaneous photoexcitation, *i.e.* the light source is turned off immediately after photoexcitation takes place. For continuous irradiation, the photoexcitation step needs to be taken into account when determining the rate of decay of the photoexcited species. The kinetic scheme for the overall reaction, including the photoexcitation step, is $A + h\nu \rightarrow A^* \rightarrow A$ and Equation 1.35 takes the form:

$$\frac{d[A^*]}{dt} = k_{\text{abs}}[A] - k_{\text{R}}[A^*] - k_{\text{NR}}[A^*] \tag{1.36}$$

where $[A]$ is the concentration of the non-photoexcited species and $[A^*]$ is the concentration of the photoexcited species (as above); in discussing excited state decays, the "concentration" is taken to be the population of the decaying excited state. Morevoer, k_{abs} corresponds to the rate constant associated with light absorption and k_{R} and k_{NR} correspond to the rate constants associated with radiative and non-radiative decay processes, respectively.

For the ultrafast laser spectroscopy experiments discussed and presented in later chapters, since ultrashort laser pulses are used, it is assumed that photoexcitation is instantaneous and the ensuing kinetics are therefore satisfactorily described by Equation 1.35. In light of this assumption, the decay of excited state population over time is given by the integrated rate law corresponding to Equation 1.35:[62]

$$A^*(t) = A_0^* \, e^{-kt} \tag{1.37}$$

Hence, the relaxation of excited states is an exponential process, the timescale of which is determined by the values of the rate constant k. Other important quantities that are often referred to when discussing the kinetics of the decay of excited states are the *lifetime*

and *half-life* of the excited state. A lifetime, τ, is defined as the point in time at which the excited state population is reduced to $1/e$ of its initial value, given by $\tau = 1/k$. One half-life, on the other hand, is the time taken for the excited state population to fall to half of its initial value, defined as $\tau_{1/2} = \ln 2/k$. This terminology will be used throughout ensuing discussion to describe the decay of excited states.

For the remainder of this section, we shall explore the decay pathways that are available to a photoexcited molecule. These pathways are usually grouped into "radiative" and "non-radiative" categories; together, they constitute a molecule's *photophysics* as they do not involve any chemical reactions, *i.e.* breaking or forming of molecular bonds. Such chemical processes (which are also non-radiative) may also occur, however, and those would instead be referred to as the molecule's *photochemistry*. The combination of photophysical and photochemical processes undergone by a given molecule are referred to as the molecule's *photodynamics*.

1.2.3.2.1 Non-Radiative Decay Pathways

There are several mechanisms by which a photoexcited molecule may dissipate excess energy non-radiatively, *i.e.* with no emission of radiation. Such mechanisms typically take place on a femto- to picosecond timescale (10^{-15} to 10^{-12} s, respectively)[63] and tend to play an important role in the photodynamics of effective sunscreens, as will be made clearer in the following chapters.

(a) Vibrational Relaxation (VR)

We refer here to vibrational relaxation (VR) in general terms to describe the process by which a molecule's excess energy is redistributed amongst a number of vibrational states or dissipated as heat to its surroundings. It is important to note that VR processes are distinct for molecules in vacuum and in solution.[64,65] In vacuum, the molecule is isolated and thus there is no sink for its excess energy, which can thus only be redistributed amongst the molecule's own vibrational states. As a consequence, the VR process in vacuum is usually termed *intramolecular vibrational redistribution* (IVR). When in solution, on the other hand, the photoexcited molecule is surrounded by a solvent *bath* onto which excess energy may be transferred. The VR process in solvent thus includes contributions from IVR and *intermolecular energy transfer* (IET).

It is usually said that VR processes, in particular those which take place intramolecularly, are faster when molecules are photoexcited to higher energies, so that higher vibrational levels are accessed. This is a reflection of *Fermi's Golden Rule*[66,67] which states

that the rate of VR, k_{VR}, is proportional to the density of states, $\rho(E)$:

$$k_{\mathrm{VR}} = \frac{2\pi}{\hbar}|V|^2\rho(E). \tag{1.38}$$

Therefore, closer to the limit of a continuum of vibrational states, where the density of states is of course much higher, k_{VR} would be larger. However, note that k_{VR} is also proportional to the coupling between states, $|V|^2$, which implies that a higher density of states will only lead to more efficient VR providing the additional states are sufficiently coupled.[64]

(b) Internal Conversion (IC)

Internal conversion (IC) refers to the transition between electronic states of the same spin multiplicity, often facilitated by conical intersections (CIs).[42] CIs, which are a result of the breaking of the Born-Oppenheimer approximation discussed earlier in this chapter, are ubiquitous in nature, having been shown to play crucial roles in the photodynamics of many biologically relevant systems.[68,69] In light of the Born-Oppenheimer approximation, often said to be an *adiabatic* approximation, the motion of nuclei and electrons is considered to be independent, or *decoupled*. As the existence of CIs demonstrates, however, there are important cases for which this approximation breaks down and the coupling between nuclei and electrons is no longer negligible. Therefore, CIs are *non-adiabatic* phenomena, inherently quantum mechanical due to the coupling of nuclei and electrons. Moreover, the passage of excited state population through a CI depends both on the initial conditions of the system and the topology of the PES, such that CIs are inherently dynamical. As such, it is reasonable to describe these phenomena using the time-dependent Schrödinger equation (of the form of Equation 1.7) for a given molecule under study, now including nuclei-electron motion coupling:[68]

$$[\widehat{\mathrm{KE}}_n + \mathbb{V} - \hat{\mathbf{\Lambda}}]\chi = i\hbar\frac{\partial\chi}{\partial t} \tag{1.39}$$

where $\widehat{\mathrm{KE}}_n$ is the nuclear kinetic energy operator, $\mathbb{V}$ is a matrix representing the potential energy surface of the molecule, χ is the nuclear wavefunction and $\hat{\mathbf{\Lambda}}$ is the matrix of *non-adiabatic coupling operators*. If we consider only states i and f for the molecule under study, described by the electronic wavefunctions ψ_i and ψ_f, the corresponding non-

adiabatic coupling operator, $\hat{\Lambda}_{if}$, is given by:[68]

$$\hat{\Lambda}_{if} = \frac{1}{2m}\left(2\mathbf{F}_{if} \cdot \nabla + G_{if}\right) \tag{1.40}$$

where m is a suitable mass-scale and ∇ is a derivative operator with respect to nuclear coordinates. The terms $\mathbf{F}_{if}$ and G_{if} are the derivative coupling vector and scalar coupling, respectively, defined as:[68]

$$\mathbf{F}_{if} = \langle\psi_i|\nabla\psi_f\rangle$$
$$= \frac{\langle\psi_i|\nabla\hat{H}_{elec}|\psi_f\rangle}{\Delta E_{if}} \tag{1.41}$$

and

$$G_{if} = \langle\psi_i|\nabla^2\psi_f\rangle. \tag{1.42}$$

In the equations above, $\hat{H}_{elec}$ is the electronic Hamiltonian, ΔE_{if} is the energy difference between states i and f, and $\nabla^2 = \nabla \cdot \nabla$ is the Laplacian operator, already defined in Equation 1.12. Importantly, from Equations 1.39 – 1.41, it is clear that the non-adiabatic coupling operator is inversely proportional to the energy difference between the PES for each state — as the energies of states i and f approach degeneracy, the coupling between nuclear motion on different surfaces increases, so that excited state population initially on the PES for state i may spread into the PES for state f without losing energy,[68] *i.e.* it may undergo IC from state i to state f. The topology of the PES of state i and f will resemble a double cone meeting at the point of degeneracy, which justifies the name of these *conical* intersections.[68] The plane which includes the point of degeneracy is called the *branching space* and, orthogonal to this plane, is the intersection space, a $N - 2$ dimensional seam of CIs (where N is the number of internal coordinates of the molecules);[68] there are then $3N - 8$ potential points of transition between the PES of two states *via* a conical intersection. As such, there will be a number of molecular motions undergone by photoexcited sunscreen molecules that may drive them towards a CI between two given electronic states. In the context of sunscreen molecules, CIs between any excited and the ground electronic states are of particular importance, since they allow for efficient relaxation to take place, as is ideal for a sunscreen molecule.[70,71] Both IC processes and CIs feature heavily in the following chapters since, as will be demonstrated later in the discussion, they are essential for ideal sunscreen photodynamics.

(c) Intersystem Crossing (ISC)

Intersystem crossing (ISC) involves a transition between states of different multiplicity, for example from an excited singlet (S) to an excited triplet (T) state.[42] Population of triplet states *via* ISC is usually rare given the formally forbidden character of the S $\to$ T transition in light of the spin selection rules we have discussed earlier in this chapter. Nevertheless, coupling between the angular momenta of electrons and orbitals, called *spin-orbit coupling*, enhances ISC processes.[72] According to *El-Sayed's rule*, spin-orbit coupling is preferred between singlet and triplet states of different symmetry and thus it follows that a $^3\pi\pi^* \to {}^1n\pi^*$ is more likely to occur than a $^3\pi\pi^* \to {}^1\pi\pi^*$, for example (where the superscripts one and three indicate a singlet or a triplet state, respectively).[72] El Sayed's rule will be of relevance to the discussion in Chapter 3. Being a forbidden transition, ISC is usually the slowest of the non-radiative pathways and it may occur over several hundreds of picoseconds and, indeed, usually much longer.[63]

1.2.3.2.2 Radiative Decay Pathways   These are pathways by which the molecule releases the excess energy by emitting a photon of the energy corresponding to the energy difference between the states involved in the transition.[42] The same selection rules that apply for absorption of a photon are valid also in the case of emission. While, in principle, such a transition can occur between any combination of excited and ground states, *Kasha's rule* states that radiative pathways occur preferentially from the lowest excited state for a given multiplicity,[73] *i.e.* a radiative $S_1 \to S_0$ transition will predominantly occur, rather than $S_2 \to S_0$, for example. Radiative decays occur over much longer timescales than non-radiative decays: fluorescence lifetimes may vary between few nanoseconds (ns) to microseconds (μs), while those for phosphorescence may reach several seconds.[63]

(a) Fluorescence

The allowed radiative transition between two states of the same spin multiplicity (generally an excited state and the ground state) is called fluorescence.[42] If the absorption step takes place to the ground vibrational level of the excited electronic state, *i.e.* a transition of the type $S_n(v = 0) \leftarrow S_0(v = 0)$, for example, the radiation emitted by fluorescence should have the same energy as the energy absorbed. However, as we have discussed before, vibronic transitions may populate higher energy vibrational states of a given excited state, *i.e.* a $S_n(v > 0) \leftarrow S_0(v = 0)$ transition may take place. In this case, VR processes and nuclear rearrangement on the excited state are likely to occur on much faster timescales

than fluorescence, dissipating or redistributing some of the energy initially provided to the molecule before a photon is emitted. When the system eventually radiatively decays, therefore, the radiation emitted is of lower energy than that was absorbed. Experimentally, this manifests as a red-shift in the emission spectrum for a given molecule in comparison to its absorption spectrum, commonly referred to as a *Stokes shift*.[74] For similar reasons, solvent re-arragements around the photoexcited molecule may also produce a measurable red-shift in its emission spectrum.

(b) Phosphorescence

Once the manifold of triplet states is populated *via* ISC, excited state population may radiatively decay onto the ground state, the transition being called phosphorescence (the same term applying for any transition between states of different multiplicity).[42] This $T_n \rightarrow S_0$ transition is formally forbidden and hence phosphorescence may occur over several seconds.[63] Since excited triplet states are usually lower in energy than their singlet state counterparts (recall Hund's rule of maximum multiplicity for singly occupied orbitals), the radiation emitted by phosphorescence from the low vibrational levels of a triplet state (see Figure 1.13) is usually of lower energy than fluorescence. The earlier discussion regarding Stokes shifts in fluorescence also applies for phosphorescence.

1.2.3.2.3   Dissociation and other Photochemistry   The excess energy provided to a molecule upon photoexcitation may result in its photodissociation, which is a non-ideal scenario for a sunscreen molecule. Excited state photodissociation can occur if the molecule is excited directly to a dissociative state, but it is more common that a bright bound state is populated first, followed by excited state population migration to a dissociative state *via* a CI.[42,75] If a sunscreen molecule dissociates upon photoexcitation the sunscreen formulation will degrade and lose its photoprotective capabilities faster, which is clearly not ideal. If the resulting photodissociation products are reactive, the sunscreen molecule poses further risks for use in sunscreen formulations.[32] Moreover, a sunscreen molecule may transfer energy to other molecules in its surroundings;[76] energy transfer to the environment is particularly concerning in a sunscreen context given that it could initiate potentially harmful side reactions in other components of the sunscreen formulations or, indeed, in the skin.[77] Longer excited state lifetimes increase the probability of such energy transfer taking place, hence why it is desirable that a sunscreen molecule dissipates the excess energy on an ultrafast timescale.
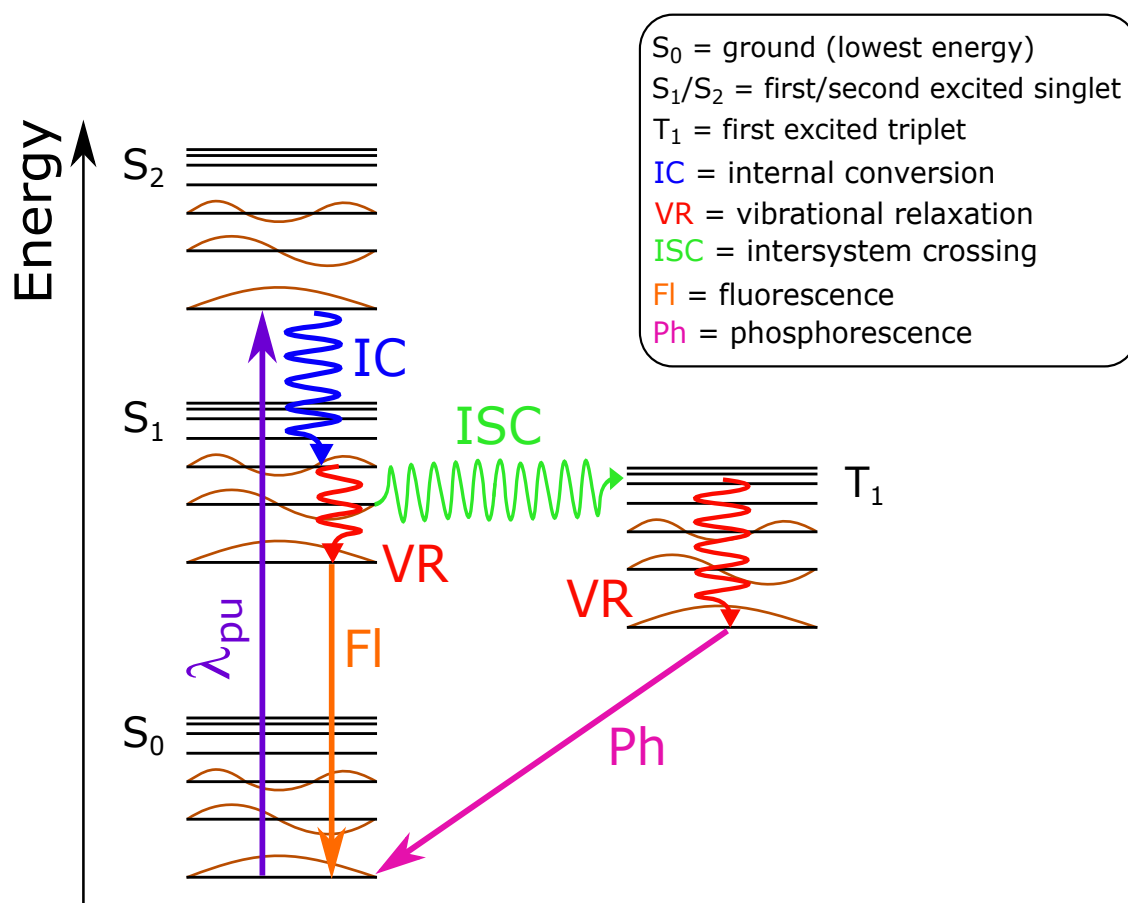
Figure 1.13: Jablonski diagram demonstrating several photophysical processes by which absorbed energy (λ_{pu}) may be dissipated. The singlet and triplet manifold of states are presented next to each other by convention. Internal conversion (blue), vibrational relaxation (red) and intersystem crossing (green) are non-radiative decay pathways; fluorescence (orange) and phosphorescence (pink) are radiative decay pathways. Note that while IC is represented as a downwards arrow along the energy axis (for simplicity), this process does not, in fact, lead to loss of energy: rather, the energy is distributed along coordinates orthogonal to the one represented in this figure. The internal energy of the system thus remains constant but is redistributed between different molecular vibrational modes ('dissipated as heat'). The case of VR is more complex, as it is environment dependent. In vacuum, there is no sink for excess energy and hence, as just discussed, this energy is redistributed amongst the vibrational modes of the molecule, the internal energy of the system remaining constant; the process is then referred to as IVR. If a molecule is solvated, however, while IVR processes may still take place, the solvent can now act as a sink for excess energy: the molecular internal energy does decrease and the red downward arrows representing VR in this figure would be an accurate description of the process. In this case, the process is referred to as IET. See main text for more details.

Even though one, or a combination, of the photophysical processes just described may constitute the predominant relaxation pathway for a given molecule, it is likely that all of them may occur to a certain extent. Importantly, a real system does not consist of an isolated molecule but a collection of molecules. Therefore, the experimentally observed behaviour is the average behaviour of an *ensemble* of molecules. We then refer to the *quantum efficiency*, q_{Pi}, of a photophysical process, P, (with a rate constant k_{Pi}), which corresponds to the fraction of excited molecules in state i which decay *via* photophysical process P:[78]

$$q_{Pi} = \frac{k_{Pi}}{k_i} \tag{1.43}$$

where k_i is the overall rate constant for decay from state i. The quantity q_{Pi} in the above equation is usually referred to the as *quantum yield*, Φ, of a given photophysical process.[78] The photophysical process for which the quantum efficiency or quantum yield is highest constitutes the molecule's predominant relaxation pathway.

The photons emitted by radiative decay pathways can be easily detected and hence it is fairly straightforward to map and time these relaxation mechanisms. In the case of non-radiative decay pathways, however, not only do the transitions involved not produce a measurable signal, they also tend to take place on ultrafast timescales, as mentioned earlier. The study of such relaxation pathways thus requires ultrafast spectroscopic techniques that are able to follow these events; the field of science concerned with such ultrafast processes, an overview of which is given in the next section, is commonly referred to as *laser femtochemistry*.

1.3   Laser Femtochemistry

The potential energy surfaces (PES) that describe a given chemical event in light of the Born-Oppenheimer approach, both discussed earlier in this chapter, are at the core of the current understanding of molecular dynamics.[79] For any chemical event taking place from reactants to products, the *transition states* can be said 'to encompass all [molecular] configurations significantly perturbed from the potential energy of the reagents or the products'.[80] In 1994, the observation of the transition state for a chemical reaction was listed as one of the "Holy Grails" of chemistry, but 'the dream goes beyond understanding of the PES':[80] the ultimate achievement of laser femtochemistry, defined by Ahmed H. Zewail as the field of science which is 'concerned with the very act of the molecular motion

that brings about chemistry (...) on the femtosecond (...) timescale',[81] will be to map, understand, predict and manipulate the molecular dynamics for any chemical event.[80]

The short timescale on which molecular motions on the transition state occur — femtoseconds (10^{-15} s) to picoseconds (10^{-12} s) — is the main challenge for observing these motions in real time.[80–82] These timescales remained unmeasurably short until the advent of ultrashort laser pulse generation techniques, an overview of which will be given in the next chapter. With ultrashort laser pulses, one is able to begin to map the complete evolution of a chemical event at a molecular level by employing *pump-probe* methods, also referred to as *time-resolved* methods.[79–81] Femtosecond transition-state spectroscopy (FTS), as Zewail initially referred to these pump-probe laser femtochemistry experiments,[83] can be interpreted in light of classical and quantum mechanics; the two approaches are complementary in this context.

The dynamics of a chemical reaction are governed by its PES. Consider, for example, a photodissociation reaction $AB + h\nu \rightarrow A + B$ (where $h\nu$ refers to the energy provided by a photon): the corresponding potential energy curve (PEC, since we are now depicting only a 1D cross section of the multi-dimensional surface) can, from a classical mechanics point of view, be assumed to resemble that presented in Figure 1.14. The FTS experiment starts at *time-zero*, with a pump laser pulse of wavelength λ_{pu}, which photoexcites the molecule under study from its lowest PEC, V_0 (corresponding to its bound ground-state), to the excited state of interest, *e.g.* V_1. As we have discussed in the last section, a molecule is never found at zero energy: there is a thermal Boltzmann distribution of vibrational levels. Thermal motion therefore makes it likely for the molecule to be found away from its equilibrium position, such that photoexcitation may not necessarily occur from the equilibrium position, R_e, as shown in Figure 1.14. Large deviations from the molecule's position of equilibrium may imply significant population of higher energy vibrational levels which may complicate spectra. As we will discuss in further detail in Chapter 2, section 2.2, cooling mechanisms can be employed in sample delivery systems for pump-probe experiments, particularly in vacuum, to avoid significant population of such high energy vibrational levels.

Once the pump laser pulse is over, the ensemble of photoexcited molecules prepared by λ_{pu} is allowed to evolve freely over time, their dynamics being entirely determined by the PES of the excited state.[83] Therefore, for a photodissociation reaction, as depicted in Figure 1.14, the excited state population follows the V_1 curve, the internuclear separation

between A and B increasing over time (as the A—B bond dissociates). As the chemical event takes place, it is probed at each one of several pump-probe time delays, Δt. The signal obtained from the probe step can be, for example, fluorescence to a given vibronic state in the ground electronic state or ion yield resulting from ionisation by a probe laser pulse of wavelength λ_{pr}. Changes in population of the probed excited state over time may then result in changes to the measured signal, providing information on excited state decay at each one of the probe steps. The collection of "pictures" of the time evolution of the system that each probe step yields is then pieced together to produce a "movie" of the complete evolution of the chemical dynamics (almost analogous to a "stop motion" approach to a dynamic event).

In what we have so far described and presented in Figure 1.14, it is the transition state that is monitored over time. A sharp increase in signal would be expected for the first probe step immediately after photoexcitation, reflecting the build-up in excited state population induced by the pump pulse. For consequent pump-probe time-delays (Δt), as the excited state population relaxes away from the initially prepared state, the signal would be expected to decay, with the resulting transient providing a unique window into the landscape of the excited state PES.[83] Alternatively, however, the system could be probed by a λ_{pr} laser pulse resonant with the absorption of one of any free fragments that might be formed during the chemical event. In this case, the signal is initially negligible but increases over time, as the bond breaks and fragments are produced. The signal
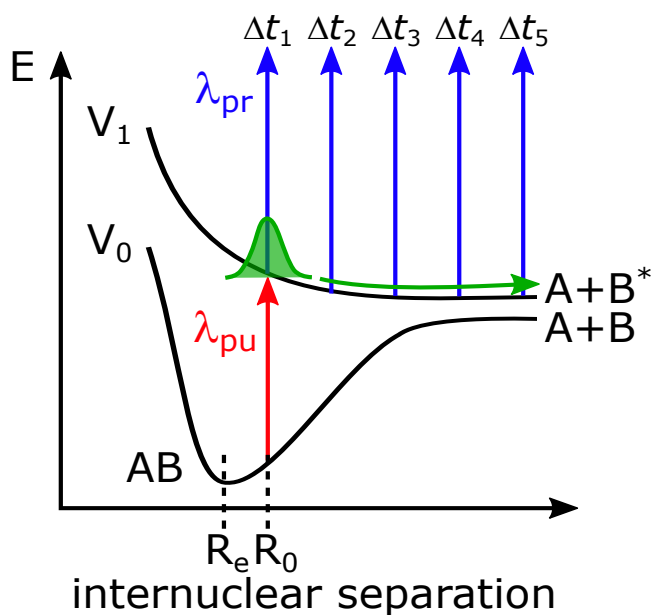
Figure 1.14: The pump-probe concept from a classical perspective.

from the fragment will eventually reach a plateau once the ensemble of molecules has undergone photodissociation; the time taken for bond breaking can thus be determined. For the example of photodissociation, the transition state would eventually reach the final, dissociated state and, therefore, its decay should be related to the appearance time for the photofragment.[83] In both cases ("build-up and decay" or photofragment transients), however, the transients will be affected by the temporal widths of the pump and probe laser pulses: the experimental transient is, in fact, a convolution of the function which describes the time-dependent behaviour of the system with the cross-correlation function between the pump and probe pulses.[83] The latter is usually termed *instrument response function* (IRF) and will be discussed in further detail in Chapter 2, section 2.4.3.

A quantum mechanical approach to the FTS measurements just described is based on *wavepacket* theory. In terms of wavepacket dynamics, pump-probe experiments may be described in three main steps, illustrated in Figure 1.15.[79] As before, the experiment starts at time-zero ($\Delta t = 0$), when the spectral bandwidth of the pump laser pulse interacts with the ensemble of molecules under study and thus prepares a coherent superposition of eigenstates, called a wavepacket and represented by $\chi(\Delta t)$. Once the pump pulse is over, the initially photoexcited eigenstates will be free to interact with a manifold of vibronic levels and thus there will be a dynamic evolution of the wavepacket, which evolves freely over time according to:[79]

$$|\chi(\Delta t)\rangle = \sum_n \tilde{a}_n |\Psi_n\rangle e^{-i2\pi c E_n \Delta t} \tag{1.44}$$

where the $\tilde{a}_n$ coefficient accounts for the amplitudes (populations) and phases of the initial eigenstates $|\Psi_n\rangle$ and E_n reflects their energies. As the wavepacket evolves in time, the probe laser pulse projects it onto a specific final state $|\Psi_f\rangle$ at each Δt. The time-dependence of the signal $S_i(\Delta t)$ resulting from the projection of eigenstates n and m onto a common final state, can be written:[79]

$$S_i(\Delta t) = \sum_n \sum_{m \leq n} |\tilde{b}_n||\tilde{b}_m| \cos[(E_n - E_m)2\pi c \Delta t + \phi_{nm}] \tag{1.45}$$

where ϕ_{nm} is a phase factor and the coefficients $\tilde{b}_n$ and $\tilde{b}_m$ include the information contained in the $\tilde{a}$ coefficients for each eigenstate (with amplitudes and phases) as well as the probe transition dipole moment and vibronic overlap factors to the final state.[79,84]
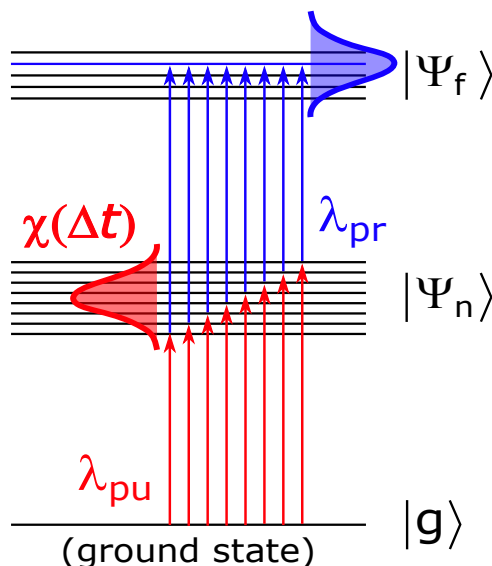
Figure 1.15: Wavepacket approach to pump-probe techniques.

As is true for the pump step of these experiments, the broad spectral bandwidth of the femtosecond probe pulse may photoexcite the system to several final states such that the final observable signal includes contributions from all of them. Differential detection techniques, such as photoelectron spectroscopy and dispersed fluorescence (which will be discussed in Chapter 2, sections 2.2.1.3 and 2.3.1, respectively), can disperse the experimentally observed signal with respect to specific final states.[84] As a result, these techniques contain interferences between degenerate two-photon transitions, which manifest experimentally as a modulation of the signal as a function of time at frequencies $E_n - E_m/\hbar$.[79,84] These modulations are referred to as *quantum beats* and carry more detailed information regarding the eigenstate energy spacings and their overlaps with the final state. In Chapter 4, we will explore the phenomenon of quantum beats in more detail using one of the sunscreen molecules considered in our studies as an example. The quantum beat information may become undetectable, however, for integral detection techniques, such as those which detect total ion yield (time-resolved ion yield, for example, discussed in Chapter 2, section 2.2).[84] In these cases, signal is proportional to the total population in the set of all energetically accessible final states and, since these may have different overlaps with the wavepacket, the interference between degenerate transitions may be rendered indistinguishable. Signal decay observed with integral detection techniques is still reflective of the time evolution of excited state population hence chemical dynamic information may still be obtained, as we will discuss in later chapters.

Pump-probe techniques should thus allow for molecular events to be monitored from

time-zero, through the transition state and, ultimately, to the system's final state. The "proof of principle" FTS studies were performed by Zewail and co-workers in 1987, looking into the gas-phase dissociation of cyanogen iodide, ICN, represented by $ICN^* \to [I \cdots CN]^{\ddagger} \to I + CN$ (where $*$ and $\ddagger$ indicate an excited and a transition state, respectively).[83,85,86] In these pioneering experiments, Zewail and co-workers photoexcited an ICN gaseous sample with $\lambda_{pu} = 306$ nm and monitored the fluorescence induced by the probe laser pulse. In probing the system resonantly with the CN fragment, the authors measured a signal appearance lifetime of 205 ± 30 fs, corresponding to the I—CN bond breaking timescale.[85] Off-resonance experiments yielded "build-up and decay" transients, as we have previously discussed (*vide supra*), with the extracted values agreeing with on-resonance measurements.[85] Moreover, the authors found their experimental observations to agree with theoretical results produced using both classical and quantum mechanical models of FTS, thus supporting the validity of the FTS methodology and the conclusions drawn.[85] In 1988, soon after their studies on ICN, Zewail and co-workers investigated the ultrafast dynamics of NaI and observed an oscillatory behaviour for the FTS signal — quantum beats, as we have defined them earlier — which the authors assigned to the oscillations of excited population within potential energy surface of the covalent NaI excited state.[82] Many more FTS studies followed by Zewail's and other research groups, some of which were reported in a 2004 special issue of *Chemical Reviews*, dedicated to *Femtochemistry* and edited by Marcus Dantus and Ahmed Zewail.[87]

These and later revolutionary studies on femtochemistry ultimately led Ahmed Zewail to becoming a Chemistry Nobel Prize Laureate in 1999 'for his studies of the transition states of chemical reactions using femtosecond spectroscopy'. However, in Zewail's own words, 'ultrafast laser techniques are the essential part of femtochemistry'.[81] Therefore, a discussion on laser femtochemistry would not be complete without a discussion on the generation of ultrashort laser pulses. Before reviewing laser science and femtosecond laser generation techniques in Chapter 2, we will provide a brief overview of computational chemistry in the next section, which has proven instrumental for the interpretation of the experimental results obtained from laser femtochemistry techniques, as we will demonstrate in later chapters.

1.4   Computational Chemistry: a brief overview

We have mentioned before that computational chemistry methods are a valuable tool for the interpretation of experimental chemical dynamics results, as we will demonstrate in Chapters 3 and 4. We have also mentioned the Hartree-Fock method as the stepping stone for the multitude of computational techniques that are now available to provide approximate solutions to the Schrödinger equation. These solutions, albeit approximate, provide crucial information regarding complex systems such as the sunscreen molecules with which we are concerned. As we have employed such computational techniques in the work described herein, it is relevant to provide a brief overview of the topic to enable us to better understand computational results and connect them to experimental observation.

First of all, let us recall that the wavefunction which describes a molecular orbital can be expressed as a linear combination of atomic orbitals, in accordance with the LCAO approach we have previously discussed (see Section 1.2.2). The set of basic atomic orbitals that are combined to describe the final molecular orbital wavefunction is referred to as a *basis set*. If one was able to evaluate an infinite basis set, the best possible solution to the Schrödinger equation for the system under study would be found (for a given computational technique).[55] However, infinite basis sets cannot be employed in practice and, therefore, it is necessary to decide how many AOs to take into account, *i.e.* how large to make the basis set. Moreover, it is necessary to define how to describe the AOs mathematically by selecting the type of *basis function* to be employed, such as Slater-type orbitals (closely resembling hydrogenic AOs) or Gaussian-type orbitals.[55,88] While a larger basis set will more accurately describe a given system, the computational cost of simulations also increases with increasing basis set size and, therefore, a compromise must be reached.

The type of basis function in the basis set is usually chosen so that the amplitudes of the basis function approximately match the electron probability density of the molecular orbital.[55] There are now a number of different common basis sets used routinely in computational chemistry studies. Often, these basis sets also include functions (additional to the basis functions) to allow for particular aspects of the system to be more accurately modelled, such as polarisation, orbital diffusion, *etc.* For example, in the work presented in Chapter 3, we refer to a 6-31G* Pople basis set, which employs ten basis functions: six Gaussian functions describe the core orbitals and the valence orbitals are split into

two separate basis functions described by three and one Gaussian functions, respectively. Employing such a split-valence approach (which allows for a more detailed description of the valence orbitals, the most relevant to chemical reactivity) has been shown to provide a better description of the relative energies and of some geometrical features of molecules.[90] The * character in the 6-31G* Pople basis set indicates that additional polarisation functions are employed[55,89] to provide additional probability density flexibility in the region of chemical bonds.[89,91,92] In the work presented in later chapters we have also employed Dunning's *correlation-consistent polarised Valence Double Zeta* basis set,[93–95] which we abbreviated as cc-pVDZ in Chapters 3 and 4. The "correlation consistency" of the Dunning's basis set refers to the fact that basis functions include electron correlation effects (electron-electron interactions);[55,93] Dunning's basis set also includes polarisation functions, and focuses on modelling valence orbitals. The "zeta quality" of the Dunning's basis set reflects the number of different basis functions used to describe the same AO: two for double zeta, three for triple zeta, *etc.*[55,93–95]

The basis set chosen to describe the system under consideration constitutes an initial guess of its parameters. The quality of this initial guess can be evaluated by how low the energy of the system is, since, in light of the *variational theorem*, expectation values for the energy of the system are always higher than the true value (*i.e.* than the exact solution value).[55] Therefore, the lowest energy that can be calculated for a given system, described by a given basis set, is the closest to the real energy value.[55] The initial guess for the description of the system can be optimised by minimising the energy for all possible linear combinations of the basis functions in the basis set. The lowest energy wavefunction obtained from this process can then be used as a "second guess" and the process is repeated iteratively until the latest calculated energy value is insignificantly lower from the last, an approach commonly termed *self-consistent field* (SCF) method.[55] Each of these iterations may be performed by evaluating each basis function analytically for the whole basis set — in which case we are employing an *ab initio* method — or by estimating the results for the same functions based on known spectroscopic data or other physical properties; the method is then said to be *semi-empirical*. While the variational theorem and the SCF method just described are common to several computational chemistry techniques, other methods of obtaining approximate solutions to the Schrödinger equation for a given system can be employed, such as perturbation theory; however, these will not be discussed any further.[55]

An example of a successful computational technique that we have employed in our studies (and which employs a variational theorem approach) is *density functional theory*, DFT. Instead of explicitly attempting to model the wavefunction corresponding to a given system, DFT focuses on its electron density, $\rho(r)$, where r relates to electron position.[42,55] In DFT, electrons are considered to interact with one another as well as with an external potential resulting from the attractive forces between nuclei; electron correlation is taken into account in DFT methods by describing the Hamiltonian for the system as a *non-interacting* sum of one-electron Kohn-Sham operators:[55]

$$h_i^{\text{KS}} = -\frac{1}{2}\nabla_i^2 - \sum_k^{nuclei} \frac{Z_k}{|r_i - r_k|} + \int \frac{\rho(r)}{|r_i - r_k|}\,\mathrm{d}r + V_{xc} \qquad (1.46)$$

where V_{xc} is an unknown exchange and correlation potential. DFT accounts for explicit electron-electron interaction by having its initial Kohn-Sham functional guess be a system of non-interacting electrons whose ground-state electron density is defined as that of a real system for which electrons *do* interact.[55] As before, from this initial guess the functionals are evaluated iteratively and self-consistently.[42] The quality of the initial guess of DFT depends on how accurately the initial Kohn-Sham functional describes the exchange and correlation potential, which can be done by employing a variety of approaches; this is the origin of the great collection of different functionals that can be employed with DFT. In following chapters we shall refer to one such functional, CAM-B3LYP. While the details of this functional will not be explored here, we briefly note that it includes improved descriptions of long-range interactions and provides accurate results for complex systems, such as charge transfer states, at low computational cost.[96]

Other computational techniques employed in the studies presented in Chapters 3 and 4 involve variations of the *Complete Active Space* method, abbreviated as CAS or CASSCF if we wish to be explicit about the self-consistent field character of the method.[55] CAS is, in itself, a branch of the *Multiconfiguration Self-Consistent Field Theory*, MCSCF. The need for such multiconfigurational methods arises from the fact that molecular systems may have several near-degenerate electronic configurations. MCSCF methods address this situation by taking into consideration several possible electronic configurations, described by *configuration state functions*, CSF. The variational optimum shape of the MO is found from these functions, as well as the weighting, a_n, of each CSF in the MCSCF wavefunc-

tion:[55]

$$\Psi_{\text{MCSCF}} = a_1|\text{CSF}_1\rangle + a_2|\text{CSF}_2\rangle + \dots \tag{1.47}$$

This approach requires the user to select which orbitals may be allowed to be singly occupied, the resulting selection being referred to as the *active space*, as well as which electronic configurations are to be taken into account. For a CAS calculation, all electronic configurations are allowed; the active space is then defined by valence electrons and orbitals, *e.g.* an active space with 14 valence electrons and 12 orbitals would be represented as (14,12). If, instead of selecting an active space, *all* electrons in *all* orbitals are considered, we would be dealing with a *full configuration interaction* calculation. These methods are of course rather thorough in their approach to the modelling of the system under study, however, as a result, they also present a significant computational expense.[55]

Choosing an appropriate computational method is, therefore, an exercise of comparing the "value for money" relationship of each one and choosing the method that yields reasonably accurate results for a given system at an affordable computational cost. However brief, this description of the computational methods used in the work presented in later chapters should provide a working understanding of how the results were produced and what they describe. Further details pertaining to the specific problems at hand and the methodologies used to solve them will be given as appropriate in Chapters 3 and 4.

1.5 Expediting the Molecular Design of Sunscreen Agents

Having introduced the importance of sunscreens to modern society and explored the scientific intricacies which, in the following chapters, will guide our understanding of their photoprotective function, it is important to highlight the challenges which this work aims to address, as well as the rationale behind our approach to this task.

The sunscreen industry, worth US\$8.3 billion (£6.3 billion), globally, in 2015, and expected to rise to US\$14.1 billion (£10.7 billion) by 2024,[97] faces significant challenges related to the UV filters currently available for commercial use.[32] One of these challenges is to provide the necessary photoprotection in the UVA wavelength range, since most UV filters authorised for use in commercial sunscreens are UVB absorbers. There is, therefore, a gap in the wavelength range that sunscreens are currently able to protect against. In addition, there have been concerns regarding the photostability of a number of sunscreen

molecules currently and previously available on the market.[32] Avobenzone, for example, which is one of the most important UVA absorbers on the market, is known to degrade under UV radiation. *Para*-aminobenzoic acid (PABA), for example, was one of the first and most popular UV filters to be used in commercial sunscreen formulations until it was found to be a photoallergenic for a significant number of sunscreen users and to lead to an aesthetically unpleasant yellowing of the sunscreen lotion. The sunscreen industry therefore has the need for innovative sunscreen molecules that not only deliver optimum photoprotection but are also safe, user-friendly and affordable.[32]

The main argument defended in this thesis, built from the overarching conclusions drawn from the results presented, is that the challenges being faced by the sunscreen industry can be addressed by developing a rationale for molecular design, based on laser femtochemistry measurements, to develop tailor-made sunscreen molecules and thus optimise photoprotection. Once the photoprotective mechanisms of action are established by laser femtochemistry studies, the molecular structure of sunscreen agents can be manipulated in order to either enhance the desired energy redistribution mechanisms or hinder any relaxation pathways that may lead to harmful side photochemistry or energy transfer to neighbouring species. For example, consider, hypothetically, a sunscreen molecule which is found to dissipate excess energy *via* photoisomerisation, but whose large substituent is hindering rapid isomerisation and thus heightening the probability of other, undesirable, relaxation mechanisms taking place. The substituent in question may be changed for a smaller one in order to encourage rapid photoisomerisation and thus optimise photoprotection. Of course, such an approach necessarily requires that the molecular events occurring in sunscreen molecules upon irradiation are clearly established so that they can then be manipulated — this initial step is the main concern of the present thesis. The ensuing discussion relies strongly on a *bottom-up approach* to rational molecular design, for which the molecular complexity of the system under study is incrementally increased. Such an approach involves studying sunscreen molecules first in isolation (in vacuum) so that their intrinsic properties are understood and the effects of substituent position/functional group are evaluated. In order to understand the real-life behaviour of the active ingredients in a sunscreen formulation, solvent effects on sunscreen photodynamics then need to be explored. Pushing the current boundaries of knowledge in this field will involve studying sunscreen mixtures in different solvents, thin films, and, ultimately, *in vivo*.

In the discussion that follows, Chapter 2 will cover the background and details of

the experimental techniques and methodology employed in the studies on the ultrafast photodynamics of sunscreen molecules presented in this thesis. Chapters 3 and 4 will present the results and conclusions for such studies on example molecules of the cinnamate and anthranilate sunscreen categories, respectively. Chapter 5 aims to contextualise our work (including additional unpublished results not presented in Chapters 3 and 4) with respect to concurrent advances in the field of ultrafast sunscreen photodynamics. Finally, the overall conclusions from this work will be drawn and an outlook for the future of this avenue of research will be given in Chapter 6.

1.6 References

[1] Martynov, A. I. The solar cult and the tree of life. *Arctic Anthropology* **25**, 12–29 (1988).

[2] Iqbal, M. *An Introduction to Solar Radiation* (Academic Press Canada, Ontario, 1983).

[3] Calbó, J., Pages, D. & González, J. Empirical studies of cloud effects on UV radiation: A review. *Reviews of Geophysics* **43**, RG2002 (2005).

[4] Bratney, A. B., Santos, M. L. M. & Minasny, B. On digital soil mapping. *Geoderma* **117**, 3–52 (2003).

[5] Lacis, A. A. & Hansen, J. A parameterization for the absorption of solar radiation in the Earth's atmosphere. *Journal of the Atmospheric Sciences* **31**, 118–133 (1974).

[6] National Renewable Energy Laboratory. `http://rredc.nrel.gov/solar/spectra/am1.5` (Accessed: 16 October 2017).

[7] Frederick, J. E., Snell, H. E. & Haywood, E. K. Solar ultraviolet radiation at the Earth's surface. *Photochemistry and Photobiology* **50**, 443–450 (1989).

[8] Rapf, R. J. & Vaida, V. Sunlight as an energetic driver in the synthesis of molecules necessary for life. *Physical Chemistry Chemical Physics* **18**, 20067–20084 (2016).

[9] Blankenship, R. E. *Molecular Mechanisms of Photosynthesis* (Blackwell Science, Ltd., 2002).

[10] Diffey, B. L. Solar ultraviolet radiation effects on biological systems. *Physics in Medicine and Biology* **36**, 299–328 (1991).

[11] Shahparnia, M., Packirisamy, M., Juneau, P. & Zazubovich, V. Micro photosynthetic power cell for power generation from photosynthesis of algae. *Technology* **3**, 119–126 (2015).

[12] Holick, M. F. Vitamin D deficiency. *The New England Journal of Medicine* **357**, 266–281 (2007).

[13] Brenner, M. & Hearing, V. J. The protective role of melanin against UV damage in human skin. *Photochemistry and Photobiology* **84**, 539–549 (2008).

[14] Pludowski, P. *et al.* Vitamin D effects on musculoskeletal health, immunity, autoimmunity, cardiovascular disease, cancer, fertility, pregnancy, dementia and mortality — a review of recent evidence. *Autoimmunity Reviews* **12**, 976–989 (2013).

[15] Kataria, S., Jajoo, A. & Guruprasad, K. N. Impact of increasing ultravioletB (UV–B) radiation on photosynthetic processes. *Journal of Photochemistry and Photobiology B* **137**, 55–66 (2014).

[16] Schmidt, E. C., Nunes, B. G., Maraschin, M. & Bouzon, Z. L. Effect of ultraviolet–B radiation on growth, photosynthetic pigments, and cell biology of *Kappaphycus alvarezii* (rhodophyta, gigartinales) macroalgae brown strain. *Photosynthetica* **48**, 161–172 (2010).

[17] Brown, B. E. Coral bleaching: causes and consequences. *Coral Reefs* **16**, 129–138 (1997).

[18] Matsumura, Y. & Ananthaswamy, H. N. Toxic effects of ultraviolet radiation on the skin. *Toxicology and Applied Pharmacology* **195**, 298–308 (2004).

[19] Lo, J. A. & Fisher, D. E. The melanoma revolution: From UV carcinogenesis to a new era in therapeutics. *Science* **346**, 945–949 (2014).

[20] Parrish, J. A., Jaenicke, K. F. & Anderson, R. R. Erythema and melanogenesis action spectra of normal human skin. *Photochemistry and Photobiology* **36**, 187–191 (1982).

[21] de Gruijl, F. R. Photocarcinogenesis: UVA *vs.* UVB. *Methods in Enzymology* **319**, 359–366 (2000).

[22] McLaren, A. D. & Shugar, D. *Photochemistry of proteins and nucleic acids. International series of monographs on pure and applied biology* (Pergamon Press Ltd., Oxford, 1964).

[23] Batista, L. F. Z., Kaina, B., Meneghini, R. & Menck, C. F. M. How DNA lesions are turned into powerful killing structures: Insights from UV-induced apoptosis. *Reviews in Mutation Research* **681**, 197–208 (2009).

[24] Brash, D. E. UV signature mutations. *Photochemistry and Photobiology* **91**, 15–26 (2015).

[25] Sinha, R. P. & Hadër, D.-P. UV-induced DNA damage and repair: a review. *Photochemical and Photobiological Sciences* **1**, 225–236 (2002).

[26] Lacour, J. P. Carcinogenesis of basal cell carcinomas: genetics and molecular mechanisms. *British Journal of Dermatology* **146**, 17–19 (2002).

[27] D'Orazio, J., Jarrett, S., Amaro-Ortiz, A. & Scott, T. UV radiation and the skin. *International Journal of Molecular Sciences* **14**, 12222–12248 (2013).

[28] Battie, C. *et al.* New insights in photoaging, UVA induced damage and skin types. *Experimental Dermatology* **23 Suppl 1**, 7–12 (2014).

[29] Poon, F., Kang, S. & Chien, A. L. Mechanisms and treatments of photoaging. *Photodermatology, Photoimmunology and Photomedicine* **31**, 65–74 (2015).

[30] Gilchrest, B. A. & Eller, M. S. DNA photodamage stimulates melanogenesis and other photoprotective responses. *Journal of Investigative Dermatology Symposium Proceedings* **4**, 35–40 (1999).

[31] Eller, M. S. & Gilchrest, B. A. Tanning as part of the eukaryotic SOS response. *Pigment Cell Research* **13**, 94–97 (2000).

[32] Wang, S. Q. & Lim, H. W. *Principles and Practice of Photoprotection* (ADIS, Switzerland, 2016).

[33] Urbach, F. The historical aspects of sunscreens. *Journal of Photochemistry and Photobiology B: Biology* **64**, 99–104 (2001).

[34] Lowe, N. J. & Shaath, N. A. *Sunscreens: Development, Evaluation and Regulatory Aspects* (Marcel Dekker Inc., New York, 1990).

[35] Gasparro, F. P. *Sunscreen Photobiology* (Springer, New York, 1997).

[36] Jansen, R., Osterwalder, U., Wang, S. Q., Burnett, M. & Lim, H. W. Photoprotection:

part II. Sunscreen: development, efficacy, and controversies. *Journal of the American Academy Dermatology* **69**, 867e1–867e14 (2013).

[37] Standardisation mandate assigned to CEN concerning methods for testing efficacy of sunscreen products. `http://ec.europa.eu/consumers/sectors/cosmetics/files/doc/sunscreen_mandate_en.pdf` (Accessed: 22 January 2018).

[38] Onoue, S. *et al.* Chemical photoallergy: photobiochemical mechanisms, classification, and risk assessments. *Journal of Dermatological Science* **85**, 4–11 (2016).

[39] Nash, J. F. & Tanner, P. R. Relevance of UV filter/sunscreen product photostability to human safety. *Photodermatology, Photoimmunology and Photomedicine* **30**, 88–95 (2014).

[40] Maxwell, J. C. A dynamical theory of the electromagnetic field. *Philosophical Transactions of the Royal Society of London* **155**, 459–512 (1865).

[41] Smith, G. S. *An Introduction to Classical Electromagnetic Radiation* (Cambridge University Press, Cambridge, 1997).

[42] Atkins, P. & de Paula, J. *Atkin's Physical Chemistry* (Oxford University Press, Oxford, 2014), 10th edn.

[43] Ranganath, G. S. Black-body radiation. *Resonance* **13**, 115–133 (2008).

[44] Planck, M. On the law of distribution of energy in the normal spectrum. *Annalen der Physik* **4**, 553 (1901).

[45] Einstein, A. On a heuristic point of view concerning the production of transformation of light. *Annalen der Physik* **17**, 132–148 (1905).

[46] MacKinnon, E. De Broglie's thesis: A critical retrospective. *Americal Journal of Physics* **44**, 1047–1055 (1976).

[47] Davisson, C. J. & Germer, L. H. Reflection of electrons by a crystal of nickel. *Proceedings of the National Academy of Sciences* **14**, 317–322 (1928).

[48] Dürr, S. & Rempe, G. Can wave-particle duality be based on the uncertainty relation? *American Journal of Physics* **68**, 1021–1024 (2000).

[49] Schrödinger, E. Quantisierung als eigenwertproblem. *Annalen der Physik* **384**, 361–376 (1926).

[50] Atkins, P. W. & Friedman, R. S. *Molecular Quantum Mechanics* (Oxford University Press, New York, 1997), 3rd edn.

[51] Born, M. Zur quantenmechanik der stoßvorgänge. *Zeitschrift für Physik A Hadrons and Nuclei* **37**, 863–867 (1926).

[52] Bohr, N. I. On the constitution of atoms and molecules. *Journal The London, Edinburgh, and Dublin Philosophical Magazine and Journal of Science* **26**, 1–25 (1913).

[53] Rydberg, J. R. XXXIV. On the structure of the line-spectra of the chemical elements. *Journal The London, Edinburgh, and Dublin Philosophical Magazine and Journal of Science* **29**, 331–337 (1890).

[54] Bethe, H. A. & Salpeter, E. E. *Quantum Mechanics of One- and Two-Electron Atoms* (Academic Press Inc., New York, 1957).

[55] Cramer, C. J. *Essentials of Computational Chemistry: Theories and Models* (John Wiley & Sons, Ltd., England, 2004), 2nd edn.

[56] Heisenberg, W. Über den anschaulichen inhalt der quantentheoretischen kinematik und mechanik. *Zeitschrift für Physik A Hadrons and Nuclei* **43**, 172–198 (1927).

[57] Willock, D. J. *Molecular Symmetry* (John Wiley & Sons, Ltd., Chichester, 2009).

[58] Hamermesh, M. *Group Theory and its Application to Physical Problems* (Addison-Wesley Publishing Company, Inc., Massachusetts, 1964).

[59] Moore, J. H. & Spencer, N. D. *Encyclopedia of Chemical Physics and Physical Chemistry*, vol. II: Methods (IOP Publishing, England, 2001).

[60] Menzel, R. *Photonics: Linear and Non-linear interactions of laser light and matter* (Springer, Berlin, 2007), 2nd edn.

[61] Hollas, J. M. *Modern Spectroscopy* (John Wiley & Sons, Chichester, 2004).

[62] Houston, P. L. *Chemical Kinetics and Reaction Dynamics* (McGraw-Hill Higher Education, New York, 2001), 1st edn.

[63] Evans, R. C., Douglas, P. & Burrows, H. D. *Applied Photochemistry* (Springer, Dordrecht, 2013).

[64] Nesbitt, D. J. & Field, R. W. Energy flow in highly excited molecules: Role of

intramolecular vibrational redistribution. *The Journal of Physical Chemistry* **100**, 12735–12756 (1996).

[65] Owrutsky, J. C. Vibrational relaxation dynamics in solutions. *Annual Review of Physical Chemistry* **45**, 519–555 (1994).

[66] Dirac, P. A. The quantum theory of the emission and absorption of radiation. *Proceedings of the Roayl Society of London A* **114**, 243 (1927).

[67] Fermi, E. *Nuclear Physics* (University of Chicago Press, Chicago, IL, 1950).

[68] Worth, G. A. & Cederbaum, L. S. Beyond Born-Oppenheimer: Molecular dynamics through a Conical Intersection. *Annual Review of Physical Chemistry* **55**, 127–158 (2004).

[69] Domcke, W. & Stock, G. Theory of ultrafast nonadiabatic excitedstate processes and their spectroscopic detection in real time. In Prigogine, I. & Rice, S. A. (eds.) *Advances in Chemical Physics*, 1–169 (John Wiley & Sons, Inc., 1997).

[70] Bernardi, F., Olivucci, M. & Robb, M. A. Potential energy surface crossings in organic photochemistry. *Chemical Society Reviews* **25**, 321–328 (1996).

[71] Fuß, W. *et al.* Pathway approach to ultrafast photochemistry: potential surfaces, conical intersections and isomerizations of small polyenes. *Chemical Physics* **232**, 161–174 (1998).

[72] Baba, M. Intersystem crossing in the $^1n\pi^*$ and $^1\pi\pi^*$ states. *The Journal of Physical Chemistry A* **115**, 9514–9519 (2011).

[73] Kasha, M. Characterization of electronic transitions in complex molecules. *Discussions of the Faraday Society* **9**, 14–19 (1950).

[74] Lichtman, J. W. & Conchello, J.-A. Fluorescence microscopy. *Nature Methods* **2**, 910–919 (2005).

[75] Roberts, G. M. & Stavros, V. G. The role of $\pi\sigma^*$ states in the photochemistry of heteroaromatic biomolecules and their subunits: insights from gas-phase femtosecond spectroscopy. *Chemical Science* **5**, 1698–1722 (2014).

[76] Matsumoto, S., Kumasaka, R., Yagi, M. & Kikuchi, A. Triplet-triplet energy transfer between UV absorbers in solutions at room temperature. *Journal of Photochemistry and Photobiology A: Chemistry* **346**, 396–400 (2017).

[77] Wang, S. Q. & Lim, H. W. Current status of the sunscreen regulation in the United States: 2011 Food and Drug Administration's final rule on labeling and effectiveness testing. *Journal of the American Academy of Dermatology* **65**, 863–9 (2011).

[78] Birks, J. B. Fluorescence quantum yield measurements. In Mielenz, K. M., Velapoldi, R. A. & Mavrodineanu, R. (eds.) *Standardization in Spectrophotometry and Luminescence Measurements*, 1–11 (US Department of Commerce, National Bureau of Standards, Gaithersburg, Maryland, 1975).

[79] Stolow, A. Femtosecond time-resolved photoelectron spectroscopy of polyatomic molecules. *Annual Review of Physical Chemistry* **54**, 89–119 (2003).

[80] Polanyi, J. C. & Zewail, A. H. Direct observation of the transition state. *Accounts of Chemical Research* **28**, 119–132 (1995).

[81] Zewail, A. H. Laser femtochemistry. *Science* **242**, 1645–1653 (1988).

[82] Rosker, M. J., Rose, T. D. & Zewail, A. H. Femtosecond real-time dynamics of photofragment-trapping resonances on dissociative potential energy surfaces. *Chemical Physics Letters* **146**, 175–179 (1988).

[83] Rosker, M. J., Dantus, M. & Zewail, A. H. Femtosecond real-time probing of reactions. i. the technique. *The Journal of Chemical Physics* **89**, 6113–6127 (1988).

[84] Stolow, A., Brgg, A. E. & Neumark, D. M. Femtosecond time-resolved photoelectron spectroscopy. *Chemical Reviews* **104**, 1719–1757 (2004).

[85] Dantus, M., Rosker, M. J. & Zewail, A. H. Real-time femtosecond probing of "transition states" in chemical reactions. *The Journal of Chemical Physics* **87**, 2395–2397 (1987).

[86] Dantus, M., Rosker, M. J. & Zewail, A. H. Femtosecond real-time probing of reactions. ii. the dissociation reaction of icn. *The Journal of Chemical Physics* **89**, 6128–6140 (1988).

[87] Dantus, M. & Zewail, A. *Femtochemistry* (Chemical Reviews, Volume 104, Issue 4, 2004).

[88] Grant, G. H. & Richards, W. G. *Computational Chemistry* (Oxford University Press, Oxford, 1995).

[89] Rassolov, V. A., Pople, J. A., Ratner, M. A. & Windus, T. L. 6-31G* basis set for atoms K through Zn. *The Journal of Chemical Physics* **109**, 1223–1229 (1998).

[90] Binkley, J. S., Pople, J. A. & Hehre, W. J. Self-consistent molecular orbital methods. 21. Small split-valence basis sets for first-row elements. *Journal of the American Chemical Society* **102**, 939–947 (1980).

[91] Krishnan, R., Binkley, J. S., Seeger, R. & Pople, J. A. Self-consistent molecular orbital methods. XX. a basis set for correlated wave functions. *The Journal of Chemical Physics* **72**, 650–654 (1980).

[92] Pople, P. H. J. A. The influence of polarization functions on molecular orbital hydrogenation energies. *Theoretica Chimica Acta* **28**, 213–222 (1973).

[93] Dunning, T. H. Gaussian basis sets for use in correlated molecular calculations. I. the atoms boron through neon and hydrogen. *The Journal of Chemical Physics* **90**, 1007–1023 (1989).

[94] Kendall, R. A., Dunning, T. H. & Harrison, R. J. Electron affinities of the first-row atoms revisited. Systematic basis sets and wave functions. *The Journal of Chemical Physics* **96**, 6796–6806 (1992).

[95] Woon, D. E. & Dunning, T. H. Gaussian basis sets for use in correlated molecular calculations. V. core-valence basis sets for boron through neon. *The Journal of Chemical Physics* **103**, 4572–4585 (1995).

[96] Yanai, T., Tew, D. P. & Handy, N. C. A new hybrid exchange-correlation functional using the coulomb-attenuating method CAM-B3LYP. *Chemical Physics Letters* **393**, 51–57 (2004).

[97] Sun protection products market 2017 by current & upcoming trends. `https://marketersmedia.com/sun-protection-products-market-2017-by-current-upcoming-trends/244910` (Accessed: 03 February 2018).

2 Techniques and Methodology

'I have no dress except the one I wear every day. If you are going to be kind enough to give me one, please let it be practical and dark so that I can put it on afterwards to go to the laboratory.'

Marie Curie (1867–1934)

2.1 Laser Technology: Generating Femtosecond Pulses

The beginning of laser technology, where 'LASER' stands for *Light Amplification by Stimulated Emission of Radiation*, dates back to 1960, when Theodore Harold Maiman achieved laser action from a ruby crystal.[1,2] However, the most fundamental concept that allows for laser (or *lasing*) action — that of stimulated emission of radiation — had already been predicted by Albert Einstein in 1917.[3] In this section, the basic principles of laser science will be presented, along with an overview of the techniques used for the generation of the femtosecond laser pulses needed for our studies on the photophysics of sunscreen molecules.

2.1.1 Laser Science

We have encountered the concepts of absorption and emission of radiation in the previous chapter, section 1.2; specifically, we were referring to *stimulated* absorption (since it is prompted by the interaction with a photon) and *spontaneous* emission (which happens without the need for an external trigger). To understand laser technology, however, it is necessary to mention *stimulated* emission of radiation, a process in which absorption of a photon by an already excited state prompts the emission of two *coherent* (in-phase) photons of the same frequency and polarisation, travelling in the same direction.[4,5]

The rates of stimulated absorption (termed simply "absorption" from here on for simplicity), stimulated emission and spontaneous emission are dependent on the populations of the states involved in the transition.[4,5] Statistically, if there is a system with two energy

states, m and p, with energies E_m and E_p (where $E_p > E_m$) and degeneracies g_m and g_p, at thermal equilibrium particles will populate these states according to a Boltzmann distribution:[4]

$$\frac{N_p}{N_m} = \frac{g_p}{g_m} \exp\left(\frac{-\Delta E}{k_B T}\right) \tag{2.1}$$

where N_m and N_p are the population densities for each state, ΔE is the energy difference between states m and p, k_B is the Boltzmann constant (1.381×10^{-23} JK^{-1}) and T is the temperature in Kelvin (K). Therefore, the ratio between the excited and ground state populations for a given system at room temperature ($\sim$ 293 K) is $N_p/N_m \sim 0$ for electronic energy levels ($\Delta E \sim 10^2 - 10^3$ kJmol^{-1}), while for vibrational energy levels $N_p/N_m \sim 10^{-3}$ ($\Delta E \sim 10$ kJmol^{-1}).[4] Moreover, the rate of a transition $p \leftarrow m$ depends on the density of the photons at frequency ν interacting with the system, $\rho_\nu = \mathcal{N}_\nu h\nu$, where $\mathcal{N}_\nu$ is the number of photons. Specifically, the rate of absorption is given by:[5]

$$r_{p \leftarrow m} = N_m \rho_\nu B_{mp} \tag{2.2}$$

where B_{mp} is a constant. Analogously, the rate of stimulated emission is:

$$r_{p \rightarrow m} = N_p \rho_\nu B_{pm} \tag{2.3}$$

while that of spontaneous emission is:

$$r_{p \rightarrow m} = N_p A_{pm} \tag{2.4}$$

and the total rate of emission is the sum of equations 2.3 and 2.4 (assuming no losses to the environment). The constants B_{mp}, B_{pm} and A_{pm} are called the *Einstein coefficients*.[5] These coefficients are related by the requirement that, at thermal equilibrium, the total rate of absorption must equal the total rate of emission.[4,5]

The terminology used to describe the Einstein coefficients can also be used to describe the change in irradiance for a collimated beam (low divergence, with photons travelling parallel to each other) of perfectly monochromatic (single wavelength) light passing through a homogeneous absorbing medium, such as a crystal of thickness x. If I_0 is the incident radiation on the crystal, the variation of irradiance across the thickness of the crystal is given by:[5]

$$I(x) = I_0 e^{-\alpha x} \tag{2.5}$$

where α is an absorption coefficient which, as discussed earlier for the Einstein coefficients, depends on the population of the states involved in the absorption and on the radiation incident on the crystal. Specifically, α can be related to the Einstein coefficient for absorption, B_{mp}, by:[5]

$$\alpha = \left(\frac{g_p}{g_m} N_m - N_p \right) \frac{B_{mp} h \nu_{mp} n}{c} \qquad (2.6)$$

where c is the speed of light, ν_{mp} is the frequency of the $p \leftarrow m$ transition and n is the refractive index of the absorbing medium. Since, for a given medium, both the degeneracies and the $(B_{mp} h \nu_{mp} n)/c$ term are constant, it can be seen from Equation 2.6 that, if $N_m > N_p$, α is positive and thus, according to Equation 2.5, the irradiance of the light beam decreases as it travels through the absorbing medium. If, on the other hand, $N_m < N_p$, α is negative and the irradiance of the beam increases across the crystal, *i.e.* the light is *amplified*, and the crystal would then be referred to as an *amplification medium*. Under these conditions, *lasing action* (the stimultated emission of amplified radiation) would be achieved. Note that in this example we have considered the effects of collimated light only, *i.e.* the randomly oriented photons emitted by spontaneous emission are ignored, hence the amplification of radiation arising from the calcutions above must have its origin in stimulated emission.

However, as discussed with regards to Equation 2.1, at room temperature, the population of the ground state is always larger than that of the excited state ($N_m > N_p$), hence special conditions need to be created to allow for *population inversion*, *i.e.* the non-equilibrium distribution where $N_m < N_p$. Also according to Equation 2.1, increasing the temperature of the system or decreasing the energy difference between the states involved in the transition of interest (the *lasing transition*) would increase the population of the excited state, however, not to an extent that would allow lasing action.[5] Therefore, population inversion is commonly achieved by *pumping* the system: providing energy to the amplification medium (often by irradiation) in order to force population onto the excited state and thus enhance stimulated emission processes. For a two-level system, such as the one we have thus far described, pumping can only achieve equal populations of the ground and excited states.[5] For a three-level system, with states of increasing energy E_0, E_1 and E_2, as the one in Figure 2.1(a), the fast $E_2 \rightarrow E_1$ transition enhances the population of the excited state involved in lasing; nevertheless, achieving sufficient pumping is still challenging in this case.
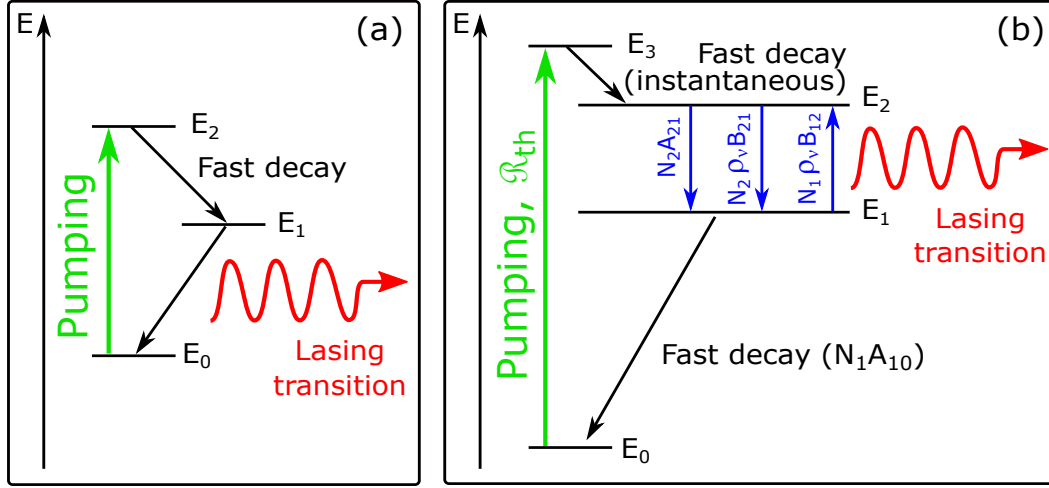
Figure 2.1: Diagrammatic representations of (a) three- and (b) four-level laser systems.

Most of the solid-state lasers currently in use adopt a four-level system instead, such as the one presented in Figure 2.1(b). In such systems, the energy difference between the ground and excited states is considerable, such that the thermal population of E_1 is minimised. Thus, any population reaching E_2 by means of initial pumping to E_3 and subsequent fast $E_3 \rightarrow E_2$ results in significant population inversion being achieved between E_2 and E_1; $E_2 \rightarrow E_1$ is, therefore, the lasing transition. Moreover, in order to maintain population inversion, the rate of spontaneous emission between E_1 and E_0 should be greater than that for the lasing transition ($A_{21} < A_{10}$). In other words, the E_2 state should have a longer lifetime (be *longer-lived*) than E_1, *i.e.* $\tau_2 \gg \tau_1$, where τ_2 and τ_1 are the lifetimes of states E_2 and E_1, respectively. This ensures a constant population in E_2 as well as a constant driving force for the lasing transition to occur. For a system for which $\tau_2 \gg \tau_1$, the threshold population inversion for lasing action to occur, $\mathcal{N}_{th}$, is related to a threshold pumping rate (to E_3), $\mathcal{R}_{th}$, by:[5]

$$\mathcal{R}_{\text{th}} = \mathcal{N}_{th} A_{21} \qquad \text{or} \qquad \mathcal{R}_{th} = \frac{\mathcal{N}_{th}}{\tau_2}. \tag{2.7}$$

Despite the conditions for sufficient population inversion being created, the high powers commonly achieved with laser light sources require more than a single pass through an amplifying crystal, commonly referred to as a *laser medium* or *gain medium*. In fact, in modern laser systems the gain medium is placed within an optical cavity (essentially a pair of mirrors, as shown in Figure 2.2) so that photons emitted by stimulated emission of radiation travel along the axis of the system. The mirrors in the cavity reflect these
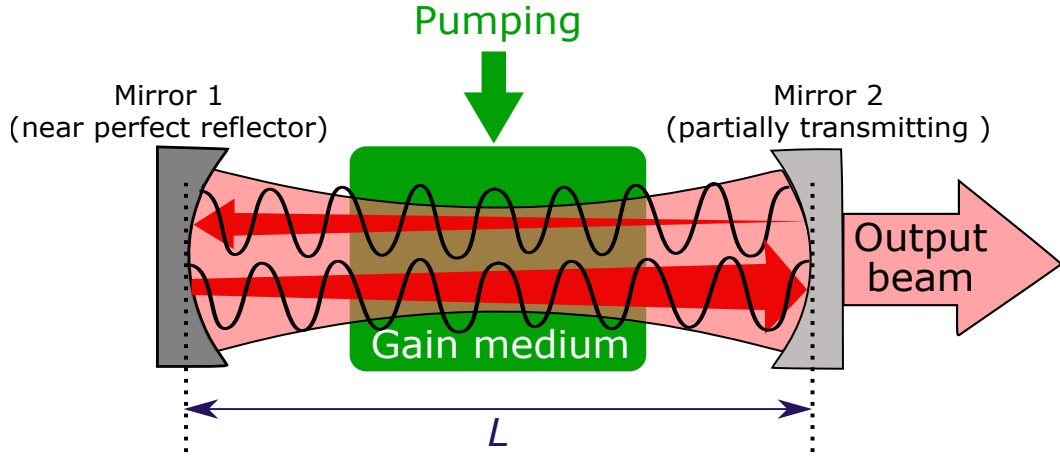
Figure 2.2: Diagrammatic representation of a general laser optical cavity of length L. The laser, or gain medium (in green) is placed between two mirrors, one of which is a near perfect reflector, while the other is partially transmissive as to allow for the extraction of the output laser beam. As the laser modes (the light waves of given spatial and frequency distributions whose oscillations are supported within the laser cavity) travel within this cavity, the beam of light passes throught the gain medium several times, with radiation being amplified at each pass.

photons back towards the laser medium and thus, through this optical feedback, further light amplification takes place. Despite the high reflectivity of cavity mirrors, photon losses inside the cavity due to absorption, transmission or scattering off the mirrors is unavoidable. The total gain, G, in irradiance after a complete photon trajectory inside the cavity is given by:[5]

$$G = \frac{\text{final irradiance}}{\text{initial irradiance}} = R_1 R_2 \ e^{2(k-\gamma)L} \tag{2.8}$$

where R_1 and R_2 are the reflectances of each of the mirrors in the optical cavity, k is the *effective gain coefficient*, γ is the *effective loss coefficient* and L is the length of the optical cavity. Lasing action can only be sustained for $G > 1$; the threshold gain, k_{th}, for lasing action is, therefore:[5]

$$k_{th} = \gamma + \frac{1}{2L} \ln\left(\frac{1}{R_1 R_2}\right) \tag{2.9}$$

The final laser output depends on the aforementioned *threshold conditions* for population inversion, pumping rate and gain, which depend on the conditions established within a given system but are also characteristic of different lasing media. Above the threshold conditions, output laser power is proportional to pumping power. The final output laser beam is extracted from the cavity through one of the cavity mirrors, which is partially transmitting for this purpose.[5]

As light travels inside the optical cavity, with photons parallel to each other but travelling in opposite directions (as they are reflected back from the cavity mirrors at different points in time) the multiple light waves interfere such that *standing waves* are created. Only standing waves whose frequencies ν satisfy the condition[4,5]

$$\nu = \frac{nc}{2L} \tag{2.10}$$

where c is the speed of light and n is an integer, may oscillate within the cavity. Therefore, the *resonant laser modes* — the light waves of given spatial and frequency distributions whose oscillations are supported within the laser cavity — are integer multiples of the wavelength of the laser light. Laser emission thus occurs in discrete frequencies, with adjacent laser modes separated by $\Delta\nu = c/2L$, as shown in Figure 2.3(a). However, only the standing waves whose frequencies are contained within the laser emission's *lineshape function*, $g(\nu)$, akin to the pictorial representation in Figure 2.3(b), will oscillate within the cavity. The irradiance of the discrete laser modes resulting from oscillations within the optical cavity is, therefore, modulated by the lineshape function corresponding to the broadened laser emission spectrum, as shown in Figure 2.3(c).

The spectral broadening of the laser radiation emission is partly due to the transitions in the laser medium taking place between vibronic (rather than pure electronic) energy levels, as we have discussed in Chapter 1. However, there are other sources of spectral broadening, commonly categorised as *homogeneous* and *inhomogeneous* broadening.[5] The effects responsible for homogeneous broadening affect all emitting particles equally, so that they all emit at the same centre or peak frequency, ν_0. An example of such effects would be collision broadening, which is a result of the emitting species within a crystal interacting with lattice quantised vibrations, called phonons. Homogeneously broadened spectra will follow a Lorentzian lineshape, described mathematically as:[5]

$$g(\nu) = \frac{\Delta\nu}{2\pi} \left[(\nu - \nu_0^2) + \left(\frac{\Delta\nu}{2} \right)^2 \right]^{-1} \tag{2.11}$$

where $\Delta\nu$ is the frequency difference measured between the two points where the lineshape function falls to half of its maximum, shown in Figure 2.3(b), also commonly referred to as *linewidth* or *full with at half maximum* (FWHM).

The effects responsible for inhomogeneous broadening, on the other hand, affect each
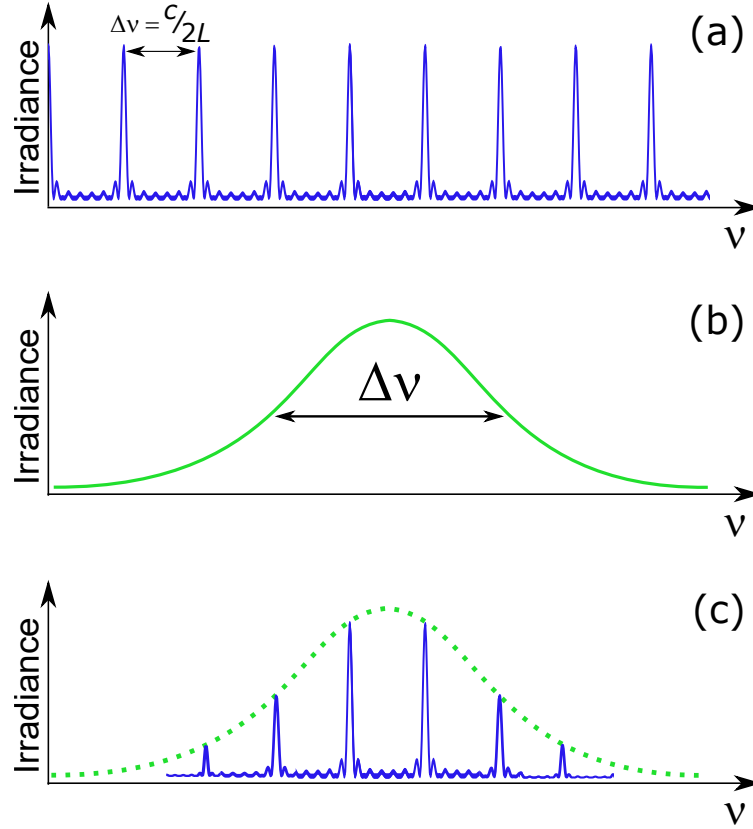
Figure 2.3: (a) Laser cavity modes which oscillate within an optical cavity, with frequencies separated by $c/2L$. (b) Lineshape corresponding to broadened laser emission, of linewidth $\Delta\nu$. (c) Representation of the modulation of the cavity modes by the laser emission spectra; the output laser modes are the cavity modes contained within the laser emission lineshape.

emitting particle differently, so that the observed spectrum is an average of the emission of all particles. In laser systems for which the laser medium is a gas or a liquid, the predominant source of inhomogeneous broadening is the Doppler effect (for which the observed frequency depends on the velocity of the emitting particle), while in solid-state laser systems inhomogeneous broadening may result from crystal lattice imperfections. In both cases, temperature and pressure are also sources of inhomogeneous spectral broadening in laser radiation. An inhomogeneously broadened spectrum is best described by a Gaussian lineshape:[5]

$$g(\nu) = \frac{2}{\Delta\nu}\sqrt{\left(\frac{\ln 2}{\pi}\right)} \exp\left[-(\ln 2)\left(\frac{\nu - \nu_0}{\Delta\nu/2}\right)^2\right]. \tag{2.12}$$

The quality of an optical cavity is measured in terms of *Q-factor*, $Q = \nu/\Delta\nu$, which is a measure of the frequency spread of the laser modes inside the cavity with respect to the lasing frequency; in effect, this is a measure of the monochromaticity of the laser light.

Lasers are a very particular source of light owing to the high power, highly monochromatic and highly collimated beams of coherent photons they produce.[4,5] The laser found applications in several fields of science, technology and industry and, therefore, its invention was revolutionary.[5,6] Furthermore, the relatively recent possibility for generation of short laser pulses,[7–10] albeit at the expense of perfect monochromaticity, as we will explore in ensuing discussion, is incredibly valuable for the study of ultrafast photodynamic processes.

2.1.2 Generation of Femtosecond Pulses

Apart from the high power, highly monochromatic beams of light that can be achieved with laser technology, the study of the ultrafast photophysical processes occurring in the sunscreen molecules we are interested in also requires high time-resolution. Specifically, the minimum time interval of the laser pulse, Δt, must be shorter than the timescale of the process under investigation[6] — on the order of femtoseconds, in the cases we shall consider in later chapters. There are different methods to generate sudden pulses of high power radiation, such as *Q-switching.* In Q-switched lasers, the threshold conditions for lasing action are "turned off" by an optical switch.[5,6] This switch may simply take the form of a moveable cavity mirror: the mirror is moved to avoid reflection of radiation into the lasing medium, turning the cavity "off", and is then replaced in the correct position so that laser modes may oscillate within the cavity again.[5,6] The lasing medium is continuously pumped, however, so that a large population inversion is generated and, when the cavity is turned off, excited state population accumulates (providing spontaneous emission is sufficiently slow). The energy thus stored in the excited state of the lasing medium is then released when lasing conditions are suddenly re-established and thus a high power laser pulse, of approximately nanosecond time width, is generated.

Shorter laser pulses can be generated with *mode-locking* techniques. As we have discussed previously, a typical laser cavity may support the oscillation of several laser modes. In particular, femtosecond laser systems may support the oscillation of thousands of such modes, which has important implications to the spectral bandwidth femtosecond laser pulses, as we now discuss. The electric field of the output beam, $\mathcal{E}(t)$, depends on the

frequencies, amplitudes and relative phases of the N laser modes, such that:[5]

$$\mathcal{E}(t) = \sum_{n=0}^{N-1} \mathcal{A}_n \; e^{[i(\omega_n t + \delta_n)]} \tag{2.13}$$

where $\mathcal{A}_n$, ω_n and δ_n are the amplitude, angular frequency and phase of the nth mode, respectively. In the absence of external influence, the laser modes oscillating within a cavity will do so with a random phase distribution with respect to each other, as shown in Figure 2.4(a). Due to this incoherence of the laser modes, the laser output irradiance is the sum of irradiances for each individual mode. Assuming the amplitude is the same for all modes, which we denote as $\mathcal{A}_0$, this translates as $I(t) = N\mathcal{A}_0^2$.[5] However, an optical modulator — a device which alters the characteristics of light — can be used to fix the phases of the laser modes relative to each other, so that $\delta_n = \delta$, and thus force coherence between them, the so-called *active mode-locking*. The electric field of the output light is, in this case, the sum of the electric fields for each mode, rather than of their irradiances, such that:[5]

$$\mathcal{E}(t) = \mathcal{A}_0 \; e^{i\delta} \sum_{n=0}^{N-1} e^{i\omega_n t} \tag{2.14}$$

Since the laser modes are in-phase, the term in Equation 2.14 which depends on the
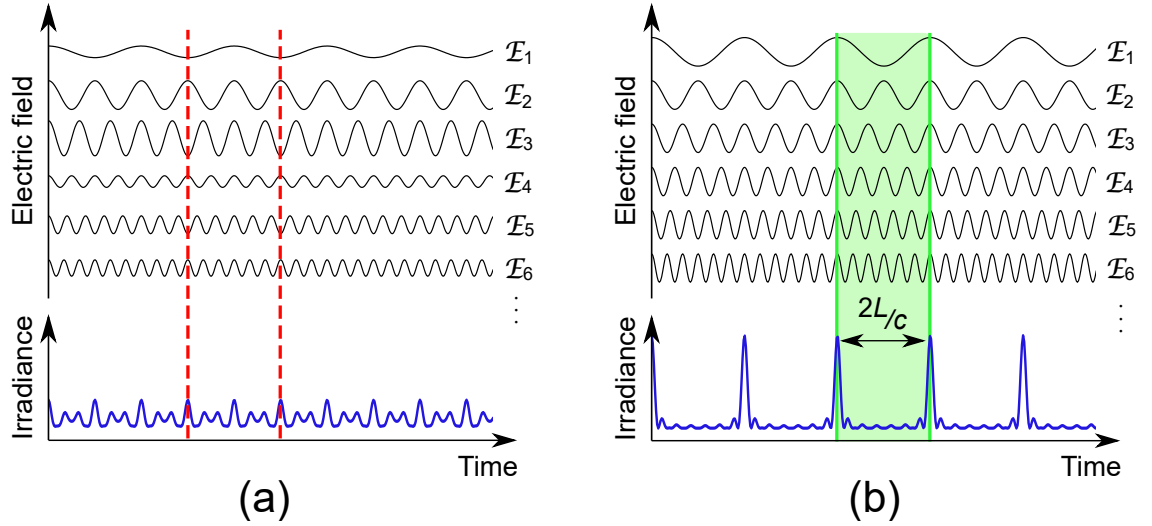
Figure 2.4: In a non-modelocked laser cavity (a), the laser modes are randomly distributed so that the laser output is the sum of the irradiances and only weak, poorly-defined oscillations are present. (b) Mode-locking forces coherence between laser modes and thus the electric field of the output light is the sum of the electric fields for each mode, resulting in periodic bursts of irradiance — laser pulses — separated by $2L/c$ which are increasingly narrower for an increasing number of locked modes.

angular frequency can be replaced by a progression of modes separated by $2L/c$.[5] This ultimately results in the irradiance of the final output light being given by:[4,5]

$$I(t) = \mathcal{A}_0^2 \, \frac{\sin^2(N\pi ct/2L)}{\sin^2(\pi ct/2L)}. \tag{2.15}$$

It is clear from Equation 2.15 that the irradiance is periodic, with maxima being separated by $t = 2L/c$, corresponding to the time taken by a photon to complete a full round-trip inside the cavity. Moreover, pulses become narrower with increasing N, thus intense, short duration laser pulses as the ones depicted in Figure 2.4(b) require broad laser transitions.

The above conclusion that ultrashort pulses can only be generated at the expense of the monochromaticity of laser light — a broader laser spectral width provides more modes to mode-lock and thus leads to shorter pulses — has serious practical implications for laser spectroscopy, since it implies that temporal and frequency resolution cannot be achieved simultaneously. This relationship has its origins in the uncertainty principle, which is valid for the time and frequency pair of observables. The general time and frequency evolutions of a laser pulse, $\mathcal{E}(t)$ and $\mathcal{E}(\omega)$, respectively, can be described by the Fourier transforms:[11]

$$\mathcal{E}(t) = \frac{1}{2\pi} \int_{-\infty}^{+\infty} \mathcal{E}(\omega) \, e^{-i\omega t} \mathrm{d}\omega \qquad \text{and} \qquad \mathcal{E}(\omega) = \int_{-\infty}^{+\infty} \mathcal{E}(t) \, e^{i\omega t} \mathrm{d}t \tag{2.16}$$

In the above equation, we refer to *angular* frequency, defined as $\omega = 2\pi\nu$. The temporal and spectral widths of these pulses can be described in terms of their variance, defined as the expectation of the squared deviation of the variable from its mean:[11]

$$\langle \Delta t \rangle = \frac{\int_{-\infty}^{+\infty} t|\mathcal{E}(t)|^2 \mathrm{d}t}{\int_{-\infty}^{+\infty} |\mathcal{E}(t)|^2 \mathrm{d}t} \qquad \text{and} \qquad \langle \Delta\omega^2 \rangle = \frac{\int_{-\infty}^{+\infty} \omega^2|\mathcal{E}(\omega)|^2 \mathrm{d}\omega}{\int_{-\infty}^{+\infty} |\mathcal{E}(\omega)|^2 \mathrm{d}\omega} \tag{2.17}$$

Experimentally, these values are most commonly measured as the temporal and spectral FWHM of the laser pulse, Δt and $\Delta\nu$, respectively. These quantities are then related by the time-frequency uncertainty principle, such that:[11]

$$\Delta\nu\Delta t \geq K \tag{2.18}$$

where K is a constant which depends on the shape of the pulse, for example, $K = 0.441$ for a Gaussian pulse, and $K = 0.142$ for a Lorentzian pulse.[11] A *Fourier-transform limited pulse* is one for which the equality in Equation 2.18 is reached. At this limit, a 20 fs laser pulse (20×10^{-15} s), for example, corresponds to a spectral bandwidth of

$\Delta\nu = 2.2 \times 10^{13}$ s^{-1}; relative to a central emission wavelength of *e.g.* $\lambda_0 = 800$ nm, this corresponds to $\Delta\lambda = 47.2$ nm (for a Gaussian lineshape).

The temporal width and spectral lineshape of laser pulses are also affected by their interactions with optical media, including the laser medium. The large intensities of laser pulses induce non-linear optical effects, that is, changes in the properties of the optical medium which respond non-linearly to the electric field of the incident light. For example, the change in refractive index as a function of applied field is given by:[5]

$$\Delta\left(\frac{1}{n^2}\right) = P\mathcal{E} + \mathcal{K}\mathcal{E}^2 \tag{2.19}$$

where n is the refractive index of the optical medium and $\mathcal{K}$ is the quadratic electro-optic coefficient responsible for the non-linear, intensity-dependent changes in refractive index of the optical medium, called the Kerr effect; P is the linear electro-optic coefficient, referred to as the Pockels effect, which will also be relevant in later discussion. As a result of the Kerr effect, a laser pulse will experience a different refractive index as it travels through the optical medium. The change in refractive index, Δn, depends on the intensity of the light, I, and the total refractive index of the medium is:[12]

$$n = n_0 + \Delta n = n_0 + n_2 I(r) \tag{2.20}$$

where n_0 and n_2 are the linear and non-linear components of the refractive index, and $I(r)$ is the spatial intensity distribution of a Gaussian beam with a circular beam profile (cross-section), given by:[13]

$$I(r) = I_0 \exp\left(-\frac{2r^2}{w^2}\right) \tag{2.21}$$

where I_0 is the intensity at the beam centre and w is the beam waist. Hence, the refractive index changes according to the intensity distribution of the laser pulse across its diameter. Thus, given that the intensity distribution of a Gaussian beam reaches its maximum at the centre and gradually declines along the radial direction of the medium, the refractive index of the medium $n = n_0 + n_2 I(r)$ will also gradually decrease along the radial direction. This inhomogeneous change in refractive index affects the end cross-section of the laser beam by altering its convergence angle θ_s, such that:[12]

$$n_0 \sin(\theta_s) = \sqrt{n^2(0) - n^2(R)} \tag{2.22}$$

where $n(0)$ and $n(R)$ are the total refractive index at the centre and at the edges of the light beam, respectively. It can further be shown, as in reference 12, that the convergence angle of the light beam is related to the change in refractive index it induces by:

$$\theta_s^2 \approx \frac{2\Delta n}{n_0} \tag{2.23}$$

In practice, this relationship describes *self-focusing*: the effects of the light on the optical medium ultimately result in a reduction of the beam waist, *i.e.* convergence or focusing (if $n_2 > 0$; if $n_2 < 0$ divergence of the beam can also be observed). An optical medium for which this self-focusing is observed is referred to as a *Kerr lens*. The phenomenon of self-focusing is important, since the focal length of a laser medium which acts simultaneously as a Kerr lens has an impact on the laser cavity's stability.[6] Moreover, self-focusing can be used to shorten a laser pulse by using an aperture which selects only the core of the focused laser pulse and thus produces a pulse of narrower temporal width. This is usually referred to as *Kerr lens mode-locking* and can produce sub-100 fs laser pulses.[6]

The light intensity-induced changes in refractive index of the optical medium also have an effect on the spectral width of the laser pulse. In particular, the change in refractive index induces a phase change of the light propagating in the medium. For a pulse of light of central wavelength λ_0 propagating through a Kerr lens of length L, the induced phase change $\Delta\phi$ is given by:[12]

$$\Delta\phi = \frac{2\pi L}{\lambda_0}\Delta n \tag{2.24}$$

The angular frequency of the pulse at a given point in time — the *instantaneous* angular frequency — corresponds to the time derivative of the phase:[6,11]

$$\omega(t) = \frac{\mathrm{d}\phi}{\mathrm{d}t} = \omega_0 - \left(\frac{2\pi L n_2}{\lambda_0}\right)\frac{\mathrm{d}I(t)}{\mathrm{d}t} \tag{2.25}$$

for a Gaussian pulse with a temporal distribution of $I(t) = I_0 \exp\left[-4\ln 2\left(\frac{t^2}{\mathrm{FWHM}^2}\right)\right]$ and central frequency ω_0. The dependence described in the above equation results in the laser pulse being initially shifted to lower frequencies (longer wavelengths) due to a positive value of $\mathrm{d}I(t)/\mathrm{d}t$. As the pulse evolves in time, the phase changes so that later parts of the laser pulse are shifted to higher frequencies (shorter wavelengths) due to a negative value of $\mathrm{d}I(t)/\mathrm{d}t$. As a result, the earlier edge of the laser pulse is red-shifted, while the later edge is blue-shifted, as shown in Figure 2.5. This phenomenon, referred to as *self-*
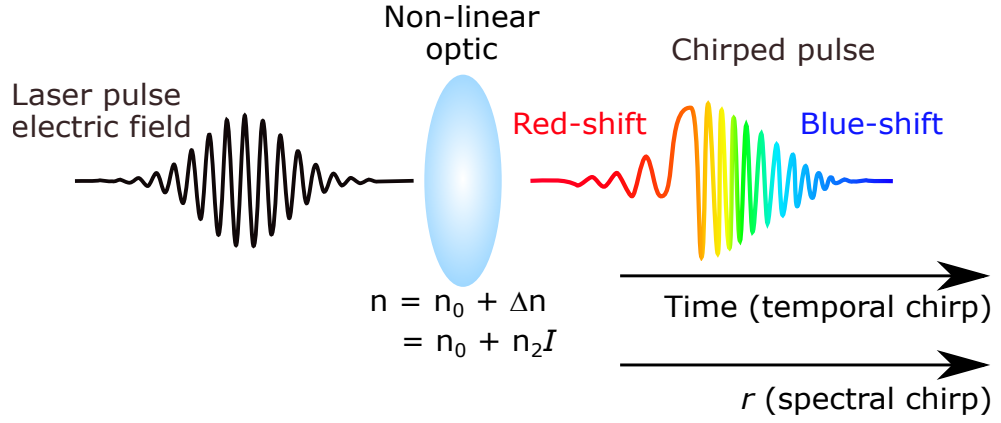
Figure 2.5: Representation of the generation of a chirped laser pulse. If the chirp is spectral, *i.e.* we are concerned with the spectral distortion of the Gaussian pulse, the phenomenon is referred to as SPM; the laser pulse is spatially or spectrally chirped. A laser pulse may also be temporally chirped due to GVD, which affects the temporal distribution of the laser pulse, $I(t)$. While the two phenomena are similar (in that they both chirp a laser pulse, even though they affect different pulse characteristics), they originate from distinct effects: SPM is a non-linear optical effect, while GVD is a result of different wavelengths travelling through a given medium with different velocities.

phase modulation (SPM), results in a broadening of the spectral profile of the laser beam; the laser beam would then be said to be spectrally *chirped*.

An optical medium may also create a temporally chirped laser pulse due to *group velocity dispersion* (GVD), which is not a non-linear optical effect but is instead related to the frequency-dependent velocity of light travelling through an optical medium. In travelling a distance x through any transparent medium, a laser pulse is delayed by an amount $t_g = x/v_g$, where v_g is the group velocity, given by:[11]

$$v_g \approx v_\phi \left(1 - \frac{\omega}{n(\omega)} \frac{\mathrm{d}n(\omega)}{\mathrm{d}\omega} \right) \tag{2.26}$$

where v_ϕ is the phase velocity and $n(\omega)$ is the refractive index of the medium for the specific frequency component ω. The shape of the pulse along the travelling distance x, described by a shape factor $\Gamma(x)$, is given by:[11]

$$\frac{1}{\Gamma(x)} = \frac{1}{\Gamma} + 2i \left[\frac{\mathrm{d}}{\mathrm{d}\omega} \left(\frac{1}{v_g(\omega)} \right) \right] x \tag{2.27}$$

In the equation above, Γ is a constant for a given pulse shape (*e.g.* Gaussian, Lorentzian, *etc.*); the term in square brackets is the group velocity dispersion term, which describes the pulse distortion as a function of both the angular frequency ω and the group velocity v_g. Dispersion can be interpreted as a measure of the separation between the different wave-

lengths of light incident on a dispersive medium.[14] Dispersion can be positive, in which case higher frequency components of the light travel slower than their lower frequency counterparts, or negative, for which the opposite is true. A pulse subject to positive dispersion is said to be "positively chirped" or "up-chirped", while negative dispersion yields "negatively chirped" or "down-chirped" pulses.[14] The GVD-induced distortion of the laser pulse has an effect on its temporal width, which can be described by:[6]

$$\Delta t' = \Delta t \sqrt{1 + \left(\frac{\Delta t_c}{\Delta t}\right)^4} \qquad \text{with} \qquad \Delta t_c = 2^{5/4}\sqrt{\left(\frac{x}{v_g}\right)^2 \left(\frac{\partial v_g}{\partial \omega}\right)} \qquad (2.28)$$

where Δt and $\Delta t'$ are the original and broadened laser pulses, respectively, and Δt_c represents a critical pulse width for which Δt is broadened by a factor of $\sqrt{2}$. For laser pulses shorter than Δt_c, the relative broadening increases with decreasing temporal width of the incident pulse. However, given the uncertainty relationship between $\Delta \nu$ and Δt, expressed by Equation 2.18, SPM (which broadens $\Delta \nu$) counteracts the effects of GVD to a certain extent. Nevertheless, the need for ultrashort pulses requires GVD-induced temporal broadening of the laser pulse to be corrected for during the experiment.

Before exploring the pulse compression techniques used in ultrafast laser systems to correct for chirping and thus obtain ultrashort pulses, it is important to note that pulse stretching also has applications in high power ultrashort pulse generation. The light amplification from a single mode-locked laser cavity produces pulse energies on the order of nano-Joules (nJ),[6] which is often insufficient for ultrafast spectroscopy experiments. Further amplification is possible simply by using a second laser medium within a second cavity, however, the large pulse peak power that would thence result may not only induce further undesirable non-linear pulse distortions, but it may in fact cause significant damage to optical media.[15] The pulse peak power P_p (units of Js^{-1}) is related to the pulse energy E_p (units of J) and to the temporal width of the pulse (expressed in terms of FWHM) by:[16]

$$P_p = \Gamma \frac{E_p}{\text{FWHM}} \qquad (2.29)$$

where Γ is a constant shape factor, *e.g.* $\Gamma \sim 0.94$ for a Gaussian pulse. Thus pulse peak power is inversely proportional to Δt (FWHM) — temporally stretching laser pulses therefore allows for further amplification whilst avoiding damage to optical components.

Employing chirped pulses for light amplification within a laser system is commonly referred to as *chirped-pulse amplification* (CPA). A typical CPA system consists of both
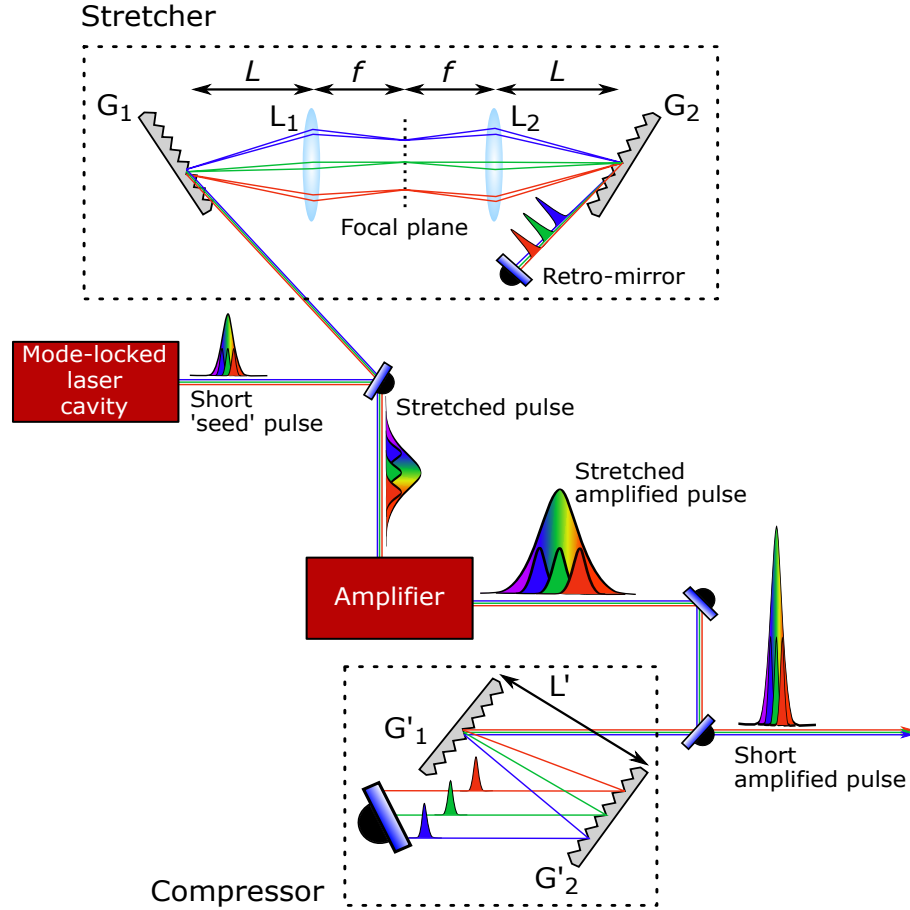
Figure 2.6: Conceptual schematic for chirped-pulse amplification. Pulses from a mode-locked laser cavity are initially stretched by a pair of gratings, G_1 and G_2, placed in an anti-parallel arragement. Two lenses, L_1 and L_2, both of focal length f, are placed at a distance L from each grating. The stretched pulse is amplified and then compressed: the gratings in the compressor are parallel to each other and can be aligned so that negative dispersion is achieved, correcting previous positive dispersion and thus resulting in a short, amplified pulse. Pulse stretching or compression can be achieved by other methods or grating arragements, however, the configuration hereby presented is typical for the laser systems employed in the studies presented in following chapters.

a pulse stretcher and a compressor, both of which achieve dispersion with, for example, a pair of diffraction gratings.[15] Diffraction gratings are reflective optical components with a periodic structure — a finely grooved surface of groove spacing d — which separate the different wavelengths of incident light by diffracting them in different directions.[14] The diffraction generated by a grating can be written as:[11]

$$\lambda = d(\sin \theta_i + \sin \theta_d) \tag{2.30}$$

where θ_i and θ_d are the angles of incidence and diffraction, respectively, of the light of wavelength λ. In the dispersive pulse stretcher shown in Figure 2.6, two diffraction

gratings, G_1 and G_2, are arranged anti-parallel to each other. The short pulse from the first laser cavity is sent towards G_1, which separates the wavelengths of the incident light and sends them along separate paths towards G_2. Between the two gratings, two achromatic lenses L_1 and L_2 of focal length f are placed at a distance L from each grating. These two lenses form a telescope which ensures the beams of different wavelengths travel parallel to each other between the gratings and that the angles of incidence and diffraction are the same at each grating.[14] Providing that $L < f$, this arrangement results in positive dispersion: red (longer wavelength) pulses travel shorter distances than blue (shorter wavelength) pulses.[14,17] A retro-mirror is employed in the pulse stretcher setup to return the dispersed pulse back into the optical arrangement and thus increase pulse stretching. The pulse can be stretched $\sim 10^4$ times,[14] and can then be sent into a second laser cavity, where it undergoes amplification in a separate laser medium.

Amplification at this stage can be achieved with a *regenerative amplifier*, rather than a laser cavity as we have previously described it, the main distinction lying in the selective amplification and trapping of laser pulses. A mode-locked laser cavity will produce a train of laser pulses at a rate of $\sim$ MHz (10^6 Hz) but only a portion of these, usually at a kHz (10^3 Hz) repetition rate, are injected into the amplifier, *i.e.* ~ 1 pulse every millisecond (ms).[6] This selection of pulses is done with a Pockels cell, a setup combining polarisers with an electro-optic crystal which makes use of the linear counterpart of the Kerr effect, given by the P factor in Equation 2.19. As discussed before for the Kerr effect, an electrical field applied to an optical medium may change its properties. In the case of the Pockels effect, the applied electric field affects the crystal structure (and thus the crystal's refractive index) such that a phase shift is induced and the polarisation of the light is altered.[5] Since the crystal is thus able to rotate the plane of polarisation of light passing through it, it is said to be *optically active*. By placing polariser optics before and after an optically active crystal it is possible to take advantage of electric field-induced polarisation changes to selectively transmit light. The transmittance, I/I_0, of a Pockels cell is dependent on the voltage, V, applied to the crystal:[5]

$$\frac{I}{I_0} = \sin^2\left(\frac{\pi}{2}\frac{V}{V_{max}}\right) \tag{2.31}$$

where V_{max} is the voltage required for maximum transmission ($I = I_0$). By varying the voltage applied to a Pockels cell, the transmission of light can thus be turned "off" and "on". A regenerative amplifier will typically employ two Pockels cells: one before the

amplifier to select the pulses from the mode-locked laser cavity (one pulse every ms, as mentioned earlier) and one after amplification, to *trap* the pulse in the cavity. The pulse to be amplified is made to go through the amplifying crystal inside the regenerative amplifier cavity as many times as necessary to completely exhaust the population inversion achieved by pumping and, only then, the final Pockels cell is switched "on" so that the amplified laser pulse is released to the compressor and the process is repeated for the next selected pulse. Note that this is different from a *multipass amplifier*, for which the number of passes through the amplifying medium is fixed.

The final stage in CPA consists of compression of the stretched and amplified laser pulse. In this step, two gratings G'$_1$ and G'$_2$ are arranged parallel and at a distance L' to each other, as shown in Figure 2.6. In this arrangement, dispersion D is given by:[6]

$$D = -\frac{L' \, \lambda}{d^2 \left[1 - \left(\frac{\lambda}{d} - \sin\theta_i \right)^2 \right]^{2/3}} \tag{2.32}$$

with d being the grating groove spacing and θ_i the angle of light incidence, as before. Therefore, the relative distance and angles of the gratings can be adjusted to achieve dispersion that results in compression of the pulse.[6,11] For such a compressor, red wavelengths travel longer than blue wavelengths. Hence, the red edge of the pulse is delayed compared to the blue edge, correcting the opposite effects of the pulse stretcher and thus producing the final, amplified and temporally compressed laser pulse.[6] The ultimate limit for the energies of the femtosecond pulses that can be achieved by CPA is the damage threshold of the optical components involved, namely that of the diffraction gratings.[15] In the laser systems described later in this chapter, pulse energies in the order of mJ are typically achieved, however, CPA approaches can produce pulses of several J of energy (equating approximately to tera – petawatt peak powers, *i.e.* $10^{12} - 10^{15}$ W).[15] After compression, temporal widths of $\sim 20 - 100$ fs are typically achieved with CPA.[6] Femtosecond laser systems thus produce, as we have described in this section, the necessarily short pulses for the study of chemical dynamics.

2.1.3   Frequency Conversion

Regardless of its spectral width, laser emission is centred at a single wavelength. However, different molecules absorb at a range of different wavelengths; sunscreen molecules,

for example, commonly display broad absorption spectra within the UVA/UVB range (280 – 400 nm). Therefore, it is essential for an ultrafast laser spectroscopy technique to allow for the pump and probe wavelengths to be flexibly selected; for studies in solution, as we shall discuss later, it is also important that pulses of white light (containing much of the visible light spectrum) are generated. Such frequency selection requirements are satisfied by taking advantage of various non-linear phenomena which occur in certain optical media and allow for frequency conversion, as explored in the remainder of this section.

2.1.3.1   Sum Frequency Generation

The nuclei and associated electrons within an optical medium may form charges, or electric dipoles, within that medium. As light of angular frequency ω propagates through the crystal, it interacts with these electric dipoles and causes them to oscillate (and thus emit electromagnetic waves) at an angular frequency ω'.[5] The electric polarisation $\mathcal{P}$ of the optical medium (dipole per unit volume) can be described as a power series expansion in the applied electric field of magnitude $\mathcal{E}$ by:[5]

$$\mathcal{P} = \epsilon_0(\chi\mathcal{E} + \chi_2\mathcal{E}^2 + \chi_3\mathcal{E}^3 + \ldots) = P^{(1)} + P^{(2)} + P^{(3)} + \ldots \qquad (2.33)$$

where ϵ_0 is the vacuum permittivity. In this context, the aforementioned Pockels and Kerr effects relate to the linear term χ and to the (second-order) non-linear optical coefficient χ_2 in the equation above, respectively; higher order frequency effects (χ_3 and above) require much higher light intensities and will therefore not be discussed further.

If the electric field incident upon a non-linear optical medium consists of two distinct frequency components ω_1 and ω_2, the total electric field interacting with this optical medium is given by:[12,18]

$$\mathcal{E}(t) = \mathcal{E}_1 e^{-i\omega_1 t} + \mathcal{E}_2 e^{-i\omega_2 t} \qquad (2.34)$$

The second-order non-linear coefficient, $P^{(2)}(t) = \chi_2\mathcal{E}(t)^2$ is, therefore:[12,18]

$$P^{(2)}(t) = \epsilon_0\chi_2[\mathcal{E}_1^2 e^{-2i\omega_1 t} + \mathcal{E}_2^2 e^{-2i\omega_2 t} + 2\mathcal{E}_1\mathcal{E}_2 e^{-i(\omega_1+\omega_2)t} + 2\mathcal{E}_1\mathcal{E}_2 e^{-i(\omega_1-\omega_2)t}] \quad (2.35)$$

Each term in brackets in Equation 2.35 describes a physical process taking place when the separate frequency components interact within the non-linear optical medium. In particular, the first two terms, for which the frequency of the resulting wave is $2\omega_1$ or $2\omega_2$
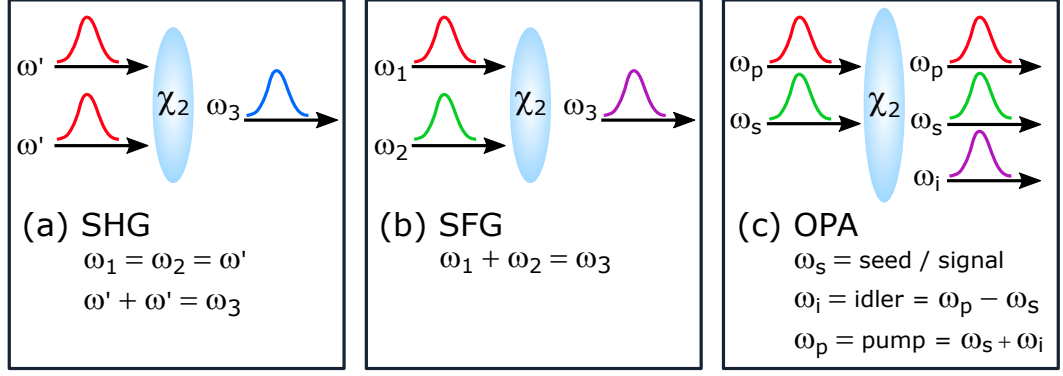
Figure 2.7: Schematic representing the non-linear optical processes described in this section: (a) SHG, (b) SFG and (c) OPA. These non-linear phenomena are exploited experimentally to allow for frequency conversion and thus a larger flexibility in choice of pump and probe frequencies.

describe optical frequency doubling. In the next two terms, $\omega_1 + \omega_2$ is the result of optical sum frequency, or *sum frequency generation* (SFG), shown in Figure 2.7, and $\omega_1 - \omega_2$ the result of *optical difference frequency*. A special case of SFG arises when the frequencies of the light incident on the non-linear medium are the same, *i.e.* when $\omega_1 = \omega_2 = \omega'$, so that the total electric field is, simply, $\mathcal{E} = \mathcal{E}_n \sin \omega' t$. In this case, $P^{(2)}(t) = \frac{1}{2}\chi_2 \mathcal{E}_0^2 (1 - \cos 2\omega' t)$ and the term $2\omega'$ corresponds to a wave of twice the frequency, called a *second harmonic*, of the incident light — this process is, therefore, termed *second harmonic generation* (SHG).[5]

Providing an appropriate medium is employed, the aforementioned non-linear phenomena allow for the fixed frequency of laser emission to be converted, either into its second-harmonic (twice the frequency) *via* SHG or to another frequency by combination with another frequency *via* SFG. The efficiencies of these processes can be rather low, however; in fact, when SHG was first observed in 1961 by Franken and co-workers, conversion efficiency was $\sim 10^{-6} - 10^{-4}\%$.[5] Low conversion efficiencies are due to dispersion, which results in the different frequencies (ω_1, ω_2 and the resulting ω_3) travelling at different speeds within the non-linear optical medium and in the corresponding waves ultimately destructively interfering. The phase mismatch arising from dispersion within the crystal can be described as:[12]

$$\Delta k = (k_1 + k_2) - k_3 \tag{2.36}$$

where the k values correspond to the wavevectors for the waves at each frequency. The conversion efficiency, η, defined as the ratio of the intensity of generated light to the

intensity of incident light, depends on both Δk and the thickness of the crystal, l:[12]

$$\eta \propto \mathrm{sinc}^2\left(\frac{\Delta k\, l}{2}\right) \tag{2.37}$$

The intensity of the generated light fluctuates through the crystal with a periodicity of l_c, known as the *coherence length* and defined as $l_c = \pi/\Delta k$;[5] higher conversion efficiencies are achieved when $l < l_c$.[12] Moreover, the sinc function is a function for which:

$$\mathrm{sinc}(x) = \begin{cases} 1 & \text{if } x = 0 \\[2mm] \frac{\sin x}{x} & \text{if } x \neq 0 \end{cases} \tag{2.38}$$

hence the maximum conversion efficiency is achieved when $\Delta k = 0$, which would correspond to the case where all waves involved in the conversion process are in phase, and that momentum and energy conservations laws are obeyed: $\hbar k_3 = \hbar k_1 + \hbar k_2$ and $\hbar\omega_3 = \hbar\omega_1 + \hbar\omega_2$, respectively.[12]

Based on this analysis, we may conclude that in order to increase the efficiency of frequency conversion by SHG and SFG processes it is necessary to achieve some level of *phase matching*, which would be possible if the refractive indexes within the non-linear optical medium were the same for all frequencies involved, *e.g.* $n_{\omega'} = n_{2\omega'}$ for the case of SHG. Phase matching is usually achieved by exploiting the birefringent characteristics of a non-linear optical medium, *i.e.* polarisation dependent refractive index, such that $n_{\parallel} \neq n_{\perp}$, where $n_{\parallel}$ and $n_{\perp}$ refer to the refractive indexes for parallel and perpendicular light polarisations, respectively. It is possible to find a direction of propagation through the crystal for which the orthogonal polarisations of each incident frequency have the same refractive index, *e.g.* $n_{\parallel}(\omega') = n_{\perp}(2\omega')$ if we once again use the example of SHG.[5,12] Therefore, careful selection of the angle of propagation through the non-linear optical medium negates phase mismatch and thus improves frequency conversion efficiencies, which usually have values of $\sim 20\%$ for a single pass through the crystal.[5]

2.1.3.2   Optical Parametric Amplification

A slightly more complex non-linear process, optical parametric amplification (OPA) provides further flexibility for frequency conversion; its use is incredibly important for the spectroscopic techniques we shall explore in later chapters.

When referring to OPA, the two interacting frequencies at the non-linear optical medium can be referred to as *pump* (ω_p) and *seed* (ω_s). The output, called *idler* (ω_i), is simply the result of optical difference frequency, so that $\omega_i = \omega_p - \omega_s$. The particularity of OPA is that the intensity of the output does not have an oscillatory dependence, as for SFG (for which frequency conversion is described by a sinc function, given in Equation 2.38). Instead, it can be shown that the intensities of both the seed and idler pulses experience exponential growth during OPA.[18] Hence, not only is an idler generated, but the seed light is also amplified, thus becoming the *signal* after OPA. This process can be understood in terms of a photon and energy level diagram approach, as shown in Figure 2.8: ω_p photoexcites the system to a virtual (unobservable due to infinitely short lifetime) excited state and ω_s then prompts stimulated emission of photons at frequency ω_s (thus amplifying the seed light). Since $\omega_p \neq \omega_s$, another photon of frequency $\omega_i = \omega_p - \omega_s$ is released in order for conservation of energy to be obeyed.[5,12,18] As before, there will be a phase mismatch, in this case $\Delta k = k_i - k_p - k_s$ (where k_i, k_p and k_s relate to the idler, pump and seed beams, respectively), which will have to be minimised for improved frequency conversion efficiency (by varying the orientation of the non-linear crystal or the angle of incident radiation, for example).[18]

An OPA medium may be placed within an optical cavity, akin to those described earlier when discussing laser action, the resulting device being called an *optical parametric oscillator* (OPO); the additional cavity in an OPO can further amplify the wavelength of interest. Experimentally, both optical parametric amplifiers (OPAs) and OPOs employ
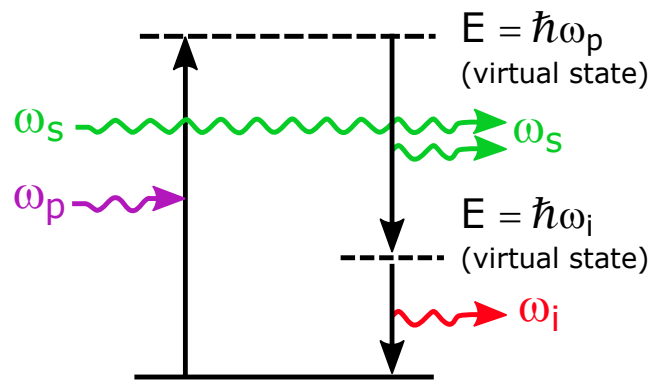
Figure 2.8: Energy level diagram for the OPA process. The pump beam, ω_p, photoexcites the system to a virtual state, from which the seed, ω_s, prompts stimulated emission of radiation. The seed beam is thus amplified and the output signal, of the same frequency ω_s, is generated. To account for the energy differences between the pump and the seed, another photon, called the idler, is emitted with frequency $\omega_i = \omega_p - \omega_s$.

a combination of non-linear frequency conversion phenomena to allow for a wide range of possible output frequencies. Both OPAs and OPOs are versatile sources of frequency-tunable radiation across the IR, Vis and UV ranges of the electromagnetic spectrum.[18]

2.1.3.3 Supercontinuum (White Light Continuum) Generation

SPM can be exploited to generate femtosecond laser pulses whose spectral width may extend from the near-IR, across all of the visible and into the UV regions of the electromagnetic spectrum, the exact spectrum depending on the crystal medium used.[19] The generation of such a white light continuum (WLC) is a high-order non-linear effect, however, and therefore it is only achieved under the high intensity conditions of laser light.[20] The threshold laser power for WLC generation is the same as for self-focusing,[21] given by:[19]

$$P_{\text{WLC}} = \frac{\lambda^2}{2\pi n_0 n_2} \tag{2.39}$$

where n_0 and n_2 are the linear and non-linear refractive index coefficients, as seen previously in Equation 2.20. Above the threshold power, self-focusing is triggered and thus the laser beam converges as described by Equation 2.23. As the power is increased above threshold, a positive feedback is established between beam waist and self-focusing: the decreasing beam waist further enhances the self-focusing effects of the Kerr lens which, in turn, prompts further convergence. The decreasing beam waist leads to an increased intensity of the light within the optical medium, which leads to a cascade of high-order non-linear effects and thus in the generation of a supercontinuum, *i.e.* an ultrashort laser pulse of white light. The point of catastrophic beam collapse (to an infinitely small beam waist) is avoided by multiphoton absorption and plasma formation processes that are triggered at critical intensities.[22] Moreover, the light intensities required for WLC generation may cause optical damage to certain media; experimentally, this is usually avoided by keeping the optical medium under continuous motion, so that contact time of the laser beam with a specific area of the crystal is minimised.

2.2　Time-Resolved Pump-Probe Spectroscopy

2.2.1　In Vacuum

As we have alluded to in the previous chapter, molecular thermal motion may result in significant population of high energy vibrational levels which may complicate spectra. To avoid these thermal effects, cooling mechanisms must be employed in sample delivery systems for pump-probe experiments, particularly in vacuum (for which a molecule usually needs to be heated for its vapour to be created, as we shall discuss later in this chapter). The current state-of-the-art technology for sample delivery in high-resolution spectroscopy experiments commonly involves the production of a *molecular beam* — a directed flow of vibrationally cold molecules created by expanding a high pressure gas or gaseous mixture through a small orifice into a vacuum; this process is referred to as *supersonic expansion*.[6,23,24] Apart from providing a collision-free sample environment and eliminating virtually all sources of inhomogeneous spectral line broadening (such as Doppler broadening, as discussed in earlier sections), the great advantage of employing molecular beams in spectroscopy is their ability to produce vibrationally cold molecules, with beam temperatures of only a few K (or even sub-K) being achievable.[25] Such low temperatures hinder the thermal population of excited states and thus the molecular population is concentrated into one or only a few internal and/or translational motions. By cooling internal degrees of freedom, molecular beams reduce spectral congestion and thus allow for highly resolved spectra from which more detailed information can be extracted.[26]

Either a pure gas and/or the vapour of a molecule of interest can be used in a supersonic expansion apparatus: gases are led to the molecular beam apparatus directly from a reservoir, while a liquid or solid sample may be vapourised within an oven and seeded into a buffer gas.[23,24] In either case, the source consists of a vessel containing a high pressure of the gaseous mixture in a "stagnation state", *i.e.* with negligibly small flow velocity.[23,26] The gas flow is accelerated through a small orifice or shaped nozzle of diameter d by a high backing pressure and, as the gas effuses from the nozzle at supersonic speeds into a vacuum, it undergoes isentropic (constant entropy) expansion. This expansion of a high pressure gas into a vacuum creates a *supersonic free jet* of temperature T_j, which is related to the temperature at the source, T_0 and the local *Mach number*, the ratio of flow velocity

to local speed of sound, $\mathcal{M}_l$, by:[27]

$$T_j = T_0 \left[1 + \frac{\gamma - 1}{2} \mathcal{M}_l \right]^{-1} \tag{2.40}$$

where γ is a heat capacity parameter. $\mathcal{M}_l$ can be found for a given nozzle diameter d and distance from the gas source x:[23]

$$\mathcal{M}_l = A \left(\frac{x}{d} \right)^{\gamma - 1} \tag{2.41}$$

with A being a constant value for a given γ.[23] Hence, as the gas expands away from the source, its temperature decreases.[27] Moreover, if an expanding (buffer) gas is seeded with a molecular vapour, *thermalisation* of the seeded molecules takes places *via* collisions with the buffer gas, which dissipates the translational energy of the seeded molecules. The molecular temperature after n collisions with the buffer gas, T_n, is related to the mass and initial temperature of the seeded molecules, m_s and T_s, respectively, and to the mass and temperature of the buffer gas, m_b and T_b, by:[28]

$$\frac{T_n}{T_b} = \left(\frac{T_s}{T_b} - 1 \right) \exp \left(\frac{-n}{\kappa} \right) + 1 \qquad \text{with} \qquad \kappa = \frac{(m_s + m_b)^2}{2 m_s m_b} \tag{2.42}$$

Hence, the collisional cooling of the seeded molecules is exponentially dependent on the number of collision with the buffer gas. Since the collision frequency is proportional to the gas density, efficient thermalisation also depends on the buffer gas density.[27,28] Supersonic expansions of large aromatic molecules seeded into a buffer gas have been shown to achieve vibrational temperatures of just a few Kelvin.[25]

The initial supersonic jet has a cold, isentropic core surrounded by higher temperature boundaries where particles have random trajectories.[27] To create a cold, directed molecular beam, the isentropic core of the supersonic jet must be extracted by employing a *skimmer*: a conically shaped aperture placed along the flow of the supersonic jet, as shown in Figure 2.9.[23,24,28] The skimmer collimates the beam, selecting the particles with near parallel velocities, isolates the coldest part of the supersonic jet and thus produces the directed flow of cold and isolated molecules that is ideal for spectroscopic studies in vacuum and referred to as a molecular beam.

The practical limit to the performance of the molecular beam method is the ability of the associated vacuum system to effectively extract the large gas discharge through

the nozzle.[23] If gas continuously effuses from the source, the increasing pressure inside the source chamber may negatively affect the propagation of the molecular beam. While the problem of excessive gas pressures may be addressed by employing large vacuum pumps, pulsed gas sources can also attenuate the problem.[26,29] A pulsed molecular beam is spatially and temporally discrete: the gas flow travels a distance δx away from the source in a certain period of time δt which corresponds to the gas pulse duration.[26] Therefore, $\delta x = v\delta t$ with v being the velocity of the molecular beam. The pulse duration δt should be sufficiently short so as to make δx comparable to the typical dimensions of the vacuum chamber and to allow for the chamber to be evacuated before the succeeding pulse.[23,26,29] Moreover, the repetition rate , *i.e.* the number of gas pulses of duration δt which are released by the nozzle per second, should also be kept as low as experimentally viable in order to avoid pressure build-up; the effects of large repetition rates may be counteracted by employing more powerful vacuum pumps. If the pressure inside the source chamber can be kept within $\lesssim 10^{-5}$ mbar ($\lesssim 7.5 \times 10^{-6}$ Torr), the supersonic expansion takes place unhindered and cooling is optimised.[29]

One of the commonly used pieces of equipment to achieve a molecular beam in modern gas-phase spectroscopy experiments — and the one used for such experiments reported in later chapters — is the Even-Lavie valve, shown schematically in Figure 2.9.[25,29,30] The valve is an electric and magnetic actuated device: at rest, the mechanism of the valve is sealed, held in place by a spring, so that no gas is released; when the valve is triggered to release a gas pulse, a short, high current signal creates a strong pulsed magnetic field which
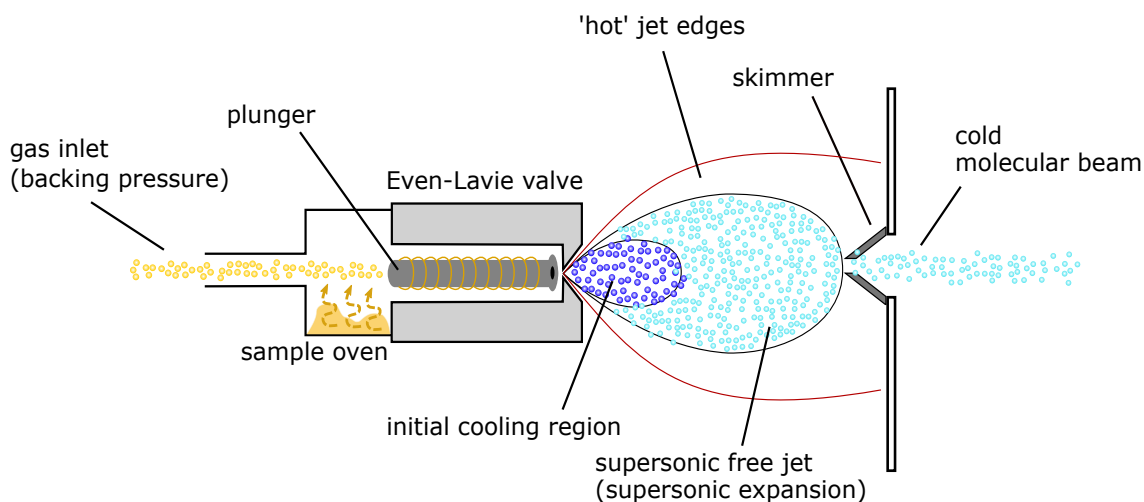
Figure 2.9: Supersonic expansion and molecular beam production with an Even-Lavie valve.

exerts a force on a plunger to release the gas.[29,30] The time for which the plunger remains open constitutes the pulse duration and it can be varied to accommodate experimental requirements; typical opening times for the time-resolved measurements described in later chapters were $12 - 15$ μs.

2.2.1.1   Time-Resolved Ion Yield

The first vacuum pump-probe technique we will review is time-resolved ion yield (TR-IY spectroscopy). This technique follows Zewail's laser femtochemistry scheme which we discussed in detail in Chapter 1, section 1.3: initially, the molecule of interest (seeded into a molecular beam) is photoexcited by a pump laser pulse; the subsequent probe pulse monitors the evolution of the system over time at several time delays Δt. In TR-IY, the probe is chosen so that the system is ionised and the measured quantity is the total ion yield for the probe step, be it the molecular (called *parent*) or fragment ions. The contributions from parent or fragment species can be distinguished due to the m/z and particle flight time selectivity of the detection methods, as we shall discuss shortly. As the molecule relaxes from its excited electronic state (by any feasible photochemical or photophysical pathway) and the excited state population decays, the resulting changes to ion signal are recorded and thus the evolution of the system as a function of Δt is monitored.

Ion detection is usually achieved using a time-of-flight (TOF) spectrometer, as shown in Figure 2.10.[31] In simple terms, a TOF spectrometer consists of a vacuum chamber with an ion source at one end, where a molecular beam interacts with the laser pulses, and an ion detector at the other. Ions are accelerated towards the detector by one or more continuous or pulsed electric fields. Before they reach the detector, the ions go through a field-free flight path, *i.e.* a region in which no forces are applied, so that the velocity of the ions in this area is dependent on their mass-to-charge (m/z) ratio.

The kinetic energy for a particle with charge q subject to an electric field of magnitude E is given by $qE = \frac{1}{2}mv^2$, where m is the particle's mass and v its velocity.[4] In this case, the flight time for the same particle travelling along a flight or drift tube of length D would be $T_D = D\sqrt{\frac{m}{2qE}}$. However, ions are formed in the interaction region at different initial positions and will be ejected with different velocities, *i.e.* different speeds and in different directions. Both these factors will have an impact in the flight time of each individual
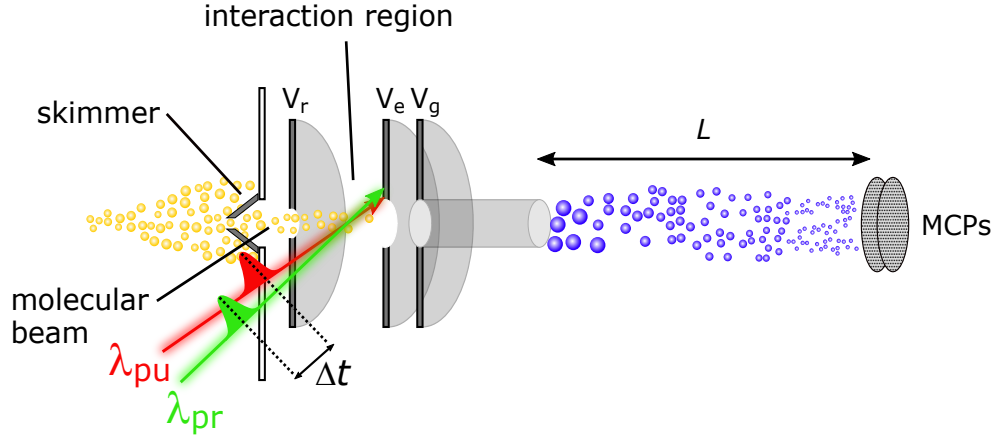
Figure 2.10: Diagram of a typical TR-IY experimental apparatus, including both a molecular beam and a TOF mass spectrometer. The molecular beam interacts with the pump and probe laser pulses, represented by the red and green arrows, respectively, in the interaction region. The resulting ions are accelerated towards the detector by a set of ion optics, V_e, V_r and V_g. After acceleration, the particles enter a field-free flight tube of length L, so that ions reach the detector at different times depending on their m/z ratio.

ion and thus give rise to a spread of arrival times at the detector for identical ions (same m/z). The resolution of a TOF spectrometer can be given in terms of the the time spread over which identical ions reach the detector, called *energy resolution*, ΔT, and given by:[32]

$$\Delta T \geq \frac{2\sqrt{2m\mathrm{KE}}}{zV} \tag{2.43}$$

where m/z and KE are the mass-to-charge ratio and kinetic energy of the detected charged particles, respectively, and V is the voltage applied to the particles to accelerate them towards the detector. The *spatial resolution* of a TOF spectrometer, on the other hand, defines the largest resolvable mass, M, and is inversely proportional to the energy time spread, *i.e.* $M = \frac{T}{2\Delta T}$, where T is the particle's flight time. Therefore, the parameters set for a TOF spectrometer always reflect a compromise between energy and spatial resolution.

Improved overall (space and energy) resolution for a TOF spectrometer can be achieved with the design by Wiley and McLaren,[31] which applies an electric field to the flying particles at two different stages. The ions formed in the interaction region are firstly subject to a "repeller" voltage, V_r, delivered by a metallic plate electrode. The repeller removes the particles from the interaction region into an intermediate zone where their positions and vector velocities are aligned. A second "extractor" voltage, V_e, is applied by an extractor electrode plate with a mesh core to accelerate the charged particles towards the detector and into the field-free drift tube. A third, ground electrode plate is also

employed in the Wiley and McLaren TOF setup, as shown in Figure 2.10. Under these conditions, the particle flight time along a TOF tube of length D is given by:[31]

$$T_D = \frac{1.02\sqrt{2m}D}{\sqrt{2U}} \tag{2.44}$$

where U is the final kinetic energy of the travelling particle, which depends on its initial kinetic energy as well as on the electric fields applied to it at the extraction and acceleration stages. Note that the expression above refers to *flight* time within the drift tube: the total time, from source to detector, also needs to take into account the time the particle spends in the extraction and accelerating zones.[31]

A TOF trace is constructed by recording ion signal against arrival time at the detector with respect to the time at which photoexcitation occurred. The detector usually consists of a chevron microchannel plate (MCP) assembly. When a particle of a given m/z ratio collides with a MCP, it generates a cascade of electrons at the point of collision, amplifying the electric signal to be detected. Moreover, coupling an MCP to a phosphor screen allows for the point of electron collision within the MCP to be mapped, thus providing spatial resolution; this is particularly important for the imaging methods we will discuss in the next two sections. Given the mass resolution of the TOF spectrometer, the mass channel corresponding to the parent cation, for example, can be monitored over time independently (see section 2.4.1 for specific experimental details). By plotting the parent cation signal as a function of pump-probe time-delay, a TR-IY transient is obtained from which the lifetime of the excited electronic state can be extracted. Importantly, by integrating over different mass channels, TR-IY transients of photofragments can also be obtained and the dynamics of their formation extracted. This is analogous to (but not the same as) Zewail's on/off resonance studies for which photoproduct formation is monitored:[33] in TR-IY, the mass selectivity of the spectrometer (in addition to the change in probe wavelength, as discussed in section 2.1 for Zewail's experiments) can be exploited to allow for these photofragment specific observations. The mass selectivity of a TOF spectrometer thus provides valuable information on the the excited state decay pathways in operation in a given molecule.[34]

2.2.1.2   Velocity Map Ion Imaging

The TOF detection method we have just described contains information on the kinetic energy of charged particles in the temporal structure of their arrival times, but any in-

formation regarding the ions' velocities at the source, that is, the directions or angles at which they are ejected, is lost in the Wiley and McLaren TOF design. The value of imaging detection methods lies in their capability to provide information on both the kinetic energy and angular distributions of ejected particles, contained within the spatial appearance of a two-dimensional (2D) image, which can be used to reconstruct the full three-dimensional (3D) picture of the system at the time of probing.[35] Reconstruction of the 3D image is achieved by employing mathematical back-projection methods, such as Abel inversion or polar onion peeling (POP).[35,36]

In this section, we consider once more the point at which the system under study is ionised and focus particularly on the ions, or charged photofragments, which are thus produced. Upon photoionisation, ions are ejected at different velocities from the central point of interaction, forming a spherical ionic cloud around this central point (the same principles apply for photoelectrons, as we discuss in the next section). This set of expanding nested spheres resulting from photoionisation is usually referred to as a *Newton sphere.* The Eppink and Parker *velocity map imaging* (VMI) setup, shown in Figure 2.11, accelerates the Newton sphere towards detection by a set of three-electrode electrostatic lens (with voltages V_r, V_e and V_g), almost exactly as described for the Wiley and McLaren TOF setup.[31,35] The main difference in the VMI setup lies in the hollow cores of the extractor and ground electrode plates (as opposed to the mesh found in the TOF arrangement) to allow for maximum particle transmission.[35] After passing through a field-free flight tube (akin to the TOF setup) the 3D Newton sphere reaches the MCP assembly detector and is "compressed" onto a plane, becoming a 2D image (essentially, an assembly of nested circles). The VMI detector is also equipped with a phosphor screen, creating a position-sensitive detector which images the 2D projection of the Newton sphere; the image from the phosphor screen is then captured by a charge coupled device (CCD) camera.[35]

In order to obtain detailed information on the 3D distribution of the Newton sphere, it is important to improve the quality of the 2D image produced at the detector by sharply focusing it. The 2D image is focused by finely tuning the voltages on the electrostatic lenses arrangement; this is a crucial step, since it ensures that all charged photofragments formed at the source with the same initial velocity will be mapped onto the same point in the focal plane.[35] Eppink and Parker found that such focusing is achieved in their design when the ratio between the voltages on the repeller and extractor plates is $V_e/V_r \sim 0.71$, at which point the spatial resolution of the technique is limited by the detection system.
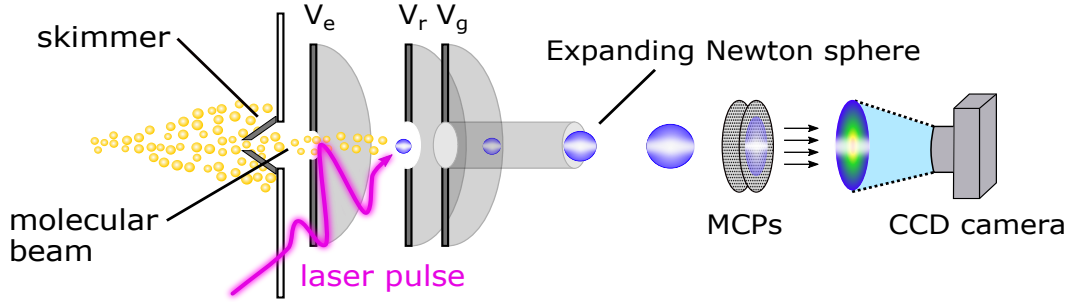
Figure 2.11: Diagram of a typical VMI experimental apparatus, consisting of a set of ion optics which accelerate the 3D Newton sphere created at the point of interaction between the laser pulses and the molecular beam towards a position-sensitive detector (a set of MCPs coupled to a phosphor screen), creating a 2D projection of the 3D Newton sphere. Importantly, all charged particles with the same initial velocity will be mapped onto the same point on the detector, independently of their position at the point of creation of the 3D Newton sphere. Note: only one laser pulse is shown here, for simplicity, however, time-resolved VMI follows the pump-probe scheme we have discussed in this chapter and Chapter 1.

Once a reliable image is produced, the radius R of a given VMI feature (a ring in the 2D image) is related to the speed v and flight time t of the ions corresponding to that feature by $R = Nvt$, where N is a magnification factor for which calibration is necessary. The kinetic energy of the photofragment is, therefore, given by $^1\!/\!_2 m[R/(Nt)]^2$, *i.e.* the kinetic energy is proportional to R^2, the square of the radius obtained from the 2D image.[35] However, the 2D image produced at the detector is a convolution of nested Newton spheres and, therefore, the 2D radial distribution we have just described is not a true representation of the velocity (and thus, energy) distribution of each individual 3D Newton sphere.

The 1D energy spectrum corresponding to the initial 3D velocity distribution, $F(r, \theta, \phi)$ in Figure 2.12, is given by $I(v)$:[37,38]

$$I(v) \propto \int_0^{2\pi} \int_0^{\pi} F(r, \theta, \phi) r^2 \sin\theta \, \mathrm{d}\theta \, \mathrm{d}\phi \tag{2.45}$$

where r is the radius of the Newton sphere, and θ, ϕ are the zenith and azimuthal angles, respectively. In the 2D projection (produced at the detector) of this 3D distribution, shown in Figure 2.12 as $G(R, \alpha)$, for radius R and angle α, the azimuthal angle information (ϕ in the 3D distribution) is lost. The fundamental aim of the reconstruction of the 3D Newton sphere from its 2D projection is to obtain the central 3D "slice" of the Newton sphere, for which $\phi = 0$.[36] For processes which possess cylindrical symmetry about the polarisation vector of the pump laser pulse, $\varepsilon_{\mathrm{pu}}$ (such as photodissociation and photoionisation), the $\phi = 0$ slice can be used to extrapolate $F(r, \theta, \phi)$, which can then be used to solve Equation

2.45.[36] Note, however, that angular information is only recoverable if ε_{pu} is parallel to the detector as, otherwise, the signal will appear isotropic. While several methods to achieve the reconstruction of a 3D sphere from its 2D projection are available, in the experiments presented in Chapters 3 and 4 we have employed a Polar Onion Peeling (POP) algorithm,[36] a short discussion of which follows.

The POP process starts by an analysis of the angular distribution of the charged particles at the interaction region, which manifests in the VMI 2D image as anisotropy, *i.e.* a non-uniform distribution of signal intensity along a given radius.[39] When a laser pulse of linearly polarised light interacts with the ensemble of molecules in a molecular beam (or any other sample), the molecules whose transition dipole moment are aligned along the polarisation vector of the laser light, ε_{pu}, are preferentially photoexcited.[38] The angular distribution (with respect to ε_{pu}) of charged particles ejected upon the photoionisation of the thus prepared ensemble of molecules is given by $I(\theta)$:[36,37]

$$I(\theta) = N(r) \sum_n \beta_n(r) P_n[\cos \theta].$$
(2.46)
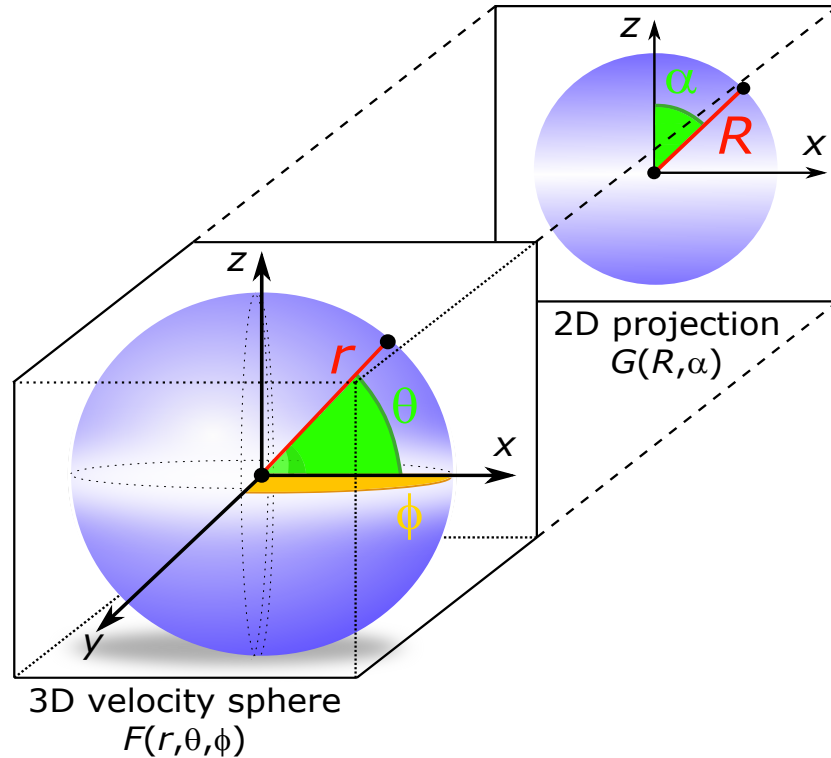
Figure 2.12: Projection of a 3D Newton sphere distribution, described in polar coordinates as $F(r, \theta, \phi)$. This 3D spherical distribution is mapped onto a 2D plane detector, the resulting distribution being described in terms of $G(R, \alpha)$.

In the equation above, θ is the angle between the ion velocity and the laser light polarisation (ε_{pu}), $N(r)$ is an intensity factor, $\beta_n(r)$ is the anisotropy parameter and $P_n[\cos\theta]$ is the nth order Legendre polynomial, determined by the physics of the process giving rise to the angular distribution.[36] In general, $I(\theta)$ is described completely for even values of n, where n can take values of up to twice the number of photons involved in the creation of the Newton spheres. For a one photon process, such as the photoionisation of an ensemble of molecules we are currently discussing, the process is described by $n = 2$, such that Equation 2.46 becomes:[40]

$$I(\theta) = \frac{\sigma}{4\pi}\left[1 + \frac{\beta_2}{2}(3\cos^2\theta - 1)\right] \tag{2.47}$$

where σ is the cross-section for charged particle ejection and β_2 is the second-order anisotropy parameter. If the ion is ejected parallel to ε_{pu}, $\beta_2 = 2$, while for perpendicular ejection with respect to ε_{pu}, $\beta_2 = -1$. Analysis of the anisotropy of a VMI image is, therefore, extremely valuable, since it can reveal preferential angles of photodissociation, for example, as well as unveil transitions between states with different transition dipole moments which may otherwise be undetectable (if the states have similar energy, for example). It is worth noting, however, that after photoexcitation the alignment induced by ε_{pu} is progressively lost over time due to molecular rotation. As such, β_2 is reduced from its limiting values (-1 to 2), eventually converging onto a small, but nonzero, absolute magnitude.[38] Such considerations regarding alignment with laser polarisation and consequent rotational dephasing are important not only in a VMI context, but throughout the experiments that will be described in later chapters. Where relevant, we will discuss how these may affect the observed behaviour and how rotational artefacts are accounted for in the analysis and interpretation of the presented data.

To reconstruct the 3D Newton sphere, the POP algorithm uses the raw 2D polar image, $G(R, \alpha)$, which corresponds to a sum over all radii, r, of the 3D image:[36]

$$G(R, \alpha) = \int_0^{r_{max}} g(r; R, \alpha)\,\mathrm{d}r. \tag{2.48}$$

Provided there is no signal of larger radius than the detector, the distribution over the outermost 2D ring radius, R_{max}, can be taken to be a function of the 3D coordinates r and θ, $i.e.$ $h(r_{max}, \theta)$, which implies the 2D and 3D radii can be assumed to be the same, $R_{max} = r_{max}$.[36] At this limit, $h(r_{max}, \theta)$ can be modelled using the angular distribution

described in Equation 2.46. The values of $N(r)$ and $\beta_n(r)$ extracted from this fit can be employed in conjunction with a set of basis functions to calculate the $g(r_{max}; R, \alpha)$ 2D "slice" (Equation 2.48). Subtraction of the $g(r_{max}; R, \alpha)$ "slice" from the overall 2D polar image, $G(R, \alpha)$, removes the initially outermost layer from the raw 2D image. This subtraction is repeated successively until the center layer of the 2D image, corresponding to $r = 0$, is reached. At each one of the subtraction steps a $h(r, \theta)$ value is generated; the collection of these values can be used to reconstruct the $F(r, \theta, \phi)$ 3D slice for which $\phi = 0$. Once this central 3D slice is known, the full 3D spherical *spatial* distribution, $I(r)$, can be reconstructed by employing a $\sqrt{r} \sin \theta$ scaling factor and integrating over all values of θ:

$$I(r) = \int_0^{2\pi} F(r, \theta, \phi = 0)\sqrt{r} \sin \theta \ d\theta \qquad (2.49)$$

Conversion of the radial spectrum to the required energy spectrum is achieved with a calibration factor which is specific to each imaging apparatus; the details regarding calibration of the Warwick imaging setup are given in section 2.4.1.

2.2.1.3 Photoelectron Spectroscopy

The Eppink and Parker VMI arrangement can be altered to detect photoelectrons ejected during ionisation of the sample simply by changing the polarity of the electrode plates, so that negatively charged particles are accelerated instead. The imaging and energy spectra recovery for photoelectrons (employing the POP algorithm just described, for example) follows essentially the same principles as that of ions. However, time-resolved photoelectron spectroscopy (TR-PES) provides complementary information to that obtained in VMI since it reveals details concerning the energy content and charge redistribution as a function of pump-probe time delay for the species under study. The first TR-PES experiments date back to 1985.[41] More recently, significant experimental and theoretical developments on the technique have been lead by authors such as Reid,[42] Stolow[41,43] and Seel and Domcke,[44,45] amongst others, which are crucial to the current understanding and applications of TR-PES.

TR-PES follows the pump-probe configuration we have now described several times. The probe laser pulse in TR-PES experiments generates free electrons through photoionisation and the quantity measured in these experiments is electron kinetic energy (eKE) and angular distribution as a function of pump-probe time delay. TR-PES is particularly

well-suited to the study of non-adiabatic processes, for which excited state population crosses a conical intersection between electronic states (discussed in more detail in Chapter 1, section 1.2), since it is sensitive to both electronic configurations and vibrational dynamics. Since TR-PES detects photoelectrons generated upon molecular photoionisation, the final state, onto which the excited state non-adiabatic dynamics are projected, will be located within the molecular ionisation continuum, which has several practical and conceptual advantages. Firstly, there are no "forbidden" photoionisation transitions due to the relaxed selection rules for this process.[41,42] Specifically, the symmetry selection rule for a transition from an excited state to the photoionisation continuum can be expressed by modifying Equation 1.32 in Chapter 1 (where the symmetry selection rule for the transition between two bound states is given) to include an electronic term:[41,46]

$$\Gamma_{ex} \otimes \Gamma_{\hat{\mu}} \otimes \Gamma_{+} \otimes \Gamma_{e-} \supseteq \Gamma^{(s)} \tag{2.50}$$

where Γ_{ex}, $\Gamma_{\hat{\mu}}$, Γ_{+} and Γ_{e-} are the irreducible symmetry representations for the excited state, the transition dipole moment, the final state in the photoionisation continuum and the electron, respectively, and $\Gamma^{(s)}$ is the totally symmetric irreducible representation. Since the photoelectron is decoupled from the ion core, the wavefunction of an ejected photoelectron transforms as the totally symmetric representation $\Gamma^{(s)}$ when the orbital angular momentum quantum number, l, is even, and as the antisymmetric representation Γ^{*} when l is odd.[46] This flexibility relaxes the overall selection rules for the photoionisation process, such that it is always an allowed transition.[41]

Other advantages of TR-PES which are related to the molecular photoionisation continuum final state include the sensitivity of charged particle detection methods and the possibility to differentially analyse the kinetic energy and angular distribution of the ejected photoelectron. Moreover, cationic states provide a stable template for "disentangling" electronic dynamics from vibrational dynamics in the excited state.[41] To elucidate on this "disentanglement" of dynamics, let us consider the non-adiabatic process shown in Figure 2.13, for which the initially excited, "bright" state α couples to a lower lying, "dark" state β. When probing the excited state α, the probe will generate an electron with a maximum kinetic energy (eKE$_{max}$), given by:

$$\mathrm{eKE}_{\max} = (h\nu_{\mathrm{pu}} + h\nu_{\mathrm{pr}}) - \mathrm{IP} \tag{2.51}$$

where $h\nu_{pu} + h\nu_{pr}$ is the total energy provided to the system, the sum of the pump ($h\nu_{pu}$) and the probe ($h\nu_{pr}$) energies; the IP, is the ionisation potential of the system, *i.e.* the energy required to eject the photoelectron. Thus, when state α is ionised to α_0^+ a photoelectron of kinetic energy eKE_1 is released, whereas state β is ionised to a different continuum, β_0^+ and hence the released photoelectron will have a different kinetic energy, eKE_2.[41] Experimentally, as depicted in Figure 2.13(b) this behaviour manifests as a photoelectron band eKE_1 being initially observed but decaying over time, as the non-adiabatic process and thus transition to state β takes place, producing a growing photoelectron spectral feature at eKE_2.[41] Apart from the information regarding electronic population dynamics which can thus be obtained, the coupled nuclear dynamics may still be monitored by analysis of the vibrational structure within each photoelectron band. While the possibility of gathering both electronic and vibrational information on a given system simultaneously has been demonstrated to be a poweful spectroscopic tool, this "disentanglement" of dynamics may be lost if either the photoexcited or final states have similar characteristics or energies, rendering the transition undetectable.[41] Moreover, vibrational information may also not be resolvable due to the large spectral bandwidths of femtosecond laser pulses.

As an imaging method, TR-PES also contains information within the angular distributions of the ejected photoelectrons; in fact, TR-PES angular distributions reflect the
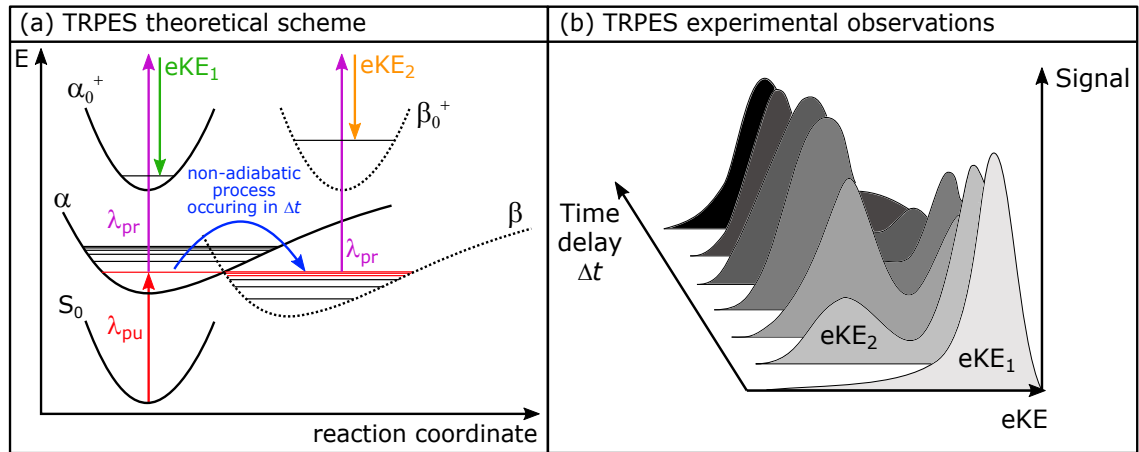
Figure 2.13: Schematic representation of TR-PES of excited state dynamics in polyatomic molecules. (a) The initially photoexcited state, α, is ionised to a particular ionisation continuum, α_0^+ producing a photoelectron band at energy eKE_1. As the non-adiabatic process takes place, and state β is populated, ionisation instead takes place onto the β_0^+ continuum, producing a photoelectron band at energy eKE_2. Experimentally, this would manifest as an initial photoelectron band, eKE_1, decaying as a new band, eKE_2, appears and grows as a function of time, as shown in (b). Adapted from references 43 and 41.

symmetry of the electronic state undergoing ionisation.[41,42] Selection rules dictate that if the symmetry of the excited state changes, so must the symmetry of the ejected electron, so that the product will remain totally symmetric (see Equation 2.50).[41] The angular distribution of ejected photoelectrons is described in terms of signal intensity as a function of ejection angle, $I(\theta, \phi)$, given by:[42]

$$I(\theta, \phi) \propto \sum_{l=0}^{l_{max}} \sum_{m=-l}^{l} B_{lm} Y_{lm}(\theta, \phi). \tag{2.52}$$

In the equation above, l and m refer to the orbital angular momentum and magnetic momentum quantum numbers, respectively; $Y_{lm}(\theta, \phi)$ is a spherical harmonic function and B_{lm} is a coefficient dependent on experimental and sample geometries, distributions and/or orientations, on the dynamics of the system, on photoionisation energy and on the orbital from which the electron is ejected. It is important to note here, since the B_{lm} coefficient depends on such experimental conditions, rotational artefacts with respect to the laser pulse polarisation need to be accounted for, as discussed earlier for VMI. Nevertheless, the measurement of time-resolved photoelectron angular distributions is particularly valuable in the study of systems for which photoelectron kinetic energy alone may not be sufficient to distinguish between different states and thus is not sufficient to follow dynamic processes.[41]

In our experiments, particularly those described in Chapter 4, TR-PES has proved valuable in the study of the mechanisms for ultrafast energy redistribution in sunscreen molecules. In particular, the sensitivity of TR-PES to the specific continuum being accessed upon photoionisation and the observation of quantum beats in our measurements revealed mechanisms and timescales for the coupling of vibrational states which may explain the molecule's behaviour as a long-lived sunscreen, as discussed in Chapter 4.

2.2.2   In Solution: Transient Electronic Absorption Spectroscopy (TEAS)

Pump-probe approaches have also been very successfully applied to the study of chemical reactions in solution. For these experiments, the sample typically consists of dilute solutions ($\sim 10^{-6}$ M) of the molecule of interest in the chosen solvent. As before, the sample is photoexcited by a pump laser pulse, with λ_{pu} being chosen so that the excited state of interest is accessed. However, in contrast with the gas-phase techniques just described, in transient electronic absorption spectroscopy (TEAS) the probe pulse consists of a white

light continuum (WLC, with wavelengths ranging from UV to IR).[20,21] The photoexcited species will then further absorb the probe wavelengths which correspond to allowed electronic transitions, effectively yielding an excited state UV/Vis absorption spectrum at each time delay.

The experimental quantity measured in TEAS setups is a change in optical density, ΔOD, which is a logarithmic quotient of the light transmitted by the sample before and after excitation for each probe wavelength, $I_0(\lambda_{\text{pr}})$ and $I^*(\lambda_{\text{pr}}, \Delta t)$, respectively:[47]

$$\Delta\text{OD}(\lambda_{\text{pr}}, \Delta t) = \log_{10}\left(\frac{I_0(\lambda_{\text{pr}})}{I^*(\lambda_{\text{pr}}, \Delta t)}\right) \tag{2.53}$$

The transient absorption spectra (TAS) recorded are a convolution of all the processes that have an effect on ΔOD, occurring on their individual timescales. An initial qualitative analysis of the TAS can be rather informative, since there are distinct spectral features that may be identified, as shown in Figure 2.14. Positive features present in TEAS transients arise from phenomena which decrease the intensity of the light transmitted through the sample after photoexcitation when compared to the unpumped sample, *i.e.* $I^*(\lambda_{\text{pr}}, \Delta t) < I_0(\lambda_{\text{pr}})$, which returns a positive $\Delta\text{OD}(\lambda_{\text{pr}}, \Delta t)$. These phenomena include absorption of probe light by the molecule's excited state, referred to simply as *excited state absorption*, or absorption of probe wavelengths by any photoproducts that may be formed as a result of photoexcitation. The appearance of a photoproduct may therefore be readily identifiable by the growth of a positive feature in the TAS.[47]
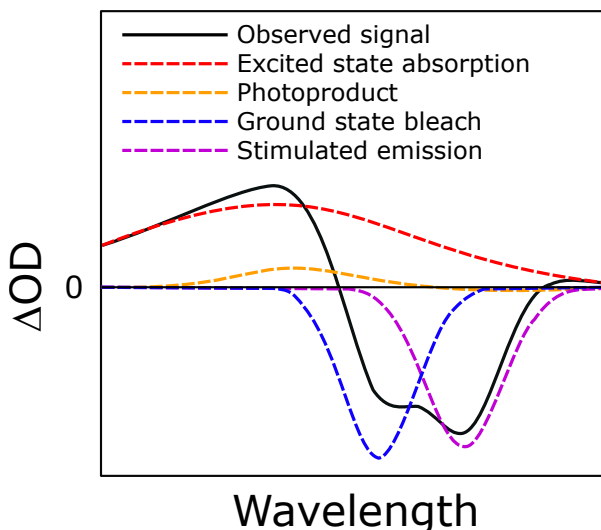
Figure 2.14: Schematic of typical TEAS features, adapted from reference 47.

On the other hand, phenomena which increase the intensity of light transmitted after photoexcitation, resulting in $I^*(\lambda_{pr}, \Delta t) > I_0(\lambda_{pr})$, produce negative TEAS features ($\Delta OD(\lambda_{pr}, \Delta t) < 0$). These situations may arise from, for example, a *ground state bleach*: the absorption of the pump pulse causes a decrease in the population of the ground state and thus a reduced absorption of radiation from this state. As a result, more light is transmitted after photoexcitation and a negative TEAS feature thus arises. However, as the excited state population relaxes, absorption from the ground state should gradually increase; the evolution of a ground state bleach feature is therefore a measure of how quickly the photoexcited molecule returns to its ground state. Moreover, a negative TEAS feature may also be due to stimulated emission being prompted by the probe laser pulse and may be indicative of a potentially fluorescing state.[47]

Identifying and quantifying the rates of appearance and/or disappearance of these features, as well as any spectral shifts, is crucial to the understanding of the photodynamics occurring in these solvated molecules (*i.e.* molecules in solution).[47] Studies in solution are particularly relevant since, in contrast to studies in vacuum, they introduce the perturbative solvent effects that are relevant in the context of sunscreen use in commercial formulations. As we will discuss in more detail in section 2.4.3, in order to deconvolute the different processes contributing to the TAS and to extract their respective time constants, the transients can be evaluated by global fitting (*i.e.* taking all probe wavelengths into account simultaneously) according to a pre-defined kinetic model.[47]

2.3   Frequency-Resolved Pump-Probe Spectroscopy

A molecule's photochemistry and photophysics are highly dependent not only on the arrangement of its constituent atoms, but also on its electronic and vibrational energy structure or, using the terminology we have introduced in the last chapter, its *vibronic structure*.[48] Therefore, an understanding of a molecule's vibronic structure aids the interpretation of its photoreactivity.[48] Frequency-resolved spectroscopy techniques can provide a picture of the vibronic structure of a given system by photoexciting molecules to specific vibrational levels and employing various detection methods to probe these excited states. As we have discussed previously, the time-frequency uncertainty relationship implies that long laser pulses (typically nanosecond pulses) are required to achieve the sub-wavenumber resolution necessary to resolve vibronic (and in some cases rovibronic) states.[48–51] While

the focus of this thesis is on time-resolved studies, we have undergone extensive collaborative work in which frequency-resolved techniques were employed to inform on the vibronic structure of the sunscreen molecules we investigated. Therefore, the next section serves as a brief overview of the frequency-resolved techniques that will be mentioned in later chapters.

2.3.1   Laser Induced Fluorescence Spectroscopy

Following the pump-probe scheme that has been the dominant topic in this chapter, in laser induced fluorescence (LIF) spectroscopy a molecule seeded into a cold molecular beam is photoexcited by a pump laser pulse from its ground vibronic state (S_0); the pump wavelength, λ_{pu}, is varied so that specific vibrational levels within a given electronic state are accessed, *e.g.* within the first excited electronic state (S_1), as represented in Figure 2.15(a).[52,53] Note, however, that the probe step in LIF does not require a probe laser pulse, since the radiative decay of the excited states provides a fluorescence signal that can be collected with a photomultiplier tube or similar photodetector. From the collected data, a plot of fluorescence intensity *vs.* excitation wavelength, called an *excitation spectrum*, is produced. Alternatively, λ_{pu} may be fixed to a wavelength resonant with a specific vibronic excited state and the resulting fluorescence signal dispersed by a grating onto a photodetector, so that the fluorescence from the excited state onto the several vibrational levels of the ground electronic state is monitored, as depicted in Figure 2.15(b); this technique is referred to as dispersed fluorescence (DFL).[54–56] Fluorescence lifetimes can be measured with either of these setups, simply by monitoring the fluorescence signal following photoexcitation over time.[57,58] The temporal resolution of these experiments is limited by detector response times (and the laser temporal profile) which, for many common photomultiplier tubes, is approximately 1 to 10 ns.[59]

LIF experiments benefit from high signal-to-noise levels and thus a higher sensitivity than absorption spectroscopy techniques since, unlike the latter, LIF detects a bright signal against a dark background.[52] Since fluorescence intensity is proportional to the population of the emitting state, LIF can provide information on the relative population of excited states.[53] However, as LIF is a one-photon process (in the pump step), it is limited by the efficiency of the transitions involved, both in excitation and fluorescence, which are governed by the same symmetry and spin selection rules of any one photon vibronic transition, as discussed in Chapter 1. As we shall demonstrate in Chapters 3 and
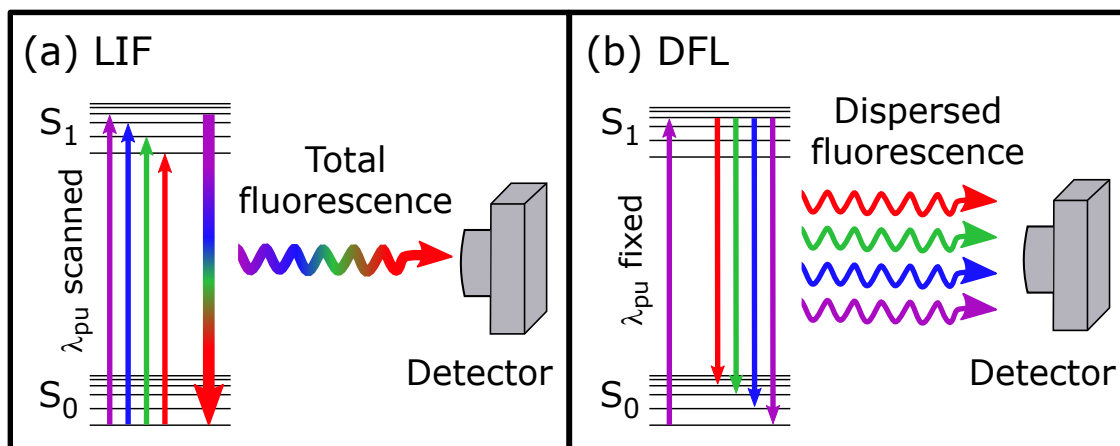
Figure 2.15: Schematic representation of (a) LIF and (b) DFL. In LIF, λ_{pu} is scanned so that any resonant wavelengths may photoexcite certain vibronic states. The photoexcited states will then radiatively decay to accessible vibrational levels in the ground electronic state (S_0, represented by thick gradient arrow in (a)); the total fluorescence signal is collected by a photomultiplier tube. In DFL, on the other hand, λ_{pu} is set to a particular vibronic state, from which fluorescence may take place to any accessible vibrational level of the S_0 state. The total fluorescence signal is dispersed by a monochromator in order to deconvolute the information on the vibrational levels of the S_0 state, and again is collected by a photomultiplier tube.

4, both LIF and DFL can be successfully applied to the study of sunscreen molecules in the gas-phase, providing valuable insight into their electronic structure.

2.3.2   Resonance Enhanced Multiphoton Ionisation Spectroscopy

Resonance enhanced multiphoton ionisation (REMPI) is a photoionisation technique which employs multiple photons to first resonantly excite (pump) and then ionise (probe) the molecule of interest.[49,60] Both the sample delivery and detection methods used in REMPI experiments are akin to those employed in vacuum time-resolved spectroscopic techniques, *e.g.* molecular beam and TOF spectrometer. The use of a TOF spectrometer in combination with REMPI spectroscopy provides the technique with mass selectivity, which allows for contamination from absorbing species other than the molecule of interest to be supressed.[60] Like LIF, REMPI spectroscopy benefits from high sensitivity which in this case arises from the capability to detect all charged particles produced by photoionisation. In addition, the ionisation (probe) step is not as constrained by symmetry selection rules as fluorescence, as we have previously discussed in the context of TR-PES (section 2.2.1.3).[61,62]
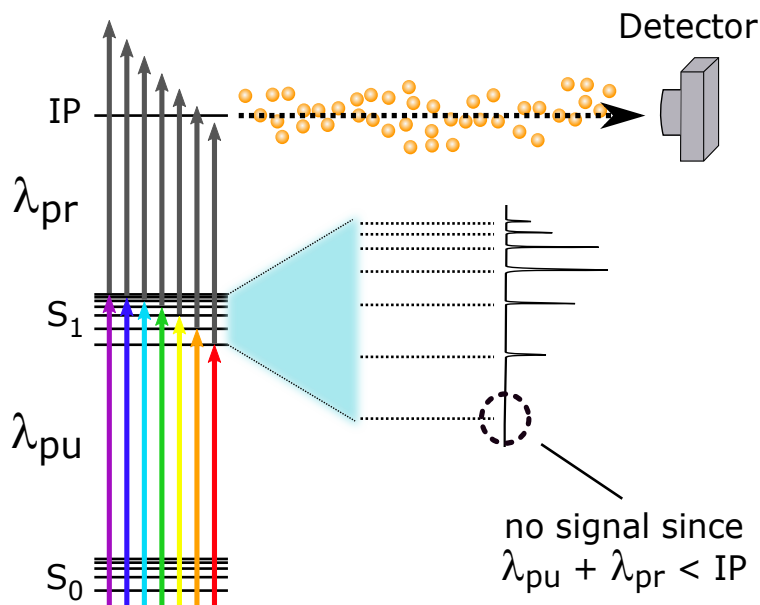
Figure 2.16: Schematic representation of the basic concept behind R2PI spectroscopy. As λ_{pu} is scanned, each vibronic state is individually accessed. These states are probed by a second photon, λ_{pr}, and resulting charged particles are directed to an appropriate detector. The intensity of the peaks corresponding to each vibrational state depend on transition strength; the factors which influence transition strength were discussed in Chapter 1. The IP of the molecule under study is found by scanning the probe wavelength until signal disappears; the energy of the probe light at this point, plus the energy of the pump, corresponds to the IP of the molecule.

REMPI schemes are usually referred to as $n + m$, where n and m correspond to an integer number of photons of a single colour used to pump and probe the system of interest, respectively.[60,63,64] When different colours are used for the pump and probe steps, this is referred to as $n + m'$.[65,66] While excited states can usually be accessed and probed simply with a (1+1) REMPI scheme — also referred to as resonant two photon ionisation or R2PI, shown in Figure 2.16 — there are cases in which several (n) photons need to be absorbed simultaneously to reach a certain electronic excited state. These multiphoton absorption processes follow an I^n power dependence on laser intensity (I) and they therefore require the high photon densities achievable only with laser technology.[67,68] Regardless of the specific ionisation scheme, in a REMPI experiment the charged particles produced by the ionisation step are monitored as a function of excitation wavelength. This produces spectral lines as each new vibronic excited state is accessed thus revealing the molecule's vibronic structure. The total ion signal as a function of probe wavelength can also be monitored in order to determine the ionisation potential (IP, Figure 2.16) of the molecule under study: the cut-off point where no ion signal is observed indicates the point at which the total energy provided to the molecule is no longer sufficient to ionise it.[69]

2.3.3   Double Resonance Spectroscopy

The ability to distinguish between conformers of the same molecule, which the mass selectivity of REMPI techniques cannot resolve, is particularly relevant when dealing with large molecules, such as the sunscreen molecules studied in this thesis. In certain cases, contributions from different conformers in vibrational spectra can be distinguished by analysis of their rotational structure;[23,70–72] however, especially for larger molecules, the typical resolution achieved with these techniques is almost never enough to resolve closely spaced rotational energy levels.[23,73] Double resonance techniques such as hole burning (HB) or depletion (ion dip) spectroscopies are useful for such cases, when the contributions from different conformers may be present in a given spectrum.[60]

Double resonance spectroscopy requires the use of three pulses: excitation (λ_{pu}) and ionisation (λ_{pr}) laser pulses, as before, and an additional *holeburn* (HB) laser pulse, λ_{HB}.[6,60] If λ_{HB} and λ_{pu} are both within the UV region, the technique is referred to as UV-UV HB spectroscopy, however other combinations are possible, such as UV-IR or IR-UV (which will mainly interrogate the vibrational structure of vibronic states).[74,75] The term "holeburn" refers to the creation of a population hole in a certain state (*e.g.* ground electronic state) by exciting the population to a higher vibronic state.[6] At energies close to the excited state origin, a wavelength that is resonant with a specific transition in conformer A, will likely not be so for a second conformer, B. Hence, with reference to Figure 2.17, if the wavelength of λ_{HB} is set to be resonant with a transition in conformer A, thus depopulating its ground state, the R2PI signal will be reduced when λ_{pu} coincides with a resonance in this conformer; however, no analogous signal difference will be observed for conformer B.[60] If the total R2PI spectrum is subtracted from the resulting holeburning spectrum (*i.e.* the R2PI spectrum obtained after the holeburn laser pulse has interacted with the system), the contribution from conformer A can be isolated, with the resulting spectrum consisting of negative peaks.

The same principles apply for depletion spectroscopy, for which the wavelength of λ_{HB} is scanned, with λ_{pu} fixed on a single transition for a given conformer.[77,78] In this case, there will be a reduction in the detected signal whenever λ_{HB} is resonant with a vibronic state in the initially photoexcited conformer. While these techniques provide complementary information, there are differences in the factors that influence ion signal intensities. Depletion spectroscopy monitors changes in ion intensity (as λ_{HB} is scanned)

compared to a constant pump-probe signal. As such, the signal intensity depends on the absorption cross-section of the transition accessed by λ_{HB}. In HB spectroscopy, on the other hand, since it is the excited state leading to ionisation that is being varied, the signal intensity depends on both absorption cross-section and also on excited state dynamics. Moreover, for both HB and depletion spectroscopy, it is assumed that, after photoexcitation by λ_{HB}, excited state population does not relax to the ground-state within the timescale of pump-probe irradiation.
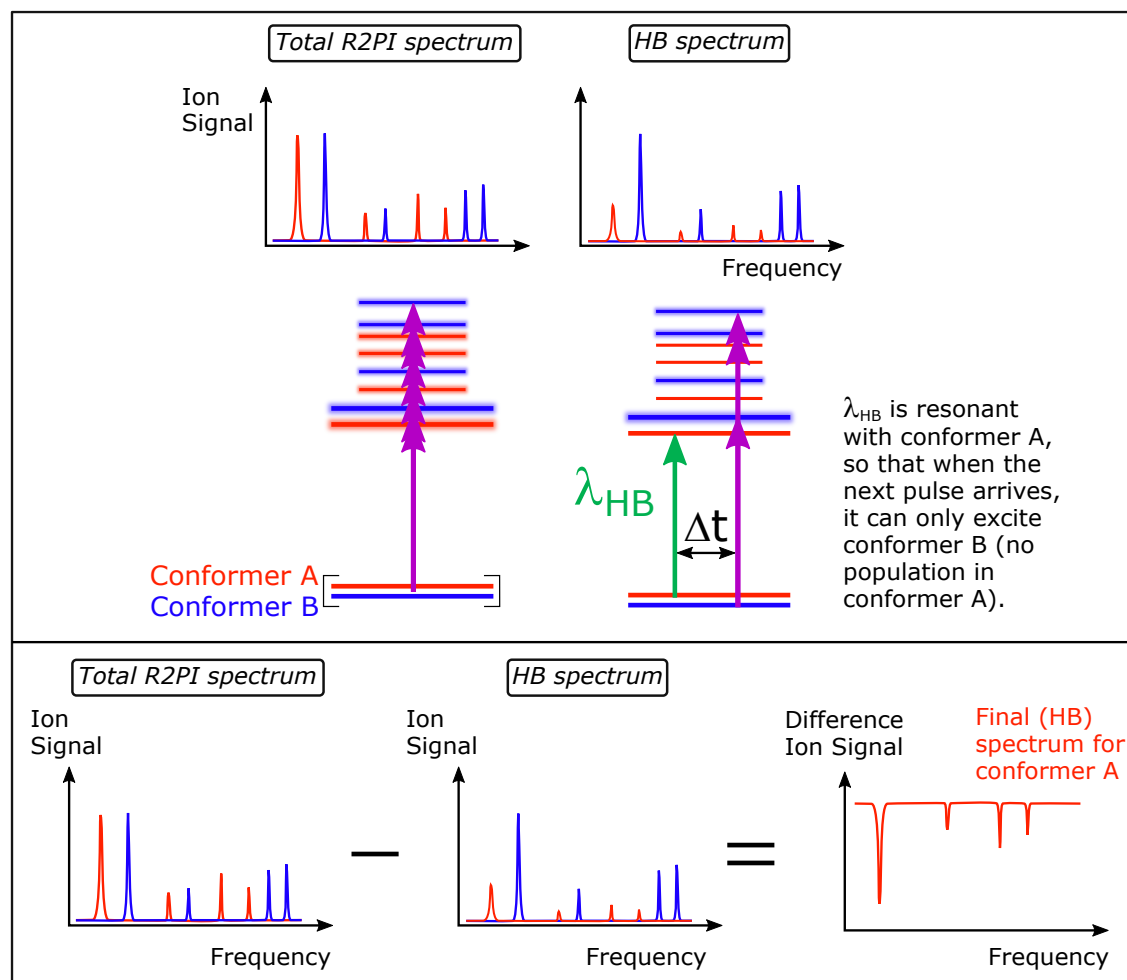
Figure 2.17: Schematic demonstration of HB spectroscopy. The HB laser creates a population hole in the ground state of one of the conformers, so that its contribution to the R2PI spectrum is decreased. Subtracting the total R2PI spectrum from the holeburning (HB) spectrum therefore yields the isolated contribution from the selected conformer in the form of negative peaks. Multiple headed purple arrows denote the wavelength scanning of the λ_{pu} laser pulse. Various detection techniques (ionisation, fluorescence, $etc.$) can be used.

2.4   The Warwick Setup

While further experimental details pertaining to specific experiments will be given in Chapters 3 and 4, it is important to provide an overview of the experimental setup used in the studies reported in this thesis and performed at the University of Warwick. All the time-resolved experiments detailed in later chapters were performed using the laser system and experimental setup shown in Figure 2.18. The laser system consists of a Spectra-Physics mode-locked oscillator (Tsunami) for which the laser medium is a titanium-doped sapphire crystal (Ti:Al$_2$O$_3$ or Ti:sapphire). The Tsunami is pumped by the Spectra-Physics Millenia, a green wavelength (532 nm) 5 W frequency-doubled, continuous wave Nd:YVO$_4$ laser, producing a pulse train consisting of < 100 fs pulses at ~ 4 nJ/pulse and at a repetition rate of 76 MHz. The Tsunami pulses have a central wavelength of 800 nm and a bandwidth of ~ 40 nm, measured at FWHM. These pulses are directed into the Spectra-Physics Spitfire XP regenerative amplifier which selects pulses with a high voltage Pockels cell at a repetition rate of 1 kHz. These seed pulses are subject to CPA in a second Ti:sapphire cavity which is pumped by a pulsed 15 W Nd:YLF laser (Spectra-Physics, Empower, 532 nm). The output of the Spitfire XP is selected by a second high voltage Pockels cell and is then recompressed. This yields the fundamental 800 nm beam, operating at a 1 kHz repetition rate, with pulse energies of ~ 3 mJ/pulse or an average power of 3 W, and a temporal bandwidth of approximately 40 fs.

The 3 W fundamental is then split into three beams. Initially, a 66% reflective mirror transmits a beam of ~ 1 W which is directed onto a gold plated retroreflector mounted on a motorised delay stage (Physik Instrumente) which provides the variable time delay between the pump and probe pulses employed in our experiments in vacuum (maximum pump-probe time delay $\Delta t \sim 1.2$ ns). The same beam is then sent to one of two frequency-conversion options so that its wavelength can be tuned to experimental requirements: *i)* an optical parametric amplifier (OPA, see section 2.1.3.2) capable of generating wavelengths in the range of $\sim 230 - 2100$ nm (Light Conversion, TOPAS-C) or *ii)* a set of β-Barium Borate (BBO) crystals capable of generating 200 nm. Conversion to 200 nm is achieved by a combination of SHG and SFG processes: firstly, SHG from the fundamental beam yields a 400 nm beam which is subsequently combined with the residual fundamental 800 nm beam to produce, due to SFG, 267 nm light. Finally, 200 nm light is produced by SFG between the 267 nm beam and the residual 800 nm.
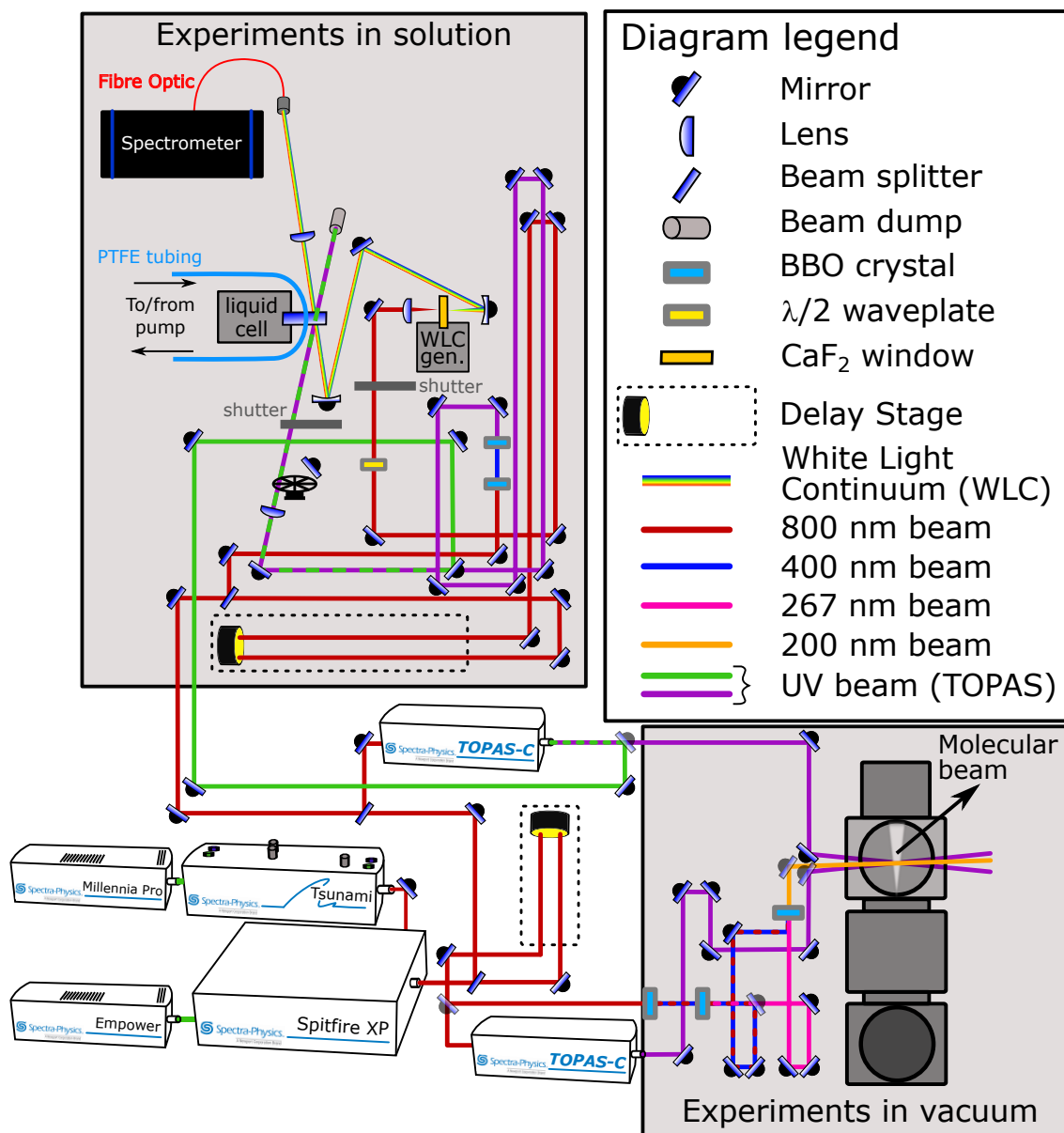
Figure 2.18: Schematic of the laser table and experimental setups used in the time-resolved experiments presented in later chapters.

The remaining 2 W beam from our fundamental is further split into two beams at 1 W each, one of which pumps a second TOPAS-C, while the other is used for our condensed-phase experiments (*i.e.* in solution). In the condensed-phase setup, the 1 W fundamental beam is split by a 95:5 beam splitter. One of the resulting beams, at 50 mW, is sent towards a second retroreflector mounted on a motorised delay stage (Physik Instrumente) which acts as the source of pump-probe delay in our TEAS experiments (maximum pump-probe time delay $\Delta t \sim 2$ ns); the same beam is then employed to produce the WLC which constitutes the probe pulse in the TEAS setup. The remaining ~ 950 mW beam is used

for SHG/SFG as an additional possible source of pump pulses for our condensed-phase experiments.

2.4.1   In Vacuum

Laser pulses from either one of the TOPAS-C or from the 200 nm beam line can be used for TR-IY, VMI or TR-PES experiments in vacuum (see Figures 2.18 and 2.19). The polarisation of the laser pulses is defined by the TOPAS-C but can be changed by the optical setup (periscopes). The polarisation of the pump laser pulse is kept parallel to the detector for imaging experiments, with the relative polarisation between the pump and probe laser pulses also parallel (to allow for the detection of anisotropy changes). For any other experiments (TR-IY), separate measurements are taken with the polarisations of the pump and probe beams parallel and perpendicular to each other in order to calculate the equivalent results at magic angle.[76]

The vacuum chambers that enclose the apparatus for these experiments are shown schematically in Figure 2.19. The source chamber encloses a pulsed solenoid Even-Lavie valve which generates the cold molecular beam of target molecules, as described in sec-
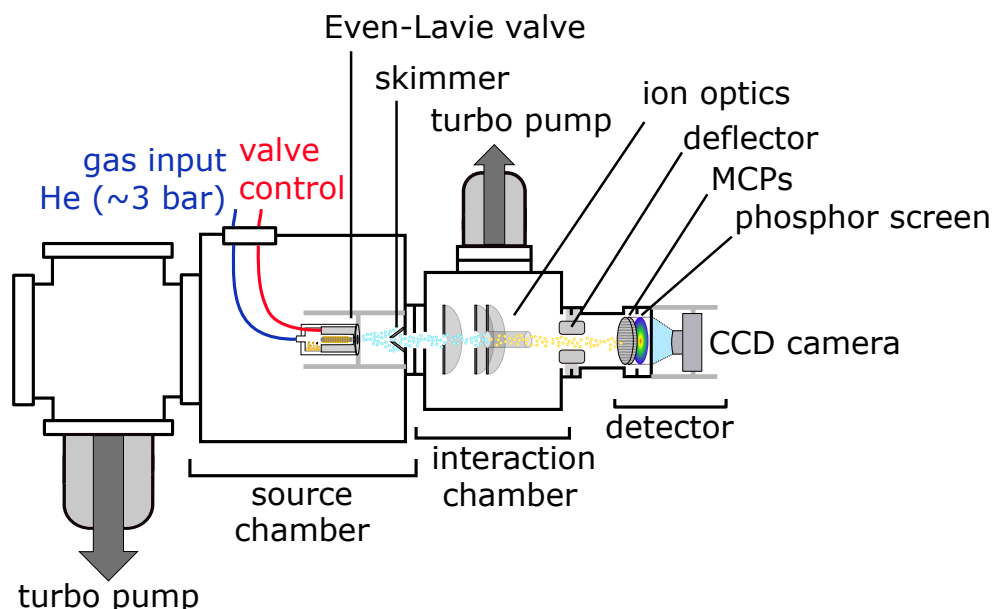
Figure 2.19: Schematic layout of the high vacuum system at Warwick, showing the chambers which enclose the apparatus for our gas-phase experiments, including the Even-Lavie valve, MCPs and CCD camera. The left most chamber serves to house the large turbo pump for the source, the middle and right vessels are the source and interaction chambers, respectively, with the detector apparatus located far right.

tion 2.2.1. The pressure within the source chamber during experiments is approximately 10^{-6} mbar, maintained by a 2200 Ls^{-1} turbo pump (Oerlikon Leybold Mag W 2200). The source chamber is separated by a gate valve from the next vessel, which encloses the interaction region. A stainless steel skimmer with a 2 mm aperture, which will serve to select the cold core of the supersonic jet to create a molecular beam, as discussed earlier in this section, is located between the source and interaction chambers. The interaction chamber houses a set of ion optics consisting of three charged metal plates: a repeller, an extractor and a ground, at voltages V_r, V_e and V_g, respectively. These ion optics accelerate species generated in the interaction region towards a short TOF tube, at the terminus of which the detection apparatus is mounted. Moreover, the interaction chamber is equipped on either side (perpendicular to the molecular beam) with a CaF$_2$ window through which the laser pulses are aligned with the centre of the electrostatic lens arrangement and made to perpendicularly intersect the molecular beam. The pressure in the interaction region is controlled by a 700 Ls^{-1} turbomolecular pump (Oerlikon Leybold Turbovac Mag W 700) and is typically maintained between $\sim 10^{-9}$ mbar at rest and $\sim 10^{-7}$ mbar during experiments, when the Even-Lavie valve is pulsing.

The detection apparatus in our vacuum setup can be changed depending on whether imaging capabilities are required. For a simple TOF spectrometer experiment, ions are focused onto two MCPs coupled to a phosphor screen. The current output from the front of the phosphor screen, gated in ion flight time over the mass channel of each parent or fragment ion, can then be measured on a digital oscilloscope (LeCroy LT372 Waverunner) and integrated as a function of Δt in order to produce TR-IY transients. Alternatively, the two MCPs coupled to a phosphor screen can be used as a position-sensitive detector for imaging experiments, such as photofragment detection (*e.g.* H-atom elimination) and TR-PES. In this case, light emitted by the phosphor screen is captured by a charge couple device (CCD) camera (Basler, A312f) which links to a custom recording program built within the LabVIEW platform.

The imaging detector must be calibrated for accurate values of energy to be obtained from our imaging results. In the case of photofragment experiments, for which a AX—H bond photodissociation takes place, for example, we refer to *total kinetic energy release* (TKER), defined as:[79,80]

$$TKER = h\nu_{\mathrm{pu}} - D_0(\mathrm{AX—H}) - E_{elec} - E_{vib} \qquad (2.54)$$

where $h\nu_{\text{pu}}$ is the pump photon energy, $D_0(\text{AX—H})$ is the AX—H bond strength, and E_{elec} and E_{vib} are the electronic and vibrational energies of the radical co-fragments, AX. Our VMI setup is calibrated for photofragment experiments with HBr photolysed with 200 nm (50 000 cm^{-1} or $\sim$ 6 eV),[80] for which the bond dissociation energy is $D_0(\text{H—Br}) = 30\,210 \pm 40$ cm^{-1} and $E_{int} = 0$ for maximum TKER ($E_{int} = E_{vib} + E_{elec}$, *i.e.* the fragment's internal energy). During the photodissociation of HBr, H-atoms are dissociated with partner bromine fragments being produced both in their spin-orbit ground and excited state ($\text{Br}(^2P_{3/2})$ and $\text{Br}^*(^2P_{1/2})$, respectively); the energy separation between these fragments has been previously reported as $\Delta E_{elec} = 3685$ cm^{-1}.[80] The dissociated H-atoms are resonantly probed with $\lambda_{\text{pr}} = 243$ nm.

The 2D VMI image resulting from photolysis of HBr ($\lambda_{\text{pu}} = 200$ nm; $\lambda_{\text{pr}} = 243$ nm) is shown in Figure 2.20(a), with the corresponding 1D spectrum (ion signal *vs.* squared image radius, r^2) being shown in Figure 2.20(b). The two highest energy peaks observed in the 1D radial spectrum, $r^2 = 36\,481$ and $r^2 = 44\,944$, correspond to the spin-orbit excited (Br*) and ground (Br) state bromine photofragments, respectively, while the two lower energy peaks are assigned to multiphoton effects. To calibrate the r^2 peaks to the appropriate TKER values of the bromine photofragments, the peaks in the radial spectrum are compared to the known values of E_{elec} of the corresponding photofragment[80] and a
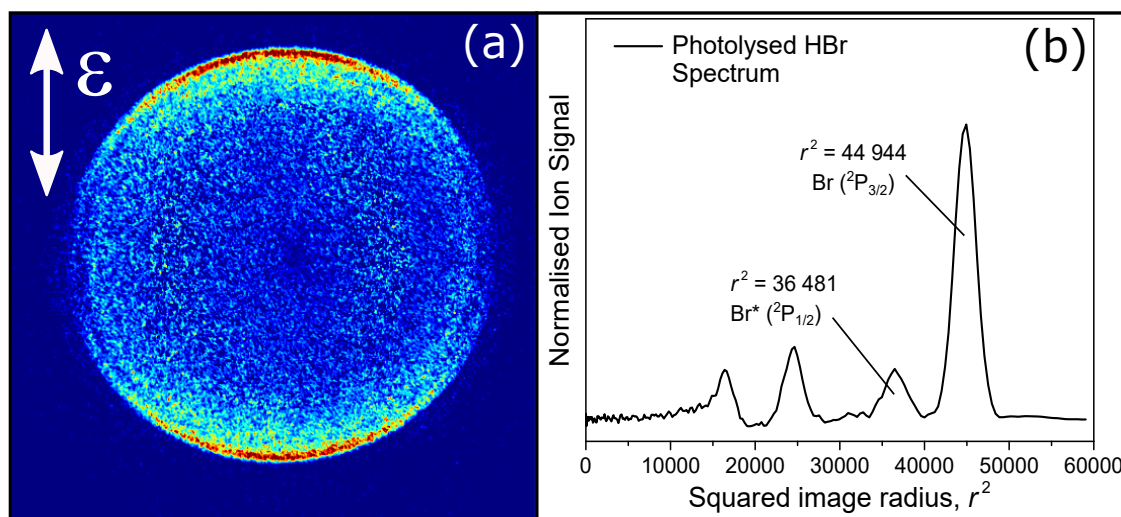
Figure 2.20: Calibration of the VMI setup for photofragment experiments with HBr photolysed with 200 nm. (a) VMI (raw) image of the H-atoms released upon photodissociation of HBr and (b) corresponding 1D spectrum, given here in terms of squared image radius, r^2. The conversion to TKER is done by comparing these results to real values for the photodissociation of HBr, as discussed in the main text.

mass factor of $m(\text{parent})/m(\text{photofragment}) = m(\text{HBr})/m(\text{Br}) = m(80.9 \text{ g mol}^{-1})/79.9 \text{ g mol}^{-1} = 1.0125$ is also taken into account. A calibration factor of $\sim 0.44 \text{ cm}^{-1} \text{ pixel}^{-2}$ is thus extracted, so that TKER $= r^2 \times$ calibration factor $\times$ mass factor. The mass factor is adjusted as necessary for each experiment, depending on the molecule under study.

A similar approach is employed for calibrating our VMI setup for TR-PES experiments in order to measure *electron kinetic energy* (eKE, encountered earlier in this chapter in section 2.2.1.3, specifically in Equation 2.51). In this case, the VMI image resulting from the photoionisation of Xe, shown in Figure 2.21(a), is used. The two peaks observed in the corresponding 1D spectrum, presented in Figure 2.21(b), are compared to known values for the first ionisation potential of Xe ($\sim 97\,833 \text{ cm}^{-1}$).[81–83] Akin to what was discussed in regards to HBr, photoionisation of Xe produces Xe ions in their ground ($^2P_{3/2}$) and excited ($^2P_{1/2}$) states, whose energies are separated by $\sim 10\,969 \text{ cm}^{-1}$.[81–83] The peak observed at $r^2 = 26\,896$ corresponds to Xe$^+$($^2P_{1/2}$), while $r^2 = 50\,625$ corresponds to Xe$^+$($^2P_{3/2}$). Since the "photofragment" in these experiments is a photoelectron, which has negligible mass compared to the parent ion, a mass factor is not included in the calibration of our TR-PES setup. The real eKE is, simply, $r^2 \times$ calibration factor, where the calibration factor takes typical values of $\sim 0.43 \text{ cm}^{-1} \text{ pixel}^{-2}$.
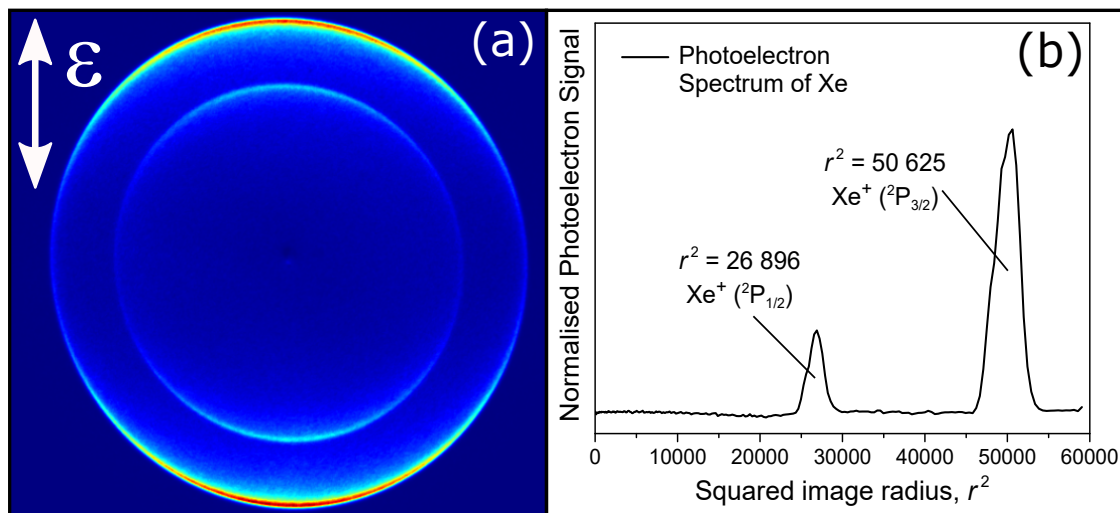
Figure 2.21: Calibration of the VMI setup for photoelectron experiments with Xe photoionised by three 251 nm photons. (a) VMI (raw) image resulting from the photoionisation of Xe and (b) corresponding 1D spectrum, given here in terms of squared image radius, r^2. The conversion to eKE is done by comparing these results to real values for the photoionisation of Xe, as discussed in the main text.

2.4.2   In Solution

The Warwick TEAS setup uses the variable wavelength laser pulses from one of the TOPAS-C as well as one of the fundamental beams. A set of BBO crystals can be used to produce the second and third harmonics of the fundamental 800 nm, corresponding to 400 nm and 267 nm, respectively, and all three wavelengths can be used individually as the pump for TEAS experiments. As mentioned earlier, the probe beam (initially with a wavelength of 800 nm) is delayed with respect to the pump by means of a motorised delay stage, after which it is focused onto a 1 or 2 mm thick CaF_2 window to prompt WLC generation. The balance between reaching the threshold for WLC generation and avoiding optical damage to the CaF_2 window is achieved by a combination of irises, filters and by controlling beam power and focusing conditions. Furthermore, the CaF_2 window is mounted on a translation stage controlled by a piezo motor (Newport Corporation) which continuously translates the window (vertically), so that the point of contact between the beam focal spot and the window is continuously changed and optical damage is minimised. CaF_2 was chosen to generate the WLC for our experiments due to the broad spectrum it produces; in our experiments we select the region from 330 nm to 675 nm. The relative polarisation between the pump and probe laser pulses is fixed at magic angle (54.7°) to avoid rotational artefacts resulting from laser-induced transition dipole moment alignment (analogous to the discussion in section 2.2.1.2, particularly with reference to Equations 2.46 and 2.47); this is achieved in the TEAS setup by employing a half-waveplate ($\lambda/2$).

Sample delivery in our TEAS setup, shown in Figure 2.22, is achieved by means of a demountable liquid flow cell by Harrick Scientific Products, Inc. The cell consists of a steel mount which holds a pair of CaF_2 windows (1 and 2 mm thick) separated by a pair of polytetrafluoroethylene (PTFE) spacers which determine the thickness of the liquid film ($\sim 100~\mu$m). The sample is drawn to the flow cell from a reservoir with a Simdos 02 diaphragm pump *via* PTFE tubing and is continuously recirculated. Sample recirculation ensures that the liquid film sample is continuously replenished and thus maintains minimal concentrations of any potential laser-induced photoproducts. In turn, this ensures that each TEAS data point is collected for fresh sample, avoiding the photoexcitation (λ_{pu}) of photoproducts instead of the initial form of the molecule under study; the interest is in *probing* photoproducts that may result from initial photoexcitation of the molecule under study. After being focused onto and passing through the sample, the transmitted
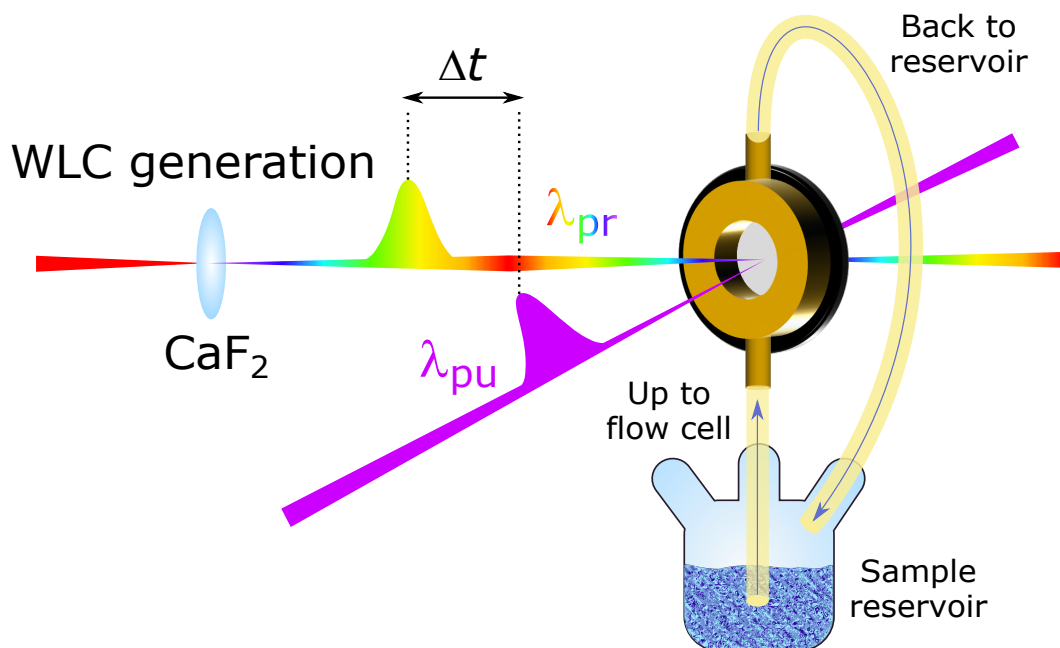
Figure 2.22: Schematic representation of the basic concept of TEAS and the Warwick liquid sample delivery system. TEAS follows the typicall pump-probe scheme, with the probe being a ultrashort laser pulse of white light, created by WLC generation in a CaF_2 window. Sample delivery in the Warwick TEAS setup is achieved with a liquid flow cell; the sample is constantly recirculated to ensure each data point is taken with fresh sample.

pump beam is blocked while the probe is collimated and then focused into an optical fibre connected to a spectrometer (Avantes AvaSpec-ULS1650F).

Each recorded data point is an intensity ratio for the transmitted probe beam before and after photoexcitation of the sample (see Equation 2.53). Experimentally, this is achieved by employing an optical chopper which intermittently blocks the pump laser pulses in order to alternate between probe alone (for I_0) and pump-probe pulse sequences ($I^*(t, \lambda)$). The removal of pump-only artefacts is also achieved during data acquisition, with automated mechanical shutters allowing for collection of pump-only scans and dark backgrounds; probe-alone artefacts are accounted for by subtracting the TAS corresponding to a negative pump-probe time delay ($\Delta t = -1$ ps).

2.4.3   Data Analysis and Kinetics Considerations

As discussed in Chapter 1, we assume the decay of excited states to follow first order kinetics. In light of this assumption, the transients obtained from our experiments (both in vacuum and in solution) can be described as an exponential rise or decay (for a positive

or negative exponent, respectively), or a sum of exponentials if more than one pathway is accessible. Fitting experimental data with such a kinetic model yields *time constants* corresponding to the lifetimes, τ, for each process, where $\tau = {}^1/k$ and k is the rate constant for each pathway, as discussed in Chapter 1, section 1.2.3.2. Both the excited state lifetimes of the molecules of interest (decay) as well as the fragment appearance lifetimes (rise) can thus be determined, providing insight into the ultrafast photodynamics of these molecules.

Additional assumptions need to be made regarding the starting point of the different processes. In general, the models used to fit transient data assume *parallel* excited state decay pathways, *i.e.* all dynamics begin at $\Delta t = 0$. However, different processes may not all start at $\Delta t = 0$: excited state population may irreversibly undergo consecutive relaxation pathways (*e.g.* A → B → C), in which case the kinetics are said to be *sequential*; the kinetics may also be *branched* if excited state population of a given intermediate state follows two or more separate relaxation pathways (see, for example, references 84 and 85). Ultimately, the choice of kinetic model to be employed is based on chemical intuition and/or quantum chemical calculations; systems need to be evaluated on an individual case basis and the kinetic model adjusted accordingly. As we shall see in Chapter 4, there may also be the need to include extra components in the models to fit experimental data in order to model certain behaviour, such as quantum beats. The particularities for these cases will be introduced at the appropriate stages throughout the next chapters; the discussion in this section will be kept general.

A final consideration for the kinetic model used to fit the decay of excited states in our experiments is the temporal widths of the pump and probe laser pulses which, as we have briefly mentioned in Chapter 1, section 1.3, will affect the final transients. This effect is quantified in terms of the cross-correlation function between the pump and probe intensities, termed the *instrument response function* (IRF). In our experiments in vacuum, the IRF is taken to be the FWHM of a Gaussian fit to the TR-IY transient for the non-resonant ionisation of Xenon (Xe); IRF values of 80 – 160 fs were typical. The same Xe transients are also used to find the maximum pump-probe temporal overlap, the "true time-zero", t_0^{true}. In solution, the IRF is obtained from "solvent-alone" transients and IRF $\sim 70 - 100$ fs are thus obtained. Example IRF scans for both our experiments in vacuum and in solution are presented in Figure 2.23.

Overall Decay Model in Vacuum

(a) 1D transients

In general, the model used to fit our 1D transients (such as TR-IY transients, signal S vs. Δt) consists of a sum of exponential decay functions which are multiplied by a step function and convoluted with a Gaussian function to model the IRF. The total model is thus:

$$S(\Delta t) = S_0 + G(\Delta t) * \sum_i A_i \exp\left(-\frac{\Delta t - t_0^{\text{true}}}{\tau_i}\right) H\left(\Delta t - t_0^{\text{true}}\right) \tag{2.55}$$

where S_0 is the signal baseline, $G(\Delta t)$ is the IRF Gaussian function, A_i are the amplitudes and τ_i the time constants of the exponential decays. Rise functions can be modelled by changing the sign of the exponent of the exponential term. The Gaussian IRF is modelled by:

$$G(\Delta t) = A \exp\left(\frac{(\Delta t - t_0^{\text{true}})^2}{2\sigma^2}\right) \tag{2.56}$$

where all the terms are as above and $\sigma = {}^{\text{FWHM}}\!/2\sqrt{2\ln 2}$. Moreover, $H(\Delta t)$ in Equation 2.55 is a step function such that:

$$H(\Delta t) = \begin{cases} 0 & \text{if } \Delta t < 0, \\ 1 & \text{if } \Delta t \geq 0. \end{cases} \tag{2.57}$$

In some cases, probe-pump signal (as opposed to pump-probe) may be observed before

(a) Xenon TR-IY, IRF scan.   (b) Methanol TEAS, IRF scan.
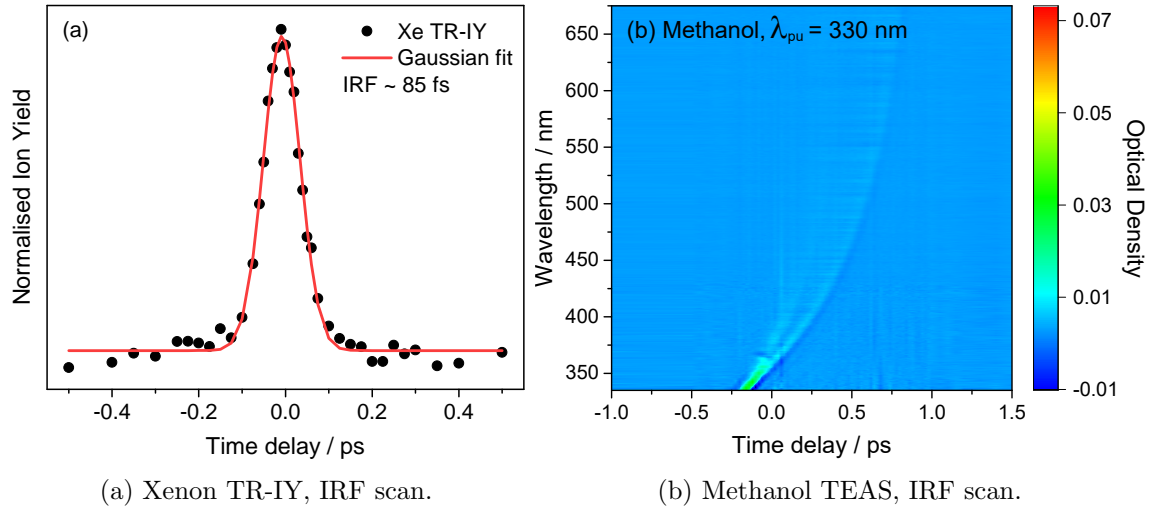
Figure 2.23: Example IRF scans for the Warwick setup: (a) TR-IY transient for the non-resonant ionisation of Xe, fit with a Gaussian function of FWHM $\sim$ 85 fs; and (b) example "solvent-alone" transient, in this case of methanol, used to measure the IRF for our experiments in solution.

time-zero. In order to accurately describe the relevant dynamics after time-zero, the kinetic fit may also need to account for these *reverse* dynamics. Specific details will be given where necessary in later chapters.

(b) Imaging data

The original 3D Newton spheres created at the point of sample photoionisation are reconstructed from the measured 2D projections using the POP algorithm described in more detail in section 2.2.1.2 and in reference 36. The POP algorithm allows for the measured 2D radial spectra to be converted to 1D energy spectra, producing signal intensity *vs.* TKER or signal intensity *vs.* eKE plots for each pump-probe time delay, Δt. Additionally, the POP algorithm also yields β_n parameters (up to $n = 4$) which allow for a quantitative analysis of the anisotropy parameter and thus of angular distributions. Integrating over a single TKER or eKE region yields a plot of signal intensity *vs.* pump-probe time delay for that particular feature, which may then be fit using the same models just described for 1D transients. Moreover, TKER or eKE spectra as a function of pump-probe time delay can also be analysed by global fitting methods, as described for the measurements in solution in the next section.

Overall Decay Model in Solution

In the case of TEAS measurements the addition of the solvent makes the kinetics more complex, and the range of probe wavelengths generates larger data sets. While 1D transients over a single probe wavelength can be produced, it is usually more informative to evaluate the evolution of the system for all probe wavelengths simultaneously. In this case, it is useful to employ *global lifetime analysis* or *global fitting*[86] in order to achieve a quantitative analysis of TAS transients. For parallel dynamics, the kinetic model is simply a sum of i exponential decays with lifetimes τ_i, convoluted with a Gaussian IRF, $G(\lambda_{\mathrm{pr}}, \Delta t)$:

$$\mathrm{TAS}_{\mathrm{model}}(\lambda_{\mathrm{pr}}, \Delta t) = G(\lambda_{\mathrm{pr}}, \Delta t) * \sum_i \mathrm{DADS}_i(\lambda_{\mathrm{pr}}) \exp\left(-\frac{\Delta t - t_0^{\mathrm{true}}}{\tau_i}\right) \tag{2.58}$$

where $\mathrm{DADS}_i(\lambda_{\mathrm{pr}})$ is the decay associated difference spectrum (DADS) for the corresponding exponential decay τ_i. For a sequential model, we refer to evolution associated difference spectra, *i.e.* EADS instead of DADS.[87] Global fitting methods, which in our experiments were applied using the Glotaran software package,[87] evaluate the pre-defined kinetic model and undergo nonlinear regression until the model values best fit the experimental data.

The Glotaran package also corrects for the chirp in the WLC probe resulting from the GVD caused by the probe pulse's interaction with the CaF_2 window. GVD effects, which cause different wavelengths to travel at different velocities through a medium, result in each probe wavelength arriving at the sample at different times and thus having different t_0^{true} values. Therefore, Glotaran employs a polynomial GVD curve to chirp correct the spectra by fitting it to the different wavelength dependent values of t_0^{true} across the probe spectrum.[86–88] The quality of the fits is evaluated upon inspection of the residual values resulting from the difference between the fit and the raw data.

2.5   References

[1] Maiman, T. H. Optical and microwave-optical experiments in ruby. *Physical Review Letters* **4**, 564–567 (1960).

[2] Maiman, T. H. Stimulated optical radiation in ruby. *Nature* **187**, 493–494 (1960).

[3] Einstein, A. The quantum theory of radiation. *Physikalische Zeitschrif* **18**, 167–183 (1917).

[4] Atkins, P. & de Paula, J. *Atkin's Physical Chemistry* (Oxford University Press, Oxford, 2014), 10$^{\text{th}}$ edn.

[5] Wilson, J. & Hawkes, J. *Optoelectronics: An Introduction* (Prentice Hall Europe, London, 1998), 2$^{\text{nd}}$ edn.

[6] Demtröder, W. *Laser Spectroscopy: Basic Concepts and Instrumentation* (Springer, Berlin, 2003), 3$^{\text{rd}}$ edn.

[7] Shank, C. V., Fork, R. L., Yen, R. & Stolen, R. H. Compression of femtosecond optical pulses. *Applied Physics Letters* **40**, 761–763 (1982).

[8] Shank, C. V. Investigation of ultrafast phenomena in the femtosecond time domain. *Science* **233**, 1276–1280 (1986).

[9] Moulton, P. F. Spectroscopic and laser characteristics of Ti:Al_2O_3. *Journal of the Optical Society of America B* **3**, 125–133 (1986).

[10] Roy, R., Schulz, P. A. & Walther, A. Acousto-optic modulator as an electronically selectable unidirectional device in a ring laser. *Optics Letters* **12**, 672–674 (1987).

[11] Rullière, C. *Femtosecond Laser Pulses: Principles and Experiments* (Springer, New York, 2004), 2nd edn.

[12] Li, C. *Nonlinear Optics: Principles and Applications* (Springer, Singapore, 2017).

[13] Liu, J. *Photonic Devices* (Cambridge University Press, Cambridge, 2005), 1st edn.

[14] Palmer, C. *Diffraction Grating Handbook* (Thermo RGL, Rochester, 2002), 5th edn.

[15] Jovanovic, I. Chirped-pulse amplification: Ultrahigh peak power production from compact short-pulse laser systems. *Optik & Photonik* **5**, 30–33 (2010).

[16] Paschotta, R. *Field Guide to Laser Pulse Generation* (SPIE Press, Bellingham, WA, 2008).

[17] Martinez, O. E. 3000 times grating compressor with positive group velocity dispersion. *IEEE Journal of Quantum Electronics* **23**, 59–64 (1987).

[18] Boyd, R. *Nonlinear Optics* (Academic Press, Burlington, MA, 2008), 3rd edn.

[19] Johnson, P. J. M., Prokhorenko, V. I. & Miller, R. J. D. Stable UV to IR supercontinuum generation in calcium fluoride with conserved circular polarization states. *Optics Express* **17**, 21488–21496 (2009).

[20] Baldeck, P., Ho, P. P. & Alfano, R. R. Effects of self, induced and cross phase modulations on the generation of picosecond and femtosecond white light supercontinua. *Revue de Physique Appliquée* **22**, 1677–1694 (1987).

[21] Alfano, R. R. *The Supercontinuum Laser Source* (Springer, New York, 2006), 2nd edn.

[22] Gaeta, A. L. Catastrophic collapse of ultrashort pulses. *Physical Review Letters* **84**, 3582–3585 (2000).

[23] Levy, D. H. Laser spectroscopy of cold gas-phase molecules. *Annual Reviews of Physical Chemistry* **31**, 197–225 (1980).

[24] Estermann, I. Molecular beam techniques. *Review of Modern Physics* **18**, 300–323 (1946).

[25] Even, U., Jortner, J., Noy, D. & Lavie, N. Cooling of large molecules below 1 K and He clusters formation. *Journal of Chemical Physics* **112**, 8068–8071 (2000).

[26] Scoles, G. *Atomic and Molecular Beam Methods* (Oxford University Press, Inc., New York, 1988).

[27] Lubman, D. M., Rettner, C. T. & Zare, R. N. How isolated are molecules in a molecular beam? *The European Physical Journal D* **86**, 1129–1135 (1982).

[28] R. de Carvalho *et al.* Buffer-gas loaded magnetic traps for atoms and molecules: A primer. *The European Physical Journal D* **7**, 289–309 (1999).

[29] Even, U. The Even-Lavie valve as a source for high intensity supersonic beam. *EPJ Techniques and Instrumentation* **2**, 1–22 (2015).

[30] Even, U. Pulsed supersonic beams from high pressure source: Simulation results and experimental measurements. *Advances in Chemistry* **2014**, 1–11 (2014).

[31] Wiley, W. C. & McLaren, I. H. Time-of-flight mass spectrometer with improved resolution. *Review of Scientific Instruments* **26**, 1150–1157 (1955).

[32] Sanzone, G. Energy resolution of the conventional Time-of-Flight mass spectrometer. *Review of Scientific Instruments* **41**, 741–742 (1970).

[33] Rosker, M. J., Dantus, M. & Zewail, A. H. Femtosecond real-time probing of reactions. I. The technique. *The Journal of Chemical Physics* **89**, 6113–6127 (1988).

[34] Staniforth, M. & Stavros, V. G. Recent advances in experimental techniques to probe fast excited-state dynamics in biological molecules in the gas phase: dynamics in nucleotides, amino acids and beyond. *Proceesings of the Royal Society A* **469**, 1–23 (2013).

[35] Eppink, A. T. J. B. & Parker, D. H. Velocity map imaging of ions and electrons using electrostatic lenses: Application in photoelectron and photofragment ion imaging of molecular oxygen. *Review of Scientific Instruments* **68**, 3477–3484 (1997).

[36] Roberts, G. M., Nixon, J. L., Lecointre, J., Wrede, E. & Verlet, J. R. R. Toward real-time charged-particle image reconstruction using polar onion-peeling. *Review of Scientific Instruments* **80**, 1–7 (2009).

[37] Ashfold, M. N. R. *et al.* Imaging the dynamics of gas phase reactions. *Physical Chemistry Chemical Physics* **8**, 26–53 (2006).

[38] Staniforth, M., Young, J. D. & Stavros, V. G. Probing rotational motion in 4-tert-

butylcatechol through H atom photofragmentation: Deviations from axial recoil. *The Journal of Physical Chemistry A* **119**, 12131–12137 (2015).

[39] Parker, D. H. & Eppink, A. T. J. B. Photoelectron and photofragment velocity map imaging of state-selected molecular oxygen dissociation/ionization dynamics. *The Journal of Chemical Physics* **107**, 2357–2362 (1997).

[40] Eppink, A. T. J. B., Wu, S. M. & Whitaker, B. J. *Imaging in molecular dynamics: technnology and applications* (Cambridge University Press, Cambridge, 2003).

[41] Stolow, A., Bragg, A. E. & Neumark, D. M. Femtosecond time-resolved photoelectron spectroscopy. *Chemical Reviews* **104**, 1719–1757 (2004).

[42] Reid, K. L. Photoelectron angular distributions. *Annual Reviews of Phyisical Chemistry* **54**, 397–424 (2003).

[43] Stolow, A. Femtosecond time-resolved photoelectron spectroscopy of polyatomic molecules. *Annual Review of Physical Chemistry* **54**, 89–119 (2003).

[44] Seel, M. & Domcke, W. Model studies on femtosecond time-resolved ionization spectroscopy of excited-state vibrational dynamics and vibronic coupling. *Chemical Physics* **151**, 59–72 (1991).

[45] Seel, M. & Domcke, W. Femtosecond time-resolved ionization spectroscopy of ultrafast internalconversion dynamics in polyatomic molecules: Theory and computational studies. *The Journal of Chemical Physics* **95**, 7806–7822 (1991).

[46] Signorell, R. & Merkt, F. General symmetry selection rules for the photoionization of polyatomic molecules. *Molecular Physics* **92**, 793–804 (1997).

[47] Baker, L. A. & Stavros, V. G. Observing and understanding the ultrafast photochemistry in small molecules: applications to sunscreens. *Science Progress* **99**, 282–311 (2016).

[48] Pratt, D. W. High resolution spectroscopy in the gas phase: Even large molecules have well-defined shapes. *Annual Review of Physical Chemistry* **49**, 481–530 (1998).

[49] Ashfold, M. N. R. & Howe, J. D. Multiphoton spectroscopy of molecular species. *Annual Review of Physical Chemistry* **45**, 57–82 (1994).

[50] Boesl, U., Neusser, H. J. & Schlag, E. W. High resolution lifetime measurements of isolated vibronic levels in naphthalene. *Chemical Physics Letters* **31**, 1–6 (1975).

[51] Mokhtari, A. & Chesnoy, J. Femtosecond time- and frequency-resolved fluorescence spectroscopy of a dye molecule. *Chemical Physics Letters* **155**, 593–598 (1989).

[52] Zare, R. N. My life with LIF: A personal account of developing laser-induced fluorescence. *Annual Review of Physical Chemistry* **5**, 1–14 (2012).

[53] Kinsey, J. L. Laser-induced fluorescence. *Annual Review of Physical Chemistry* **28**, 349–372 (1977).

[54] Bouwens, R. J. *et al.* Pure vibrational spectroscopy of S_0 formaldehyde by dispersed fluorescence. *The Journal of Chemical Physics* **104**, 460–479 (1996).

[55] Abe, H., Mikame, N. & Ito, M. Fluorescence excitation spectra of hydrogen-bonded phenols in a supersonic free jet. *The Journal of Physical Chemistry* **86**, 1768–1771 (1982).

[56] Fabbi, J. C., Langenberg, J. D., Costello, Q. D., Morse, M. D. & Karlsson, L. Dispersed fluorescence spectroscopy of jet-cooled AgAu and Pt_2. *The Journal of Chemical Physics* **115**, 7543–7549 (2001).

[57] Brian, T. R. O. & Lawler, J. E. Radiative lifetimes in Si from laser-induced fluorescence in the visible, ultraviolet, and vacuum ultraviolet. *Physical Review A* **44**, 7134–7143 (1991).

[58] Chin, W. *et al.* Tautomer contributions to the near UV spectrum of guanine: towards a refined picture for the spectroscopy of purine molecules. *The European Physical Journal D - Atomic, Molecular, Optical and Plasma Physics* **20**, 347–355 (2002).

[59] Hakamata, T. *et al. Photomultiplier tubes: Basics and applications* (Hamamatsu Photonics, 2006).

[60] Dessent, C. E. H. & Müller-Dethlefs, K. Hydrogen-bonding and van der Waals complexes studied by ZEKE and REMPI spectroscopy. *Chemical Reviews* **100**, 3999–4022 (2000).

[61] Boesl, U. Multiphoton excitation and mass-selective ion detection for neutral and ion spectroscopy. *The Journal of Physical Chemistry* **95**, 2949–2962 (1991).

[62] Letokhov, V. S. *Laser Photoionization Spectroscopy* (Academic Press, Inc., London, 1987).

[63] Jacobs, D. C. & Zare, R. N. Reduction of 1+1 resonance enhanced MPI spectra to

populations and alignment factors. *The Journal of Chemical Physics* **85**, 5457–5468 (1986).

[64] Bominaar, J., Schoemaecker, C., Dam, N., Meulen, J. J. T. & Groenenboom, G. C. (2+1) REMPI on molecular nitrogen through the $^1\Sigma_g^+$ (ii)-state. *Chemical Physics Letters* **435**, 242–246 (2007).

[65] Takahashi, M. Two-color (2+1') multiphoton ionization threshold photoelectron study of the ArNO van der waals complex: Observation of intermolecular vibrational progressions of the $ArNO^+$ cation. *The Journal of Chemical Physics* **96**, 2594–2599 (1992).

[66] Müller-Dethlefs, K., Sander, M. & Schlag, E. W. Two-colour photoionization resonance spectroscopy of NO: Complete separation of rotational levels of NO^+ at the ionization threshold. *Chemical Physics Letters* **112**, 291–294 (1984).

[67] Ropers, C., Solli, D. R., Schulz, C. P., Lienau, C. & Elsaesser, T. Localized multiphoton emission of femtosecond electron pulses from metal nanotips. *Physical Review Letters* **98**, 1–4 (2007).

[68] Lin, S. H., Fujimura, Y., Neusser, H. J. & Schlag, E. W. *Multiphoton Spectroscopy of Molecules* (Academic Press, Inc., Florida, 1984).

[69] Johnson, P. M. & Otis, C. E. Molecular multiphoton spectroscopy with ionization detection. *Annual Review of Physical Chemistry* **32**, 139–157 (1981).

[70] Zwier, T. S. Laser spectroscopy of jet-cooled biomolecules and their water-containing clusters: water bridges and molecular conformation. *The Journal of Physical Chemistry A* **105**, 8827–8839 (2001).

[71] Martinez, S. J., Alfano, J. C. & Levy, D. H. Rotationally resolved fluorescence excitation spectra of phenol and 4-ethylphenol in a supersonic jet. *Journal of Molecular Spectroscopy* **152**, 80–88 (1992).

[72] Luo, X. & Rizzo, T. R. Rotationally resolved vibrational overtone spectroscopy of hydrogen peroxide at chemically significant energies. *The Journal of Chemical Physics* **93**, 8620–8633 (1990).

[73] Brumfield, B. E., Stewart, J. T. & McCall, B. J. Extending the limits of rotationally

resolved absorption spectroscopy: Pyrene. *The Journal of Physical Chemistry Letters* **3**, 1985–1988 (2012).

[74] Inokuchi, Y., Kobayashi, Y., Ito, T. & Ebata, T. Conformation of l-tyrosine studied by fluorescence-detected UV-UV and IR-UV double-resonance spectroscopy. *The Journal of Physical Chemistry A* **111**, 3209–3215 (2007).

[75] Sakota, K. *et al.* IR-dip and IRUV hole-burning spectra of jet-cooled 4-aminobenzonitrile(H_2O)$_1$. observation of π-type and σ-type hydrogen-bonded conformers in the CN site. *Chemical Physics* **283**, 209–219 (2002).

[76] Imanbaew, D., Gelin, M. F. & Riehn, C. Rotational and vibrational dynamics in the excited electronic state of deprotonated and protonated fluorescein studied by time-resolved photofragmentation in an ion trap. *Structural Dynamics* **3**, 4, 043211.1-043211.13 (2016).

[77] Mehta-Hurt, D. N. *et al.* The spectroscopy and photochemistry of quinioline structural isomers: (E)- and (Z)-phenylvinylnitrile. *The Journal of Chemical Physics* **143**, 1–14 (2015).

[78] Tan, E. M. M. *et al.* Conformational heterogeneity of methyl 4-hydroxycinnamate: A gas-phase UV-IR spectroscopic study. *The Journal of Physical Chemistry B* **117**, 4798–4805 (2013).

[79] Roberts, G. M. & Stavros, V. G. The role of $\pi\sigma^*$ states in the photochemistry of heteroaromatic biomolecules and their subunits: insights from gas-phase femtosecond spectroscopy. *Chemical Science* **5**, 1698–1722 (2014).

[80] Regan, P. M., Langford, S. R., Orr-Ewing, A. J. & Ashfold, M. N. R. The ultraviolet photodissociation dynamics of hydrogen bromide. *The Journal of Chemical Physics* **110**, 281–288 (1999).

[81] Compton, R. N., Miller, J. C. & Carter, A. E. Resonantly enhanced multiphoton ionization of xenon: Photoelectron energy analysis. *Chemical Physics Letters* **71**, 87–90 (1980).

[82] Altiere, E. *et al.* High-resolution two-photon spectroscopy of a $5p^56p \leftarrow 5p^6$ transition of xenon. *Physical Review* **97**, 012507.1–012507.5 (2018).

[83] Kramida, A., Ralchenko, Y., Reader, J. & NIST ASD Team. NIST Atomic Spectra

Database (version 5.5.6). Available online: `https://physics.nist.gov/asd`. National Institute of Standards and Technology, Gaithersburg, MD. (Accessed April 2018).

[84] Thompson, J. O. F., Klein, L. B., Sølling, T. I., Paterson, M. J. & Townsend, D. The role of novel Rydberg-valence behaviour in the non-adiabatic dynamics of tertiary aliphatic amines. *Chemical Science* **7**, 1826–1839 (2006).

[85] Chatterley, A. S., Roberts, G. M. & Stavros, V. G. Timescales for adiabatic photodissociation dynamics from the $\tilde{A}$ state of ammonia. *The Journal of Chemical Physics* **139**, 1–10 (2013).

[86] van Stokkum, I. H. M., Larsen, D. S. & van Grondelle, R. Global and target analysis of time-resolved spectra. *Biochimica et Biophysica Acta: Bioenergetics* **1657**, 82–104 (2004).

[87] Snellenburg, J. J., Laptenok, S., Seger, R., Mullen, K. M. & van Stokkum, I. H. M. Glotaran: A Java-based graphical user interface for the R Package TIMP. *Journal of Statistical Software* **49**, 1–22 (2012).

[88] Kovalenko, S. A., Dobryakov, A. L., Ruthmann & Ernsting, N. P. Femtosecond spectroscopy of condensed phases with chirped supercontinuum probing. *Physical Review A* **59**, 2369–2384 (1999).

3 Cinnamates

'If one proves the equality of two numbers a and b by showing first that "a is less than or equal to b" and then "a is greater than or equal to b", it is unfair. One should instead show that they are really equal by disclosing the inner ground for their equality.'

Amalie Emmy Noether (1882–1935)

3.1 Overview

The strong impetus for the development of novel sunscreens with broader absorption and effective and safe energy dissipation mechanisms, discussed in detail in Chapter 1, has prompted recent efforts towards understanding sunscreen excited state photodynamics. Nevertheless, crucial questions regarding the ideal photophysical sunscreen behaviour, as well as what affects this behaviour and how, remain unanswered. For instance, a comprehensive understanding of molecular level photoinduced mechanisms for the release of reactive oxygen species (ROS) in commercial sunscreen active ingredients is still lacking, even though release of such reactive species could result in sunscreens increasing the risk of melanoma, rather than reducing it.[1] Moreover, there is no in-depth knowledge of how the solvents and other components of commercial sunscreen formulations may affect the photoprotection mechanisms of a given sunscreen molecule.

In an effort to explore some of these issues, we have started our studies on the ultrafast photoprotection mechanisms occuring in sunscreen molecules by studying an example molecule from a family of sunscreens that has recently received significant attention — the cinnamates.[2–6] Ethyl 4-hydroxy-3-methoxycinnamate (ethyl ferulate, EF), shown in Figure 3.1(c), is part of the cinnamate sunscreen family and demonstrates strong absorption across the UVA and UVB regions of the electromagnetic spectrum, as shown in Figure 3.2. Moreover, EF has antioxidant (radical scavenging) properties which, alongside its strong UV absorption, justify its current use in commercial sunscreen formulations.[7–9] Similar to all active sunscreen ingredients, EF is used in photoprotective lotions as part of a combination of UV filters and other compounds (solvents, emolients, *etc.*) in order to

achieve a user-friendly lotion with optimum photoprotection across the entire UVA and UVB range.

The research presented in this chapter explores the excited state photodynamics of EF, building on previous studies of sunscreen molecules published in recent years.[2,10–12] EF presents itself as an extremely relevant system to be studied, due to its practical relevance as a sunscreen molecule. Moreover, the carbonyl moiety in EF (as part of the ester group functionality) may provide insight into how increasing molecular complexity influences the photochemistry of EF and other structurally related sunscreen molecules. To explore the influence of increasing molecular complexity on the observed photodynamics, the subunits of EF, 2-methoxy-4-vinylphenol (MVP) and 4-hydroxy-3-methoxycinnamyl alcohol (coniferyl alcohol, ConA) shown in Figure 3.1(a) and (b), respectively, were also studied. In addition, we have explored how the gas-phase photodynamics of EF are altered by the addition of a solvent in order to more closely model the environment in which EF would be found within a commercial sunscreen formulation.
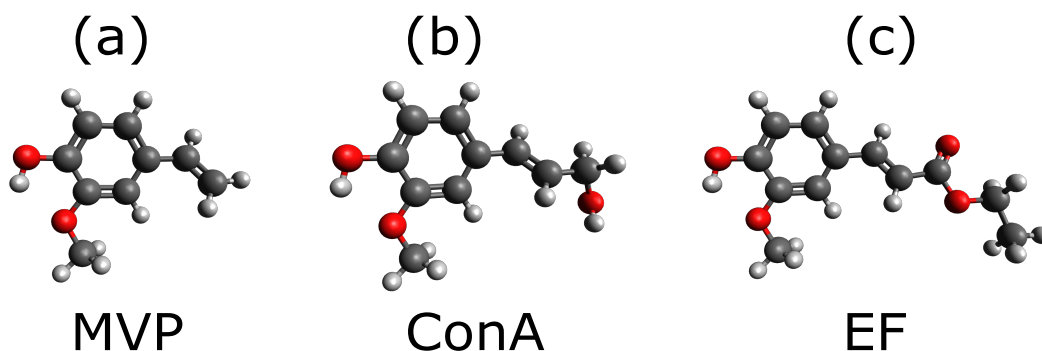
Figure 3.1: Diagrams of the molecular structures of (a) 2-methoxy-4-vinylphenol (MVP), (b) 4-hydroxy-3-methoxycinnamyl alcohol (coniferyl alcohol, ConA), and (c) ethyl 4-hydroxy-3-methoxycinnamate (ethyl ferulate, EF).

3.2 Experimental Methods

3.2.1 Time-Resolved Ion Yield (TR-IY)

The experimental setup has been described in great detail in Chapter 2; a summary of the details pertaining to these specific studies is provided here. The previously mentioned commercial femtosecond (fs) Ti:sapphire oscillator (Spectra-Physics Tsunami) and regenerative amplifier (Spectra-Physics Spitfire XP) were used to produce ~ 40 fs laser pulses centred at 800 nm at ~ 3 mJ per pulse. The fundamental 800 nm output was subsequently
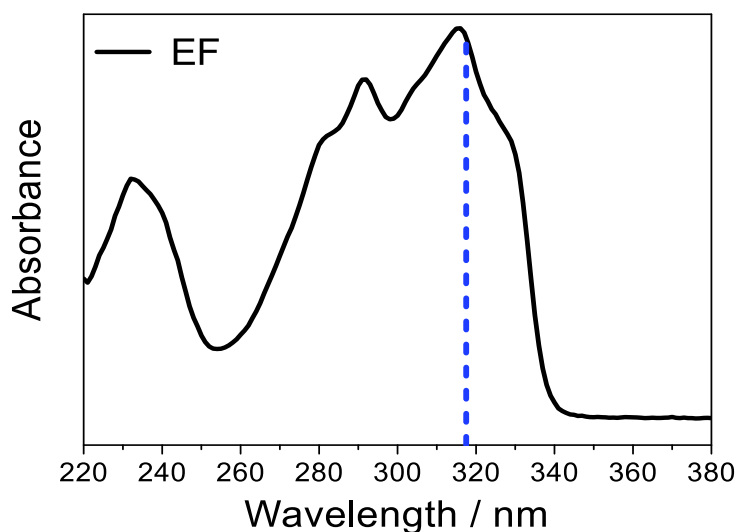
Figure 3.2: UV/Vis absorption spectrum of EF in cyclohexane. The blue dashed line represents the origin band $(S_1(v = 0))$ of EF in vacuum at 317.5 nm.

split into three beams, each ~ 1 mJ per pulse, with one of these beams used to pump an optical parametric amplifier (Light Conversion, TOPAS-C) in order to generate the pump (λ_{pu}) pulses. λ_{pu} was centred on the S_1 origin band $(S_1(v = 0))$ of each molecule studied (305 nm, 306 nm and 317.5 nm for MVP, ConA and EF, respectively; *vide infra*). The set of BBO crystals described in Chapter 2, section 2.4, was used to produce a 200 nm laser beam which served as the probe (λ_{pr}) pulse in these experiments. Alternatively, a second TOPAS-C was used to generate 243 nm or 322 nm probe pulses. The pump and probe pulses were temporally delayed with respect to each other by way of a gold retroreflector mounted on a motorised delay stage, allowing a maximum temporal delay (Δt) of 900 ps ($\lambda_{pr} = 200$ nm) or 1.2 ns ($\lambda_{pr} = 243$ nm, 322 nm). Separate measurements were taken with the polarisations of the pump and probe beams parallel and perpendicular to each other in order to calculate the resulting magic angle equivalent transient.[13]

The two laser beams intercepted a molecular beam produced by seeding the target molecules (EF, Sigma-Aldrich, 98%; ConA, Sigma-Aldrich, 98%; or MVP, VWR International Ltd., 97%), heated to their melting points (55 – 95°C), into helium (~ 3 bar). This was then expanded into a vacuum ($\sim 10^{-7}$ mbar) using an Even-Lavie pulsed solenoid valve, as described in Chapter 2, section 2.2.1.[14] At the point of intersection, λ_{pu} excited the species in the molecular beam and λ_{pr} ionised any photoexcited or photodissociated species. The resulting ions were focused onto the detector by an ion optic arragement

following the Eppink and Parker design (see Chapter 2, section 2.2.1.2).[15] The current output from the detector MCP, gated in ion flight time over the mass channel of each parent ion (MVP$^+$, ConA$^+$ and EF$^+$), was measured on a digital oscilloscope (LeCroy LT372 Waverunner) and integrated as a function of Δt in order to produce time-resolved ion yield (TR-IY) transients.

3.2.2   Velocity Map Imaging (VMI) of H-atoms

Velocity map imaging (VMI) was used to monitor any H-atom elimination from the molecules of interest following photoexcitation. Any photodissociated H-atoms were resonantly ionised to form H$^+$ with a 243 nm probe pulse set at $\Delta t = 1.2$ ns relative to the pump pulse. H$^+$ ions were then accelerated by an electrostatic potential towards a position-sensitive detector such that ions with the same initial velocity are mapped onto the same point on the detector, as discussed in Chapter 2, section 2.2.1.2.[15] The original 3D H$^+$ velocity distribution is reconstructed from the measured 2D projection using a polar onion peeling algorithm[16] from which the desired 1D total kinetic energy release (TKER) spectrum can be derived using an appropriate energy calibration factor and by consideration of the co-fragment's mass. The spectrometer is calibrated using the TKER spectrum of photolysed HBr (see Chapter 2, section 2.4, for further details).[17]

3.2.3   Resonant Two-Photon Ionisation (R2PI) and Ionisation Potential (IP) Determination of EF

Mass-resolved resonant two-photon ionisation (R2PI) studies, an overview of which was given in Chapter 2, section 2.3.2, were carried out by the research group led by Professor Timothy S. Zwier (University of Purdue) for EF using a molecular beam time-of-flight mass spectrometer (TOF-MS) apparatus described in detail elsewhere.[18] Solid sample was wrapped in glass wool and inserted into a glass sample holder which was placed inside a stainless-steel reservoir behind a general valve (Parker, Series 9) operating at 20 Hz. The sample and valve assembly were heated (90 – 95°C) in order to achieve sufficient vapour pressure of the sample. The sample was then entrained in a neon (Ne) backing gas (2 – 4 bar) and expanded through a pin-hole nozzle (800 μm) forming a supersonic expansion. The supersonic expansion was skimmed downstream forming a molecular beam which travelled to the extraction region of the TOF spectrometer where the cold, isolated

molecules interacted with the laser beams.

The frequency doubled output of a Nd:YAG (Continuum SureLite II) pumped dye laser was used to generate a UV beam (310 – 319 nm, DCM dye, < 1 mJ per pulse) which was loosely focused into the interaction region. R2PI spectra were recorded by collecting the molecular ion yield as a function of laser wavelength. The ionisation potential (IP) of each of the EF conformers was determined by employing two-colour R2PI (2C-R2PI), which has been described in Chapter 2, section 2.3.2 and in separately published work.[19–21] In order to determine the (adiabatic) IP, the two-colour signal enhancement is maximised; the second colour is then scanned towards increasingly longer wavelength until the two-colour contribution to the ion signal goes to zero at threshold. If the geometry change between the excited state and the ion is sufficiently small, a sharp onset is observed at threshold, providing an accurate measure of the IP. The energy of the two photons at the threshold of ionisation corresponds to the IP of the molecule.

3.2.4   UV-UV Hole-Burning (UVHB)

Conformer specific, high resolution UV spectra were also recorded for EF at the University of Purdue by Professor Timothy S. Zwier's research group. The UVHB studies on EF were performed using a setup described in reference 18. The doubled output of a Continuum SureLite II Nd:YAG pumped dye laser (Lambda-Physik ScanMate), operating at 10 Hz and < 2 mJ per pulse, was fixed on the origin band ($S_1(v = 0)$) of each of the two conformers of EF present (determined from analysis of the R2PI spectra obtained as described above) thus serving as the hole-burn laser. The burn laser was spatially overlapped with a UV probe laser (Radiant Dyes NarrowScan, 0.5 – 1 mJ per pulse, 20 Hz), preceding it temporally by $\sim$ 200 ns. The probe laser was scanned over the frequency range of interest (310 – 319 nm). The difference between the signal with and without the presence of the hole-burn laser was recorded using active baseline subtraction in a gated integrator (Stanford Research SRS250).

3.2.5   Dispersed and Total Fluorescence

The dispersed fluorescence apparatus has been described in detail in reference 18; these studies were also carried out by the research group led by Professor Timothy S. Zwier (University of Purdue). EF was heated to approximately 90 – 95° C, seeded into $\sim$ 3 bar

of helium, and pulsed into a vacuum through a 800 μm orifice (Parker General Valve Series 9) to produce a supersonic jet expansion. The sample was photoexcited downstream in the collision-free regime using the doubled output of a LambdaPhysik, ScanMate dye laser and the total resulting fluorescence was detected with a photomultiplier tube as a function of time. A pair of filters (340/345 nm) was used to cut out scattered light from the excitation laser when measuring fluorescence lifetimes; filters transmitting > 400 nm were used to search for phosphorescence. Dispersed fluorescence measurements were achieved by dispersing the fluorescence in a 0.75 m monochromator (Horiba Jobin Yvon, 1200 grooves per mm) outfitted with an iCCD camera (Andor, iStar 720, 25 mm). Dispersed fluorescence measurements were background subtracted with scans with no sample to remove any laser scatter present in the spectra.

3.2.6 Transient Electronic Absorption Spectroscopy (TEAS)

The experimental equipment and general procedure for the TEAS measurements reported in this chapter have been described in greater detail in Chapter 2, section 2.2.2. Briefly, the femtosecond pump pulses were generated using the TOPAS-C optical parametric amplifier and the probe WLC ($\lambda_{pr} = 330 - 675$ nm) was produced through supercontinuum generation from the 800 nm fundamental in a 2 mm thick CaF_2 window. The pump pulse wavelength (λ_{pu}) was set to 316 nm (3.92 eV) or 243 nm (5.10 eV) for EF in cyclohexane, both at a fixed fluence of $\sim$ 1 – 2 mJ cm^{-2}. The polarisations of the pump and probe pulses were held at magic angle (54.7°) relative to each other by a $\lambda/2$ waveplate. The pump-probe time delay (Δt) was varied by adjusting the optical delay of the probe pulse, with a maximum obtainable Δt of 2 ns. Changes in the optical density (ΔOD) of the samples were calculated from probe intensities, collected using a spectrometer (Avantes, AvaSpec-ULS1650F). EF (Sigma-Aldrich, 98%) samples were made to a concentration of 3 mM in cyclohexane (VWR, 99.99%). The delivery system for the samples was a flow-through cell (Demountable Liquid Cell by Harrick Scientific Products Inc.) with a 100 μm path length to limit temporal dispersion of the pump and probe pulses. The sample was recirculated using a peristaltic pump (Masterflex) from a 50 mL reservoir in order to provide each pump-probe pulse pair with fresh sample and thus avoid pumping of photoproducts (Chapter 2, section 2.2.2). Time constants were extracted from TAS measurements by global fitting[22] employing a sequential model ($A \xrightarrow{\tau_1} B \xrightarrow{\tau_2} C \xrightarrow{\tau_3} D$) with the Glotaran software package.[23] The quality of the fits was determined from the

resulting residuals (shown in section 3.7.I); a maximum deviation between the data and the fit of 5% was typically obtained.

3.2.7   Steady-State Measurements

Steady-state difference absorption spectra, herein referred to as "ΔUV/Vis spectra", were collected to assess the long term photostability of EF. ΔUV/Vis spectra were acquired by irradiating the solutions using an arc lamp (OBB, Tunable KiloArc) at the same wavelengths as λ_{pu} in TEAS measurements, *i.e.* 316 nm and 243 nm (8 nm bandwidth). The samples were irradiated for 10 min at 316 nm and 30 min at 243 nm (due to lower power of the light source at the latter wavelength). The UV/Vis spectra before and after irradiation were measured using a UV/Vis spectrometer (Cary 300, Agilent Technologies). To generate the ΔUV/Vis spectra, the "before" spectra were subtracted from the "after" spectra and then normalised.

^{1}H NMR spectra (400 MHz, CDCl$_3$) were taken before and after irradiation of EF to determine the resulting photoproducts. EF in cyclohexane was irradiated at 316 nm with the TOPAS-C used in the TEAS measurements for 7 hours, with a pump beam fluence of 0.1 mJ cm^{-2}. This corresponds to between 5 and 10% of the pump beam fluence used in the TEAS measurements. After irradiation, the cyclohexane was removed from the sample *via* lyophilisation (freeze dry) and the extracted EF was then dissolved in CDCl$_3$ in preparation for ^{1}H NMR spectra to be collected.

The fluorescence quantum yield of EF was measured in cyclohexane following a similar procedure to the one detailed in reference 24. A reference solution of *trans,trans*-1,4-diphenyl-1,3-butadiene (DPB, Alfa Aesar, 98%) in cyclohexane was prepared to a concentration of $\sim 10^{-6}$ M. A solution of EF in cyclohexane was also prepared to a similar concentration. The concentration for these solutions was chosen so that an intersection between the two spectra at 316 nm was achieved (to coincide with the pump wavelength used in TEAS measurements) and so that the UV/Vis absorbance at this wavelength was kept below 0.1; the excitation wavelength for the fluorescence measurements was then also set at 316 nm (with a bandwidth of 5 nm). The fluorescence emission of the reference solution was measured using a Horiba Scientific Fluorolog Spectrophotometer. Fluorescence data was acquired with a 2.5 nm slit width, photomultiplier tube voltage of 950 V and integration time of 0.1 s. No emission filter was used. Four fluorescence data sets

were acquired, the standard deviation between these measurements being quoted as the measurement error. The fluorescence quantum yield of EF was then determined using the mathematical relationship given in Reference 24,

$$\Phi_{f,\text{EF}} = \Phi_{f,\text{DPB}} \times \frac{F_{\text{EF}}}{F_{\text{DPB}}} \times \frac{f_{\text{DPB}}}{f_{\text{EF}}} \times \frac{n_{\text{EF}}^2}{n_{\text{DPB}}^2} \qquad (3.1)$$

where Φ_f is the fluorescence quantum yield, F is the integral photon flux and n is the refractive index at the mean emission wavelength.[24] Moreover, $f = 1 - 10^{-A}$, where A is the absorbance at the excitation wavelength.

3.3   Computational Methods

Quantum mechanical calculations were performed to obtain ground and excited state geometries for MVP, ConA, and EF. Geometry optimised structures were calculated using Gaussian09[25] with density functional theory (DFT) and the Coulomb attenuated model Becke-3rd parameter Lee-Yang-Parr (CAM-B3LYP) functional[26] combined with a 6-31G* basis set.[27] The S_0/S_3 (*E-Z* isomerisation, *vide infra*) conical intersection (CI) structure in EF was optimised at the complete active space self-consistent field (CASSCF)[28,29]/6-31G* level of theory using Gaussian09 and a 6 electron, 6 orbital (6,6) active space consisting of three occupied π and three unoccupied π^* orbitals. The CI structure between the S_1 and S_2 states ($\pi\pi^*$ and $n\pi^*$ states, respectively) was optimised at the same level of theory as above, however, employing a (10,9) active space, adding to the previous active space one occupied σ orbital, one unoccupied σ^* orbital (localised on the C=O bond) and one occupied n orbital (localised on the double bonded O atom).

Potential energy cuts (PECs) were produced by calculating the energies of the first four electronic states (S_0, $S_1(1^1\pi\pi^*)$, $S_2(1^1n\pi^*)$ and $S_3(2^1\pi\pi^*)$) of EF along linearly interpolated coordinates (LIIC) for the *E-Z* isomerisation coordinate and from the DFT optimised geometries of *i)* the S_0 to the $S_1(1^1\pi\pi^*)$ state and *ii)* the $S_1(1^1\pi\pi^*)$ to the $S_2(1^1n\pi^*)$ state *via* the $S_1(1^1\pi\pi^*)/S_2(1^1n\pi^*)$ CI, in the *E*-isomer. These calculations were performed using Molpro 2010.1[30,31] and employing fully state averaged CASSCF along with its second order perturbation theory extension (CASPT2)[32] using a cc-pVDZ basis set[33] and a (12,10) active space, adding an additional occupied π orbital to the previously described (10,9) active space.

3.4 Results

3.4.1 Excited State Dynamics in MVP

We start this section with the simplest molecule of the series studied, MVP, the molecular structure of which (for the *syn-* conformer) is shown in Figure 3.1(a). MVP has been shown to exist as two stable conformers which form a *syn/anti* pair.[11] MVP was photoexcited in our TR-IY experiments to the $S_1(v=0)$ origin band of its *syn*-conformer, which is located at 305 nm. The $S_1(v=0)$ origin band of the *anti-* conformer of MVP is 805 cm^{-1} higher in energy compared to that of its *syn-* conformer;[11] therefore, the bandwidth of the laser pulses used in these TR-IY experiments (~ 500 cm^{-1} full width at half maximum) is unlikely to allow for the simultaneous population of both conformers, and hence the dynamics inferred herein can be considered to be conformer specific. The parent TR-IY transient resulting from exciting MVP at 305 nm and probing with 200 nm is shown in Figure 3.3(a), along with the kinetic fit for these data (red line). The TR-IY transient of MVP was fit with two exponential decay functions convoluted with a Gaussian corresponding to the instrument response function (IRF ~ 160 fs), as discussed in Chapter 2,
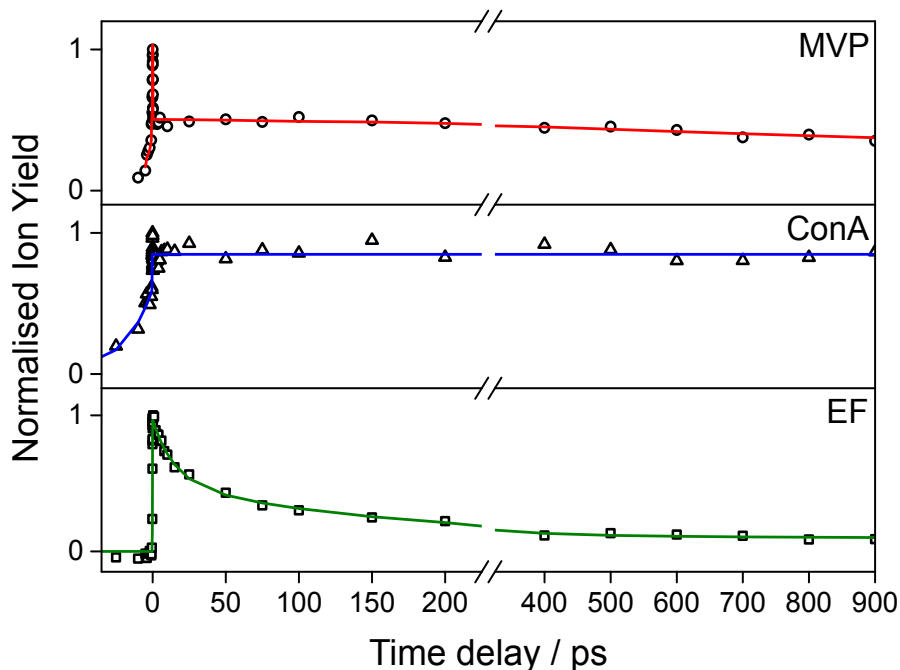
Figure 3.3: TR-IY transients of the (a) MVP, (b) ConA, and (c) EF parent ions following excitation at 305 nm, 306 nm, and 317.5 nm, respectively, corresponding to their S_1 origin bands. Also shown are the overall kinetic fits for MVP (red line), ConA (blue line), and EF (green line).

section 2.4.3. These fits returned two time constants, summarised in Table 3.1: an ultra-fast component of $\tau_1 < 50$ fs, which we attribute to multiphoton absorption and ionisation based on previous work,[34] and a slow decay with a time constant outside of the temporal window of these experiments ($\tau_2 > 900$ ps). This latter time constant is reminiscent of that seen in previous studies on the MVP subunit, guaiacol.[35] It is thus apparent that the addition of an allyl group to guaiacol (to generate MVP) does not result in a dramatic difference between the dynamics of the two molecules. While there are notable reverse (probe-pump) dynamics observable in MVP compared to guaiacol, the probe wavelength of 200 nm puts these dynamics well outside the UVA and UVB regions; they are, therefore, beyond the scope of this work and will not be discussed further.

3.4.2   Excited State Dynamics in ConA

We now increase the molecular complexity of the target molecule through the study of ConA. Once again, the molecule is photoexcited to the $S_1(v = 0)$ origin of its lowest energy conformer; in the case of ConA, this corresponds to the *syn*-conformer (shown in Figure 3.1(b)), whose origin is located at 306 nm. The origin of the *syn*-conformer of ConA lies 723 cm^{-1} lower in energy relative to the *anti*-conformer,[11] therefore, as previously discussed for MVP, the bandwidth of the laser pulses employed in these experiments is unlikely to photoexcite both conformers simultaneously and thus the results presented can be considered to be conformer specific. The TR-IY parent transient of ConA is shown in Figure 3.3(b) along with the overall kinetic fit (blue line). The TR-IY transient of ConA can be fit with a single exponential decay function which returns a time constant outside our temporal window ($\tau_1 > 900$ ps). Unlike MVP, no multiphoton absorption or ionisation artefact is observed for ConA, which serves as the only main difference between the excited state dynamics of ConA and MVP. For the sake of completeness, the reverse dynamics following photoexcitation with 200 nm in ConA should be noted, even though,

Table 3.1: Time constants extracted from TR-IY measurements for MVP, ConA, and EF.

Molecule	Time Constants		
MVP	$\tau_1 < 50$ fs		$\tau_2 > 900$ ps
ConA		$\tau_1 > 900$ ps	
EF	$\tau_1 = 15 \pm 4$ ps	$\tau_2 = 148 \pm 47$ ps	$\tau_3 > 900$ ps

for the same reasons highlighted in the case of MVP, they shall not be discussed further.

3.4.3   Excited State Dynamics in EF

3.4.3.1   R2PI and UVHB Spectroscopy

High resolution (frequency-resolved) data analogous to that referenced for MVP and ConA in the above sections was not available in the literature for EF. Therefore, in order to elucidate both the origin band(s) and the conformational distribution of EF, R2PI and UVHB studies were performed, the resulting spectra being presented in Figure 3.4. UVHB spectroscopy reveals two conformers of EF whose ground state energies differ by ~ 15 cm^{-1}, with origin bands located at 317.39 nm and 317.55 nm. We have not attempted any level of spectral assignment of the peaks in Figure 3.4, as these results were used primarily to locate (in energy) the origin bands of the conformers present in our molecular beam. Nevertheless, it is clear that given the small spectral shift between the *syn-* and *anti-*
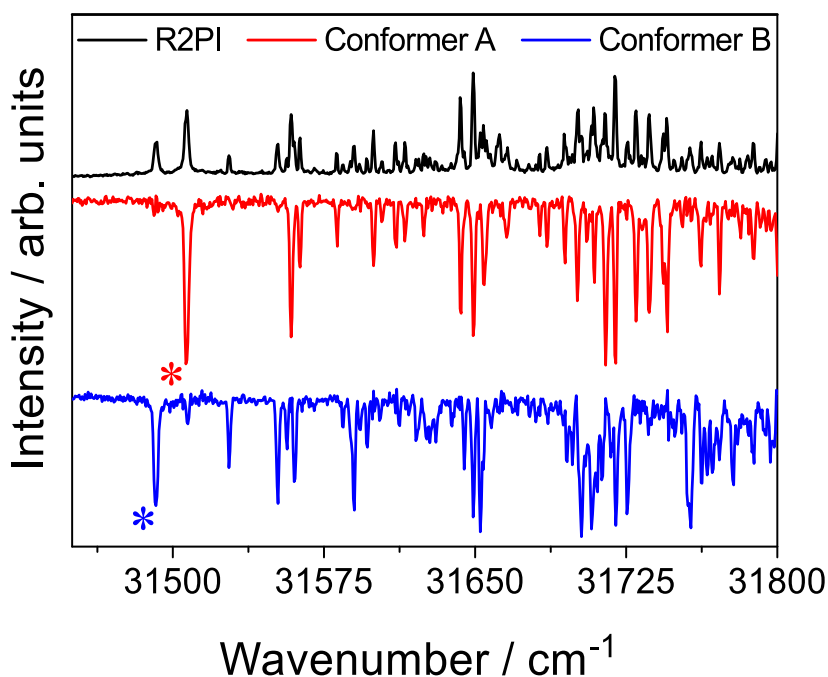
Figure 3.4: R2PI spectrum (black) and UVHB spectra of conformers A (red) and B (blue) for EF. The origin bands (labelled with *) are 317.39 nm and 317.55 nm for conformers A and B, respectively. The IP for both conformers was determined to be 7.73 eV. We note here that the signal from the R2PI spectrum has likely saturated the detector at the highest peaks. This was not avoided as, for the purposes of the current work, we were concerned only with the number of conformers present and the energies of their respective origin bands.
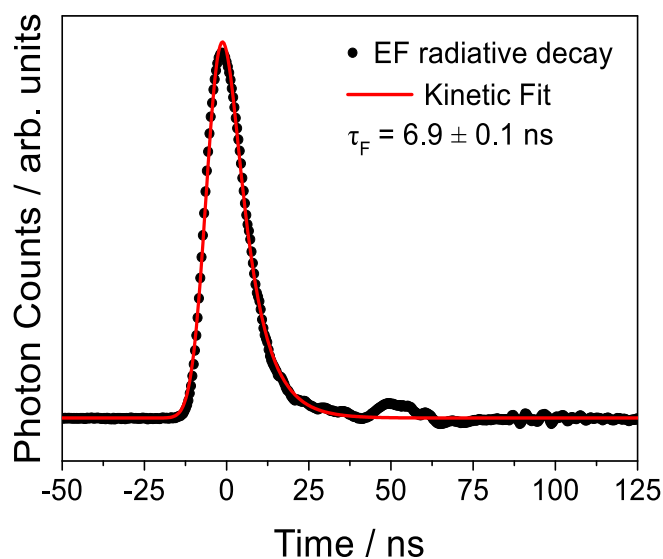
Figure 3.5: Total fluorescence lifetime measurement for EF upon photoexcitation at 317.55 nm, which yielded a radiative decay lifetime of $\tau_F = 6.9 \pm 0.1$ ns. The kinetic fit for these data follows the same principles as those for TR-IY transients (as detailed in Chapter 2, section 2.4.3), with an instrument response, in this case, of 9.2 ± 0.1 ns).
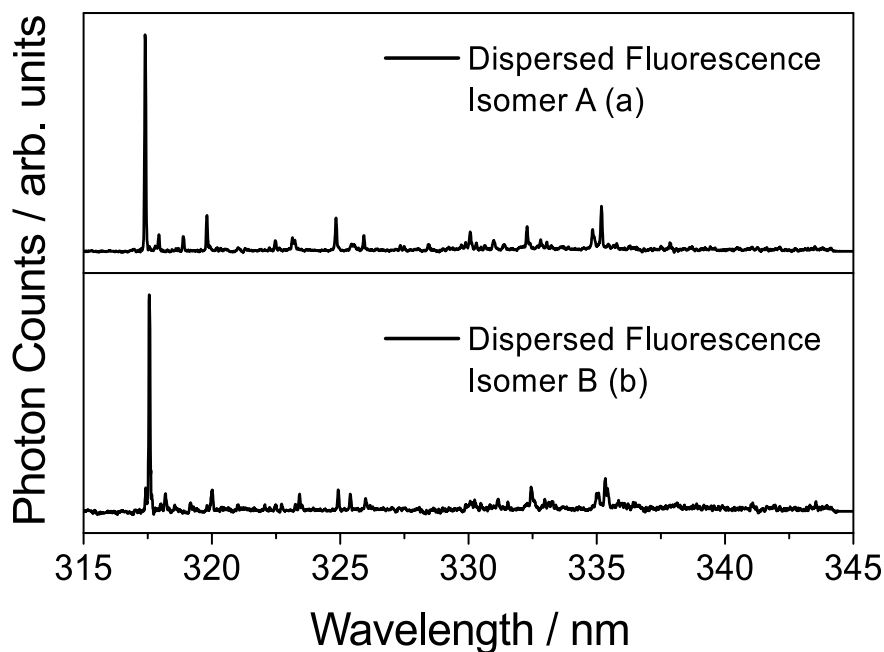
Figure 3.6: Dispersed fluorescence from the origin transitions of (a) conformer A and (b) conformer B of EF. We note that scatter is likely to contribute to the large relative intensity of the peak at the origin of both conformers.

conformers of EF and their near-degenerate energies, it can no longer be assumed that our results are conformer specific (*c.f.* MVP and ConA, *vide supra*).

3.4.3.2   Dispersed and Total Fluorescence

The total fluorescence lifetime of EF when photoexcited at the origin of conformer A was measured to be $\tau_F = 6.9 \pm 0.1$ ns, as shown in Figure 3.5. Attempts to observe any phosphorescence at longer wavelengths (> 400 nm) and/or larger time delays (100's of ns) produced no measureable signal. The dispersed fluorescence measurements following photoexcitation of the electronic origin of the two conformers presented in Figure 3.6 reveal Franck-Condon activity consistent with emission exclusively from the S_1 origin in the $315 - 345$ nm region, although there is likely a contribution to this signal from scatter of the excitation laser.

3.4.3.3   Time-Resolved Ion Yield

EF was photoexcited at 317.5 nm (S_1 origin of conformer B) and probed at 200 nm to ensure photoionisation from any low energy state that may be accessed upon relaxation of the initially photoexcited S_1 state (see section 3.5). As mentioned earlier, the ~ 500 cm^{-1} bandwidth of the pump accesses both conformers of EF simultaneously and thus conformer specific dynamics are not possible (contrary to the case for MVP and ConA). The TR-IY parent transient resulting from photoexciting EF at 317.5 nm (for $\lambda_{pr} = 200$ nm) is shown in Figure 3.3(c), along with the overall kinetic fit (green line). The TR-IY parent transient for EF requires a minimum of three exponential decays (see Figure 3.7(a) for attempted fits with one and two decays), as summarised in Table 3.1. The time constants extracted are $\tau_1 = 15 \pm 4$ ps, $\tau_2 = 148 \pm 47$ ps and a long lived component which persists beyond the temporal limit of our experiment ($\tau_3 > 900$ ps). We will explore the origins of the differences between the dynamics observed for EF and those observed for MVP and ConA in section 3.5. For completeness, we note that in the case of EF no reverse dynamics are observed.

TR-IY measurements for EF at lower probe energies (322 nm *cf.* 200 nm, Figure 3.7(b)) yield values and amplitudes for τ_1 and τ_2 which are similar to those presented in Table 3.1. The amplitude of the component associated with τ_3, on the other hand, is drastically reduced at $\lambda_{pr} = 322$ nm. In fact, comparison between the bi- and tri-exponential fits

(a) $\lambda_{pu} = 317.5$ nm and $\lambda_{pr} = 200$ nm.

(b) $\lambda_{pu} = 317.5$ nm and $\lambda_{pr} = 322$ nm.
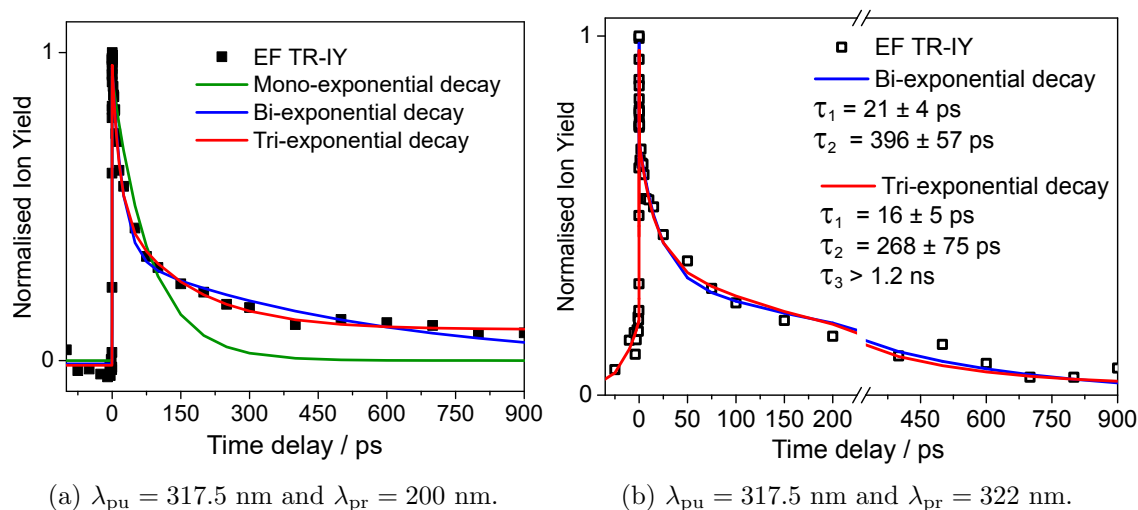
Figure 3.7: (a) Attempted kinetic fits for the TR-IY transients of EF (obtained with $\lambda_{pu} = 317.5$ nm and $\lambda_{pr} = 200$ nm) with one (green), two (blue) and three (red) exponential decays. (b) TR-IY transients for EF at $\lambda_{pu} = 317.5$ nm and $\lambda_{pr} = 322$ nm with two different kinetic fits. The first kinetic fit (blue line) yields two time constants: $\tau_1 = 21\pm4$ ps and $\tau_2 = 396 \pm 57$ ps. No long-lived step was included in this fit. The second kinetic fit (red line) yields a $\tau_1 = 16 \pm 5$ ps and a $\tau_2 = 268 \pm 75$ ps time constant, as well as a $\tau_3 > 1.2$ ns step.

shown in Figure 3.7(b) is inconclusive: the long lived component may indeed be absent at this probe wavelength. This behaviour suggests that, following photoexcitation of the S_1 origin of EF, excited state population may become trapped in a low energy potential well from which ionisation may take place at $\lambda_{pr} = 200$ nm, but not at $\lambda_{pr} = 322$ nm.

3.4.3.4   H-atom Elimination

There has been considerable interest in H-atom elimination dynamics along heteroatom-hydrogen bonds (X—H, where X is usually O or N) mediated by dissociative $\pi\sigma^*$ states localised along this coordinate. The existence of such states, localised specifically along the O—H bond in EF, is usually identified by the production of high kinetic energy (KE) H-atoms,[34,36,37] in accordance with the original postulate of Sobolewski and Domcke.[38] The H^+ TKER spectra for MVP, ConA, and EF at $\Delta t = 1.2$ ns are shown in Figure 3.8. Photoexcitation of MVP and ConA at their respective S_1 origins produces essentially featureless H-atom TKER spectra (Figure 3.8(a) and (b), respectively). In the analogous TKER spectrum of EF (Figure 3.8(c)) two features may be identified: one centred at low KE (~ 2500 cm^{-1}) and a second centred at higher KE ($\sim 12\,500$ cm^{-1}). In light of previous studies, the low KE feature can be assigned to multiphoton processes or statis-
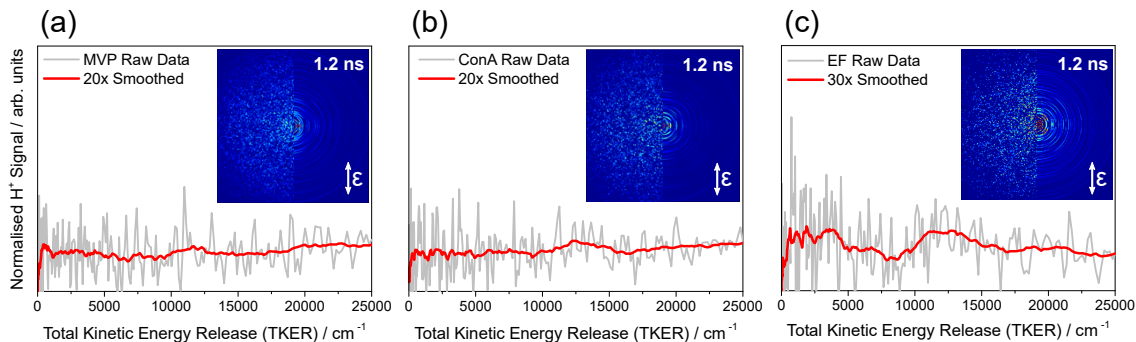
Figure 3.8: Normalised TKER spectra obtained for MVP, ConA, and EF photoexcited at their respective S_1 origins, with a pump-probe time delay of $\Delta t = 1.2$ ns. The red lines correspond to a 20 point (30 point in the case of EF) moving average through the raw data for each molecule (grey). Insets: H^+ velocity map images from which each TKER spectra was derived. Raw images (left half of each inset) are displayed along with a reconstructed slice through the centre of the original 3D ion distribution (right half). The vertical white arrows indicate the electric field polarisation vector of the pump pulse, ε.

tical unimolecular decay on S_0.[34,35] The second, high KE feature observed for EF is also attributed to multiphoton processes, based on energy considerations, as this peak appears at much higher KEs than one would anticipate for one photon absorption followed by $\pi\sigma^*$ state mediated O—H dissociation. This is discussed in further detail in section 3.5.

3.4.4   TEAS and Steady-State Measurements

We now present our results for the studies performed on EF solvated in cyclohexane, a weakly perturbing solvent which should be most akin to the environment in vacuum. The TEAS measurements shown in Figure 3.9(a) and (b) are the results following photoexcitation of EF in cyclohexane at 316 nm and 243 nm, respectively. In both cases, the transient absorption spectra (TAS) at early time (< 5 ps) are dominated by a large excited state absorption (ESA) feature that extends from 360 nm to the long wavelength limit of our WLC probe at 675 nm. The peak for the ESA feature is located at 405 nm for $\lambda_{pu} = 316$ nm and at 415 nm for $\lambda_{pu} = 243$ nm. Furthermore, the ESA peak is broader for EF photoexcited at 243 nm, which is likely due to the higher energy of the pump pulse populating a larger density of vibrational states of EF, thus enhancing intramolecular energy redistribution mechanisms. With increasing Δt, the ESA decays towards baseline values.

Two more features are observed in the TAS presented in Figure 3.9, both at probe wavelengths shorter than 360 nm: the ground state bleach (GSB) feature at ~ 330 nm
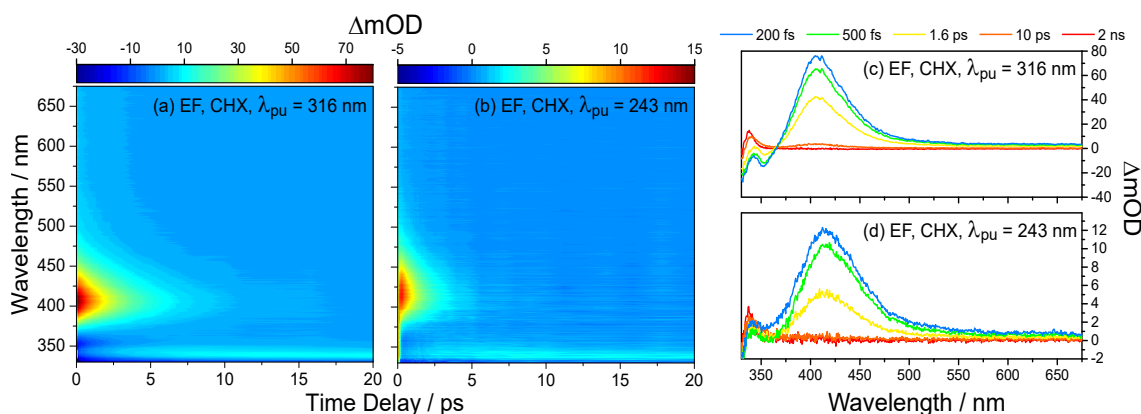
Figure 3.9: TAS for EF in cyclohexane (CHX) after photoexcitation at (a) 316 nm and (b) 243 nm. The colour mapping represents the change in optical density, ΔmOD; the colour scale is shown above each plot. Corresponding TAS at selected Δt, highlighting the evolution of key spectral features, are also shown for photoexcitation at (c) 316 nm and (d) 243 nm.

and a negative feature at $\sim$ 340 nm which grows in intensity (towards positive ΔmOD values) and narrows over time; the same negative peak also undergoes a concurrent blue shift, albeit moderate, to 335 nm. The combined behaviour of this negative peak — both a narrowing and blue shift — is indicative of vibrational relaxation of the absorbing species.[39,40] The component at 340 nm persists for the extent of the temporal window
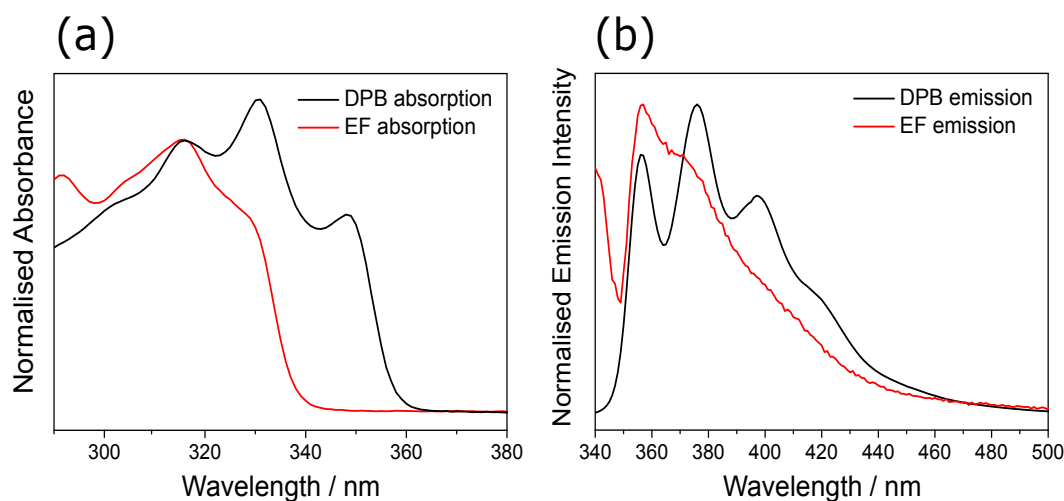
Figure 3.10: (a) UV/Vis absorption spectra of EF (red line) and DPB (black line). The wavelength of the intersection between the two spectra (in the wavelength range of interest, $\sim$ 316 nm) was used as the excitation wavelength for the fluorescence measurements. (b) Normalised fluorescence emission spectra for EF (red line) and DPB (black line). From these data, and based on Equation 3.1, the fluorescence quantum yield of EF was determined to be 0.0026 ± 0.0002.

available in these experiments, as is clear from the TAS at selected Δt values, shown in Fig. 3.9(c) and (d) (following photoexcitation at 316 nm and 243 nm, respectively). Finally, we note a separate negative feature present only in the TAS corresponding to EF photoexcited with $\lambda_{pu} = 316$ nm and located at 355 nm. Given the emission spectrum of EF after photoexcitation at 316 nm, presented in Figure 3.10(b), this negative peak in the TAS of EF at 355 nm is assigned to stimulated emission (SE), most likely between the $S_1(1^1\pi\pi^*)$ state (*vide infra*) and the ground electronic state (S_0). The SE feature decays on the same timescale as the ESA.

Four time constants were required to accurately model the TAS following photoexcitation of EF at 316 nm, while only three were required in the case of $\lambda_{pu} = 243$ nm; a summary of the time constants extracted is given in Table 3.2. The evolution associated difference spectra (EADS) resulting from the global fit analysis of the TAS for EF are presented in Fig. 3.11(a) and (b), corresponding to photoexcitation at 316 nm and 243 nm, respectively. Finally, the ΔUV/Vis spectra for EF in cyclohexane, recorded as described in section 3.2.7, are presented in Figure 3.12 (top) for (a) $\lambda_{pu} = 316$ nm and (b) $\lambda_{pu} = 243$ nm, overlaid with the corresponding TAS at $\Delta t = 2$ ns. For both excitation
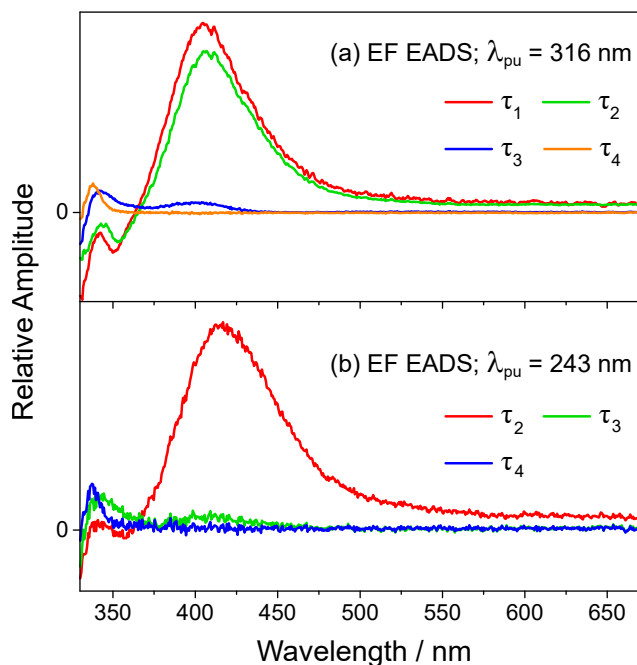
Figure 3.11: Evolution associated difference spectra (EADS) resulting from the sequential global fit of the TAS following photoexcitation of EF at (a) 316 nm and (b) 243 nm.

wavelengths, there is remarkable agreement between the ΔUV/Vis spectra and the TAS. Moreover, the results of our ^{1}H NMR studies, also shown in Figure 3.12 (bottom), confirm that EF is present mainly in its *trans*-configuration in our initial samples, while there is clear evidence for the presence of the *cis*-isomer of EF post-irradiation. The implications of these findings will be disussed further in the next section.

Table 3.2: Extracted time constants from the sequential global fit to the TEAS measurements. τ_4 in each of the fits was employed to appropriately model the proposed *cis*-isomer photoproduct (*vide infra*).

	$\tau_1/\mathbf{fs}$	$\tau_2/\mathbf{ps}$	$\tau_3/\mathbf{ps}$	τ_4
316 nm	168 ± 40	2.42 ± 0.04	15.4 ± 0.3	$\gg$ ns
243 nm	—	1.38 ± 0.04	15.1 ± 0.5	$\gg$ ns

3.5 Discussion

EF in vacuum

We begin our discussion by focusing on our gas-phase experiments, namely the H-atom elimination results obtained for MVP, ConA, and EF. As mentioned earlier, in these studies we aimed to explore H-atom elimination dynamics mediated by dissociative $\pi\sigma^*$ states localised along the O—H bonds in the molecules under study; this refers in particular to the phenolic O—H bond, *i.e.* to the OH substituent on the benzene ring for each of these molecules. It is important to first establish that the expected photofragment TKER after O—H bond photodissociation can be determined (assuming molecules begin in their ground vibronic state) according to:[17]

$$\mathrm{TKER} = h\nu_{\mathrm{pu}} - \mathrm{D}_0(\mathrm{O}\text{—}\mathrm{H}) - E_{\mathrm{int}} \tag{3.2}$$

In Equation 3.2, $h\nu_{\mathrm{pu}}$ is the pump photon energy, $\mathrm{D}_0(\mathrm{O}\text{—}\mathrm{H})$ is the adiabatic dissociation energy of the O—H bond, and E_{int} is the total internal energy of the co-fragment (electronic and vibrational). Following the aforementioned relationship, phenol derivatives typically possess $\mathrm{D}_0(\mathrm{O}\text{—}\mathrm{H})$ values of $\sim$ 27 500 – 31 500 cm^{-1} resulting in a large, broad Gaussian H$^+$ signal centred around 6500 cm^{-1} for photoexcitation energies on the order of their origin band energies.[35,41–44] Such observations are in stark contrast with the observed TKER spectra for MVP and ConA (Figure 3.8(a) and (b), respectively),
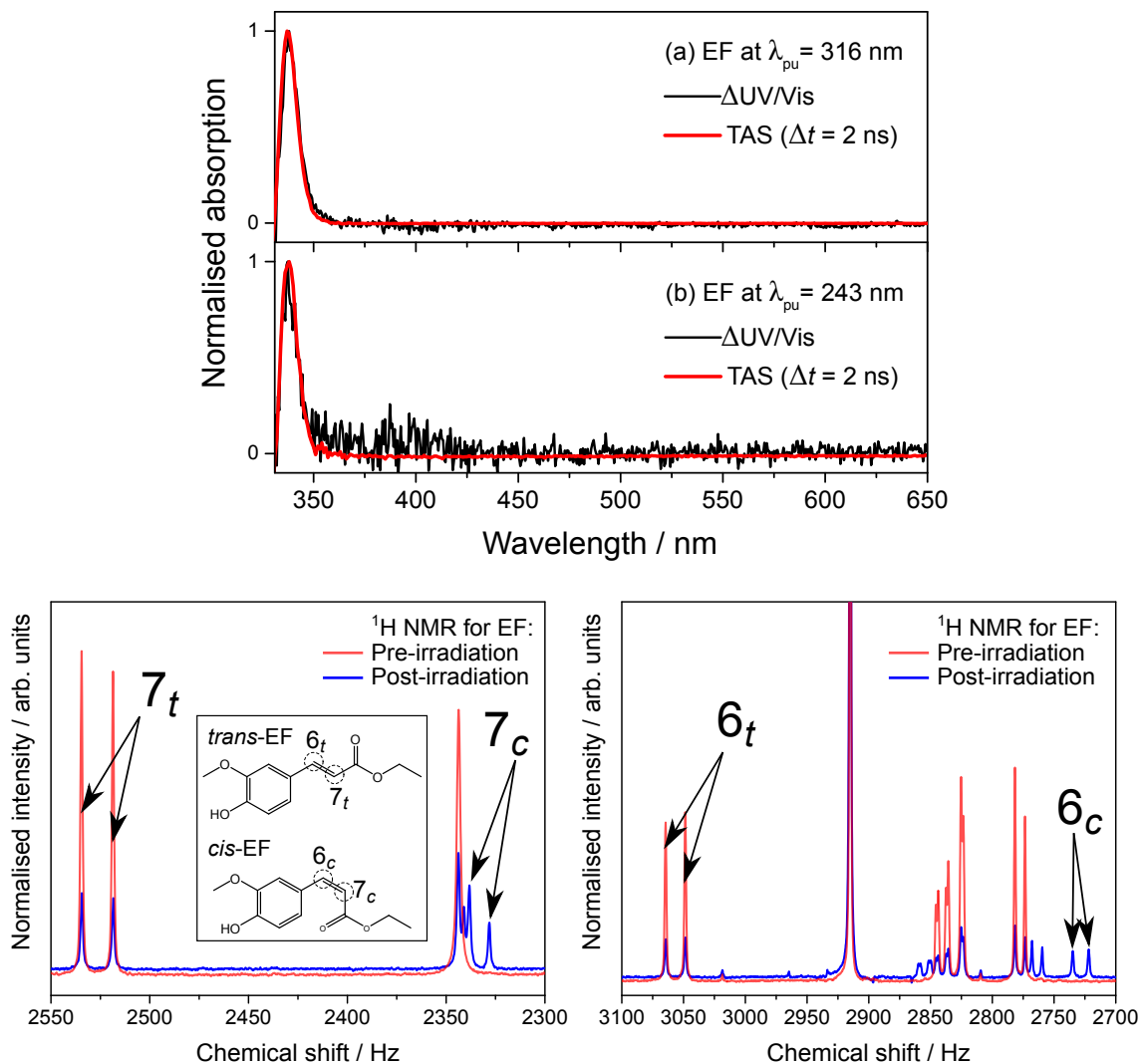
Figure 3.12: (Top) ΔUV/Vis spectra (black lines) overlaid with TAS at $\Delta t = 2$ ns (red lines) for EF photoexcited at (a) 316 nm and (b) 243 nm. (Bottom) ^{1}H NMR spectra for EF pre- and post-irradiation, represented by the red and blue lines, respectively. The simplified molecular structures for *trans*- and *cis*-EF are shown as an inset with the relevant hydrogens labelled $6_t/7_t$ for the *trans*- and $6_c/7_c$ for the *cis*-isomers. The ^{1}H NMR peaks corresponding to hydrogens 6 and 7 are shown in their appropriate spectral regions; the peaks for each hydrogen are localted at: $6_t = 3054$ and 3038 Hz; $6_c = 2724$ and 2711 Hz; $7_t = 2524$ and 2508 Hz; $7_c = 2331$ and 2318 Hz. As discussed in more detail in section 3.5, the spectra presented in this figure provide strong evidence for the presence of the *cis*-isomer of EF after irradiation, thus suggesting that UV radiation prompts *trans-cis* photoisomerisation for EF solvated in cyclohexane. Further ^{1}H NMR data and respective peak assignments can be found in section 3.17.III.

where there is no evidence of a Gaussian H^+ signal within the 1.2 ns temporal window of these experiments. We interpret the lack of evidence for O—H bond dissociation in these two molecules in light of the intramolecular H-bond between the OH and OMe ring substituents, which can be seen in the minimum energy (S_0 and S_1) geometries for these molecules, shown in Figure 3.13. This intramolecular bond is likely to introduce a large barrier to O—H dissociation, hindering fast formation of RO + H photoproducts (where R represents MVP or ConA excluding the OH group).[35] It is worth noting, however, that H-atom elimination might still occur beyond the 1.2 ns timescale that can be probed in these experiments.
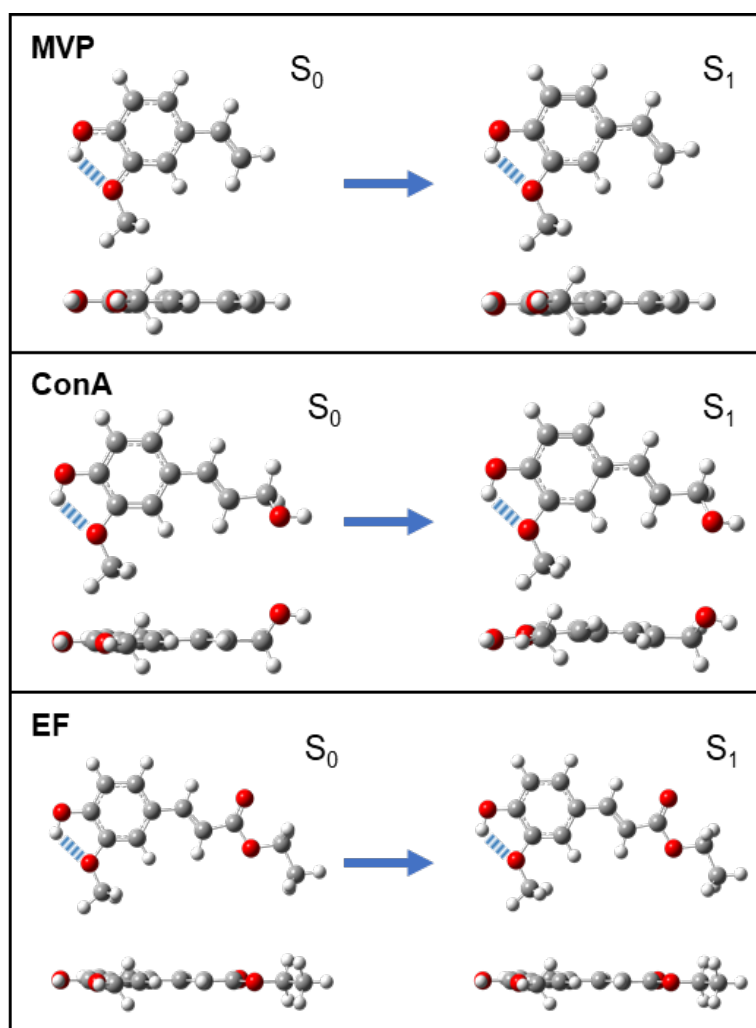
Figure 3.13: Optimised S_0 and S_1 geometries of MVP, ConA, and EF (two perspectives). Geometry optimised structures were calculated using Gaussian09[25] with density functional theory (DFT) and the Coulomb attenuated model Becke-3rd parameter Lee-Yang-Parr (CAM-B3LYP) functional[26] combined with a 6-31G* basis set.[27] Dashed blue lines indicate intramolecular hydrogen bonds.

In the case of EF, energy considerations dictate that at $h\nu_{\mathrm{pu}} = 31\,496$ cm^{-1} (317.5 nm), O—H dissociation should produce H-atoms (and therefore H$^+$ ions) at energies on an approximate range of $0 - 4000$ cm^{-1}; a definite value cannot be provided as there is no literature (to the best of our knowledge) on the experimental value of D$_0$(O—H) for EF. Nevertheless, given these energetic considerations, the small Gaussian feature at $\sim 12\,500$ cm^{-1} is likely too high in energy to correspond to single photon, $\pi\sigma^*$ mediated photodissociation. Indeed, with regards to Equation 3.2, such correspondence would require a value of D$_0$(O—H) of approximately $19\,000$ cm^{-1}, which is significantly lower than the typical values of $\sim 27\,500 - 31\,500$ cm^{-1}.[35,41–44] However, the $\sim 12\,500$ cm^{-1} feature is not present when detuning the probe wavelength from the H-atom 2s $\leftarrow$ 1s resonance (see section 3.17.II), which indicates that H-atoms are indeed being produced as a result of photodissociation. This may be reconciled by considering that high KE H-atoms may be produced after absorption of two photons of $\lambda_{\mathrm{pu}} = 317.5$ nm promoting excited state population to higher-lying dissociative states, or by dissociative ionisation processes for which the charge remains on the co-fragment.

While the feature at ~ 2500 cm^{-1} in the TKER spectrum of EF (Figure 3.8(c)) does fall within the energy range predicted by Equation 3.2, it is likely that it has its origins in multiphoton dissociative ionisation: not only does the feature remain in the off-resonance TKER spectrum of EF (see section 3.17.II), ruling out statistical unimolecular decay on S$_0$, but it also presents a Boltzmann-like distribution, rather than the Gaussian shape expected for $\pi\sigma^*$ mediated photodissociation.[34,45] Moreover, and as shown in Figure 3.13, the same hydrogen bond that was deduced to hinder H-atom dissociation in MVP and ConA is also present in EF, and thus it is unlikely that O—H bond dissociation would be a competitive relaxation pathway in the case of EF as well. The fluorescence lifetime of $\sim$ 7 ns we have measured for EF (see Figure 3.5) is further evidence that O—H dissociation is likely not a competitive relaxation pathway for EF even within longer timescales than those we can probe with our time-resolved experiments. The absence of a significant H$^+$ signal in the sunscreen molecules under study is particularly relevant, since this process would be a potential source of toxic free radicals. The lack of H-atom release from EF upon photoexcitation, as evidenced by the poor signal-to-noise in the TKER spectrum in Figure 3.8(c), may indicate that radical species are unlikely to form as a result of O—H bond fission under solar illumination, given the comparatively low power density of natural sunlight when compared to the laser pulses used in these experiments.

Finally, we note from Figure 3.13, that the planarity of the geometries in S_1 corroborate the absence of O—H fission in the presented systems in light of previous work: in monolignol building blocks, a significant distortion from planarity in S_1 was shown to weaken the intramolecular H-bond and therefore facilitate elimination of H-atoms.[46]

While the three molecules under study, MVP, ConA, and EF, behave similarly in terms of their H-atom elimination dynamics due to the intramolecular H-bond that is present in all of them, the TR-IY results presented in Figure 3.3 reveal potentially different ultrafast mechanisms ocurring for EF when compared to MVP and ConA. Two time constants were extracted from the TR-IY transients for MVP: an instrument-limited time constant of $\tau_1 < 50$ fs and a second time constant of $\tau_2 > 900$ ps. In line with previous findings for guaiacol and related chromophores,[34,46] the first time constant in MVP is attributed to multiphoton ionisation. An analogous multiphoton feature is not observed for ConA nor for EF, since multiphoton-induced fragmentation of the ester/alcohol group side chain (see section 3.17.II for the mass spectrum) required TR-IY measurements to be taken at lower laser powers, rendering multiphoton absorption negligible in these cases when compared to MVP. The second time constant observed in MVP, $\tau_2 > 900$ ps, can be related to the single time constant observed for ConA, also > 900 ps. In both cases, the large time constant likely corresponds to the persistence of their respective initially excited S_1 states (*vide supra*) which, as shown in Figure 3.3, do not undergo appreciable relaxation by 900 ps.

The clear presence of two additional time constants in the TR-IY transients of EF, $\tau_1 = 15 \pm 4$ ps and $\tau_2 = 148 \pm 47$ ps, in contrast with MVP and ConA, suggests a different (or competing) relaxation mechanism is in operation. The carboxylic acid variant of EF, ferulic acid, has been predicted to undergo *trans-cis* or *E-Z* photosiomerisation[12] and this mechanism has now been shown to be the preferred relaxation pathway for several other cinnamate derivatives.[3–6,47] It is, therefore, reasonable to evaluate the role of this relaxation mechanism in EF. To explore the hypothesis that *E-Z* photoisomerisation may be responsible for the TR-IY transients observed in our experiments for EF, we have carried out computational studies to map out the PECs along the *E-Z* isomerisation coordinate of EF, akin to those reported in reference 12. The resulting PECs, shown in Figure 3.14(a), were produced by calculating the energies of the ground (S_0) and first three singlet excited electronic states of EF ($S_1(1^1\pi\pi^*)$, $S_2(1^1n\pi^*)$ and $S_3(2^1\pi\pi^*)$) at various points along a linear interpolation of internal coordinates (LIIC) from the ground state minimum energy geometries of each isomer towards the S_0/S_3 CI. The results from these calculations suggest
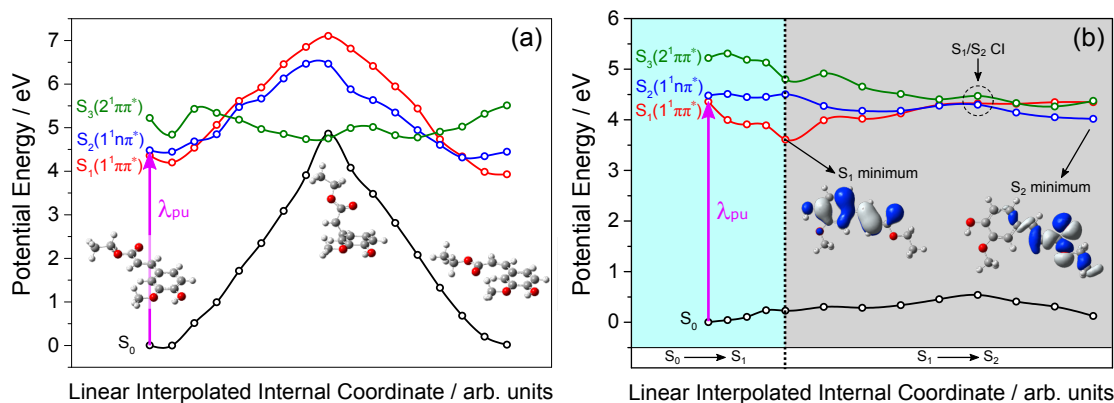
Figure 3.14: (a) PECs of the S_0 (black line), $S_1(1^1\pi\pi^*)$ (red line), $S_2(1^1n\pi^*)$ (blue line), and $S_3(2^1\pi\pi^*)$ (green line) states of EF along the E-Z isomerisation coordinate. Optimised ground state geometries for each isomer and the S_0/S_3 conical intersection (CI) are also presented. (b) PECs of same states of EF (represented with the same colour code) from the S_0 to S_1 LIICs (blue shaded area) and from the S_1 to S_2 LIICs (grey shaded area) *via* the S_1/S_2 CI. Optimised geometries for the S_1 and S_2 states are also presented.

that, while the energy minima of the E-Z isomers are similar, there is a substantial energy barrier (~ 0.8 eV) that must be overcome upon photoexcitation to the S_1 origin of EF in order for E-Z isomerisation, mediated by the $S_1(1^1\pi\pi^*)/S_3(2^1\pi\pi^*)$ CI, to occur. The large barrier to E-Z photoisomerisation thus predicted by computational methods renders this relaxation pathway extremely unlikely to take place for EF in vacuum; consequently, we rule out the isomerisation mechanism and proceed to explore other possible explanations for our experimental observations.

In light of previous work,[2,10,47] which has speculated low energy $1n\pi^*$ states to be involved in the photodynamics of similar systems to those studied herein, we have carried out further computational studies to search for such states. The PECs of the S_0, $S_1(1^1\pi\pi^*)$, $S_2(1^1n\pi^*)$ and $S_3(2^1\pi\pi^*)$ states of EF were produced along the LIIC from the DFT optimised geometries of *i)* the S_0 to the $S_1(1^1\pi\pi^*)$ state and *ii)* the $S_1(1^1\pi\pi^*)$ to the $S_2(1^1n\pi^*)$ state *via* the $S_1(1^1\pi\pi^*)/S_2(1^1n\pi^*)$ CI, in the E-isomer, as shown in Figure 3.14(b). From the results of these calculations, there appears to be a barrierless pathway through which the minimum of the $S_2(1^1n\pi^*)$ state can be accessed *via* a CI with the $S_1(1^1\pi\pi^*)$ state. Therefore, it is possible for an $S_1(1^1\pi\pi^*) \rightarrow S_2(1^1n\pi^*)$ transition to occur, with the $S_2(1^1n\pi^*)$ state then being long-lived, as observed in previous studies.[2,10] The path to the $S_2(1^1n\pi^*)$ minimum passes through a deep minimum in $S_1(1^1\pi\pi^*)$, where population may become trapped, which could then be responsible for the fluorescence

Table 3.3: Calculated vertical excitation energies for relevant singlet and triplet states of EF. These energies were calculated using Molpro 2010.1 and employing fully state averaged CASSCF along with CASPT2 using a cc-pVDZ basis set and a (12,10) active space (see main text for details).

State	Energy / cm^{-1}	Energy / eV
$S_2(1^1n\pi^*)$	36 122	4.48
$S_1(1^1\pi\pi^*)$	35 148	4.35
$T_4(1^3n\pi^*)$	33 782	4.19
$T_3(3^3\pi\pi^*)$	33 620	4.17
$T_2(2^3\pi\pi^*)$	32 752	4.06
$T_1(1^3\pi\pi^*)$	23 258	2.88

observed. However, neither of these scenarios accounts for all the dynamics observed in the TR-IY measurements of EF, since they would only yield two time constants: one to account for the $S_1(1^1\pi\pi^*) \rightarrow S_2(1^1n\pi^*)$ transition and/or motion to the $S_1(1^1\pi\pi^*)$ minimum, and the second to account for the lifetime of the final $S_1(1^1\pi\pi^*)$ and/or $S_2(1^1n\pi^*)$ state(s). Therefore, alternative or additional relaxation mechanisms need to be considered.

The photophysics of aromatic carbonyl compounds have been extensively reported in the literature to involve low-lying $n\pi^*$ states of both singlet and triplet character, with intersystem crossing (ISC) being a kinetically competitive photophysical process.[48–51] In order to evaluate the role of triplet states in the photodynamics of EF, further calculations were performed using CASSCF along with CASPT2 with a cc-pVDZ basis set and a (12,10) active space (*vide supra*) to locate any triplet states that may be involved in the photodynamics of EF. Four triplet states were identified below the $S_1(1^1\pi\pi^*)$ state energy in the vertical Franck-Condon region; their energies are presented in Table 3.3. The $T_2(2^3\pi\pi^*)$, $T_3(3^3\pi\pi^*)$ and $T_4(1^3n\pi^*)$ states are nearly isoenergetic and lie on average $\sim$ 2000 cm^{-1} lower in energy in relation to the vertical $S_1(1^1\pi\pi^*)$ state excitation energy; the $T_1(1^3\pi\pi^*)$ state lies $\sim$ 10 500 cm^{-1} below these. Apart from being close in energy to both the $S_1(1^1\pi\pi^*)$ and $S_2(1^1n\pi^*)$ states, these triplet states are also of the correct orbital type to allow for ISC to occur from either accessible singlet state in accord with El-Sayed's rule, which states that the rate of ISC will be higher for a transition where there is a change in orbital type (for example, n to π or *vice-versa*).[52] Once within the triplet manifold, the population could then undergo internal conversion (IC) to the lowest triplet state, and from there return to the ground state *via* phosphorescence (or undergo photoreaction).

Given the aforementioned considerations, the following mechanisms are suggested to be responsible for our experimental observations, as diagramatically depicted in Figure 3.15: firstly, following photoexcitation of EF to the $S_1(1^1\pi\pi^*)$, wavepacket bifurcation[53] results in population of both the $S_1(1^1\pi\pi^*)$ and $S_2(1^1n\pi^*)$ states, mediated *via* the aforementioned energetically accessible CI between these states. This is supported by the relatively flat potential energy landscape in regions removed from the vertical Franck-Condon region (Figure 3.14(b)). Intramolecular vibrational redistribution (IVR) then likely occurs on both the $S_1(1^1\pi\pi^*)$ and $S_2(1^1n\pi^*)$ states, with population moving into the deep energy well of the $S_1(1^1\pi\pi^*)$ state and the shallower well of $S_2(1^1n\pi^*)$. Energy is redistributed into coordinates orthogonal to the reaction coordinate in Figure 3.14(b), so that population gets trapped in the wells of the $S_1(1^1\pi\pi^*)$ and $S_2(1^1n\pi^*)$ states along this reaction coordinate, as represented in this figure. In competition with IVR, ISC onto the several predicted higher lying triplet states may also occur from either the $S_1(1^1\pi\pi^*)$ or $S_2(1^1n\pi^*)$ states, in accordance with El-Sayed's rule.[52] Importantly, the potential well of $S_1(1^1\pi\pi^*)$ lies lower in energy than the vertical excitation energies of the higher lying triplet states. As such, it is conceivable that, as the wavepacket progresses towards the minimum of $S_1(1^1\pi\pi^*)$, it encounters regions of strong spin-orbit (SO) coupling between the $S_1(1^1\pi\pi^*)$ state and isoenergetic triplet state(s), facilitating efficient ISC.[54–57] This SO coupling
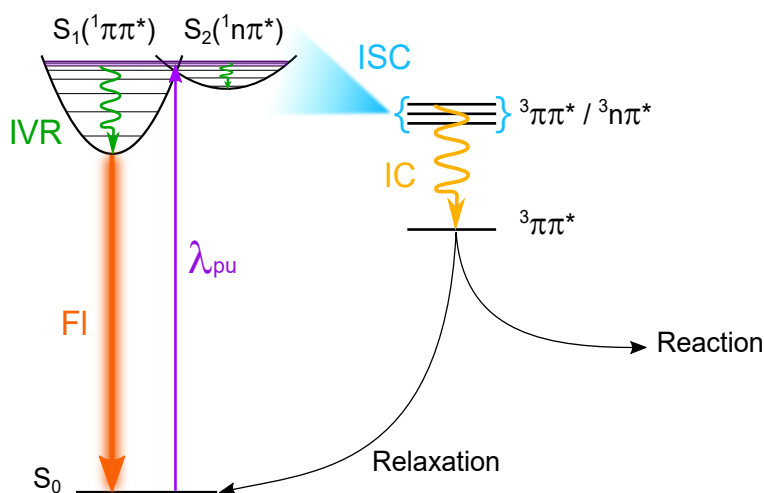
Figure 3.15: Schematic depiction of the proposed decay mechanisms for excited state relaxation in EF. IVR = intramolecular vibrational redistribution into coordinates orthogonal to the reaction coordinate (see details in the main text); ISC = intersystem crossing; IC = internal conversion; Fl = fluorescence; relaxation refers to ISC or phosphorescence back to the ground state; reaction encompasses mechanisms such as photofragmentation or photocyclisation. Note that 'reaction' has been omitted from S_1 for clarity, although it is also a valid pathway from this state.

would allow ISC to occur while still retaining population trapped in the $S_1(1^1\pi\pi^*)$ well. We suggest that all these processes (IC to $S_2(1^1n\pi^*)$ state, IVR on both the $S_1(1^1\pi\pi^*)$ and the $S_2(1^1n\pi^*)$ states and ISC from these onto nearby triplet states) will be acting in competition with each other and are overall described by $\tau_1 = 15 \pm 4$ ps, which is consistent with timescales seen in similar systems.[58–61] Following ISC onto the triplet state manifold, we suggest that $\tau_2 = 148 \pm 47$ ps corresponds to IVR and IC occurring down the triplet ladder towards the lowest triplet state $T_1(1^3\pi\pi^*)$.[61] The longer lifetime for IC (τ_2) compared to ISC (τ_1) could be explained by the relatively large energy gap between the $T_1(1^3\pi\pi^*)$ and $T_2(2^3\pi\pi^*)$ states. The remaining long-lived step would then be attributed to population trapped in $S_1(1^1\pi\pi^*)$ — which decays through fluorescence and/or photoreaction (on the order of ns, as suggested by the ~ 7 ns fluorescence lifetime measured for EF) — in conjunction with population of the lowest lying triplet state. While one might expect the triplet state to phosphoresce, the emission wavelengths observed in EF and the nanosecond lifetime of said emission suggest that there is little or no phosphorescence from triplet states in EF. This may be due to photoreaction occurring on the excited triplet states, since carbonyl compounds are known to undergo Norrish type-I and type-II reactions both from their singlet and triplet states.[62,63] Moreover, due to the low energy of the $T_1(1^3\pi\pi^*)$ state, it may be kinetically competitive for the system to then return to the S_0 *via* ISC.

In supporting our proposed mechanism, we note that the TR-IY of the EF parent ion taken at long probe wavelengths ($\lambda_{\mathrm{pr}} = 322$ nm) suggests that the long lifetime (> 900 ps) component observed in these experiments corresponds to a state lower in energy than those corresponding to τ_1 and τ_2 (*vide supra*). These probe dependent observations would be in agreement with either IVR on the $S_1(1^1\pi\pi^*)$ state or ISC followed by IC to the $T_1(1^3\pi\pi^*)$ state moving excited state population outside of the ionisation probe window of the 322 nm laser pulse: from the well of the $S_1(1^1\pi\pi^*)$ state, this probe energy leaves the system ~ 0.4 eV below the IP, and ~ 1 eV below the IP from the $T_1(1^3\pi\pi^*)$ state. An elongation of τ_2 was derived when using two exponential decay functions to fit the 322 nm probe data. Given that both a bi- or tri-exponential decay function fits the data equally well, as shown in Figure 3.7(b), it is possible that this elongation is merely an artefact of the absence of the third time constant. Since the pump wavelength is unchanged, the elongation of τ_2 is most likely an effect of the final (cationic) state accessed in the probe step, rather than a change in the dynamics of EF. However, since this change in τ_2 has

no qualitative effect on the interpretation of our results, such exploration is considered beyond the scope of this work.

Two caveats to the mechanisms proposed are in order here. Firstly, while there is precedence for ISC occurring in systems such as EF within only a few picoseconds, ISC has also been shown to occur in other related systems in hundreds of picoseconds.[64] As such, one cannot rule out τ_2 corresponding to ISC from the singlet to the triplet states, with IVR/IC then occurring between the triplet states on much faster timescales.[51] τ_1 would then correspond to IC between, and IVR on, the $S_1(1^1\pi\pi^*)$ and $S_2(1^1n\pi^*)$ states. Population trapped on these two states would then undergo ISC with time constant τ_2. Secondly, as we cannot selectively probe the individual conformers of EF identified in the UVHB experiments described above, it is possible that τ_1 and τ_2 may correspond to the dynamics of the two separate conformers. This is unlikely, however, as the structural difference and the energy separation between the two conformers is minimal. As such, one would not expect any significant difference in the excited state landscapes between conformer A and B that would justify the order of magnitude difference observed between τ_1 and τ_2.

From the discussion above, it is clear that the addition of the carbonyl moiety, through the ester group functionality, has a profound impact on the observed photodynamics, with EF (containing an ester group) behaving radically differently upon photoexcitation when compared to MVP and ConA, which are not carbonyl compounds. While the addition of the carbonyl group in EF provided alternative relaxation pathways which avoided trapping of excited state population on the S_1 state to a certain extent (*cf.* MVP and ConA), the highly complex photodynamics of EF in vacuum, which likely involve a number of competing deactivation pathways, still results in long-lived excited states, potentially including reactive triplet states; the results presented in this chapter are, therefore, insufficient to draw any general conclusions regarding the suitability of carbonyl compounds, in general, as sunscreen molecules. Moreover, while we have proposed scenarios that may account for the present experimental results, we do not discount the possibility that there may be others. For example, photofragmentation is a viable pathway in EF, evidenced by the several fragments which are observed in its TOF mass spectrum (see section 3.17.II); attempts to obtain TR-IY transients for these were not successful due to very weak signal intensities. It would be interesting to evaluate the extent of photofragmentation processes in EF, especially given the impact such fragmentation would have on the photostability

and photoreactivity of this sunscreen molecule. In particular, it is extremely relevant to evaluate if any such fragmentation processes take place when EF interacts with a solvent, as this would be an environment more closely related to the sunscreen formulations in which EF is incorporated. In order to evaluate how, if at all, solvent interactions alter the photodynamics of EF we have just described, we turn our attention to our TEAS measurements for EF solvated in cyclohexane, a solvent which, given its weakly perturbative characteristics, should be most akin to a gas-phase environment, presenting a good first step between the two different environments (vacuum *vs.* solution).

EF in solution

Considering first the photoexcitation of EF at 316 nm, which in cyclohexane corresponds to initial population of the $S_1(1^1\pi\pi^*)$ state (based on our computational results), we discuss the assignment of the extracted time constants (summarised in Table 3.2) $\tau_1 = 168 \pm 40$ fs, $\tau_2 = 2.42 \pm 0.04$ ps and $\tau_3 = 15.4 \pm 0.3$ ps, as well as the $\tau_4 \gg$ ns time constant which was included to appropriately model the long-lived component observed in the TAS in Figure 3.9. Previous studies on related systems (*e.g.* coumaric acid) have shown that photoexcitation to the $S_1(1^1\pi\pi^*)$ state may induce rapid geometry relaxation which generally manifests as spectral changes in the TAS as the excited state population moves away from the Franck-Condon region.[65–67] Indeed, this behaviour is observed for EF: following photoexcitation of EF at 316 nm, subtle spectral changes are observed in the TAS (Figure 3.9), further evidenced by the initial EADS in Figure 3.11 (red line) evolving to the following EADS (green line in Figure 3.11) for which the peak is slightly red-shifted when compared to the previous EADS. It is reasonable, therefore, to assign τ_1 to an ultrafast geometry relaxation process taking place on the surface of the $S_1(1^1\pi\pi^*)$ state of EF. Given that EF is expected to retain planarity upon photoexcitation, as predicted by our computational studies (gas-phase, Figure 3.13), the geometry changes between the vertical Franck-Condon region and the $S_1(1^1\pi\pi^*)$ minimum are not expected to be drastic, justifying the very subtle spectral differences observed in our TEAS measurements.

Before assigning the intermediate time constants τ_2 and τ_3, we consider the origins of the long-lived absorption feature evidently present in the TAS for EF at $\Delta t = 2$ ns (~ 335 nm), shown in detail in Figure 3.12(a) and (b) (black line). These spectra at large pump-probe delays were compared with ΔUV/Vis spectra, recorded as described in section 3.2.7 and presented in Figure 3.12(a) and (b) (red line). The ΔUV/Vis spectra capture absorption signatures of long-lived species, such as any stable photoproducts that

may form upon irradiation. Since the difference spectra, consisting of a photoproduct absorption peak, strongly agree with the TAS feature at $\Delta t = 2$ ns, as shown in Figure 3.12, we may firmly assign the feature at 335 nm to the ultrafast formation of a stable photoproduct which persists beyond several minutes (since it is detected in ΔUV/Vis spectra after irradiation for several minutes). ^{1}H NMR studies, the results of which are shown in Figure 3.12 (bottom), confirm that the samples used in our experiments initially consist predominantly of EF in its *E*- or *trans*-isomer; ^{1}H NMR analysis also identifies the photoproduct observed in our TEAS and ΔUV/Vis spectra as the *Z*- or *cis*-isomer of EF. Thus, comparison of ΔUV/Vis with TAS spectra and ^{1}H NMR studies strongly suggest a *trans-cis* photoisomerisation mechanism takes place upon photoexcitation of EF solvated in cyclohexane, which is in accordance with observations for similar cinnamate based systems.[3,68] Furthermore, visual inspection of the TAS indicates that the appearance of the absorption feature here assigned to the *cis*-isomer occurs on a timescale approximately concurrent with the decay of the ESA and SE ($\tau_2 = 2.42 \pm 0.04$ ps), further suggesting that the excited state decay is indeed mediated by a photoisomerisation relaxation pathway. We thus assign τ_2 to both the decay of the $S_1(1^1\pi\pi^*)$ state and photoisomerisation; this timescale is also commensurate with previous reports on the photoisomerisation of molecules structurally similar to EF.[65,69–73] It is important to note, however, that solvent rearrangement is invariably occurring alongside other excited state relaxation processes and it is likely captured within the time constant τ_2.[65]

Finally, we note that the absorption feature corresponding to the *cis*-isomer initially appears red-shifted and broader than its analogue at $\Delta t = 2$ ns, which is indicative of the photoproduct being formed in a vibrationally hot electronic ground state. This narrowing and blue-shift over time of the *cis*-isomer absorption feature at 335 nm is evident in both the TAS shown in Figure 3.9 and the EADS for τ_3 *vs.* τ_4. We thus assign $\tau_3 = 15.4 \pm 0.3$ ps to vibrational cooling of the hot *cis*-isomer by transfer of energy to the solvent bath. The remaining time constant (and corresponding EADS) relates to the long-lived vibrationally relaxed *cis*-isomer, which persists beyond the temporal window of our experiments ($\tau_4 \gg$ ns).

While the formation of the *cis*-isomer has been shown to occur upon UV irradiation of other cinnamate derivatives, its detection in previous time-resolved studies has proven challenging due to spectral overlap between the *cis*-isomer and the phenoxyl radical species.[65,71,72,74,75] The formation of the phenoxyl radical in these systems has been

attributed to a two-photon ionisation stepwise mechanism by which a solvated electron and the corresponding cationic radical are produced, with the cationic radical quickly decaying to form the phenoxyl radical.[71] However, we found no evidence for the formation of phenoxyl radicals in solvated EF: the spectral feature corresponding to *cis*-isomer absorption in our experiments shows linear dependence on laser intensity (see section 3.7.IV), confirming its origin in single-photon phenomena (instead of the two-photon process required to generate the phenoxyl radical). The absence of a phenoxyl radical in EF may once again be explained by the intramolecular hydrogen bond between the OH and OMe groups hindering the photodissociation of the phenolic O—H bond. The effect of the intramolecular hydrogen bond in hindering excited state O—H bond photodissociation of EF, which we have invoked in interpreting our gas-phase results, has also been previously demonstrated in solution for a subunit of EF, guaiacol (2-methoxy-phenol).[76]

Based on our (gas-phase) computational results, photoexciting EF in cyclohexane with $\lambda_{pu} = 243$ nm is likely to access the $S_3(2^1\pi\pi^*)$ state. The TAS resulting from photoexcitation at this shorter wavelength displays similar features to the analogous 316 nm TAS, with the exception of the ultrafast time constant (labelled τ_1), previously assigned to geometry relaxation within the $S_1(1^1\pi\pi^*)$ state (*vide supra*) and lost at this higher pump energy. Whilst minor changes in photodynamics are not wholly unexpected, given that a different state is accessed upon photoexcitation at $\lambda_{pu} = 243$ nm, one would also anticipate that a dynamical process resulting in either geometry relaxation of the $S_3(2^1\pi\pi^*)$ state or IC between the $S_3(2^1\pi\pi^*)$ and $S_1(1^1\pi\pi^*)$ states (in keeping with Kasha's rule[77]) might be captured. Instead, the only excited state dynamics observed are the decay of the ESA due to photoisomerisation, occuring within τ_2, leading to the formation of the *cis*-isomer photoproduct. We therefore propose that, while IC between the $S_3(2^1\pi\pi^*)$ and $S_1(1^1\pi\pi^*)$ states could be occurring, this process is likely taking place on a timescale much faster than our instrument response, thus being undetectable in our experiments. The dynamics hereon are comparable to those measured following photoexcitation at 316 nm, with the *cis*-isomer absorption feature appearing (on a timescale of $\tau_2 = 1.38 \pm 0.04$ ps) red-shifted and broader than its absorption at $\Delta t = 2$ ns. As discussed earlier, this is indicative of the *cis*-isomer being formed in the vibrationally excited electronic ground state. The peak proceeds to narrow and blue-shift as the vibrationally hot electronic ground state *cis*-isomer cools on a timescale of $\tau_3 = 15.1 \pm 0.5$ ps. Finally, $\tau_4 \gg$ ns is attributed to the lifetime of the long-lived *cis*-isomer photoproduct.

The comparison between our results for EF in vacuum and in solution leads to the striking conclusion that even the weakly perturbing solvent cyclohexane has a drastic effect on the photodynamics of this cinnamate. When in vacuum, there is no experimental evidence that EF undergoes photoisomerisation and gas-phase calculations suggest that photoexcitaiton to the $S_1(v = 0)$ origin of EF provides insufficient energy for the system to overcome the energetic barrier to this process. When solvated in cyclohexane, on the other hand, EF readily undergoes *trans-cis* photoisomerisation (in a few picoseconds), which suggests that interaction with the solvent results in a reordering of the excited states of EF such that a $S_1(1^1\pi\pi^*)/S_0$ CI is accessible along the photoisomerisation reaction coordinate. Upon photoexciting solvated EF with 243 nm it may also be possible for photoisomerisation to take place *via* a $S_3(2^1\pi\pi^*)/S_0$ CI, as predicted by our computational studies for EF in a vacuum environment (Figure 3.14), instead of IC to the S_1 followed by photoisomerisation *via* a $S_1(1^1\pi\pi^*)/S_0$ CI. However, as our results have shown, solvent effects have a great impact on the photodynamics of EF and, therefore, it may not be suitable to interpret the results for solvated EF in light of calcultions that mimic a vacuum environment. Therefore, it can not be concluded from our studies whether photoisomerisation of EF in cyclohexane occurs *via* a $S_1(1^1\pi\pi^*)/S_0$ or a $S_3(2^1\pi\pi^*)/S_0$ CI, particularly at $\lambda_{pu} = 243$ nm. Nevertheless, the studies we have presented highlight how solvent interactions can have a profound effect on the photodynamics of a given sunscreen molecule, thus potentially altering its photoprotective abilities.

3.6   Conclusions

The excited state photodynamics of EF, a commercial sunscreen filter molecule, have been studied in vacuum using TR-IY spectroscopy and H^+ TR-VMI. MVP and ConA were also studied in vacuum so that the effects of increasing molecular complexity on the excited state dynamics could be evaluated. Upon photoexcitation to their respective $S_1(1^1\pi\pi^*)$ origin bands, MVP and ConA show similar excited state dynamics, which contrast to those of EF. The excited state dynamics of MVP and ConA both resemble the case of guaiacol:[35,46] population of a long-lived $S_1(1^1\pi\pi^*)$ state which persists beyond the temporal window of our measurements (> 900 ps). The resemblance of MVP and ConA to guaiacol extends to H-atom elimination, where there is no clear evidence of a high KE feature in the TKER spectra that could be attributed to O—H bond fission mediated by a

$\pi\sigma^*$ dissociative state; this is, therefore, considered not to be a viable relaxation pathway in these two systems. Despite weak H^+ TKER features being observed for EF, these are concluded not to originate from one-photon $\pi\sigma^*$ mediated photodissociation (*vide supra*) and, therefore, this relaxation pathway is also renounced for EF. The lack of evidence for O—H bond photodissociation in MVP, ConA and EF is explained by the presence of an intramolecular hydrogen bond which likely results in a substantial barrier to this dissociative decay pathway. Despite the similarities regarding O—H dissociation, the excited state photodynamics of EF are notably different from those of MVP and ConA, as they are described by three separate time constants (*c.f.* one main time constant in MVP and ConA). We propose that photoexcitation of EF to its $S_1(v = 0)$ origin ($\lambda_{pu} = 317.5$ nm in vacuum) initially prompts IC to the energetically similar $S_2(1^1n\pi^*)$ state, followed by IVR on both the $S_1(1^1\pi\pi^*)$ and $S_2(1^1n\pi^*)$ states, and finally ISC from both these onto nearby triplet states; a convolution of these processes would account for the $\tau_1 = 15 \pm 4$ ps time constant. IC is then proposed to occur down the manifold of triplet states towards the lowest triplet state, $T_1(1^3\pi\pi^*)$, within $\tau_2 = 148 \pm 47$ ps. We note that this second lifetime may also be due to ISC from the accessible singlet states. The third time constant would then account for the excited state lifetime of both the $S_1(1^1\pi\pi^*)$ and $S_2(1^1n\pi^*)$ states, the former of which fluoresces (with a lifetime of 6.9 ± 0.1 ns according to our total fluorescence measurements) whilst the latter might undergo photoreactions or ISC to S_0. The stark differences between MVP/ConA *vs.* EF highlight the role of the carbonyl moiety in introducing significant changes to the vibronic structure of a molecule which, consequently, have a profound impact on the observed photodynamics.

In order to evaluate how solvents may affect the photodynamics observed in vacuum, the excited state photodynamics for EF solvated in cyclohexane were also studied, using TEAS. In our TEAS measurements two different pump wavelengths were used: $\lambda_{pu} = 316$ nm accessed the $S_1(1^1\pi\pi^*)$ state, while $\lambda_{pu} = 243$ nm accessed the $S_3(2^1\pi\pi^*)$ state. Our results suggest that excitation to either state prompts *trans-cis* photoisomerisation which occurs on a picosecond timescale *via* a CI between the electronic excited state and the electronic ground state. The resulting *cis*-isomer is observed to be formed in a vibrationally excited ground state which proceeds to dispose of its energy to the surrounding solvent bath within ~ 15 ps. The *trans-cis* photoisomerisation observed for EF solvated in cyclohexane is in stark contrast with the photodynamics observed in vacuum, which reveals the potentially drastic effect that solvent interactions (even with a weakly

perturbing solvent such as cyclohexane) may have on the photodynamics of sunscreen molecules. Ultimately, the ultrafast photoisomerisation relaxation pathways induced by solvent interactions justify the use of EF in commercial sunscreen formulations, as it allows the molecule to dissipate the excess energy obtained from absorption of UV radiation. As we shall discuss in more detail in Chapter 5, however, it is important that the resulting isomer (in the case of EF, the *cis*-isomer) is non-toxic and an equally strong UV absorber to ensure continued, safe UV absorption.

The studies presented in this chapter have important implications in the context of pursuing a comprehensive understanding of the photodynamics of sunscreen molecules. Firstly, our results reinforce the conclusions from previous studies regarding the photoisomerisation of cinnamate-based sunscreens and are thus an important addition to a series of studies which allow for a trend in the behaviour of cinnamates to be established. Moreover, the comparison between our results in vacuum and in solution highlight the fact that solvent interactions may have profound effects on the photodynamics of sunscreen molecules, having the potential to completely alter their photoprotective characteristics. Interestingly, however, the sensitivity of a given sunscreen molecule's photodynamics on its surroundings depends on the system under study, as we will demonstrate with the sunscreen systems discussed in the next chapter. Such differences in behaviour are of great significance to the development of sunscreen formulations, as they may dictate the characteristics of the delivery vehicle of the sunscreen formulation, *i.e.* the characteristics of the environment within which the desired sunscreen molecule is to be employed.

3.7   Supporting Information and Additional Data

I TEAS fitting residuals

(a) TEAS fitting residuals for $\lambda_{\mathrm{pu}} = 316$ nm.   (b) TEAS fitting residuals for $\lambda_{\mathrm{pu}} = 243$ nm.
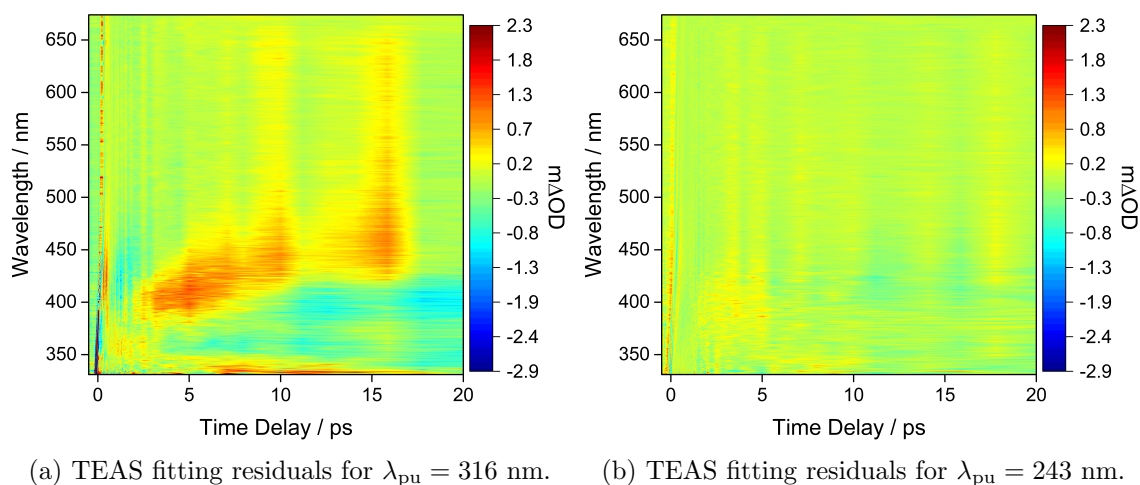
Figure 3.16: Residual signal resulting from the difference between the sequential global fit and the raw data for EF in cyclohexane with an excitation wavelength of (a) 316 nm and (b) 243 nm.

II Time-of-flight mass spectrum and off-resonance TKER spectrum for EF

(a) TOF-MS of EF.   (b) Off-resonance TKER spectrum of EF.
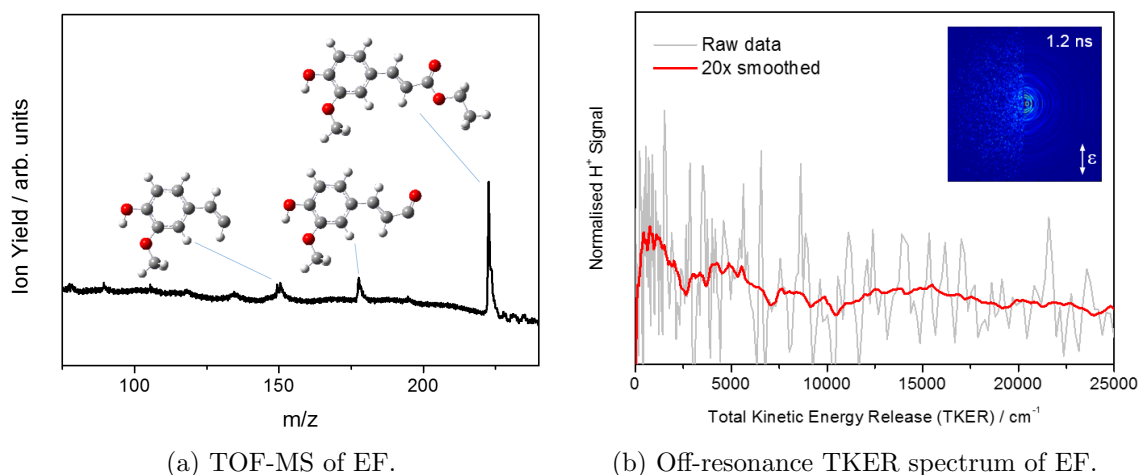
Figure 3.17: (a) Time-of-flight mass spectrum (TOF-MS) of EF showing evidence for fragmentation of the side chain of the molecule resulting in various photofragments. (b) TKER spectrum of EF off-resonance with the 2s ←1s transition in atomic hydrogen ($\lambda_{\mathrm{pr}} = 245$ nm), obtained for photoexcitation with $\lambda_{\mathrm{pu}} = 317.5$ nm. The Boltzmann distribution feature observed in other TKER spectra of EF is still present, further supporting the assignment of this feature to multiphoton dissociative ionisation processes.

III ¹H NMR spectra of EF
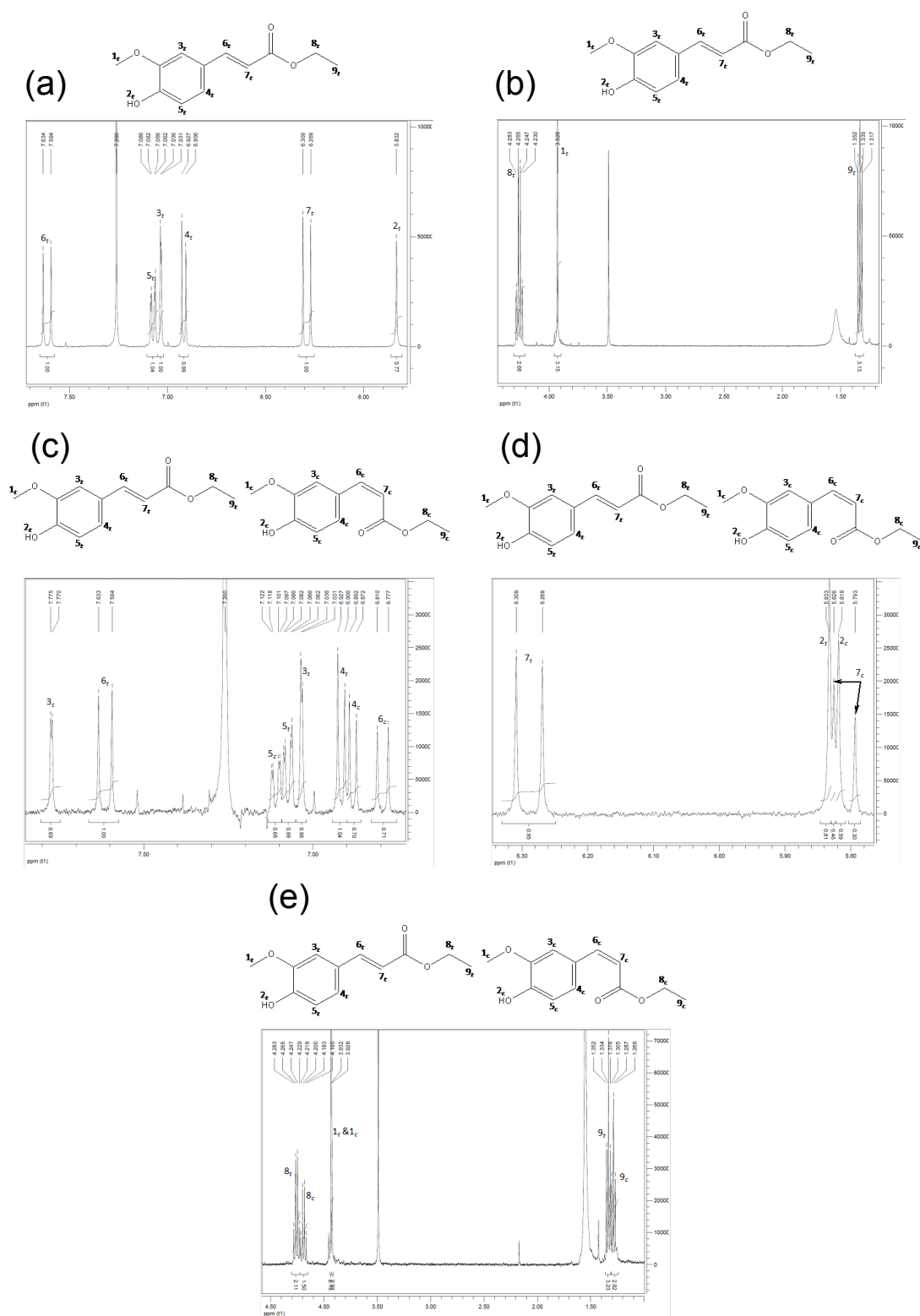
Figure 3.18: ¹H NMR spectra of EF. (a) and (b) are expanded sections of the ¹H NMR spectrum of *trans*-EF before irradiation; (c), (d) and (e) are expanded sections of the ¹H NMR spectrum of *trans*-EF after irradiation, showing peak contributions from the *cis*-isomer. All peaks are assigned in the figure and labelled in the respective insets.
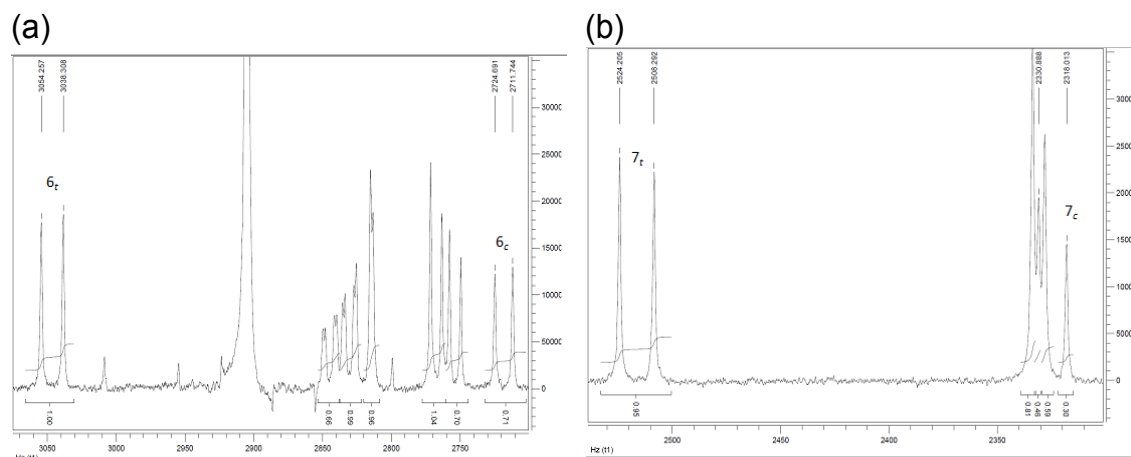
Figure 3.19: ^{1}H NMR spectra of *trans*-EF after irradiation, with the peaks associated with the hydrogens at positions (a) 6 and (b) 7, labeled in Hertz, highlighting the $^3J_{H-H}$ coupling for the *trans*-isomer (16 Hz) and the *cis*-isomer (13 Hz).

IV Power dependence of TEAS signal

(a) Power dependence for $\lambda_{pu} = 316$ nm.   (b) Power dependence for $\lambda_{pu} = 243$ nm.
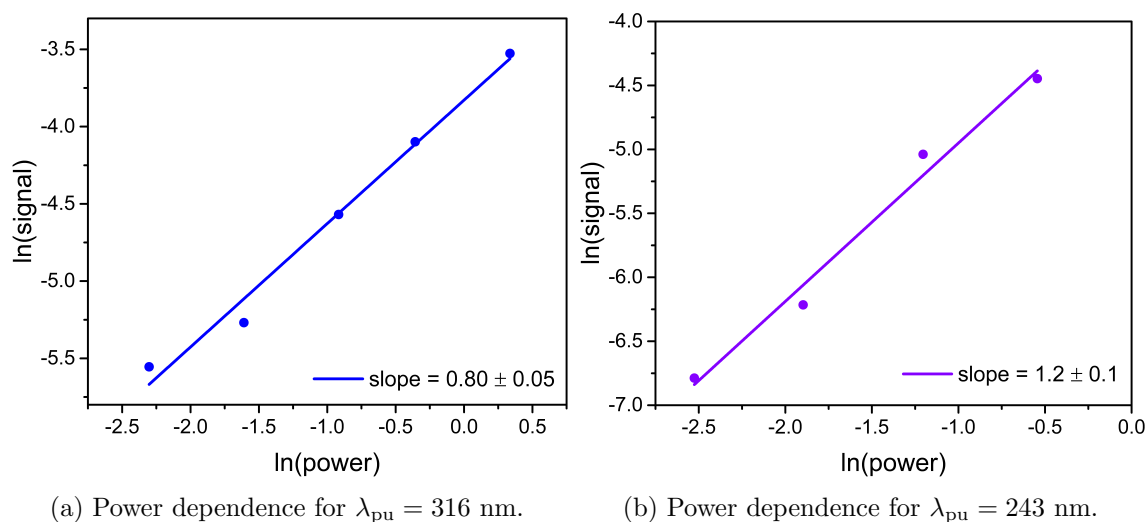
Figure 3.20: Power dependence of signal intensity at $\Delta t = 2$ ns, integrated over the wavelength range 333 – 343 nm (corresponding to the absorption of the *cis*-isomer), following photoexcitation at (a) 316 nm and (b) 243 nm.

3.8   References

[1] Maslin, D. L. Do sunscreens protect us? *International Journal of Dermatology* **53**, 1319–1323 (2014).

[2] Tan, E. M. M., Hilbers, M. & Buma, W. J. Excited-state dynamics of isolated and

microsolvated cinnamate-based UV-B sunscreens. *The Journal of Physical Chemistry Letters* **5**, 2464–2468 (2014).

[3] Peperstraete, Y. *et al.* Bottom-up excited state dynamics of two cinnamate-based sunscreen filter molecules. *Physical Chemistry Chemical Physics* **18**, 28140–28149 (2016).

[4] Shimada, D. *et al.* Nonradiative decay dynamics of methyl-4-hydroxycinnamate and its hydrated complex revealed by picosecond pumpprobe spectroscopy. *Physical Chemistry Chemical Physics* **14**, 8999–9005 (2012).

[5] Promkatkaew, M. *et al.* Absorption and emission spectra of ultraviolet b blocking methoxy substituted cinnamates investigated using the symmetry-adapted cluster configuration interaction method. *The Journal of Chemical Physics* **131**, 1–10 (2009).

[6] Pattanaargson, S. & Limphong, P. Stability of octyl methoxycinnamate and identification of its photo-degradation product. *International Journal of Cosmetic Science* **23**, 153–160 (2001).

[7] Choquenet, B., Couteau, C., Paparis, E. & Coiffard, L. J. M. Interest of ferulic acid ethyl ester in photoprotective creams: Measure of efficacy by *in vitro* method. *Natural Product Research* **22**, 1467–1471 (2008).

[8] Nazaré, A. C. *et al.* Ethyl ferulate, a component with anti-inflammatory properties for emulsion-based creams. *Molecules* **19**, 8124–8139 (2014).

[9] Kikuzaki, H., Hisamoto, M., Hirose, K., Akiyama, K. & Taniguchi, H. Antioxidant properties of ferulic acid and its related compounds. *Journal of Agricultural and Food Chemistry* **50**, 2161–2168 (2002).

[10] Dean, J. C., Kusaka, R., Walsh, P. S., Allais, F. & Zwier, T. S. Plant sunscreens in the UV-B: Ultraviolet spectroscopy of jet-cooled sinapoyl malate, sinapic acid, and sinapate ester derivatives. *Journal of the American Chemical Society* **136**, 14780–14795 (2014).

[11] Rodrigo, C. P., James, W. H. & Zwier, T. S. Single-conformation ultraviolet and infrared spectra of jet-cooled monolignols: p-coumaryl alcohol, coniferyl alcohol, and sinapyl alcohol. *Journal of the American Chemical Society* **133**, 2632–2641 (2011).

[12] Karsili, T. N. V., Marchetti, B., Ashfold, M. N. R. & Domcke, W. *Ab Initio* study of

potential ultrafast internal conversion routes in oxybenzone, caffeic acid, and ferulic acid: Implications for sunscreens. *The Journal of Physical Chemistry A* **118**, 11999–12010 (2014).

[13] Imanbaew, D., Gelin, M. F. & Riehn, C. Rotational and vibrational dynamics in the excited electronic state of deprotonated and protonated fluorescein studied by time-resolved photofragmentation in an ion trap. *Structural Dynamics* **3**, 4, 043211.1-043211.13 (2016).

[14] Even, U., Jortner, J., Noy, D. & Lavie, N. Cooling of large molecules below 1 k and he clusters formation. *The Journal of Chemical Physics* **112**, 8068–8071 (2000).

[15] Eppink, A. T. J. B. & Parker, D. H. Velocity map imaging of ions and electrons using electrostatic lenses: Application in photoelectron and photofragment ion imaging of molecular oxygen. *Review of Scientific Instruments* **68**, 3477–3484 (1997).

[16] Roberts, G. M., Nixon, J. L., Lecointre, J., Wrede, E. & Verlet, J. R. R. Toward real-time charged-particle image reconstruction using polar onion-peeling. *Review of Scientific Instruments* **80**, 1–17 (2009).

[17] Regan, P. M., Langford, S. R., Orr-Ewing, A. J. & Ashfold, M. N. R. The ultraviolet photodissociation dynamics of hydrogen bromide. *The Journal of Chemical Physics* **110**, 281–288 (1999).

[18] Zwier, T. S. Laser spectroscopy of jet-cooled biomolecules and their water-containing clusters: Water bridges and molecular conformation. *The Journal of Physical Chemistry A* **105**, 8827–8839 (2001).

[19] Walsh, P. S., Buchanan, E. G., Gord, J. R. & Zwier, T. S. Solvent-mediated internal conversion in diphenoxyethane-$(H_2O)_n$ clusters, n = 2-4. *The Journal of Chemical Physics* **142**, 1–10 (2015).

[20] Walsh, P. S., Buchanan, E. G., Gord, J. R. & Zwier, T. S. Binding water to a PEG-linked flexible bichromophore: IR spectra of diphenoxyethane-$(H_2O)_n$ clusters, n = 2-4. *The Journal of Chemical Physics* **142**, 1–10 (2015).

[21] Dean, J. C. *et al.* Conformation-specific spectroscopy and populations of diastereomers of a model monolignol derivative: Chiral effects in a triol chain. *The Journal of Physical Chemistry A* **115**, 8464–8478 (2011).

[22] van Stokkum, I. H. M., Larsen, D. S. & van Grondelle, R. Global and target analysis of time-resolved spectra. *Biochimica et Biophysica Acta: Bioenergetics* **1657**, 82–104 (2004).

[23] Snellenburg, J. J., Laptenok, S., Seger, R., Mullen, K. M. & van Stokkum, I. H. M. Glotaran: A java-based graphical user interface for the r package TIMP. *Journal of Statistical Software* **49**, 1–22 (2012).

[24] Würth, C., Grabolle, M., Pauli, J., Spieles, M. & Resch-Genger, U. Relative and absolute determination of fluorescence quantum yields of transparent samples. *Nature Protocols* **8**, 1535–1550 (2013).

[25] Frisch, M. J. *et al.* Gaussian 09, Revision E.01 (2009).

[26] Yanai, T., Tew, D. P. & Handy, N. C. A new hybrid exchange-correlation functional using the Coulomb-attenuating method (CAM-B3LYP). *Chemical Physics Letters* **393**, 51–57 (2004).

[27] Petersson, G. A., Bennett, A., Tensfeldt, T. G., Al-Laham, M. A. & Shirley, W. A. A complete basis set model chemistry. I. the total energies of closed-shell atoms and hydrides of the first-row elements. *The Journal of Chemical Physics* **89**, 2193–2218 (1988).

[28] Klene, M. & Robb, M. A. Parallel implementation of the CI-vector evaluation in full CI/CAS-SCF. *The Journal of Chemical Physics* **113**, 5653–5665 (2000).

[29] Siegbahn, E. M. A new direct C1 method for large CI expansions in a small orbital space. *Chemical Physics Letters* **109**, 417–423 (1984).

[30] Werner, H.-J., Knowles, P. J., Knizia, G., Manby, F. R. & Schütz, M. Molpro: a general purpose quantum chemistry program package. *WIREs Comput Mol Sci* **2**, 242–253 (2012).

[31] Werner, H.-J. *et al.* MOLPRO, version 2010.1, a package of ab initio programs (2010). See.

[32] Andersoon, K., Malmqvist, P.-A. & Roos, B. O. Second-order perturbation theory with a complete active space self-consistent field reference function. *The Journal of Chemical Physics* **96**, 1218–1226 (1992).

[33] Dunning, T. H. Gaussian basis sets for use in correlated molecular calculations. I.

the atoms boron through neon and hydrogen. *The Journal of Chemical Physics* **90**, 1007–1023 (1989).

[34] Roberts, G. M. & Stavros, V. G. The role of $\pi\sigma^*$ states in the photochemistry of heteroaromatic biomolecules and their subunits: insights from gas-phase femtosecond spectroscopy. *Chemical Science* **5**, 1698–1722 (2014).

[35] Chatterley, A. S. *et al.* Manipulating dynamics with chemical structure: probing vibrationally-enhanced tunnelling in photoexcited catechol. *Physical Chemistry Chemical Physics* **15**, 6879–6892 (2013).

[36] Dixon, R. N., Oliver, T. A. A. & Ashfold, M. N. R. Tunnelling under a conical intersection: Application to the product vibrational state distributions in the uv photodissociation of phenols. *The Journal of Chemical Physics* **134**, 194303.1–194303.10 (2011).

[37] Ashfold, M. N. R. *et al.* Exploring nuclear motion through conical intersections in the UV photodissociation of phenols and thiophenol. *Proceedings of the National Academy of Sciences of the United States of America* **105**, 12701–12706 (2008).

[38] Sobolewski, A. L., Domcke, W., Dedonder-Lardeux, C. & Jouvet, C. Excited-state hydrogen detachment and hydrogen transfer driven by repulsive $^1\pi\sigma^*$: A new paradigm for nonradiative decay in aromatic biomolecules. *Physical Chemistry Chemical Physics* **4**, 1093–1100 (2002).

[39] Owrutsky, J. C., Raftery, D. & Hochstrasser, R. M. Vibrational relaxation dynamics in solutions. *Annual Review of Physical Chemistry* **45**, 519–555 (1994).

[40] Aßmann, J., Kling, M. & Abel, B. Watching photoinduced chemistry and molecular energy flow in solution in real time. *Angewandte Chemie International Edition* **42**, 2226–2246 (2003).

[41] Lucarini, M., Pedrielli, P. & Pedulli, G. F. Bond dissociation energies of o—h bonds in substituted phenols from equilibration studies. *The Journal of Organic Chemistry* **61**, 9259–9563 (1996).

[42] Nix, M. G. D., Devine, A. L., Cronin, B., Dixon, R. N. & Ashfold, M. N. R. High resolution photofragment translational spectroscopy studies of the near ultraviolet photolysis of phenol. *The Journal of Chemical Physics* **125**, 133318.1–133318.13 (2006).

[43] Young, J. D. *et al.* Relaxation dynamics of photoexcited resorcinol: internal conversion versus h atom tunnelling. *Physical Chemistry Chemical Physics* **16**, 550–562 (2014).

[44] King, G. A., Oliver, T. A. A., Dixon, R. N. & Ashfold, M. N. R. Vibrational energy redistribution in catechol during ultraviolet photolysis. *Physical Chemistry Chemical Physics* **14**, 3338–3345 (2012).

[45] Chatterley, A. S. *et al.* Manipulating dynamics with chemical structure: probing vibrationally-enhanced tunnelling in photoexcited catechol. *Physical Chemistry Chemical Physics* **15**, 6879–6892 (2013).

[46] Young, J. D. *et al.* Towards understanding photodegradation pathways in lignins: The role of intramolecular hydrogen bonding in excited states. *The Journal of Physical Chemistry Letters* **5**, 2138–2143 (2014).

[47] Chang, X.-P., Li, C.-X., Xie, B.-B. & Cui, G. Photoprotection mechanism of p-methoxy methylcinnamate: A CASPT2 study. *The Journal of Physical Chemistry A* **119**, 11488–11497 (2015).

[48] Turro, N. J., Ramamurthy, V. & Scaiano, J. C. *Modern Molecular Photochemistry of Organic Molecules* (University Science Books, USA, 2010).

[49] Coyle, J. D. & Carless, H. A. J. Selected aspects of photochemistry: I Photochemistry of carbonyl compounds. *Chemical Society Reviews* **1**, 465–480 (1972).

[50] Ledger, M. B. & Porter, G. Primary photochemical processes in aromatic molecules. *Journal of the Chemical Society, Faraday Transactions 1 Physical Chemistry in Condensed Phases* **68**, 539–553 (1972).

[51] Yabumoto, S., Shigeto, S., Lee, Y. & Hamaguchi, H. Ordering, interaction, and reactivity of the lowlying $n\pi^*$ and $\pi\pi^*$ excited triplet states of acetophenone derivatives. *Angewandte Chemie* **49**, 9201–9205 (2010).

[52] El-Sayed, M. A. Triplet state. its radiative and nonradiative properties. *Accounts of Chemical Research* **1**, 8–16 (1968).

[53] Arasaki, Y. & Takatsuka, K. Pump-probe photoionization study of the passage and bifurcation of a quantum wave packet across an avoided crossing. *Physical Review Letters* **90**, 248303.1–248303.4 (2003).

[54] Ou, Q. & Subotnik, J. E. Electronic relaxation in benzaldehyde evaluated via TD-DFT and localized diabatization: Intersystem crossings, conical intersections, and phosphorescence. *The Journal of Physical Chemistry C* **117**, 19839–19849 (2013).

[55] El-Sayed, M. A. Spinorbit coupling and the radiationless processes in nitrogen heterocyclics. *The Journal of Chemical Physics* **38**, 2834–2838 (1963).

[56] Marian, C. M. Spinorbit coupling and intersystem crossing in molecules. *WIREs Computational Molecular Science* **2**, 187–203 (2012).

[57] Beljonne, D., Shuai, Z., Pourtois, G. & Bredas, J. L. Spinorbit coupling and intersystem crossing in conjugated polymers: a configuration interaction description. *The Journal of Physical Chemistry A* **105**, 3899–3907 (2001).

[58] Spighi, G., Gaveau, M.-A., Mestdagh, J.-M., Poissona, L. & Soep, B. Gas phase dynamics of triplet formation in benzophenone. *Physical Chemistry Chemical Physics* **16**, 9610–9618 (2014).

[59] Schalk, O. *et al.* Internal conversion versus intersystem crossing: What drives the gas phase dynamics of cyclic α,β-enones? *The Journal of Physical Chemistry A* **118**, 2279–2287 (2014).

[60] Moore, R., Doany, F. E., Heilweil, E. J. & Hochstrasser, R. M. Energy redistribution in large molecules. direct study of intramolecular relaxation in the gas phase with picosecond gating. *Faraday Discussions of the Chemical Society* **75**, 331–340 (1983).

[61] Lower, S. K. & El-Sayed, M. A. The triplet state and molecular electronic processes in organic molecules. *Chemical Reviews* **66**, 199–241 (1966).

[62] Fang, W.-H. & Phillips, D. L. The crucial role of the $S_1/T_2/T_1$ intersection in the relaxation dynamics of aromatic carbonyl compounds upon n$\to \pi^*$ excitation. *ChemPhysChem* **3**, 889–892 (2002).

[63] Diau, E. W.-G., Kötting, C. & Zewail, A. H. Femtochemistry of Norrish Type-I Reactions: I. Experimental and Theoretical Studies of Acetone and Related Ketones on the S_1 Surface. *ChemPhysChem* **2**, 273–293 (2001).

[64] Lobsiger, S. *et al.* Intersystem crossing rates of S_1 state keto-amino cytosine at low excess energy. *The Journal of Chemical Physics* **143**, 234301.1–234301.12 (2015).

[65] Kuramochi, H., Takeuchi, S. & Tahara, T. Ultrafast structural evolution of pho-

toactive yellow protein chromophore revealed by ultraviolet resonance femtosecond stimulated raman spectroscopy. *The Journal of Physical Chemistry Letters* **3**, 2025–2029 (2012).

[66] Kovalenko, S. A., Schanz, R., Hennig, H. & Ernsting, N. P. Cooling dynamics of an optically excited molecular probe in solution from femtosecond broadband transient absorption spectroscopy. *The Journal of Chemical Physics* **115**, 3256–3273 (2001).

[67] Ojima, S., Miyasaka, H. & Mataga, N. Femtosecond-picosecond laser photolysis studies, on the dynamics of excited charge-transfer complexes in solution. 1. charge separation processes in the course of the relaxation from the excited franck-condon state of 1,2,4,5-tetracyanobenzene in benzene and methyl-substituted benzene solutions. *The Journal of Physical Chemistry* **94**, 4147–4152 (1990).

[68] Baker, L. A. *et al.* Ultrafast photoprotecting sunscreens in natural plants. *The Journal of Physical Chemistry Letters* **7**, 56–61 (2016).

[69] Espagne, A., Changenet-Barret, P., Plaza, P. & Martin, M. M. Solvent effect on the excited-state dynamics of analogues of the photoactive yellow protein chromophore. *The Journal of Physical Chemistry A* **110**, 3393–3404 (2006).

[70] Espagne, A., Paik, D. H., ChangenetBarret, P., Martin, M. M. & Zewail, A. H. Ultrafast photoisomerization of photoactive yellow protein chromophore analogues in solution: Influence of the protonation state. *ChemPhysChem* **7**, 1717–1726 (2006).

[71] Larsen, D. S. *et al.* Incoherent manipulation of the photoactive yellow protein photocycle with dispersed pump-dump-probe spectroscopy. *Biophysical Journal* **87**, 1858–1872 (2004).

[72] Vengris, M. *et al.* Ultrafast dynamics of isolated model photoactive yellow protein chromophores: "chemical perturbation theory" in the laboratory. *The Journal of Physical Chemistry B* **109**, 4197–4208 (2005).

[73] Changenet-Barret, P. *et al.* Early molecular events in the photoactive yellow protein: role of the chromophore photophysics. *Photochemical & Photobiological Sciences* **3**, 823–829 (2004).

[74] Challice, J. S. & Williams, A. H. Paper chromatographic separation and behavior of the *cis-* and *trans*-isomers of cinnamic acid derivatives. *Journal of Chromatography A* **21**, 357–362 (1966).

[75] Foley, S. *et al.* Singlet oxygen quenching and the redox properties of hydroxycinnamic acids. *Free Radical Biology and Medicine* **26**, 1202–1208 (1999).

[76] Greenough, S. E. *et al.* Solvent induced conformer specific photochemistry of guaiacol. *Physical Chemistry Chemical Physics* **16**, 16187–16195 (2014).

[77] Kasha, M. Characterization of electronic transitions in complex molecules. *Discussions of the Faraday Society* **9**, 14–19 (1950).

4 Anthranilates

'I never am really satisfied that I understand anything; because, understand it well as I may, my comprehension can only be an infinitesimal fraction of all I want to understand about the many connections and relations which occur to me.'

Ada Lovelace (1815–1852)

This chapter will be divided into two main sections, for the sake of clarity. In section 4.1, we will focus on the differences between the photodynamics observed for the anthranilates in vacuum and in solution. Section 4.2 will then introduce evidence for quantum beats in the photoelectron spectra of the anthranilates studied and explore the mechanisms responsible for the initial steps of intramolecular energy redistribution in these sunscreen molecules. While each section will be introduced and discussed separately, in section 4.3 we will discuss the implications of both parallel studies to the ultrafast photodynamics of the anthranilates in the context of their use in commercial sunscreen formulations.

4.1   Photodynamics in Vacuum *vs.* in Solution

4.1.1   Overview

In the last chapter, a sunscreen molecule with antioxidant properties, ethyl ferulate, was used as the case study for an analysis of the photodynamics of cinnamate-based sunscreens. Through the studies presented in Chapter 3 and parallel studies by other authors, the photodynamics of cinnamates are now well-established to involve *trans-cis* photoisomerisation in solution, in stark contrast with the observations in gas-phase. Solvent effects are thus found to have a great impact on the energy dissipation mechanisms of cinnamate-based sunscreens. However, analogous information is not available for anthranilates (*ortho*-aminobenzoates) despite their biological relevance and their applications in the food and cosmetics industry.[3–7] Methyl anthranilate (MA, Figure 4.1), for example, is a food grade flavour and fragrance additive used in personal care products[8] which is also a precursor to menthyl anthranilate (MenA, commercial name Meradimate, Figure 4.1), a sunscreen component approved by the US Food and Drug Administration.[9] In general, the anthranilates

are considered to be a photostable class of sunscreens due to the intramolecular hydrogen bond facilitated by the *ortho* position of the NH_2 group with respect to the ester substituent (see Figure 4.1), which is thought to hinder the degradation of the anthranilates upon exposure to UV.[10] Interestingly, however, under anaerobic conditions, a photodegradation mechanism was found to occur for MA upon UV exposure.[11] Under aerobic (more realistic) conditions, an appreciable quantum yield of fluorescence ($\sim 0.376 - 0.549$) was observed in various solvents,[12] as well as a 280 μs triplet state lifetime in aqueous solution.[8] Smaller quantum yields for singlet oxygen sensitisation have also been reported for MA.[8] Such radiative and non-radiative processes persist in MenA, which presents large quantum yields for fluorescence (0.64 ± 0.06 in ethanol)[9] and intersystem crossing (0.34 in ethanol at room temperature).[13] The presence of triplet states in solvated MenA was confirmed by Kikuchi *et al.*[13] by using a triplet quencher; the lifetime of the triplet state was determined to be 2.36 s in ethanol at 77 K.[13]

In light of the available literature, it seems that photoexcited MA and MenA dissipate excess energy *via* radiative decay, which is perceivably not ideal in a sunscreen molecule, as discussed in more detail in Chapter 1. The radiative decay observed in MA and MenA is at odds with other sunscreen molecules, such as the cinnamates discussed in Chapter 3, which tend to decay to their ground electronic states *via* non-radiative internal conversion (IC) on an ultrafast timescale.[14–16] It is now well understood that ultrafast IC between electronic states is facilitated by conical intersections (CIs, discussed in Chapter 1) which arise when certain nuclear motions (*e.g.* isomerisation and bond-stretches) drive distinct electronic states towards degeneracies in configuration space.[17] In related sunscreen molecules, many CI geometries — ranging from *trans-cis* isomerisation to ring deformations, for example — have been identified as likely contributors driving ultrafast IC from the electronic excited to ground state.[14–16,18,19] For some sunscreen molecules, notably oxybenzone, isomerisation is preceded by an *enol-keto* type hydrogen atom motion; *keto* oxybenzone then isomerises back to ground state enol oxybenzone.[15] Such tautomerisation processes typically occur on ultrafast timescales, *i.e.* on much shorter timescales than those probed in the aforementioned MA and MenA studies.

The non-unity luminescence quantum yield of MenA suggests that other, non-radiative, photophysical processes are also involved in its relaxation mechanisms. Ultrafast spectroscopy techniques were employed in the work described in this chapter to identify the ultrafast photophysics taking place in photoexcited MenA and hence further inform on its
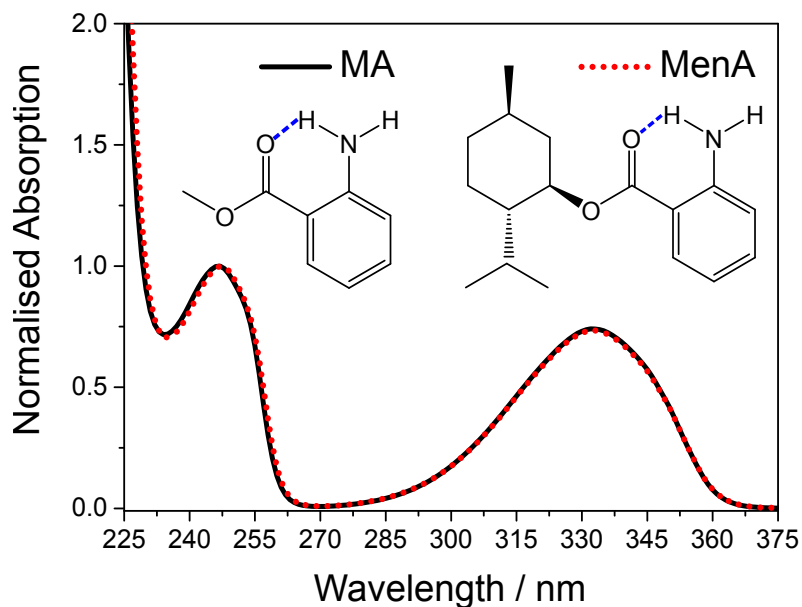
Figure 4.1: UV/Vis absorption spectrum of methyl anthranilate (MA, black solid line) and menthyl anthranilate (MenA, red dotted line) in cyclohexane. The molecular structures of each molecule are also shown, with the intramolecular hydrogen bond indicated with a blue dashed line.

suitability as a sunscreen ingredient. In keeping with a bottom-up approach, by which the effects of increasing molecular complexity are evaluated, both MA and MenA were studied. Moreover, spectroscopic techniques were employed both in vacuum and in solution to evaluate the environmental (solvent) effects on the intrinsic photodynamics of these molecules. Computational studies were also performed to complement the experimental measurements and provide further detail on the topography of the electronic states of the molecules studied. This work highlights the importance of investigative studies targeting the intrinsic molecular and electronic characteristics that provide sunscreen molecules with their photoprotection capabilities.

4.1.2   Experimental Methods

4.1.2.1   Absorption Spectra

The UV/Vis absorption spectra of MA (Alfa Aesar, 99%) and MenA (Aldrich, 98%), shown in Figure 4.1, were obtained using a PerkinElmer Lambda 850 UV/Vis spectrophotometer. The sample of each molecule was prepared by dissolving MA or MenA in cyclohexane (99%, Fisher Scientific) with a concentration of approximately 10^{-6} M.

4.1.2.2   Time-Resolved Ion Yield (TR-IY)

The time-resolved ion yield (TR-IY) set up used in this work has been described previously in Chapter 2, section 2.2.1.1, and is therefore only briefly described here, with further details on particular experimental conditions provided where necessary. The fundamental 800 nm output from the Ti:Sapphire oscillator (Spectra-Physics Tsunami) and regenerative amplifier (Spectra-Physics Spitfire XP) was split into three beams, each with ~ 1 mJ per pulse. One of these beams was used to pump an optical parametric amplifier (Light Conversion, TOPAS-C) to generate pump pulses centred either at $\lambda_{pu} = 300$ nm (4.13 eV), $\lambda_{pu} = 315$ nm (3.94 eV), or $\lambda_{pu} = 330$ nm (3.76 eV). These wavelengths were chosen to sample the UVA and UVB regions of the solar spectrum and the broad absorption feature shown in Figure 4.1, while maintaining adequate signal to noise ratios. A second laser beam of ~ 1 mJ per pulse pumped a separate TOPAS-C which was used to generate 260 nm probe pulses. The pump and probe pulses were temporally delayed with respect to each other by reflecting the pump off a hollow corner gold retroreflector mounted on a motorised delay stage allowing a maximum pump-probe temporal delay of $\Delta t = 1.2$ ns.

The two laser beams, pump and probe, intersected a molecular beam which was produced by seeding the target molecules, heated to 50°C (MA) or 90°C (MenA), into helium (~ 3 bar). The gaseous mixture was then expanded into vacuum ($\sim 10^{-7}$ mbar) using an Even-Lavie pulsed solenoid valve as described in Chapter 2, section 2.2.1. At the point of intersection, λ_{pu} excited the species in the molecular beam and λ_{pr} ionised any excited (or photodissociated) species. The resulting ions were focused onto a detector, consisting of two microchannel plates (MCPs) coupled to a phosphor screen, by three ion optics similar to the set up described by Eppink and Parker (see Chapter 2, section 2.2.1.2).[21] The current output from the front of the phosphor screen, gated in ion flight time over the mass channel of each parent ion (MA^+ and $MenA^+$), was measured on a digital oscilloscope (LeCroy LT372 Waverunner) and integrated as a function of Δt in order to produce TR-IY transients. These transients were then modelled using a sum of exponential decays convoluted with a Gaussian instrument response; more details regarding kinetic fits can be found Chapter 2, section 2.4.3. Power dependence studies were performed to ensure linear signal intensity *vs.* laser power, *i.e.* that the observed dynamics are due to single-photon photoexcitation. Separate measurements were taken with the polarisations of the pump and probe beams parallel and perpendicular to each other in order to calculate the

resulting magic angle equivalent transient.[20]

Deuterated MA (d_1-MA and d_2-MA, in which either one or two hydrogens on the amine group were substituted by deuterium atoms, respectively) was produced by stirring MA in d_4-methanol for approximately 72 hours under anhydrous N_2. The solvent was then removed under high vacuum (0.5 mbar) in an ice bath ($\sim$ 0°C); the product was immediately stored under anhydrous N_2 prior to use. The H/D exchange was inferred by the loss or reduction of ^{1}H NMR signal corresponding to the hydride position due to the formation of one or two N—D bonds (see section 4.4).

4.1.2.3   Velocity Map Imaging (VMI) of H-atoms

Velocity map imaging (VMI) was used to monitor any H-atom elimination from the molecules of interest, following excitation. Any photodissociated H-atoms were resonantly ionised to form H^+ with a 243 nm probe pulse set at $\Delta t = 1.2$ ns relative to the pump pulse. H^+ ions were then accelerated by an electrostatic potential towards a position-sensitive detector such that ions with the same initial velocity are mapped onto the same point on the detector, as discussed in Chapter 2, section 2.2.1.2.[21] The original 3D H^+ distribution is reconstructed from the measured 2D projection using a polar onion peeling algorithm[22] (see Chapter 2, section 2.2.1.2) from which the desired 1D total kinetic energy release (TKER) spectrum can be derived using an appropriate energy calibration factor and by considering the co-fragment's mass. The spectrometer is calibrated using the TKER spectrum of photolysed HBr (see Chapter 2, section 2.4, for further details).[23]

4.1.2.4   Transient Electronic Absorption Spectroscopy (TEAS)

The TEAS setup used in the present experiments has been detailed previously, in Chapter 2, section 2.2.2, and is therefore only briefly summarised here. TEAS measurements were obtained from separate $\sim$ 1 mM solutions of MA and MenA in both cyclohexane (VWR, > 99%) and methanol (Sigma-Aldrich, $\sim$ 99.6%). These solutions were recirculated through a flow cell (Harrick Scientific) consisting of two CaF_2 windows separated by 100 μm thick PTFE spacers. Transient absorption spectra (TAS) were obtained by photoexciting the sample using the same TOPAS-C output as for gas-phase experiments, *i.e.* 300 nm, 315 nm and 330 nm pump pulses, with fluences of 1 – 2 mJ cm^{-2} per pulse. The probe pulses consisted of a broadband white light continuum (330 – 675 nm), generated

by focusing a fraction of the third 800 nm fundamental beam into a 2 mm thick CaF_2 window. The relative polarisation between the pump and probe beams was held at magic angle (54.7°) by using a $\lambda/2$ waveplate. The time delay between the pump and probe pulses was controlled using a hollow corner gold retroreflector mounted on a motorised translation stage in the probe beam path; maximum $\Delta t = 2$ ns. The setup used in these experiments provides an instrument response function with a full width at half maximum of ~ 80 fs. TAS for each time delay correspond to the difference in probe pulse intensities passing through sequentially excited (I^*) and non-excited (I_0) sample prepared by a mechanical chopper in the pump beam path (see Chapter 2, sections 2.2.2 and 2.4.2).

The dynamical information from the TAS was extracted from the TAS by employing the global fitting methods described in Chapter 2, section 2.4.3, using the Glotaran software package,[24] and assuming a sequential model (*e.g.* A$\xrightarrow{\tau_1}$B$\xrightarrow{\tau_2}$C$\xrightarrow{\tau_3}$D). The quality of the fits was evaluated upon inspection of the resulting residuals shown in section 4.1.4.3.

4.1.3   Computational Methods

Computational studies were carried out by Dr. Tolga Karsili (Temple University, USA). Using Molpro2010.1,[25] relaxed potential energy curves (PECs) along the neutral singlet ground state (S_0), the first electronically excited singlet state (S_1), and the cation doublet ground state (D_0^+) were produced using the state-averaged complete active space self-consistent field (SA-CASSCF)[26,27] method coupled to a cc-pVDZ basis set.[28] These PECs were obtained by fixing the H-bonded amino-centred N—H stretch (henceforth N—H_{bound}) at various values ($R_{N—Hb}$) and allowing the remaining internal degrees of freedom to relax to their respective minima. The active space comprised ten electrons in eight orbitals (10/8), including three π, two n and three π^* valence orbitals. Following separate S_0, S_1 and D_0^+ relaxations across $R_{N—Hb}$, the energies of the S_0 and S_1 states, the first and second excited triplet states (T_1 and T_2) and the D_0^+ state were computed within each relaxation subset using the complete active space second-order perturbation theory (CASPT2), based on a SA-CASSCF reference wavefunction and a cc-pVDZ basis set. A standard imaginary level shift of 0.5 E_H was used to aid convergence and mitigate the involvement of intruder states.

Two PECs were produced for the S_1 state: one corresponding to the localised excitation (S_1LE) and a second corresponding to charge transfer (S_1CT). The S_1LE PEC

describes the case for which charge remains localised on the ring upon photoexcitation ($\pi_{\text{ring}} \rightarrow \pi^*_{\text{ring}}$): the vertical excitation geometry is fixed, and the PECs calculated by changing only the coordinate of interest. The S_1CT PEC describes instead the case for which, upon photoexcitation, charge is dislocated from the ring π orbital to the carbonyl π^* orbital ($\pi_{\text{ring}} \rightarrow \pi^*_{\text{carbonyl}}$), *i.e.* the vertical excitation geometry is relaxed, upon which the S_1 state acquires charge transfer character (see Figure 4.9(a)); the PECs are then calculated using this relaxed geometry and altering only the coordinate of interest. Similarly, two PECs associated with the S_0 of MA were calculated: the S_0 PEC was produced by optimising both the geometry and electronic configuration of the S_0 state of MA; the S_0 charge transfer (S_0CT) PEC was produced by optimising the electronic configuration of the S_0 state while keeping the geometry fixed to that of the S_1CT state at each corresponding $R_{\text{N—Hb}}$ value.

Following computations along $R_{\text{N—Hb}}$, analogous calculations of the S_0 and S_1 states were undertaken to assess the potential energy topography between $R_{\text{N—Hb}} = 1.5$ Å to a low-energy S_0/S_1 CI using the CASPT2/cc-pVDZ level of theory. The intermediate geometries between $R_{\text{N—Hb}} = 1.5$ Å and the S_0/S_1 CI were constructed using a linear interpolation of internal coordinates (LIIC). The CI was optimised using the SA-CASSCF/6-31G(d) level of theory in the Gaussian 09 computational package[29] with a reduced active space of six electrons in six orbitals (6/6).

4.1.4   Results

4.1.4.1   Time-Resolved Ion Yield (TR-IY)

TR-IY measurements of MA and MenA were taken following photoexcitation at 315 nm and 330 nm. These measurements yielded similar mono-exponential TR-IY transients, shown in Figure 4.2, both with decay lifetimes considerably longer than the temporal window of these experiments ($\gg 1.2$ ns). In contrast, photoexcitation of MA at 300 nm results in a faster mono-exponential decay, as shown in green in Figure 4.3, with a lifetime $\tau_{\text{H}} \sim 1700 \pm 200$ ps (where the superscript H refers to the hydrogenated MA sample).

Deuterated MA, both d_1-MA and d_2-MA, were also photoexcited with 300 nm and the TR-IY transients are presented in Figure 4.3, in red and blue, respectively. It is apparent that deuteration of MA yields slower photodynamics. However, two caveats must be con-
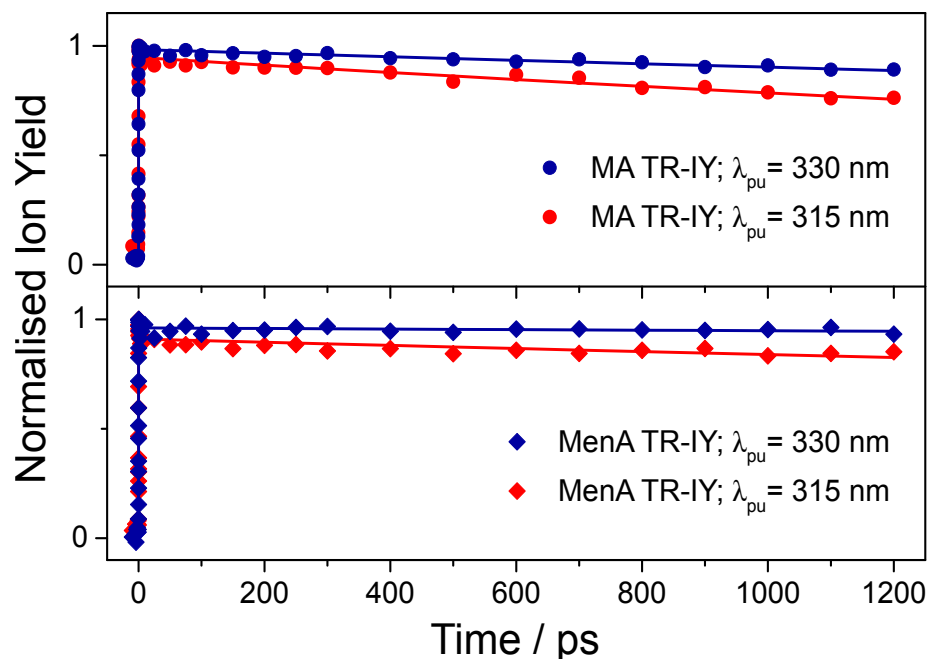
Figure 4.2: TR-IY transients resulting from the excitation of MA (top, circles) and MenA (bottom, diamonds) at 315 nm (red) and 330 nm (blue). Solid lines correspond to kinetic fits.
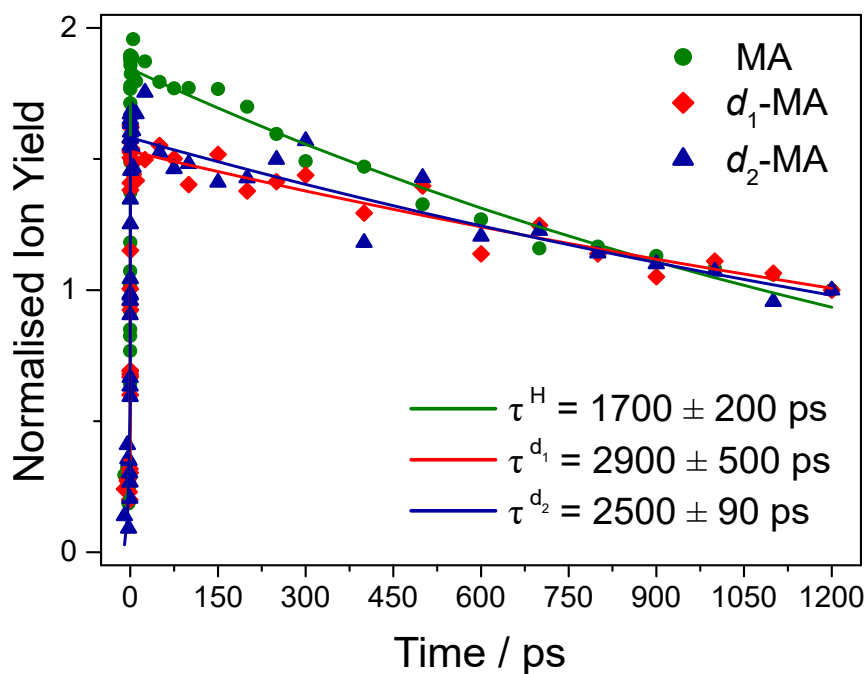

Figure 4.3: TR-IY transients resulting from the excitation of MA (green circles), d_1-MA (red diamonds) and d_2-MA (blue triangles) at 300 nm. Data were normalised to their last data point. Solid lines correspond to the kinetic fits used to extract lifetimes.

sidered in the interpretation of our TR-IY results for deuterated MA. Firstly, the lifetimes extracted from kinetic fits are still outside the temporal window of our experiments and hence the ratio between the lifetimes of MA and d_1/d_2-MA is the focus of our discussion, rather than their absolute values. Secondly, we note the low signal-to-noise ratio of our data, particularly in the d_2-MA transient — this is due to a combination of exciting MA at the tail of its absorption (see Figure 4.1) and the high levels of D/H exchange experienced during the course of our measurements. Bearing these caveats in mind, we nevertheless quote the extracted lifetimes as follows: $\tau_{d_1} \sim 2900 \pm 500$ ps and $\tau_{d_2} \sim 2500 \pm 90$ ps (where τ_{d_1} and τ_{d_2} refer to the decay time constants of d_1-MA and d_2-MA, respectively). An average kinetic isotope effect (KIE) of 1.5 ± 0.4 is thus determined from the TR-IY time constants extracted from d_1-MA and d_2-MA.

4.1.4.2 Velocity Map Imaging (VMI) of H-atoms

The H-atom TKER spectra of MA at $\lambda_{\mathrm{pu}} = 300$ nm, 315 nm and 300 nm are presented in Figure 4.4. While photoexcitation of MA with both 330 nm and 315 nm yields essentially featureless TKER spectra, a small feature at $\sim 19\ 000$ cm^{-1} is observed in the TKER spectrum of MA at $\lambda_{\mathrm{pu}} = 300$ nm. Analogous spectra for MenA, at pump wavelengths of 330 nm and 315 nm, are shown in Figure 4.5; in both cases, a broad TKER feature at high TKER values is present. The origins of these features will be discussed in section 4.1.5.

4.1.4.3 Transient Electronic Absorption Spectroscopy (TEAS)

All TAS data, evolution associated difference spectra (EADS) and residuals are shown in Figures 4.6 for MA and 4.7 for MenA. A summary of the time constants extracted for both MA and MenA upon photoexcitation with 315 nm and 330 nm can be found in Table 4.1.

Cyclohexane

The results of MA in the weakly perturbing solvent cyclohexane are presented first, as this should be most akin to the environment in vacuum. The TAS for photoexcitation of MA with both 315 nm and 330 nm (see Figure 4.6) display similar spectral features and their temporal evolutions are also analogous. As such the results for both wavelengths shall be discussed concurrently. The TAS consist of four features that are apparent after the initial excitation. The negative feature at 385 nm corresponds to stimulated emission (SE) from the initial electronic excited state, which is in good agreement with the measured

fluorescence emission wavelength of MA (in ethanol).[30] Alongside this SE, there is a broad excited state absorption (ESA), again from the initial excited state, spanning 420 nm to 675 nm, with three distinct peaks at 455 nm, 525 nm and 580 nm. The dynamics of MA in cyclohexane, from black to red in Figure 4.6(a)(ii) and (b)(ii), can be described simply as a narrowing of the excited state spectrum (*e.g.* the decrease in intensity around 625 nm) and a slight blue shift of all features (most easily seen in the negative feature at ~ 380 nm) within τ_1, with excited state population then persisting beyond 2 ns (τ_2). A third time component is also necessary to successfully fit the TAS; this is shown in Figure 4.6(a)(ii) and (b)(ii) as the blue EADS and is associated with the decay time constant $\tau_3 > 2$ ns. Equivalent spectra for MenA are very similar (see Figure 4.7): features are observed within the same wavelength ranges and qualitatively the same time dependent behaviour
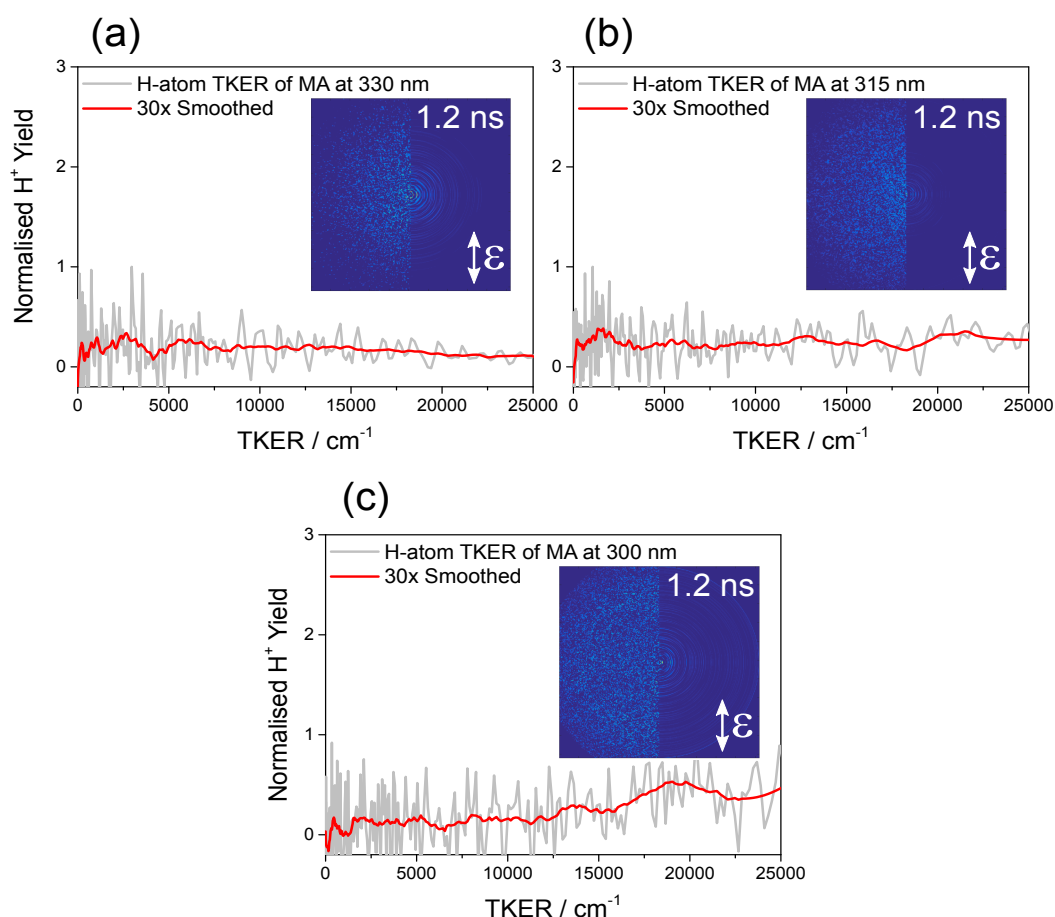
Figure 4.4: H-atom TKER spectra for MA at (a) 330 nm, (b) 315 nm and (c) 300 nm, probed resonantly with 243 nm for H^+ detection, at $\Delta t = 1.2$ ns. Inset: H^+ velocity map image from which the TKER spectra of MA were derived, raw image (left half) together with a reconstructed slice through the centre of the original 3D ion distribution (right half). The vertical white arrow indicates the electric field polarisation vector of the pump laser pulse, ε_{pu}.
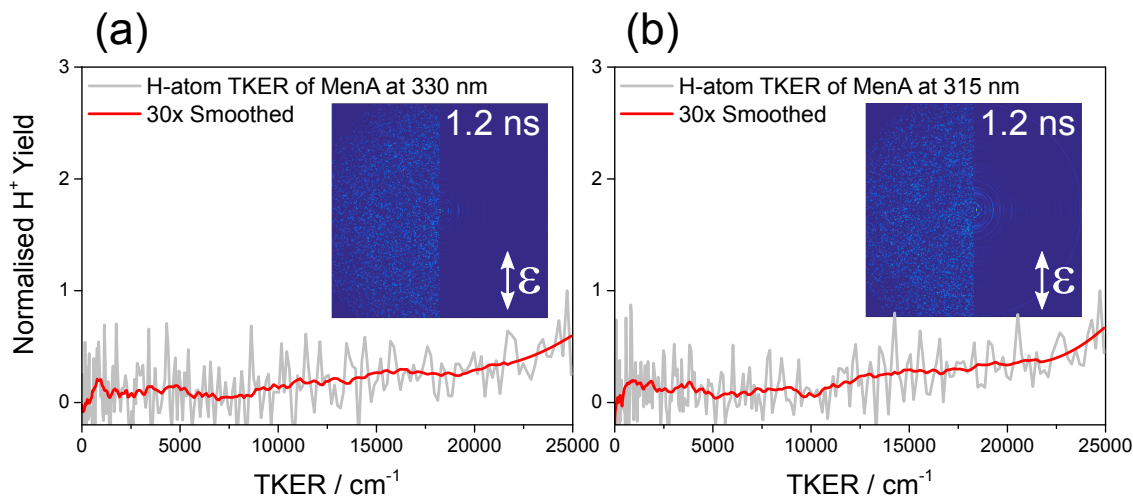
Figure 4.5: H-atom TKER spectra for MenA at (a) 330 nm and (b) 315 nm, probed resonantly with 243 nm for H^+ detection, at $\Delta t = 1.2$ ns. Inset: H^+ velocity map image from which the TKER spectra of MenA were derived, raw image (left half) together with a reconstructed slice through the centre of the original 3D ion distribution (right half). The vertical white arrow indicates the electric field polarisation vector of the pump laser pulse, ε_{pu}.

is observed, albeit with some differences in extracted time constants, as summarised in Table 4.1.

Methanol

TEAS measurements were also carried out in methanol, a more perturbing solvent than cyclohexane given its polarity. The TAS for MA and MenA at both excitation wavelengths also display similar features in methanol (see Figures 4.6 and 4.7). The time constants obtained for MA and MenA in methanol are summarised in Table 4.1. In all cases (both molecules and pump wavelengths), the TAS consist of three main features which appear upon photoexcitation. A SE feature from the first excited electronic state is observed at 400 nm, which is in good agreement with the reported fluorescence emission wavelength of MenA in ethanol.[13] The broad ESA in methanol extends from 430 nm to 675 nm, with prominent peaks at 450 nm and 600 nm. Similar to the observation in cyclohexane, the dynamics of both MA and MenA in methanol can be described as a narrowing and spectral shift of the observed features, as discussed above. However, τ_3 is not required in methanol to properly fit the data.
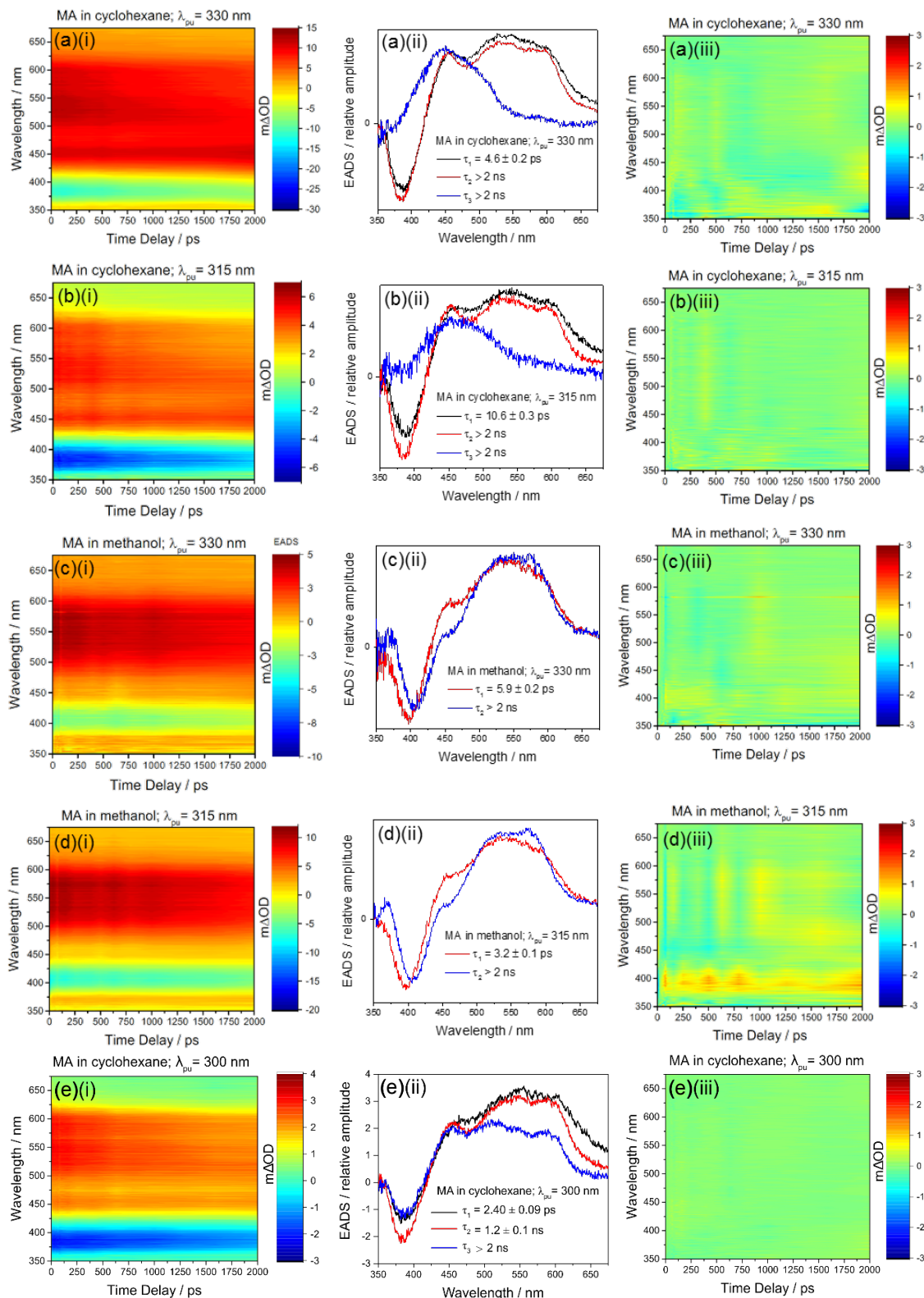
Figure 4.6: TEAS results for MA in cyclohexane after photoexcitation at (a) 330 nm, (b) 315 nm and (e) 300 nm, and in methanol after photoexcitation at 330 nm (c) and 315 nm (d). For each set of data (i) are the raw TAS spectra, (ii) the corresponding EADS and (iii) fit residuals.
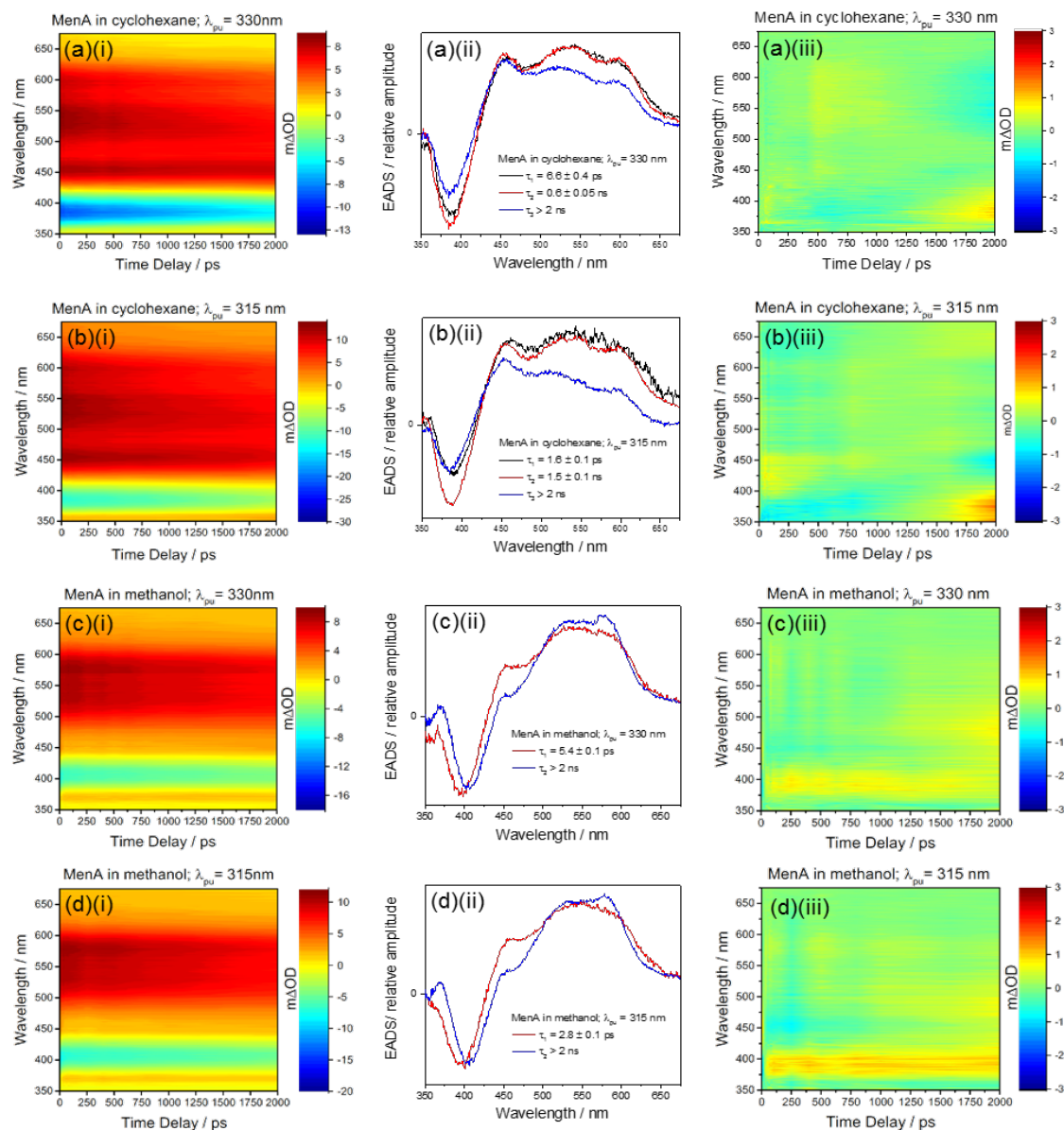
Figure 4.7: TEAS results for MenA in cyclohexane after photoexcitation at 330 nm (a) and 315 nm (b), and in methanol after photoexcitation at 330 nm (c) and 315 nm (d). For each set of data, (i) are the raw TAS spectra, (ii) the corresponding EADS and (iii) fit residuals.

Table 4.1: Summary of the time constants extracted from the TEAS results for MA and MenA, in cyclohexane (CHX) and methanol (MeOH), at both excitation wavelengths used. In vacuum time constants are also presented for comparison.

λ_{pu}	315 nm	330 nm
MA		
Vacuum	$\tau_1 > 1.2$ ns	$\tau_1 > 1.2$ ns
CHX	$\tau_1 = 10.6 \pm 0.3$ ps $\tau_2 > 2$ ns $\tau_3 > 2$ ns	$\tau_1 = 4.6 \pm 0.2$ ps $\tau_2 > 2$ ns $\tau_3 > 2$ ns
MeOH	$\tau_1 = 3.2 \pm 0.1$ ps $\tau_2 > 2$ ns	$\tau_1 = 5.9 \pm 0.2$ ps $\tau_2 > 2$ ns
MenA		
Vacuum	$\tau_1 > 1.2$ ns	$\tau_1 > 1.2$ ns
CHX	$\tau_1 = 1.6 \pm 0.1$ ps $\tau_2 = 1.5 \pm 0.1$ ns $\tau_3 > 2$ ns	$\tau_1 = 6.6 \pm 0.4$ ps $\tau_2 = 0.6 \pm 0.05$ ns $\tau_3 > 2$ ns
MeOH	$\tau_1 = 2.8 \pm 0.1$ ps $\tau_2 > 2$ ns	$\tau_1 = 5.4 \pm 0.1$ ps $\tau_2 > 2$ ns

4.1.4.4 Computational Studies

The relaxed potential energy curves (PECs) for several excited states of MA were calculated, namely: the ground state (locally excited, S_0LE, and charge transfer, S_0CT), the first electronically excited singlet state (locally excited, S_1LE, and charge transfer, S_1CT), the first and second excited triplet states (T_1 and T_2) and the cation doublet ground state (D_0^+). These PECs are presented in Figure 4.8 and a summary of the vertical excitation energies calculated for the S_1, S_1CT, T_1 and T_2 states of MA is given in Table 4.2.

The PECs in Figure 4.8(a) were calculated as a function of length of the intramolecular N—H bond, $R_{\text{N—Hb}}$, from $R_{\text{N—Hb}} = 1$ Å (*keto* tautomer) to $R_{\text{N—Hb}} = 1.5$ Å (*enol* tautomer). The S_0 optimised geometry, corresponding to the *keto* tautomer, is also displayed in Figure 4.8(a), along with the proton transfer (*enol*) geometry. These PECs reveal a lack
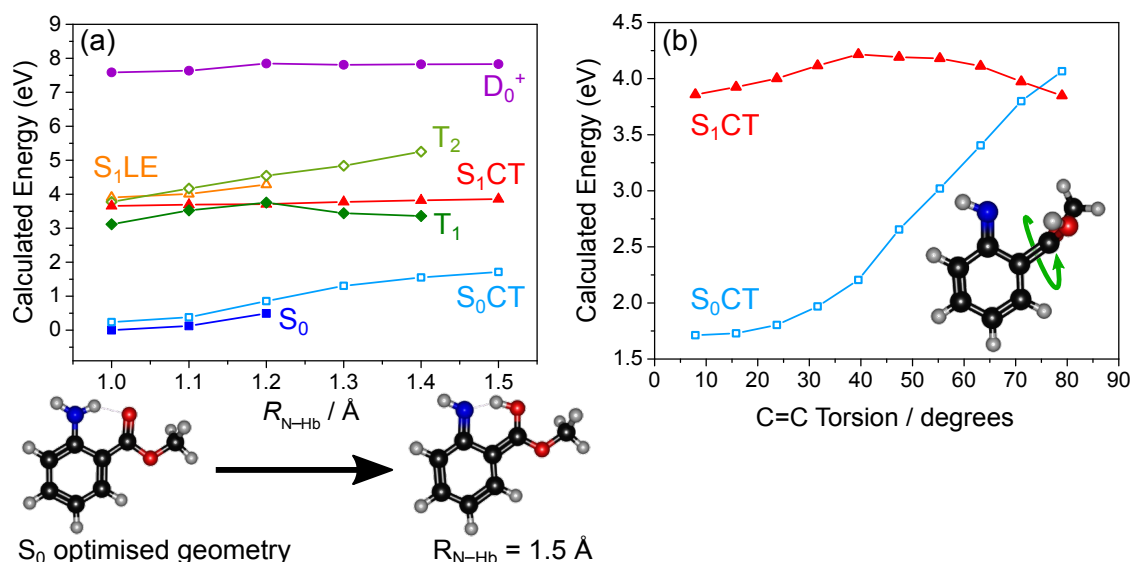
Figure 4.8: (a) PECs for various electronic states of MA along the $R_{\text{N—Hb}}$ coordinate, for which a hydrogen migrates from the amine group towards the neighbouring carbonyl oxygen. Below the plot, the S_0 optimised geometry (*keto*, left) and the proton transfer geometry, *i.e.* at $R_{\text{N—Hb}} = 1.5$ Å (*enol*, right), are also shown. Presented here are the ground state (S_0, blue squares) and the charge transfer ground state (S_0CT, hollow light blue squares), the locally excited first singlet state (S_1LE, hollow orange triangles) and first excited singlet state, which has charge transfer character (S_1CT, red triangles), the first and second triplet states (T_1, green diamonds, and T_2, hollow light green diamonds, respectively) and the first cationic surface (D_0^+, purple circles). (b) PECs for the S_0CT and S_1CT states along the coordinate corresponding to the twisting motion around the C—C bond connecting the phenyl ring and the ester substituent, starting at the $R_{\text{N—Hb}} = 1.5$ Å geometries towards the S_1/S_0 CI. This motion is illustrated by the inset on the lower right corner.

of driving force for complete proton transfer on both the S_0 and S_1CT states, evidenced by their increase in molecular potential energy along the $R_{\text{N—Hb}}$ coordinate (1.5 eV rise for S_0 and 0.21 eV for S_1CT). The PECs for MA presented in Figure 4.8(a) also suggest a strong degeneracy of the S_1CT and T_1 states (near $R_{\text{N—Hb}} = 1.2$ Å).

Table 4.2: Calculated vertical excitation energies for some of the singlet and triplet excited states of MA.

Electronic state of MA	Vertical excitation energy / cm^{-1}	Vertical excitation energy / eV
$S_1(\pi\pi^*)$	31 534	3.91
$T_2(\pi\pi^*)$	30 324	3.76
$S_1CT(\pi\pi^*)$	29 518	3.66
$T_1(\pi\pi^*)$	25 163	3.12

PECs for the S_0CT and S_1CT states of MA from the geometries at $R_{N—Hb} = 1.5$ Å and then along the C=C twisting motion coordinate (*i.e.* rotation of the ester group with respect to the phenyl ring) were also produced and are displayed in Figure 4.8(b). While the upper limit barrier to this twisting motion in MA was calculated to be 0.4 eV above the S_1CT energy at $R_{N—Hb} = 1.5$ Å, this motion was also found to lead to a S_1/S_0 CI. The calculated geometry at this CI is also presented in the inset of Figure 4.8(b). Additional computational results are presented in Figure 4.9, including *i)* PECs along the $S_1LE \rightarrow S_1CT$ coordinate; *ii)* the N—H bond dissociation coordinate; and *iii)* O—Me bond dissociation coordinate.

4.1.5   Discussion

In broad terms, all the dynamics observed for both MA and MenA at various pump energies and various environments are long-lived and strikingly similar, particularly in vacuum: the TR-IY transients, albeit qualitatively faster at higher pump energy, all show lifetimes > 1.2 ns. In solution, there are other differences brought on by solvent-solute interaction. The behaviour of MA and MenA in cyclohexane is described by three time constants, rather than the two required to fit the data in methanol (*vide infra* for further discussion). Nevertheless, regardless of environment or pump wavelength, both MA and MenA display similar photodynamics, always with a long-lived excited state which is observed to persist for at least 1 – 2 ns. Moreover, the UV/Vis spectra for MA and MenA (Figure 4.1) are strikingly similar, indicating that the additional menthyl unit in MenA does not perturb the low energy electronic states of the system, as could be expected given the non-perturbative character of the menthyl unit (*i.e.* since the menthyl unit does not provide any extra conjugation or otherwise significantly alter the electronic density of MA). Therefore, the dynamics of MA and MenA will be discussed jointly throughout this section, with attention being drawn to any differences between them as appropriate.

For MA, the first band in the UV/Vis spectrum, ranging from 360 nm to 290 nm, is assigned to the $S_1(\pi\pi^*)$ state based on the calculated vertical excitation energies (Table 4.2). Hence, excitation within the 330 nm $\geq \lambda_{pu} \geq$ 300 nm pump wavelength range (3.76 – 4.13 eV) used in these experiments is likely to exclusively populate the S_1 state. In the gas-phase, photoexcitation at either 315 nm or 330 nm yields a mono-exponential TR-IY transient that does not recover to the baseline within the timescale observable in these experiments, *i.e.* 1.2 ns. When MA is photoexcited at 300 nm, however, there is a marked
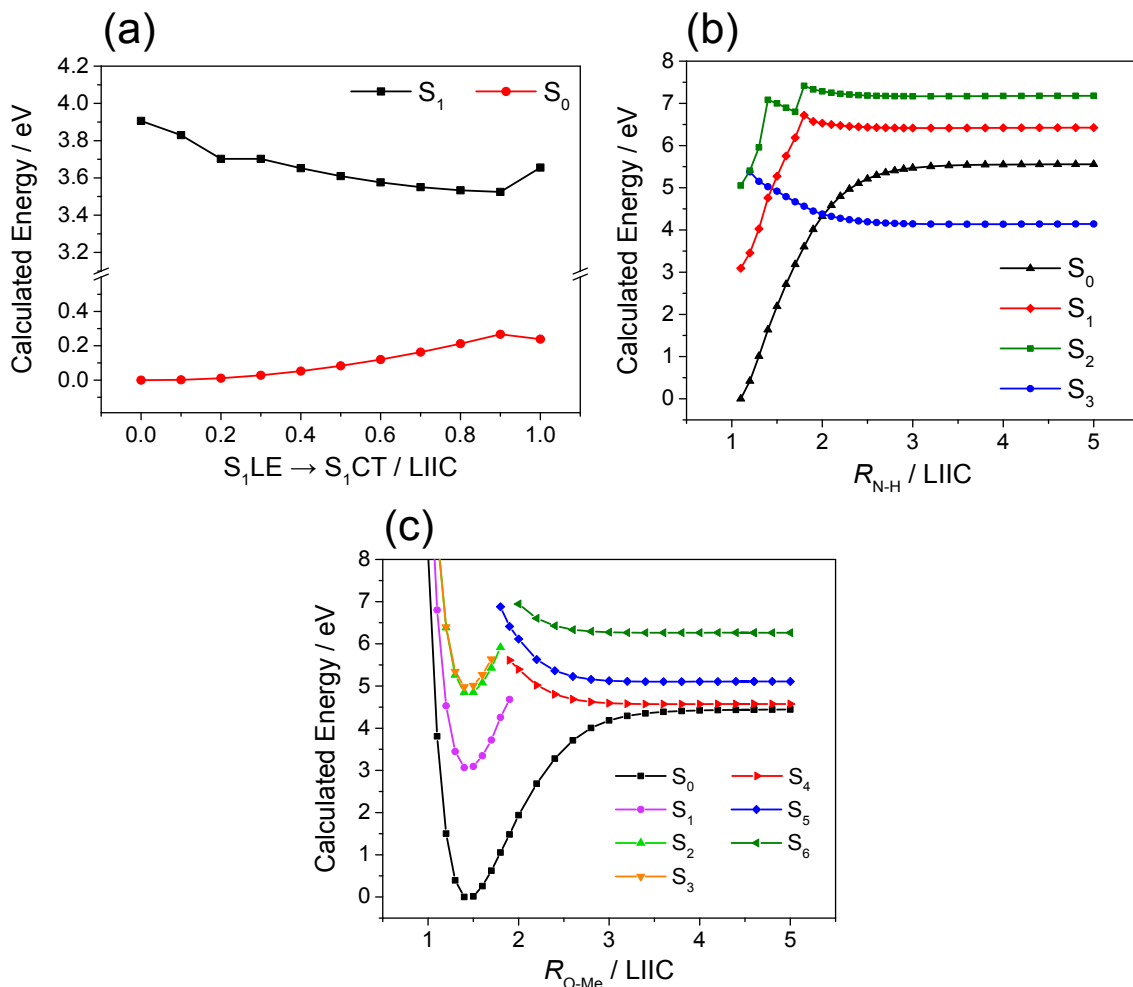
Figure 4.9: (a) PECs for the S_0 (red circles) and S_1 (black squares) states of MA, from the S_1 locally excited (S_1LE) state to the S_1 charge transfer (S_1CT) state (*i.e.* along the S_1LE → S_1CT coordinate). The points at LIIC = 0 correspond to the optimised geometries of the locally excited states (S_0LE and S_1LE), while those at LIIC = 1 correspond to the optimised geometries of the charge transfer states (S_0CT and S_1CT). Also presented in this figure are the PECs for several excited states of MA along the (b) N—H$_{free}$ and (c) O—Me bond dissociation coordinates. All intermediate geometries were produced by means of the linear interpolation in internal coordinates (LIIC). The computational results in (b) and (c) suggest that any N—H$_{free}$ or O—Me dissociative states are too high in energy to be accessed by the pump wavelengths used in these experiments, *i.e.* 330 nm (3.7 eV), 315 nm (3.9 eV) and 300 nm (4.1 eV). N—H$_{free}$ or O—Me bond dissociation are, therefore, not considered viable relaxation pathways for MA.

difference in the resulting transient, in that a single lifetime of $\tau_H \sim 1700 \pm 200$ ps is now extracted (with some certainty, since the half-life is within our temporal probe window). The long-lived photodynamics observed suggest that any fast relaxation pathways from the S_1 state are negligible and that photoexcited population is trapped in the S_1 state for at least a nanosecond.

Considering the amine group of MA, one of the intuitive ultrafast decay pathways to consider would be N—H_{free} (non-intramolecularly bound) bond dissociation, as has been observed in aniline.[31] Experimentally, however, resonantly probing H-atoms (with a 243 nm probe) upon photoexcitation of MA with with both 330 nm and 315 nm results in featureless TKER spectra, as shown in Figure 4.4. This lack of TKER features strongly suggests that N—H bond fission mediated by dissociative state(s) is not a viable decay pathway for MA within the 1.2 ns time window that can be probed in the reported experiments. Upon photoexcitation with 300 nm, however, the TKER spectrum of MA does show a small feature at $\sim 19\,000$ cm^{-1}. The maximum TKER expected for H-atoms resulting from N—H bond fission of photoexcited aniline-type molecules is given by:[31]

$$\text{TKER} = h\nu_{pu} - E_{int} - D_0(N\text{—}H) \tag{4.1}$$

where $h\nu_{pu}$ is the energy of the pump photon used to photoexcite the molecule of interest, E_{int} is the internal energy of the radical co-fragment (zero for maximum TKER) and $D_0(N\text{—}H)$ is the N—H bond strength, which has a value of $\sim 31\,630$ cm^{-1} in aniline.[32] These calculations would place the maximum TKER for H-atoms from MA photoexcited with $\lambda_{pu} = 300$ nm at 1703 cm^{-1}, much lower energy than the observed feature ($\sim 19\,000$ cm^{-1}). Given these energetic considerations, the feature observed at $\sim 19\,000$ cm^{-1} in the TKER spectrum of MA photoexcited at 300 nm is assigned to multiphoton effects, and we thus conclude that the TKER spectra for MA (Figure 4.4) shows no evidence for H$^+$ signal that could be attributable to the formation of single-photon induced N—H_{free} bond fission along a dissociative excited state.[31] This same reasoning and energetic considerations apply for the the high TKER features observed in the analogous spectra for MenA, shown in Figure 4.5; we therefore conclude that N—H_{free} bond photodissociation is also not a viable decay pathway for MenA. Furthermore, computational studies on MA, shown in Figure 4.9(b), reveal a large barrier to N—H_{free} bond fission relative to the S_1 minimum, further suggesting that this is not a viable relaxation mechanism for MA. Analogous calculations predict a bound first excited state along the O—Me

bond fission coordinate for MA (Figure 4.9(c)), which also rules out O—Me bond photo-sdissociation as a viable relaxation pathway for MA. We note, however, that dissociation could still occur on timescales beyond the temporal window of the experiments reported herein. Prefulvenic pathways are also unlikely to be responsible for the photodynamics observed in our experiments since they are usually accessed at energies much higher than our photoexcitation range.[31,33]

In other systems structurally similar to MA/MenA,[14,34,35] such as salicylic acid,[36,37] an initially locally excited $^1\pi\pi^*$ state may couple to a low-lying charge transfer (CT) state upon photoexcitation, which can mediate proton transfer along an intramolecular hydrogen bond. This type of excited state intramolecular proton transfer (ESIPT) is well reported in the literature[38–41] and has been observed in the sunscreen molecule oxybenzone.[15] While salicylic acid undergoes a complete hydrogen transfer,[36,37] anthranilic acid (the carboxylic acid variant of MA) has been reported to instead undergo excited state hydrogen atom dislocation, with one of the amine hydrogens migrating towards the carbonyl oxygen (akin to an incomplete *keto-enol* tautomerisation).[42] Complementary photoelectron spectroscopy measurements on MA and MenA, the experimental details of which will be given as part of section 4.2 (where they are more pertinent) are shown in Figure 4.10. The photoelectron spectra of MA/MenA did not yield the expected distinctive features for a complete proton transfer mechanism, that is, there were no discrete electron kinetic energy features that could be assigned to the *keto* and/or *enol* forms of MA.[43] Hence, it is plausible to conclude that, similar to the case of anthranilic acid, hydrogen atom dislocation along the intramolecular hydrogen bond takes place in photoexcited MA, instead of complete proton transfer.

The possibility of hydrogen atom dislocation occurring in MA was evaluated experimentally by comparing the TR-IY transients for MA, d_1-MA and d_2-MA photoexcited at 300 nm. From the time constants extracted, an average kinetic isotope effect (KIE) of 1.5 ± 0.4 (approximately $\sqrt{2}$) was determined, suggesting that non-tunnelling hydrogen atom motion is indeed involved in the dynamics observed for MA.[44,45] Further evidence supporting a hydrogen dislocation mechanism in MA is provided by the PECs displayed in Figure 4.8(a), which reveal a lack of driving force for complete proton transfer on these states, as previously discussed. However, excitation in the 330 nm $\geq \lambda_{\text{pu}} \geq$ 300 nm pump wavelength range (3.76 – 4.13 eV) is likely to provide sufficient energy for the relatively shallow S_1CT state to be sampled, and hence for the aforementioned hydrogen
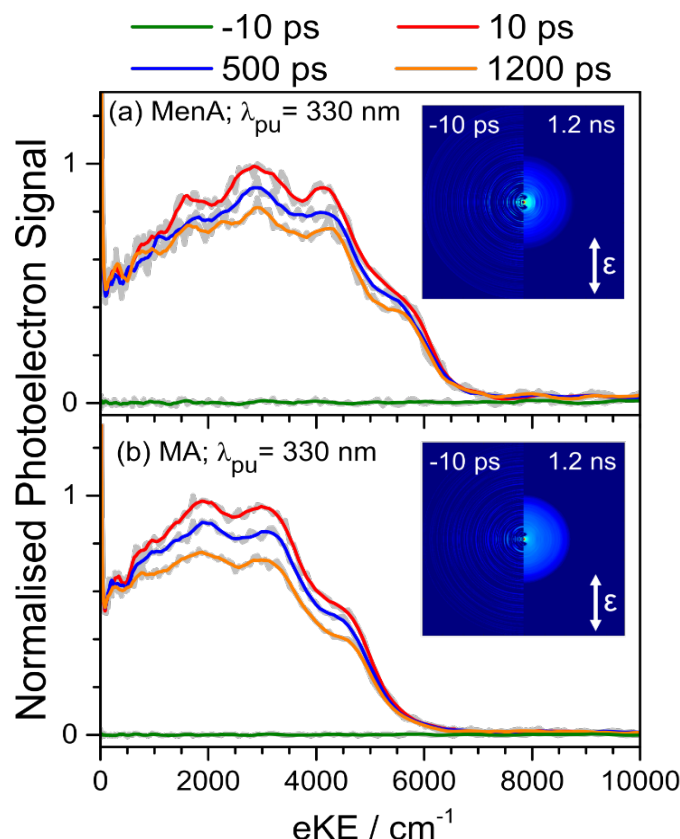
Figure 4.10: PES spectra for (a) MenA and (b) MA, both at $\lambda_{pu} = 330$ nm. Grey lines are raw data; solid coloured lines correspond to a 10 point moving average through the raw data. Inset: reconstructed VMI images for each data set at $\Delta t = 10$ ps (left) and $\Delta t = 1.2$ ns (right). The vertical white arrow indicates the electric field polarisation vector of the pump laser pulse, ε_{pu}. The features observed on top of the broader eKE peaks are, given the spacing between them, likely a result of vibrational resolution. These PES spectra do not show evidence for complete proton transfer, or *keto-enol* tautomerisation, which usually presents itself as two main eKE features with different time-dependent behaviours (see reference 43). Further details on the experimental methods and further data from PES measurements on MA and MenA are given as part of section 4.2, where they are more pertinent.

atom dislocation to take place. Given the experimentally determined KIE for MA and upon analysis of the PECs in Figure 4.8, we propose that, after photoexcitation with 330 nm $\geq \lambda_{pu} \geq 300$ nm, the excited state population of MA relaxes from the locally excited ($\pi_{ring} \rightarrow \pi^*_{ring}$) S_1 state to the more stable CT ($\pi_{ring} \rightarrow \pi^*_{carbonyl}$) S_1 state, where it is then trapped in a relatively shallow well (see Figure 4.9(a)). The lack of direct evidence for this S_1LE $\rightarrow S_1$CT transfer in our gas-phase experiments (*i.e.* no corresponding decay time constant), could be due to this process happening on a timescale faster than that measurable in these experiments. Such charge migration phenomena have been observed to occur on sub-femtosecond timescales (see, for example, reference 46), which would make

it impossible to resolve with our experimental setup.

In other systems, including other sunscreen molecules, proton transfer is followed by a twisting motion which eventually leads to a low-energy S_1/S_0 CI.[14,15,34–36] The analogous motion in MA would be around the C=C bond connecting the phenyl ring and the ester substituent, as demonstrated in Figure 4.8(b). However, the barrier to this motion in MA is much higher when compared to that of similar molecules (*e.g.* 0.4 eV in MA *vs.* 0.1 eV in salicylic acid).[36] This barrier may explain the marked difference in behaviour for MA photoexcited at 315 nm or 330 nm ($\tau \gg 1.2$ ns, see Figure 4.2) when compared to photoexcitation at 300 nm ($\tau_H \sim 1700 \pm 200$ ps, see Figure 4.3), since 300 nm (4.1 eV) would provide just enough energy to surmount the barrier, thus accelerating the overall decay of MA (when compared to photoexcitation at 315 nm or 330 nm). The existence of a barrier *en route* to the S_1/S_0 CI is also consistent with the proposed trapping of the excited state population in the S_1CT state. Despite the impact that a barriered process may have on the photodynamics of MA, the fact that a KIE is observed in our studies (while N—H$_{free}$ bond fission is not) shows that it is hydrogen motion along the intramolecular hydrogen bond that acts as the "rate determining step" in the excited state relaxation of MA at 300 nm. Presumably, it would be the coupling of the N—H—O motion to other vibrational modes or electronic states that ultimately facilitates the final decay of MA.

With excited state population trapped in the S_1CT state, and with no direct evidence for any CIs or any dissociative relaxation pathways that can be accessed on an ultrafast timescale from the S_1CT state, photoexcited MA would be expected to radiatively decay to its ground state. As mentioned in section 4.1.1. the introduction, there is extensive reporting of luminescence for both MA and MenA in the literature. Significant fluorescence quantum yields have been reported for both molecules,[9,12,13] with the observed emission wavelength being approximately 400 nm ($\sim$ 3.1 eV). We note here that this emission wavelength of 400 nm matches best with the calculated energy difference between the S_1CT and the S_0CT states in the region closer to the vertical excitation region of the PEC. Hence, while the excited state population may sample the entirety of the S_1CT state, transition to the ground state appears to be more likely at short N—H$_{bound}$ bond distances. This apparent dependence of emission on geometry, namely on N—H$_{bound}$ bond distances, further highlights the significance of the hydrogen motion in the photodynamics of MA, as discussed earlier.

Finally, despite the $S_1CT(\pi\pi^*) \rightarrow T_1(\pi\pi^*)$ transition not meeting the requirements of El Sayed's rule,[47] the strong degeneracy of singlet and triplet states in MA (near $R_{N—Hb} = 1.2$ Å, see Figure 4.8(a)) could facilitate intersystem crossing (ISC) and, consequently, phosphorescence. While there is no direct evidence for ISC in the gas-phase experiments reported here, previous studies in solution have found photoexcitation of MA to result in an excited triplet state with a lifetime of 280 μs.[8] In MenA, the reported triplet state lifetime is 2.36 ± 0.01 s, with a phosphorescence quantum yield of $\Phi_P = 0.092\pm0.009$.[13] The insensitivity of our gas-phase experiments to ISC ($S_1CT \rightarrow T_1$) may be due to the very similar surfaces of their respective PECs (see Figure 4.8(a)). The transition between these states ($S_1CT \rightarrow T_1$) may be difficult to distinguish in these experiments due to very similar ionisation cross sections, the effect likely being accentuated by the shallow character of the PEC of the first cationic state, D_0^+. Therefore, it is reasonable to assume that, while ISC occurs in both MA and MenA, it may be convoluted and hence indistinguishable in our gas-phase experiments. It is also possible that ISC occurs outside the temporal window of these experiments (as our TEAS results suggest, *vide infra*).

The results from our experiments in solution reveal a similar decay mechanism for both MA and MenA, with evidence for luminescence. Immediately obvious is the agreement between the wavelength of the SE component observed in our experiments and the previously measured emission wavelength of both MA and MenA, both at ~ 400 nm,[9,12,13] which provides evidence for fluorescence. Evidence for the existence of triplet states in both MA and MenA — and, hence, phosphorescence — can be drawn from a close analysis of the EADS and extracted decay time constants, as is now discussed. The sequential model fit of the obtained TAS in cyclohexane yields $\tau_1 \sim 2 - 11$ ps (depending on specific molecule and pump wavelength). This time constant is assigned to vibrational energy transfer (VET), which includes both intramolecular vibrational redistribution (IVR) and intermolecular energy transfer (IET). Since IET is a process by which vibrational cooling is achieved by energy transfer to the solvent bath, this is a process that cannot occur in the gas-phase, hence we would not expect (and, indeed, do not observe) a time constant in our gas-phase results that is analogous to this τ_1 in solution. The variation in τ_1 accross our several measurements can then be understood in terms of varying degrees of solvent-solute interactions which will have an effect on the rate of IET.[48] The TAS for both molecules in cyclohexane (at either pump wavelength) require two more time constants for a successful fit. For MA, τ_2 is simply assigned to the decay of the relaxed S_1 state, akin to our obser-

vations in vacuum; τ_3 is assigned to the decay of the triplet state of MA, since the EADS corresponding to τ_3 are spectrally very similar to the triplet state transient absorption spectrum of MenA previously obtained by Kikuchi *et al.*[13]

There are two main differences for the analogous time constants extracted for MenA. Firstly, in the case of MenA the EADS associated with τ_3 (henceforth referred to as EADS(τ_3)) do not resemble the aforementioned spectra by Kikuchi *et al.*[13]. It is possible that the processes associated with EADS(τ_2) and EADS(τ_3) in MenA are convoluted to such an extent that our sequential model is not able to completely isolate them; it is also possible that triplet state appearance is slower in MenA than in MA, therefore not being properly captured within the probe time window of our experiments. Upon visual inspection of the EADS shown in Figure 4.11(a) and (b), we speculate that, for MenA in cyclohexane, τ_3 would correspond to the convolution of the lifetimes of both the fluorescent S_1 state and the long-lived triplet state. To test this hypothesis, EADS(τ_2) and EADS(τ_3) were normalised to their respective intensities at 600 nm, since this feature is outside the wavelength range of the triplet state absorption region according to Kikuchi *et al.*.[13] The thus normalised EADS, shown in Figure 4.11, were then subtracted (EADS(τ_3) − EADS(τ_2)). The resulting spectrum (blue line in Figure 4.11) is, indeed, similar to the transient absorption spectrum of the triplet state of MenA.[13] This spectral similarity leads us to conclude that the excited state population of MenA (in cyclohexane, upon photoexcitation at either 315 nm or 330 nm) does populate a triplet state and EADS(τ_3) in this case corresponds to a convolution of the excited state absorptions of both the fluorescent S_1 state and the long-lived triplet state of MenA. The observations and analysis described above are also valid for MA in cyclohexane, photoexcited at 300 nm, as shown in Figure 4.11(c). This similarity between MA and MenA (albeit pump wavelength dependent) leads us to the conclusion that our sequential model cannot always isolate the contributions from the very convoluted processes occurring in our experiments. Nevertheless, the fact that (in the cases discussed in this section) EADS(τ_3) retains some spectral features of EADS(τ_2) supports our hypothesis for a long-lived S_1 state; the formation of triplet states in these molecules is supported by phosphorescence measurements available in the literature.[13] Extensive convolution of the processes associated to τ_2 and the appearance of a triplet state may also explain the second main difference for the experimental results for MenA *vs.* MA, *i.e.* the variation in τ_2 between $\sim 0.6 - 1.5$ ns (*c.f.* > 2 ns for MA): the shortening of τ_2 may not be a reflection of a faster decay of the S_1 state, but
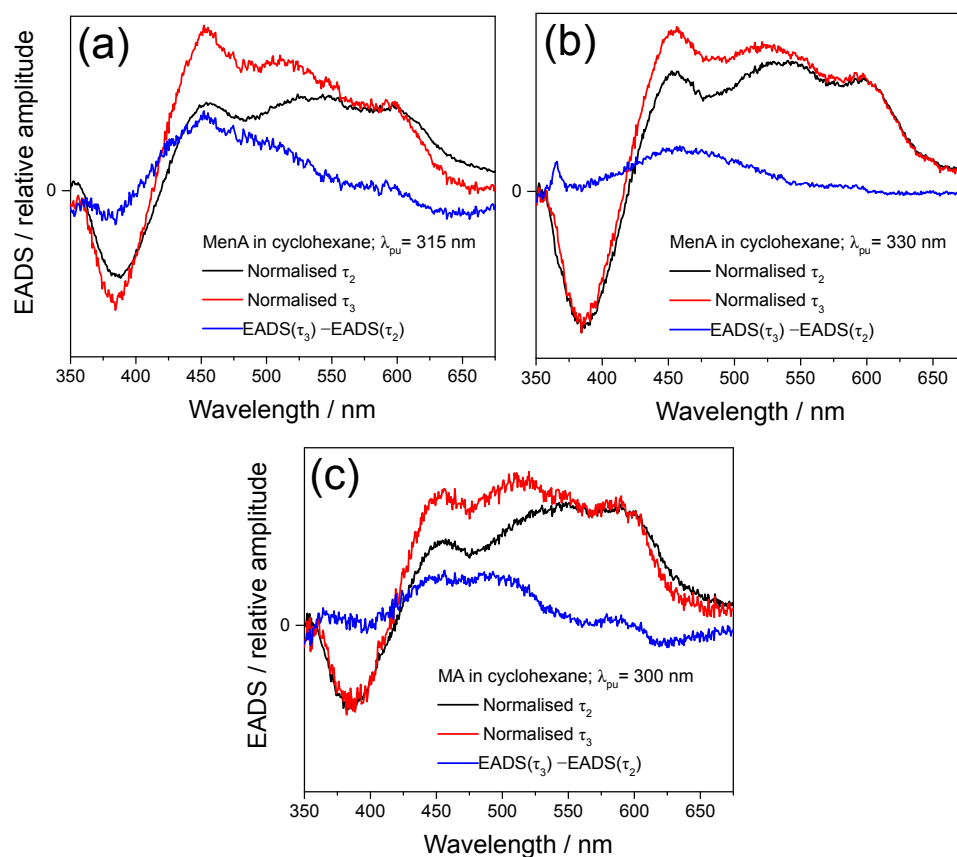
Figure 4.11: EADS for MenA in cyclohexane upon photoexcitation with 315 nm (left) and 330 nm (right). The black and red traces are the EADS corresponding to τ_2 and τ_3, respectively, normalised to their respective intensities at 600 nm. The blue trace is the result of subtracting the normalised EADS(τ_3) from the EADS(τ_2) EADS.

rather a result of our sequential model not being able to deconvolute the processes associated with τ_2 and τ_3. Indeed, the fact that the long-lived component observed for MenA in cyclohexane ($\tau_3 > 2$ ns) contains spectral features similar to the EADS corresponding to τ_2 suggests that the S_1 state is still populated at 2 ns (the limit of the probe window of these experiments).

To conclude the discussion of our results in cyclohexane, we note that, contrary to the observation in vacuum, photoexcitation of MA at 300 nm does not drastically accelerate its decay (see Figure 4.6(e)). It is likely that IET in solution facilitates faster relaxation to the S_1 minimum, from which the barrier to twisting motion can no longer be overcome (*vide supra*). Moreover, we note that EADS for MA in cyclohexane at 300 nm are similar to those of MenA (at other excitation wavelengths), which supports the theory that the spectral/temporal discrepancies discussed earlier are due to the sequential model used to fit these data, rather than any chemical or physical differences between MA or MenA.

In methanol, only two time constants are necessary to fit the TAS of each molecule; there is no evidence for triplet states in this solvent for either MA or MenA. However, triplet states were previously observed in MenA in ethanol,[13] hence it is highly likely that triplet states are formed in methanol for both MA and MenA outside the temporal window of our TEAS experiments. Assuming dislocation of the intramolecularly bound hydrogen atom is as relevant in solution as we proposed in the discussion of our results in vacuum, and hence considering that hydrogen motion facilitates ISC, it would not be surprising that a polar protic solvent would affect the observed behaviour of MA and MenA.

In summary, regardless of pump wavelength (315 nm *vs.* 330 nm, and 300 nm for MA), environment (vacuum *vs.* solution), and/or solvent polarity (cyclohexane *vs.* methanol), the photodynamics of MA and MenA can essentially be described as a slow decay corresponding to long-lived excited states which will likely luminesce. The differences in molecular structure between MA and MenA do not change the observed photodynamics (as is the observation for other sunscreen molecules and their precursors)[16,18] to such an extent that would justify the use of either molecule as a sunscreen, as far as photochemical and/or photophysical factors are concerned. The lack of a drastic solvent effect on the photodynamics of MA or MenA, on the other hand, is in stark contrast with our observations for the cinnmate-based sunscreen EF, discussed in Chapter 3, and similar observations by other authors,[16,18] which reinforces the importance of a fundamental understanding of sunscreen photophysics.

It transpires from our experiments that the intramolecular hydrogen bond present in MA and MenA affords them a first singlet excited state in which the intramolecularly bound hydrogen is dislocated from the amine towards the carbonyl oxygen, with the proton transfer never being complete. Thus, the intramolecular hydrogen bond of the anthranilates is responsible for the observed long-lived excited state. The enhanced stability of their excited states means that photoexcitation of MA/MenA with UVA and UVB radiation — the wavelength range of interest in a sunscreen context — provides insufficient energy for excited state population to access any CIs that would facilitate ultrafast relaxation. This, in turn, is a non-ideal scenario for sunscreen molecules since the long lifetime of any excited (potentially reactive) states may increase the chance for undesirable intra- or intermolecular chemical reactions. Nevertheless, MenA is used in the sunscreen industry — albeit scarcely — which raises the question: what is the fate of the excess energy in MenA after absorption of UV radiation by a sunscreen lotion? To address this question, our studies

on isolated molecules (in vacuum or single-solvent solvation) will need to be expanded towards complex mixtures of sunscreen molecules, solvents, stabilisers, *etc.* Of particular relevance in this respect are the recent studies by Matsumoto *et al.*,[49] which have reported diffusion-controlled (highly efficient) triplet-triplet energy transfer processes from MenA to other sunscreen molecules (octocrylene and octyl methoxycinnamate). These studies by Matsumoto *et al.* highlight the importance of identifying and understanding the fates of excess energy in a sunscreen context.[49] In addition, further research into the photophysics of sunscreen molecules is necessary to identify the molecular and/or electronic features that allow for ideal photoprotective characteristics.

4.1.6   Conclusion: The Anthranilates in Vacuum *vs.* in Solution

The similarity of the results for MA and MenA in vacuum are in accordance with observations for other sunscreen molecules, which have similar photodynamics to those of their precursors.[16] Nevertheless, molecular structure alterations — particularly those of a more perturbative nature — will of course have an impact in a molecule's photodynamics, as has been demonstrated for our studies on the cinnamate-based sunscreen EF, discussed in Chapter 3, for which the addition of a carbonyl moiety (through an ester functional group) results in markedly different photodynamics when compared to those of its non-carbonyl compound precursors. External environment factors, such as solvents, also tend to have a great impact in the observed photodynamics; this is indeed the case for EF and other cinnamates.[16,18] However, interestingly, this is not the case for the anthranilates. We have shown that, photophysically speaking, both MA and MenA behave as non-ideal sunscreens independently of external environment. Moreover, we suggest that the intramolecular hydrogen bond stabilises the excited states of MA and MenA, preventing any molecular fragmentation from occurring but ultimately hindering effective dissipation of potentially harmful excess energy. The S_1/S_0 CI along a twisting motion coordinate, common for other ESIPT molecules, is inaccessible in these anthranilates (upon photoexcitation with UVA/UVB). Our work therefore highlights two aspects of the anthranilates that may be interrogated in order to drive faster excited state decays in MA and MenA: *i)* alterations to the intramolecular hydrogen bond, *e.g.* changing the amine group by a different substituent, change its ring position or eliminate it altogether; and *ii)* changing the substituent functional groups in an attempt to lower the barrier to the twisting motion. In addition, these studies on isolated molecules (in vacuum or single-solvent solvation) will

need to be expanded towards more realistic environments in the sunscreen context, *i.e.*
complex mixtures of sunscreen molecules, solvents, stabilisers, *etc.*

4.2   Timing Mode-Specific Vibrational Decoherence

4.2.1   Overview

In the previous section, we have shown that irradiating MA in the 330 nm $\geq \lambda_{\mathrm{pu}} \geq 300$ nm
pump wavelength range accesses its first singlet excited state (S_1) resulting in hydrogen
dislocation along the intramolecular hydrogen bond. No evidence of a CI accessible from
the S_1 state of MA was found for photoexcitation at these wavelengths, which ultimately
hinders fast and efficient relaxation to the ground electronic state. The excited state
population of MA is thus trapped in the S_1 state, which we observed to have a lifetime of
more than 1.2 ns. To better understand the mechanisms behind the trapping of excited
state population in its S_1 state, we have sought further insight into the processes occurring
immediately after photoexcitation of MA, *i.e.* within the first few picoseconds. For this
purpose, we have employed time-resolved photoelectron spectroscopy (TR-PES), described
in greater detail in Chapter 2, section 2.2.1.3. As previously discussed, TR-PES carries
both electron kinetic energy (eKE) and angular distribution information and is sensitive
to both electronic configuration and vibrational dynamics; TR-PES is thus a particularly
useful tool for mapping energy flow in polyatomic molecules.[43,50,51]

In this section, we are particularly concerned with the wavepacket interpretation of
pump-probe measurements, described in further detail in Chapter 1, section 1.3. Briefly,
upon photoexcitation of the molecule of interest, the pump laser pulse (λ_{pu}) is said to
create a coherent superposition of n eigenstates of wavefunction Ψ_n and energy E_n — the
wavepacket — which then evolves freely in time according to:[43]

$$|\chi(\Delta t)\rangle = \sum_n \tilde{a}_n |\Psi_n\rangle e^{-i2\pi c E_n \Delta t} \tag{4.2}$$

with $\tilde{a}_n$ accounting for both amplitudes (*i.e.* populations) and initial phases of the molec-
ular eigenstates. After some time delay (Δt), the probe laser pulse (λ_{pr}) projects the
wavepacket dynamics onto a final state — in the case of TR-PES, a cationic state — gen-
erating a measurable photoelectron signal. Interference between the transitions from the

different wavepacket eigenstates, n and m, onto the same final state leads to an oscillating modulation in the time-dependent photoelectron signal at frequencies $\omega = (E_n - E_m)/\hbar$, a phenomenon commonly referred to as *quantum beats* (see Chapter 1, section 1.3). Quantum beats (and, indeed, molecular quantum beat spectroscopy, independently of detection methods) can provide detailed information regarding intramolecular state couplings as well as the dynamics of energy redistribution in polyatomic molecules.[52–56]

In the work presented in this section, the observation of quantum beats in the TR-PES of MA is used to explore interactions between the photoactive vibrational states and the molecular bath, *i.e.* the initial steps of intramolecular vibrational energy redistribution (IVR), and thus garner insight into the photoprotective mechanisms of the anthranilates. We aim to further elucidate the ultrafast vibrational coupling occurring in MA to discern the mechanism by which excited state population is trapped on the S_1 state. In addition, we briefly present quantum beat results from MenA in order to evaluate the effects of the additional menthyl group on the ultrafast processes of this sunscreen molecule.

4.2.2 Experimental Methods

4.2.2.1 Laser Induced Fluorescence (LIF)

The laser induced fluorescence (LIF) apparatus is described in detail elsewhere;[57] the LIF experiments reported here were carried out by the research group led by Professor Timothy S. Zwier (University of Purdue). A liquid sample of MA (Sigma-Aldrich, 99%) was placed in an unheated glass sample holder behind an 800 μm diameter nozzle (Parker General Valve series 9), entrained in $\sim$ 3 bar He, and pulsed into a vacuum chamber at 20 Hz, giving rise to a supersonic expansion. Approximately 8 mm downstream from the nozzle the frequency doubled output of a dye laser (LambdaPhysik, Scanmate) loaded with LDS 698 dye (Exciton), pumped with the second harmonic of a Nd:YAG laser (532 nm, Quantel, Q-Smart 450), interacted with the vibrationally cooled molecular expansion in the focal point of two 4-inch diameter spherical mirrors, the bottom mirror containing a 1 cm hole through which the fluorescent photons were focused. These spherical mirrors steered the fluorescence photons onto a 2-inch diameter plano-convex collimating lens and onto a photomultiplier tube.

The dye laser frequency was scanned through the $S_1 \leftarrow S_0$ (origin, *i.e.* 0-0 transition)

region of the molecule; the width of the emission from the LDS 698 allowed for these measurements to be achieved at once, with no need to change dye. The DC voltage output from the photomultiplier tube was digitised by an oscilloscope (Tektronix, model 3052B), sent to a computer, and plotted as a function of excitation wavelength.

4.2.2.2   Time-Resolved Photoelectron Spectroscopy

The apparatus used in this work has been described in greater detail in Chapter 2, section 2.4.1; it consists of a commercially available femtosecond (fs) laser system, a molecular beam source and a photoelectron spectrometer which resembles the design of Eppink and Parker.[21] The output from the Ti:Sapphire oscillator (Spectra-Physics Tsunami) and regenerative amplifier (Spectra-Physics Spitfire XP) system was used to pump an optical parametric amplifier (Light Conversion TOPAS-C) to generate pump (λ_{pu}) pulses, with centers varied between 330 – 351 nm. A second 800 nm laser beam pumped a separate TOPAS-C which was used to generate probe (λ_{pr}) pulses, centered at 285 nm for MA and 296 nm for MenA. As before, the pump and probe pulses were temporally delayed with respect to each other (maximum $\Delta t = 1.2$ ns) by reflecting the pump fundamental off of a hollow corner gold retroreflector mounted on a motorized delay stage.

The pump and probe laser beams intersected a molecular beam which was produced by seeding MA (Alfa Aesar, 99%) heated to 55°C or MenA (Aldrich, 98%) heated to 90°C into helium (~ 3 bar). This gas mixture was then expanded into vacuum ($\sim 10^{-7}$ mbar) using an Even-Lavie pulsed solenoid valve.[58,59] At $\Delta t \geq 0$, the pump laser pulse excited MA and the probe ionised the excited species. The resulting photoelectrons were focused onto a position-sensitive detector, consisting of two microchannel plates (MCPs) coupled to a phosphor screen, such that electrons with the same initial velocity were mapped onto the same point on the detector irrespective of their initial formation position within the laser-molecular beam interaction volume. The original 3D electron distribution was reconstructed from the measured 2D projection using a polar onion peeling algorithm[22] (see Chapter 2, section 2.2.1.2) from which the desired 1D photoelectron spectrum, *i.e.* photoelectron signal *vs.* electron kinetic energy (eKE), was derived using an appropriate energy calibration factor. The spectrometer was calibrated using the well-known photoelectron spectrum of photoionized Xe (more details are given in Chapter 2, section 2.4.1).[60]

4.2.3   Fitting procedures

The kinetic model used to fit our 1D transient data (photoelectron signal *vs.* electron kinetic energy, eKE), obtained by integrating over a given eKE region, follows the same principles described in Chapter 2, section 2.4.3: it consists of a sum of exponential decay functions which are multiplied by a step function and convoluted with a Gaussian function to model the instrument response function (IRF). Moreover, our 2D transient data (all eKE *vs.* all Δt) were fit using global lifetime analysis,[61,62] following a similar approach to that used to fit TAS for measurements in solution, also described in further detail in Chapter 2, section 2.4.3). The following functional form is then employed:

$$S(\Delta t, \text{eKE}) = g(\Delta t) * \left[\sum_i \text{DAS}_i(\text{eKE}) \cdot \exp\left(-\frac{\Delta t - t_0^{\text{true}}}{\tau_i} \right) H\left(\Delta t - t_0^{\text{true}} \right) \right] \qquad (4.3)$$

where $\text{DAS}_i(\text{eKE})$ are the eKE-dependent exponential decay amplitudes for a given time constant.[61]

For 1D transients with observable beat frequencies, sine functions were added to Equation 2.55 (Chapter 2) such that the total model becomes:

$$S_{\text{beat}}(\Delta t) = S(\Delta t) \times B \exp\left(-\frac{\Delta t - t_0^{\text{true}}}{\tau_{\text{beat}}} \right) \sum_j A_j \sin\left[\omega_j \cdot \left(\Delta t - t_0^{\text{true}} \right) + \phi_j \right] \qquad (4.4)$$

where τ_{beat} is the dampening lifetime of the total beat signal B, A_j are the amplitudes of each frequency ω_j, and ϕ_j are phase shifts ($S(\Delta t)$ and the remaining terms are defined in Chapter 2, specifically Equation 2.55).

To isolate the temporal behaviour of the quantum beats, the raw data were "normalised" by dividing the measured signal by the model fit (either the exponential decay or global fit model for 1D and 2D transients, respectively), resulting in a "flattened" transient, as shown in Figure 4.12(b). Thus, decreases in quantum beat intensity due to decreased total signal intensity are removed and any remaining temporal behaviour may be exclusively attributed to dynamics associated with the quantum beats. These "isolated" transients were then either fit with Equation 4.4 (with $S(\Delta t)$ becoming S_0 in this case, an additive baseline offset), and/or prepared for fast Fourier Transform (FFT) analysis as described in reference 55 to reveal the frequency of the quantum beats. To minimise interference from the rise in signal at $\Delta t = 0$, all isolated transient fits and FFT analyses
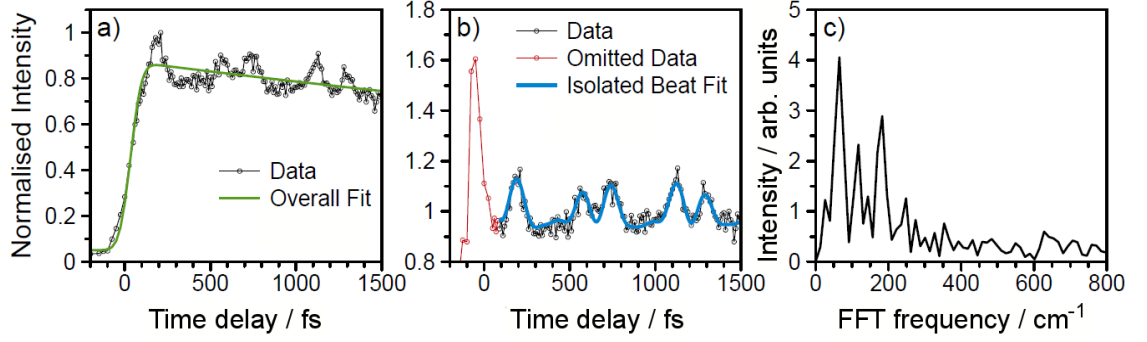
Figure 4.12: (a) Example 1D transient at $\lambda_{\text{pu}} = 344$ nm fit with an overall exponential decay model fit. (b) The resulting isolated transient along with a fit using Equation 4.4 (with S_0 instead of $S(\Delta t)$, see main text). Data shown in red were omitted from the fit and FFT analysis due to the distortion near $\Delta t = 0$. (c) 1D FFT spectrum from an isolated transient at $\lambda_{\text{pu}} = 344$ nm.

were performed on transient signal from $\Delta t > 0$, with any other data being omitted (see Figure 4.12 (b)). Examples of the resulting FFT spectra are shown in Figure 4.12(c) and on the insets of Figure 4.18.

In addition to the 1D FFT spectra generated from the total photoelectron signal (all eKE and Δt), FFT spectra were also generated as functions of eKE and Δt, as presented throughout this section. The former were produced by averaging the photoelectron signal in a fixed window in photoelectron velocity (v_{e^-}), then performing an FFT analysis on this average signal for all Δt. The window is then shifted by one velocity bin and a new FFT spectrum generated. This procedure is repeated until the high velocity edge of the window reaches the maximum v_{e^-}. The resulting FFT(v_{e^-}) are then transformed into FFT(eKE) using the average eKE of each velocity window. Window size was chosen to maximize FFT signal while maintaining eKE resolution.

Similarly, FFT(Δt) were produced by first averaging the "isolated" 2D transient over a given eKE. FFT analysis was then performed on the 1D transient over a fixed Δt window. As before, the window was then advanced one time delay and the FFT analysis repeated until the high Δt edge of the window reached the maximum time delay. The final Δt values presented are the first time delay in each window. Window size was chosen to be the smallest number of time delays that reproduced an FFT spectrum with the observed quantum beat frequencies. The production of both FFT(eKE) and FFT(Δt) are shown schematically in Figure 4.13.
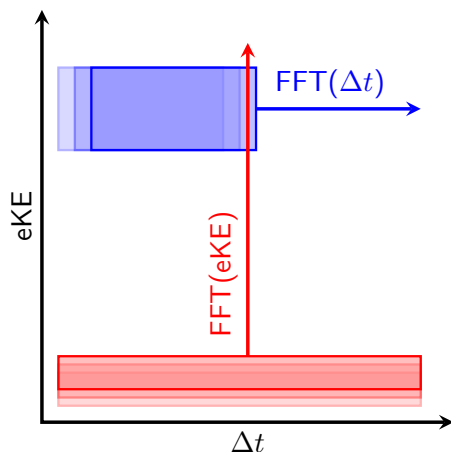
Figure 4.13: Schematic representation of the production of FFT(eKE) and FFT(Δt).

4.2.3.1 Computational Methods

All calculations were performed using the GAMESS computational package.[63,64] The geometry of MA was optimized at the aug-cc-pVDZ[28,65]/(TD-)CAM-B3LYP[66] level of theory on both the S_0, S_1, and D_0^+ surfaces. Harmonic frequencies were calculated at the S_0 equilibrium ($S_{0,eq}$), S_1 vertical Franck-Condon ($S_{1,vFC}$), S_1 equilibrium ($S_{1,eq}$), D_0^+ vertical Franck-Condon ($D_{0,vFC}^+$), and D_0^+ equilibrium ($D_{0,eq}^+$) geometries. The Franck-Condon active vibrational modes were identified from the LIF results (*vide infra*). Potential energy cuts (PECs) along these normal modes were generated by a Cartesian coordinate offset from a starting geometry (*e.g.* $S_{1,eq}$) using the wxMacMolPlt program.[67] Single-point energies were then calculated at each set of offset coordinates and fit with a harmonic potential.

4.2.4 Results and Analysis

We start this section by presenting our frequency-resolved results. Laser induced fluorescence (LIF) measurements, shown in Figure 4.14, are in good agreement with a previous measurement.[68] The measured vibronic origin (v = 0) of the S_1 state of MA is located at 28 851 cm^{-1} (approximately 347 nm), in close proximity to that of its carboxylic acid variant anthranilic acid (AA).[42] The vibrational progressions observed in the LIF spectra of both MA and AA are also similar: in MA, two prominent vibrational progressions are observed at 179 cm^{-1} and 421 cm^{-1}, in comparison with 252 cm^{-1} and 418 cm^{-1} in AA.[42] Based on our computational studies, the 179 cm^{-1} vibrational mode (henceforth referred to as ν_{179}) corresponds to an in-plane bend of the ester group, as shown in Figure 4.14, while

198
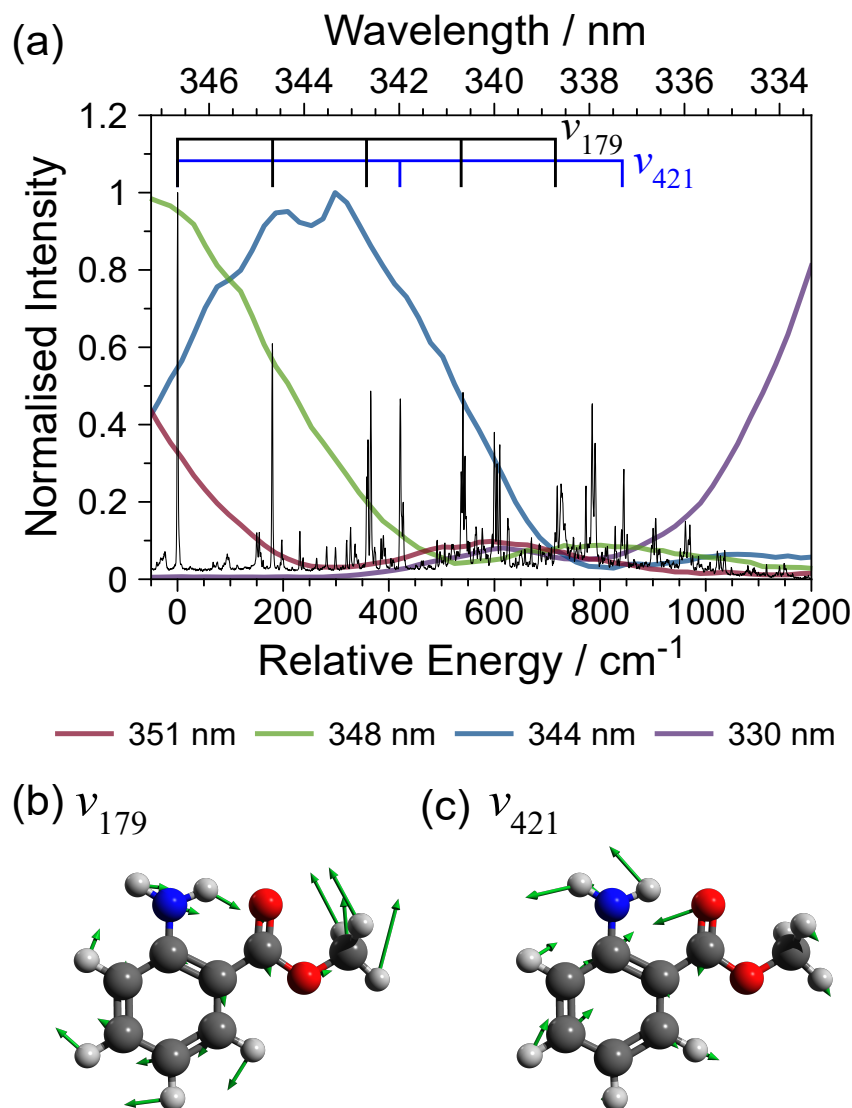
Figure 4.14: (a) LIF spectrum of MA (black line). Overlaid are the spectral profiles of the pump laser pulses used in the time-resolved experiments. Shown below are vector displacement diagrams for the (b) 179 cm^{-1} mode and (c) 421 cm^{-1} vibrational modes on the S$_1$ state.

the 421 cm^{-1} vibrational mode (denoted as ν_{421}) corresponds to a bending motion of the carbonyl and amino groups with some distortion of the phenyl ring; similar motions were assigned to the LIF active modes in AA.[42] Furthermore, as shown in Figure 4.15, PECs along these coordinates show a geometry change upon excitation to the S$_1$ state, again similar to the results from AA.[42] Table 4.3 lists the lowest ten vibrational frequencies calculated for the S$_{0,eq}$, S$_{1,eq}$, and D$_{0,eq}^+$ states of MA.

Having established the vibrational modes that are active in the close-to-origin photoexcitation of MA, it is important to specify which levels of these modes are accessed
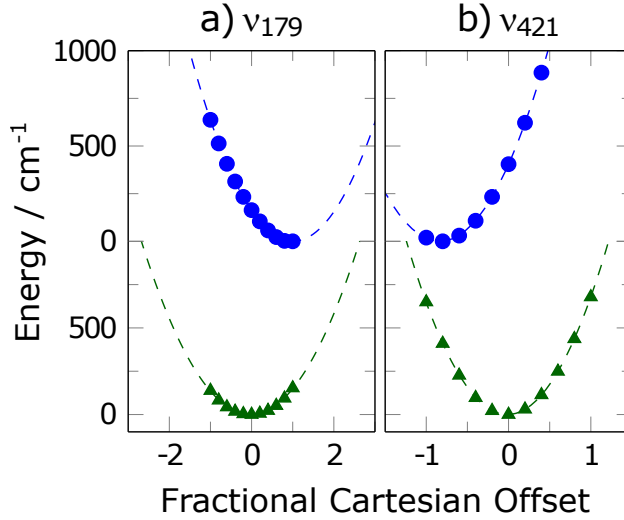
Figure 4.15: PECs along the (a) 179 cm^{-1} and (b) 421 cm^{-1} normal mode coordinates on the $S_{0,eq}$ (green triangles) and $S_{1,vFC}$ (blue circles) surfaces of MA.

by the large bandwidth ($\sim$ 500 cm^{-1} full width at half maximum) laser pulses used in our time-resolved experiments. As shown in Figure 4.14, at $\lambda_{pu} = 351$ nm the laser pulse accesses mainly the $S_1(v = 0)$ level of MA, while $\lambda_{pu} = 348$ nm also accesses the v = 1 and v = 2 levels of ν_{179}. At $\lambda_{pu} = 344$ nm, a much more complex combination of vibrational levels, spanning over both progressions, is accessed, $i.e.$ v = 0 − 3 of ν_{179}, and v = 1 of ν_{421}. Finally, at $\lambda_{pu} = 330$ nm, several vibrational excited levels of both the ν_{179} and ν_{421} modes are accessible.

To aid the interpretation of the TR-PES results, the potential energy cuts (PECs) along the ν_{179} and ν_{421} coordinates on the $S_{1,eq}$ and $D_{0,vFC}^+$ states, as shown in Figure 4.16, were produced. These PECs reveal a misalignment of the energy wells of the $S_{1,eq}$

Table 4.3: Low lying vibrational frequencies calculated on the $S_{0,eq}$, $S_{1,eq}$, and $D_{0,eq}^+$ states of MA, along with experimentally observed frequencies (S_1 exp.).

$S_{0,eq}$ / cm^{-1}	$S_{1,eq}$ / cm^{-1}	$D_{0,eq}^+$ / cm^{-1}	S_1 exp. / cm^{-1}
51	80	75	—
75	88	120	—
127	124	155	—
157	160	167	—
182	**185**	**180**	**179**
196	223	248	—
261	331	331	—
342	339	361	—
364	378	417	—
421	**431**	**419**	**421**

and $D_{0,vFC}^{+}$ states. For ν_{421} this misalignment suggests that the $S_{1,eq}(v = 1)$ level will have the greater Franck-Condon overlap with the $D_{0,vFC}^{+}$ (v = 0), as shown schematically in Figure 4.16. Conversely, while the ν_{179} coordinate is also displaced upon ionisation, visual inspection of the wavefunction probabilities suggests that each level of this mode may overlap with several of the vibrationally excited levels in the cationic state.

At all wavelengths studied, the TR-PES spectra of MA, examples of which are shown in Figure 4.17, show two peaks separated by approximately 1200 – 1400 cm^{-1}, the origins of which will be discussed in section 4.2.5. The TR-PES 1D transients of MA are obtained by integrating an energy region of interest in the TR-PES spectra as a function of pump-probe time delay, which results in the 1D intensity *vs.* time delay transients shown in Figure 4.18. Such 1D transients produced from the TR-PES measurements for MA reveal signal oscillations and thus provide clear evidence for quantum beats. To quantify the observed quantum beats, the transients were normalised to isolate the time behaviour of the quantum beats and then fit with a kinetic model which includes a sum of sine waves, as discussed earlier. Examples of the resulting transients and fits are shown in Figure 4.12 for $\lambda_{pu} = 344$ nm and in Figure 4.17 for $\lambda_{pu} = 351$ nm and $\lambda_{pu} = 348$ nm. The frequencies extracted from the sine wave fitting model were compared to the FFT results to ensure agreement.
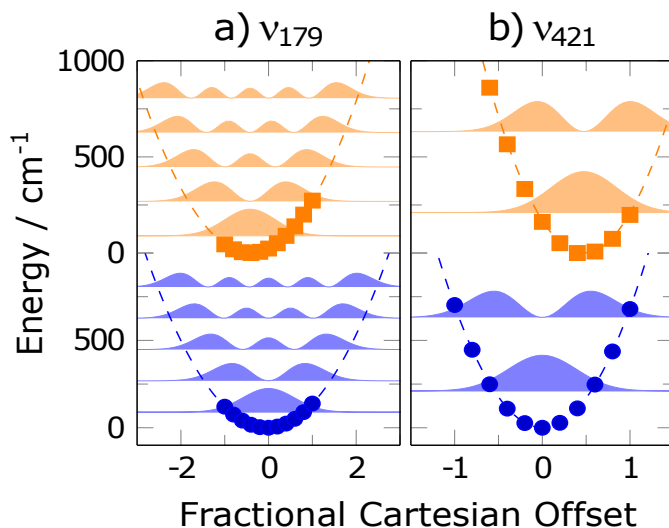
Figure 4.16: Potential energy cuts along the (a) 179 cm^{-1} and (b) 421 cm^{-1} normal mode coordinates on the $S_{1,eq}$ (blue circles) and $D_{0,vFC}^{+}$ (orange squares) surfaces. Quadratic fits to the calculated points are shown as dashed lines of the same color. Probability densities of the solutions to a quantum harmonic oscillator are shown for each vibrational level. The motion corresponding to positive Cartesian offset is shown by the vector displacements in Figure 4.14.
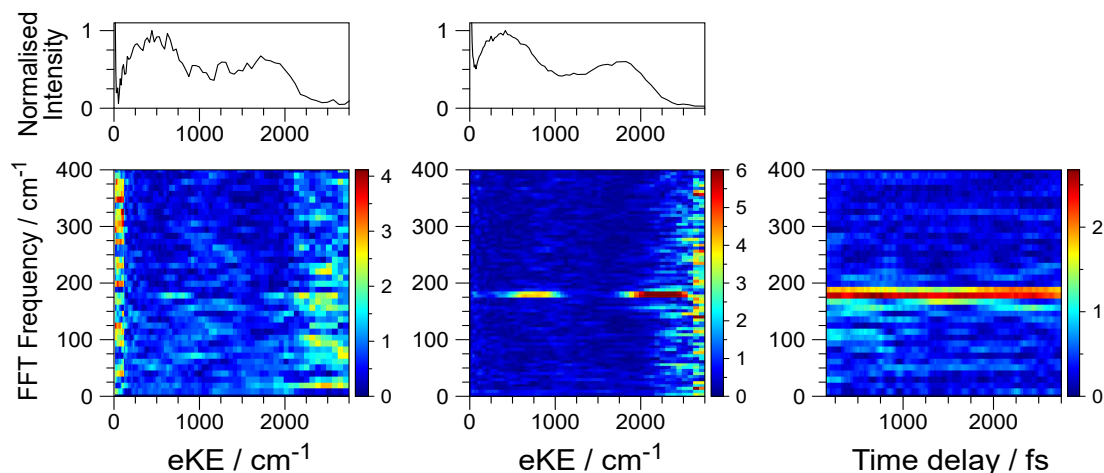
Figure 4.17: FFT(eKE) spectrum for MA photoexcited at (left) 351 nm and (middle) 348 nm, with the corresponding TR-PES spectra shown above. On the right, the FFT(Δt) spectrum for MA at λ_{pu} = 348 nm, resulting from the 1D spectrum obtained by integrating over $\sim$ 1800 – 2600 cm^{-1} eKE range, is also shown.
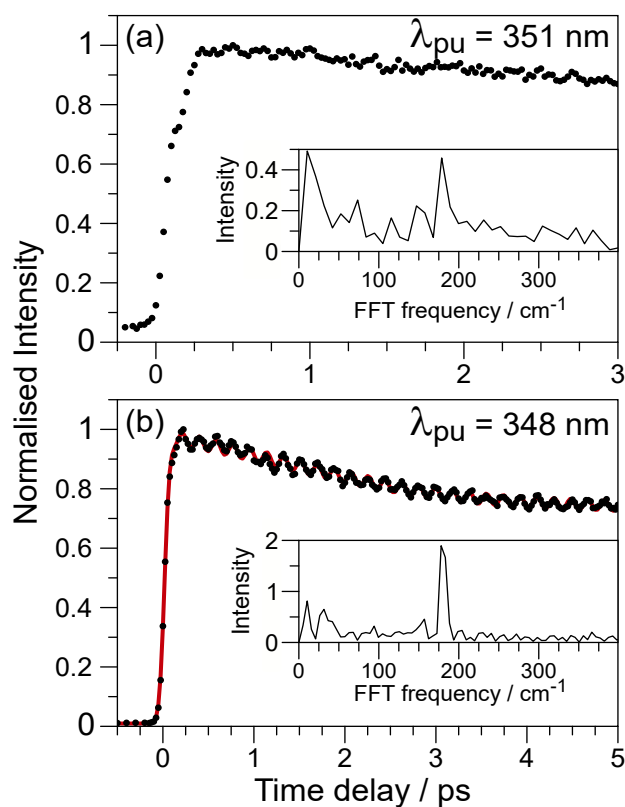
Figure 4.18: TR-PES transients for MA at (a) λ_{pu} = 351 nm and (b) λ_{pu} = 348 nm pump wavelengths. Data are shown as black circles with the red line showing a fit. Insets show the corresponding FFT spectra.

As expected from the spectra in Figure 4.14, the observed quantum beat frequencies are pump wavelength dependent. As evidenced by the transient shown in Figure 4.18(a), at the lowest energy photoexcitation, λ_{pu} = 351 nm, no clear oscillations are observed in the transient, suggesting that this pump energy is primarily populating the ground vibrational state of S_1. We note, however, a near-negligible feature at $\sim$ 180 cm^{-1} in the FFT spectrum (inset in Figure 4.18(a)), the appearance of which is likely due to the edge of the 351 nm pulse exciting the v = 1 level of ν_{179}, as shown in Figure 4.14. At λ_{pu} = 348 nm, a single beat frequency of 179 cm^{-1} (ω_{179}) is extracted from both the FFT spectrum and sine wave fit to the TR-PES transient, consistent with the excitation of v = 0 and v = 1 of ν_{179} (see Figure 4.14). With a slight increase in pump energy, at λ_{pu} = 344 nm, several beat frequencies emerge from sine wave fits to the data and FFT analysis: 60, 115, 180 and 240 cm^{-1}, the latter becoming more apparent upon fitting the "isolated" transient in Figure 4.19(c). As before, the 180 cm^{-1} beat frequency may be assigned to interference between the v = 0 and v = 1 levels of ν_{179}. The 240, 60 and 115 cm^{-1} frequencies are in good agreement with the expected interference between the v = 1 level of ν_{421} and the first, second, and third overtones of ν_{179} (ω_{242}, ω_{63}, and ω_{116}, respectively). Finally, at λ_{pu} = 330 nm, while a single beat frequency of 178 cm^{-1} produces a satisfactory sine wave fit to the 1D transients (Figure 4.20), both FFT(eKE) and FFT(Δt) reveal further beat frequencies at ω_{63}, ω_{116}, and ω_{179}, as shown in Figure 4.21.

In all the aforementioned cases, the several quantum beat frequencies are observed to be dependent on eKE. As shown in Figure 4.17 for λ_{pu} = 351 nm and 348 nm, Figure 4.19 for λ_{pu} = 344 nm and Figure 4.21 for λ_{pu} = 330 nm, ω_{179} consistently appears closer to each photoelectron intensity maximum, while the high eKE edges reveal evidence of interference with ν_{421} (*i.e.* appearance of ω_{63} and ω_{116}). As discussed further in section 4.2.5, this dependence of beat frequencies on eKE is consistent with the $S_{1,eq}/D_{0,vFC}^{+}$ misplacements calculated as shown in Figure 4.16.

The temporal behaviour of the observed quantum beats is also of interest. The oscillations of the 1D transients for MA photoexcited at λ_{pu} = 348 nm show little evidence of dampening or disappearance of the oscillations by 5 ps (Figure 4.18), suggesting that population in the v = 1 level of ν_{179} persists for much longer than the duration of these experiments. For λ_{pu} = 344 nm, on the other hand, FFT(Δt) elucidate the temporal behaviour of each of the several beat frequencies present at this pump wavelength. Inte-
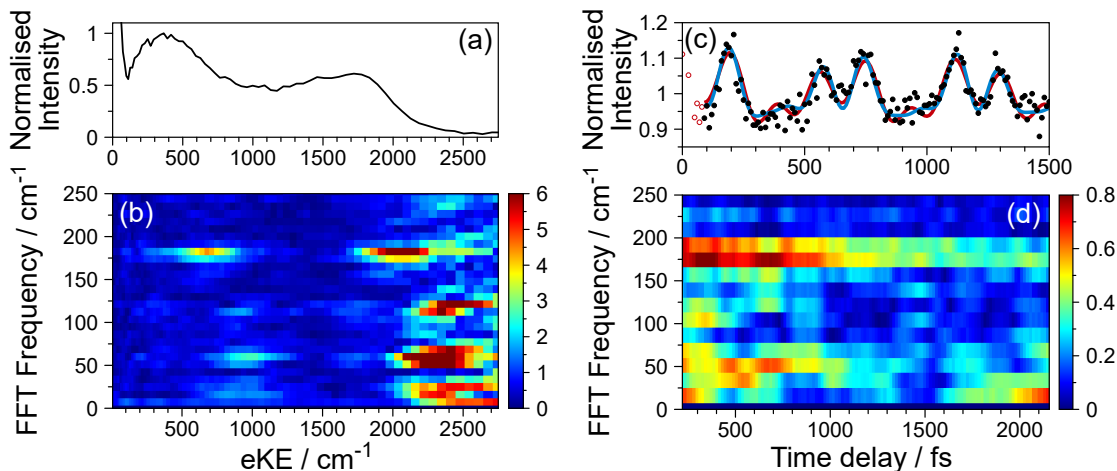
Figure 4.19: (a) TR-PES spectrum of MA upon photoexcitation at $\lambda_{pu} = 344$ nm, along with corresponding (b) FFT(eKE) spectrum, (c) isolated transient at high eKE including trial fits to the quantum beats, for which data are shown as solid circles and fits with and without ω_{242} are shown as blue and red solid lines, respectively, and (d) FFT(Δt) spectrum for eKE $\sim 1100 - 2600$ cm^{-1}

.

grating over low eKE (to examine ω_{179}) reveals an initial decay over the first picosecond followed by a much longer decay, apparently persisting for longer than 2 ps. While ω_{242} does not appear in these transients, ω_{63} and ω_{116} decay with timescales on the order of ~ 1.5 ps and 1 ps, respectively. We note here that the discussion of beat frequency decay times is qualitative: FFT(Δt) spectra were not fit to a kinetic model. As such, the "timescales" mentioned are visual estimates of the time until the FFT intensity of a particular beat returns to the baseline. Nevertheless, as discussed below, we draw confidence that these estimated timescales are representative of the quantum beat lifetimes from comparison with results at $\lambda_{pu} = 330$ nm.

For $\lambda_{pu} = 330$ nm, there is no evidence for a long-lived ω_{179} as λ_{pu} does not significantly populate the v $= 0$ level of ν_{179} (see Figure 4.14). Moreover, as presented in Figure 4.21(c), the quantum beats observed at $\lambda_{pu} = 330$ nm have a much shorter beat dampening time than at $\lambda_{pu} = 348$ nm. The shorter dampening times observed at $\lambda_{pu} = 330$ nm consequently allow for the dampening time of the 1D transient to be fit with a kinetic model (see Figure 4.20(a)). The extracted beat frequency decay lifetime of 1.5 ± 0.2 ps is in good agreement with the ~ 1.5 ps dampening time estimated from visual inspection of Figure 4.21(c). Thus, the qualitative timescale estimates appear to be representative of one dampening lifetime; this assumption will be made throughout the ensuing discussion.
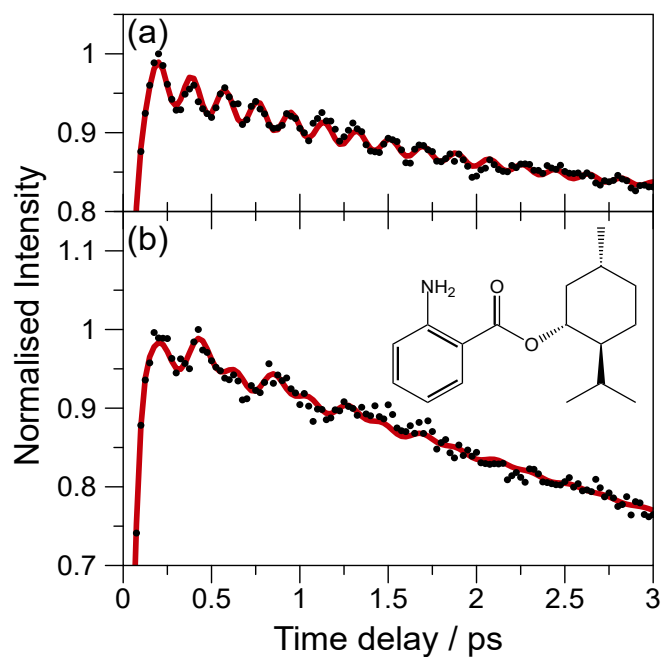
Figure 4.20: Example TR-PES transients at $\lambda_{pu} = 330$ nm for (a) MA and (b) MenA. Data are shown as black circles with fits shown as a red line. Inset: structure of MenA.
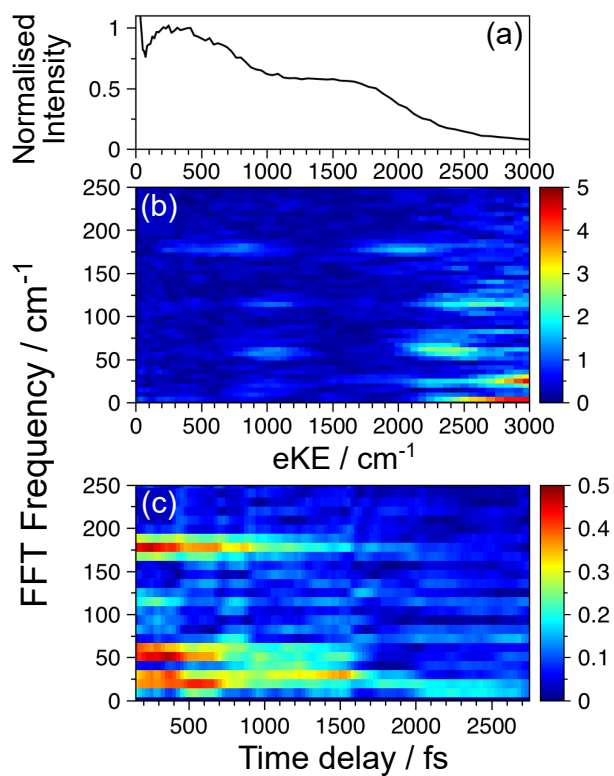
Figure 4.21: Results of the FFT analysis for MA photoexcited at $\lambda_{pu} = 330$ nm including (a) the TR-PES spectrum, (b) FFT(eKE) spectrum and (c) FFT(Δt) for eKE $\sim 300 - 2900$ cm^{-1}.

.
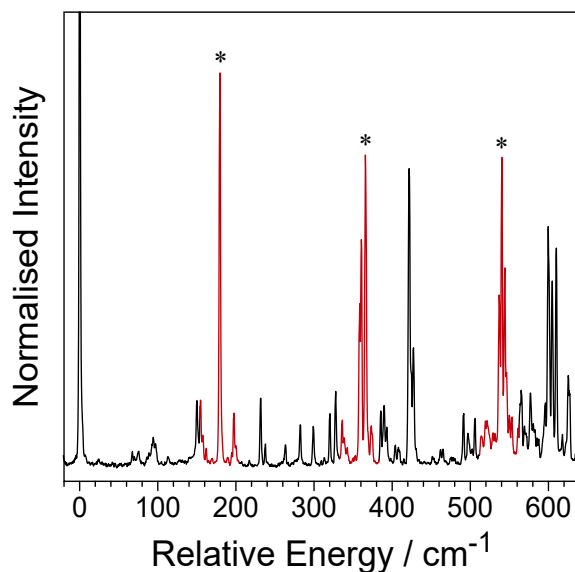
Figure 4.22: Enlarged LIF spectrum of MA showing the satellite features within 25 cm^{-1} (red line) of each ν_{179} progression peak (*).

For completeness, an additional beat frequency present for both $\lambda_{pu} = 344$ nm and $\lambda_{pu} = 330$ nm at ~ 25 cm^{-1}, should be noted. For $\lambda_{pu} = 344$ nm, this beat frequency is mostly evident from the FFT(eKE) data, where it follows the same eKE dependence as the assigned quantum beats (see Figure 4.19(b)); this FFT feature is less clear in the FFT(Δt) data due to a reduced accuracy of our FFT analysis at these lower frequencies and overall weaker signal intensity, both resulting in considerable surrounding noise. Nevertheless, and even though this feature cannot be assigned with certainty, the recurrence of this ω_{25} feature across different data sets encourages a tentative assignment to two different possible sources. Firstly, ω_{25} appears to decay roughly on the same timescale as ω_{116}, suggesting an interference between the v = 3 level of ν_{179} and a nearby vibrational mode. Several features within 25 cm^{-1} of the v = 3 level of ν_{179} are visible in the detail of the LIF spectrum of MA shown in Figure 4.22, supporting such an assignment. At $\Delta t > 1.5$ ps, the ω_{25} intensity appears to recover on approximately the same timescale as depopulation of the v = 2 level of ν_{179} (i.e. the timescale of the dampening of ω_{63}), suggesting that the v = 2 level of ν_{179} is efficiently coupled to neighbouring lower frequency modes (see Table 4.3). When populated, these neighbouring modes would presumably give rise to the interferences responsible for the reappearance of a beat frequency at ~ 25 cm^{-1}.

While the results at $\lambda_{pu} = 330$ nm also reveal ω_{25}, it is unlikely that this beat may be attributed to the same interference as that just discussed for $\lambda_{pu} = 344$ nm. As can be

seen in Figure 4.21(c), the time dependence of ω_{25} does not match that of ω_{179}, with ω_{25} persisting for ~ 2 ps compared to ≤ 1.5 ps for other frequencies. Given our assignment of ω_{179} to ν_{179}, this difference in decay timescales implies it is unlikely that, in this case, ω_{25} would be related to activity of ν_{179}. Thus, ω_{25} at $\lambda_{\mathrm{pu}} = 330$ nm is likely due to interference between other, higher energy vibrational modes which are contained within the higher density of vibrational states accessed at this pump wavelength (see Figure 4.14) but that we are unable to firmly assign with our current results.

Finally, we note the 1D transient of MenA photoexcited at $\lambda_{\mathrm{pu}} = 330$ nm, shown in Figure 4.20(b). The analogous transient for MA, as discussed earlier and shown in Figure 4.20(a), requires a single beat frequency (178 cm^{-1}) to produce a satisfactory sine wave fit. As discussed above, the fit for the MA transient also returns a dampening lifetime of 1.5 ± 0.2 ps, in good agreement with the "timescale" estimate from the FFT(Δt) spectrum in Figure 4.19(c). Upon replacing the methyl group with the larger menthyl group, the beat pattern and dampening time in MenA are substantially altered: the fit to the transient now requires two beat frequencies of 77 and 159 cm^{-1} and a dampening lifetime of 1.0 ± 0.3 ps. Nevertheless, in both cases (MA and MenA), the overall S$_1$ decays are long-lived, in agreement with the observations reported in section 4.1.

4.2.5   Discussion

We start this section with a closer analysis of the TR-PES spectra and the eKE dependence of the quantum beats of MA. At $\lambda_{\mathrm{pu}} = 348$ nm, the FFT intensity of ω_{179} is broadly peaked ~ 200 cm^{-1} below the highest eKE for each TR-PES feature (see Figures 4.17), suggesting that several levels of ν_{179} of the cation may serve as the final state onto which the wavepacket, described in Equation 4.2, may be projected. This trend continues at $\lambda_{\mathrm{pu}} = 344$ nm and 330 nm, where ω_{179} peaks ~ 300 cm^{-1} below the highest eKE and only the highest energy edge of the eKE features show any evidence for interference between ω_{179} and ν_{421}. This beat frequency dependence upon eKE provides insight into the Franck-Condon overlaps between the S$_1$ and the D$_0^+$ states of MA, as it suggests that ν_{179} (of the S$_1$ state) couples best to v > 0 levels of the equivalent mode on the D$_0^+$ state, while the v $= 1$ level of ν_{421} couples exclusively to the v $= 0$ level of the D$_0^+$ state. These observations are in line with the calculated PECs shown in Figure 4.16, which show that the potential energy surfaces of the S$_1$ and the D$_0^+$ states of MA are dislocated, resulting in different Franck-Condon overlaps for each level in ν_{179} and ν_{421}. Thus, the dependence

of the appearance of each beat frequency in eKE can be explained by the relative overlap of the S_1 and D_0^+ surfaces, further supporting the assignments of each observed beat to specific levels of the observed vibrational modes.

The double-peak TR-PES spectra of MA (see Figures 4.17, 4.19 and 4.21) are also consistent with different couplings between the S_1 state and the corresponding vibrational modes in the D_0^+. TR-PES spectra with a double peak are common for molecules in which excited state proton transfer, akin to a *keto-enol* tautomerisation, may occur.[43] However, given that MA does not undergo excited state proton transfer, as we have discussed in section 4.1, it is unlikely that the two peaks observed in the TR-PES spectra of MA are due to different tautomers. Furthermore, as seen in the FFT(eKE) spectra, the quantum beats appear in the same positions relative to each eKE peak. We thus propose that the observed structure in the TR-PES spectrum of MA is due to the S_1 preferentially coupling with two cationic vibrational states, likely the $D_0^+(v = 0)$ and the $v = 1$ level of a ~ 1400 cm^{-1} vibrational mode. Indeed, the TR-PES shown in Figure 4.10 (in section 4.1), obtained with a higher energy probe wavelength ($\lambda_{pr} = 260$ nm in the experiments reported in section 4.1 *vs.* $\lambda_{pr} = 285$ nm for those in this section) show additional peaks with the same energy progression, supporting the conclusion that the PES structure is due to vibrational excitation of the cationic mode accessed upon photoionisation of photoexcited MA.

With a firm assignment of the origin of each quantum beat, we now focus on the pump wavelength dependent decay times of these beats. At $\lambda_{pu} = 348$ nm, where we photoexcite only the lowest vibrational levels of MA, the persistence of ω_{179} is a signature of both a low density of states[69] and lack of "doorway states" (which mediate coupling between an initially populated state and a molecular bath of states) creating a bottleneck in the energy redistribution process.[69–71] As a result, excited state population is trapped in the $v = 1$ level of ν_{179} and we observe a long-lived ω_{179}. Conversely, at $\lambda_{pu} = 330$ nm a rapid dampening of the beats is observed; this may be due to coupling of each vibrational level to other degrees of freedom, potentially resulting in wavepacket decoherence.[72] Interestingly, the different beat frequencies appear to decay on different timescales, presenting an opportunity to investigate the level-specific coupling strengths of these vibrational modes and explore the initial steps of IVR.

Of particular interest is the similar dampening time (at $\lambda_{pu} = 330$ nm) for ω_{179} and ω_{63}, *i.e.* ~ 1.5 ps, while ω_{116} disappears within a few hundred femtoseconds (see Figure 4.21(c)). Recalling the assignment of ω_{63} and ω_{116} to interference between ν_{179} ($v =$

2) or ν_{179} (v = 3) and the v = 1 level of ν_{421}, respectively, the fact that these beats dampen on different timescales suggests that the observed dynamics are controlled by coupling between the different excited levels of ν_{179} and neighbouring vibrational states, potentially doorway states which facilitate coupling to the molecular bath. Specifically, the observed behaviour can be assigned to coupling of the v = 3 level of ν_{179} (on the dampening timescale of ω_{116}) and of the v = 2 level (approximately 1.5 ps, the dampening time of ω_{63}). The complete decay of ω_{179} at $\lambda_{\mathrm{pu}} = 330$ nm is consistent with the spectral "tail" of this pump wavelength (see Figure 4.14) photoexciting only the v $\geq$ 1 levels of ν_{179} (as opposed to $\lambda_{\mathrm{pu}} = 348$ nm, for which only ν_{179} (v = 1) is populated and thus ω_{179} is long-lived, as just discussed). We note, however, two important caveats: first, that ω_{63} and ω_{116} may actually have similar temporal behaviour as the weak FFT intensity at ~ 115 cm^{-1} may artificially shorten the observed dampening time. Secondly, the dampening time of ω_{63} may be due to loss of population from v = 1 of ν_{421}; the results at $\lambda_{\mathrm{pu}} = 330$ nm alone are insufficient to firmly assign the origin of this dampening timescale.

To garner further insight into the origin of the dampening of ω_{63}, we now consider the results at $\lambda_{\mathrm{pu}} = 344$ nm where, again, the dampening time of ω_{116} is substantially shorter than ω_{63}. Photoexcitation at this wavelength results in ω_{242} due to interference between the v = 1 levels of ν_{179} and ν_{421} (see Figure 4.19). Unfortunately, the FFT intensity at 242 cm^{-1} is nearly indistinguishable from the baseline in Figure 4.19(d) and therefore the dampening time of the v = 1 level of ν_{421} cannot be independently determined. However, Figure 4.19(d) does reveal a marked decrease of ω_{179} intensity by 1.5 ps, though the feature persists above the baseline for the remaining time delays. This temporal behaviour is consistent with the $\lambda_{\mathrm{pu}} = 348$ and 330 nm results: population in v > 1 of ν_{179} will undergo coupling to other molecular degrees of freedom while population in the v = 1 level of ν_{179} is isolated and remains trapped. Visual inspection of the FFT(Δt) plots (Figure 4.19(c)) suggest that ω_{63} is coupling to other states on a similar timescale to that of ω_{179} ($\sim$ 1.3 ps), reinforcing the previous assignment of ω_{63} to activity on the v = 2 level of ν_{179}. Furthermore, since ω_{63} arises from a ν_{179}/ν_{421} interference, the above argument would imply that the decay time of the v = 1 level of ν_{421} is $\geq$ 1.5 ps: both vibrational modes need to be populated for interference to take place, hence ν_{421} must be populated for at least as long as ω_{63} persists. This suggests that, similar to the v = 1 level of ν_{179}, population may be trapped in the v = 1 level of ν_{421}. In summary, our results provide clear evidence that ν_{179} (v = 3) has stronger interactions with the molecular bath than ν_{179}

($v = 2$), while population in ν_{179} ($v = 1$) remains isolated; these interactions constitute the crucial initial steps of IVR.[73–75]

Finally, and once again for completeness, we note a significant difference between the 1D total integrated photoelectron transient (*i.e.* without polar onion peeling deconvolution) shown in Figure 4.23 and the TR-IY transients presented in section 4.1: while TR-IY transients showed mono-exponential decay behaviour with decay lifetimes > 1.2 ns, the magic-angle total integrated photoelectron transient, produced from separate measurements for which the polarisations of the pump and probe beams were parallel or perpendicular to each other,[20] are best fit with a bi-exponential decay. The fit to the total integrated photoelectron spectrum of MA requires an additional rapid decay with a lifetime of $\tau \sim 700$ fs; similar time constants are typically attributed to IVR on the excited state surface (see, for example, reference 16), supporting our assignment of the quantum beat decay times to the initial steps of IVR. We reconcile the observation of bi-exponential decay behaviour in our TR-PES measurements, in contrast with our TR-IY measurements, by noting that the signal-to-noise ratio in our TR-IY transients is lower than the present TR-PES work, potentially obfuscating any small changes in signal. Secondly, the additional time constant may only be observable with the longer probe wavelength used in the present study (285 nm *vs.* 260 nm); shorter probe wavelengths have been previously shown to obscure dynamics.[16] Finally, the possible observation of ultrafast IVR on the S_1
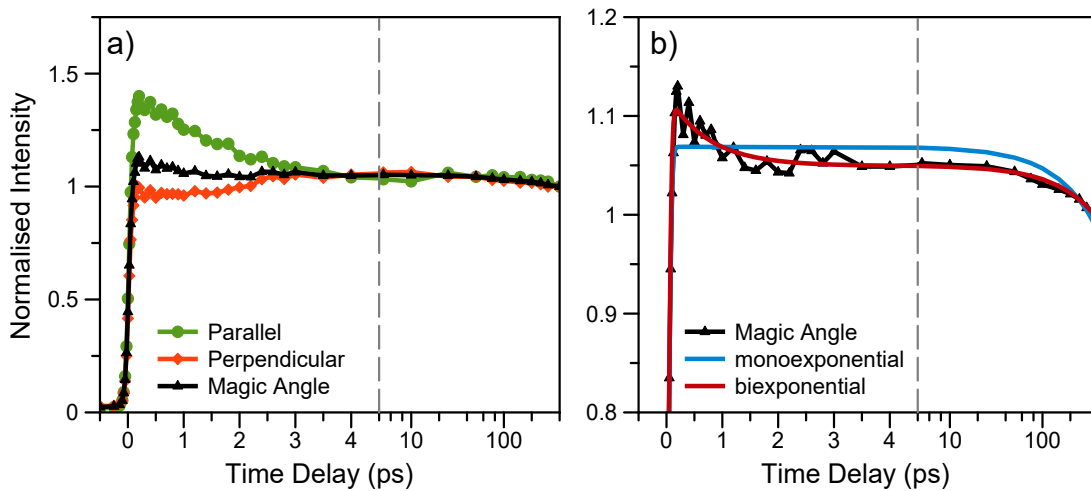

Figure 4.23: (a) TR-PES transients of MA taken at $\lambda_{pu} = 344$ nm with the pump and probe polarisations parallel (green) and perpendicular (orange). The resulting magic angle transient is shown in black. (b) Enlarged magic angle transient showing fit quality from a monoexponential (blue) or a biexponential (red) model.

state of MA in these TR-PES measurements does not alter the overarching conclusions of our previous investigation. Rather, it reinforces our conclusion that photoexcited MA is trapped near the Franck-Condon region on the S_1 surface, which we can now deduce is due to efficient coupling between the close-to-origin vibrational states of MA prompting fast IVR.

As discussed in section 4.1, the trapping of excited state population of MA in the S_1 state results in its incapability to overcome the ~ 0.4 eV barrier to a S_1/S_0 CI *via* a twisting motion of the ester group, a mechanism that has been observed in other sunscreen molecules.[15] Our TR-PES results demonstrate that this trapping may be due to efficient coupling of the photoactive modes to the molecular bath, thus decreasing the likelihood for photoexcited population to overcome the aforementioned barrier. Furthermore, as seen in Figure 4.21, the addition of the menthyl group in MenA appears to accelerate decoherence, enhance the trapping of photoexcited population, and explain the slower decay of the S_1 state of this sunscreen agent, as shown in Figure 4.2 and discussed in the previous section. At the photon energies needed to overcome the excited state barrier in MA, the trapping of excited state population due to IVR is unsurprising. However, in the present work we have observed the vibration-specific mechanisms that begin IVR, unveiling the sub-optimum photoprotection in a commercially available sunscreen precursor.

A final comment is needed here to highlight the fact that this work was still in progress at the time of publication of this thesis. Importantly, while the interpretation of results herein presented is plausible, it may be necessary to extend the limited temporal window for which these experiments were performed (up to ~ 7 ps). Namely, the loss of coherence observed in these experiments could simply be explained by the loss of coherence of the initial wavepacket as it evolves in time, rather than by the coupling between vibrational states as previously discussed at length. If the observed loss of coherence is, indeed, due to the evolution of the wavepacket, revivals would be expected, *i.e.* the signal for each frequency should reappear as the wavepacket evolution reaches another point of coherence. Therefore, a firm and final interpretation of the results presented in this section will need further investigation into longer time delays. This work is currently under-way in our laboratory.

4.2.6 Conclusion: Quantum Beats in the Anthranilates

The studies reported in this section have provided valuable insight into the vibrational energy redistribution processes occurring in MA (a sunscreen precursor) immediately after photoexcitation with UV radiation. With strong support from frequency resolved measurements and computational studies, we have mapped the time evolution of individual vibrational excited states of the S_1 state of MA. The LIF and quantum beats also provide insight into the Franck-Condon activity of the $S_1 \leftarrow S_0$ transition, as well as the relative geometries of the S_1 and D_0^+ states. Our results also suggest that vibrational coupling in MA may allow for ultrafast interactions between the photoprepared vibrational states and the molecular bath, further elucidating the trapping mechanism of excited state population of MA.

By understanding the fate of energy absorbed by a sunscreen precursor, we can unveil the key mechanisms that afford — or hinder — effective photoprotection in sunscreen active ingredients. The results presented herein highlight two possible avenues for rational sunscreen design: ensuring that Franck-Condon active vibrational modes are involved in the rapid return to the ground state and, when possible, using a molecule with fewer low frequency vibrational modes that can transfer energy away from the internal conversion reaction coordinate (*e.g.* MA or AA instead of MenA). This work thus presents an innovative approach to rational molecular design of state-of-the-art photoprotective materials with the potential to revolutionise the sunscreen industry.

4.3 Overall Conclusions and Further Comments

It is clear from the discussion in this chapter and Chapter 3 that, to identify the factors that contribute towards photoprotective capabilities it is necessary to consider the effects of molecular structure and environment on the electronic energy topography of the chromophore. Systematic evaluation of these effects should ultimately culminate in a comprehensive understanding not only of light absorption, but also of the ensuing photodynamics in sunscreen molecules, with behavioural trends being established across the range of current (and potential) sunscreen active ingredients. Such extensive knowledge of photoprotective mechanisms of action may then inform molecular structure manipulation of sunscreen molecules: efficient energy redistribution mechanisms may be enhanced, or

relaxation pathways that lead to undesirable side reactions or energy transfer hindered. In the next chapter, the findings presented in Chapters 3 and 4 are placed in the context of concurrent developments in the field of ultrafast sunscreen photodynamics in order to explore any trends identified thus far, in terms of preferred photoprotective mechanisms and how such mechanisms are affected by molecular structure or environmental factors.

4.4   Supporting Information and Additional Data

I ^{1}H NMR spectra of MA and deuterated MA
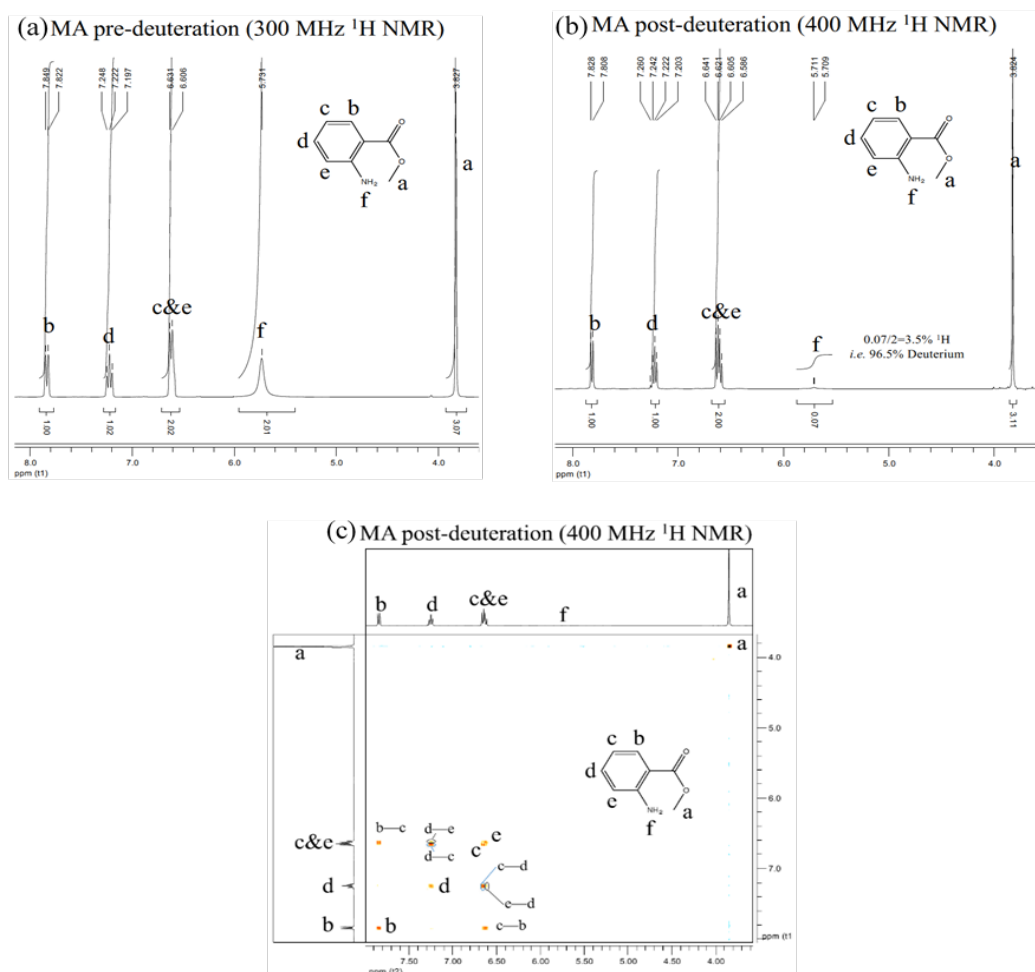
Figure 4.24: ^{1}H NMR of MA (a) and d_2-MA (b) with assigned peaks. 96.5% of the amine hydrogens have been exchanged; this includes both singly and doubly deuterated MA (with one or both hydrogens in the amine group being substituted by deuterium, respectively). (c) Correlation ^{1}H NMR of d_2-MA.

4.5 References

[1] Dean, J. C., Kusaka, R., Walsh, P. S., Allais, F. & Zwier, T. S. Plant sunscreens in the UV-B: Ultraviolet spectroscopy of jet-cooled sinapoyl malate, sinapic acid, and sinapate ester derivatives. *Journal of the American Chemical Society* **136**, 14780–14795 (2014).

[2] Baker, L. A. *et al.* Ultrafast photoprotecting sunscreens in natural plants. *The Journal of Physical Chemistry Letters* **7**, 56–61 (2016).

[3] Ferreres, F., Ginerb, J. M. & Tomás-Barberán, F. A. A comparative study of hesperetin and methyl anthranilate as markers of the floral origin of citrus honey. *Journal of the Science of Food and Agriculture* **65**, 371–372 (1994).

[4] Moio, L. & Etievant, P. X. Ethyl anthranilate, ethyl cinnamate, 2,3-dihydrocinnamate, and methyl anthranilate: Four important odorants identified in pinot noir wines of burgundy. *American Journal of Enology and Viticulture* **46**, 392–398 (1995).

[5] Avery, M. L. *et al.* Methyl anthranilate as a rice seed treatment to deter birds. *The Journal of Wildlife Management* **59**, 50–56 (1995).

[6] Askham, L. R. Efficacy of methyl anthranilate as a bird repellent on cherries, blueberries and grapes. *Proceedings of the Fifteenth Vertebrate Pest Conference* **3**, 137–141 (1992).

[7] Yadav, G. D. & Krishnan, M. S. An ecofriendly catalytic route for the preparation of perfumery grade methyl anthranilate from anthranilic acid and methanol. *Organic Process Research & Development* **2**, 86–95 (1998).

[8] Gambetta, C., Natera, J., Massad, W. A. & Garca, N. A. Methyl anthranilate as generator and quencher of reactive oxygen species: A photochemical study. *Journal of Photochemistry and Photobiology A: Chemistry* **269**, 27–33 (2013).

[9] Beeby, A. & Jones, A. E. The photophysical properties of menthyl anthranilate: A UV-A sunscreen. *Photochemistry and Photobiology* **72**, 10–15 (2000).

[10] Lowe, N. J. *Sunscreens : development, evaluation, and regulatory aspects* (Marcel Dekker, New York, 1997), 2nd edn.

[11] Aronov, E. V. & Clark, L. Degradation studies of the nonlethal bird repellent, methyl anthranilate. *Pest Management Science* **47**, 355–362 (1996).

[12] Melhuish, W. H. Quantum efficiencies of fluorescence of organic substances: Effect of solvent and concentration of the fluorescent solute. *The Journal of Physical Chemistry* **65**, 229–235 (1961).

[13] Kikuchi, A., Shibata, K., Kumasakaa, R. & Yagia, M. Excited states of menthyl anthranilate: a UV-A absorber. *Photochemical and Photobiological Sciences* **12**, 146–253 (2013).

[14] Karsili, T. N. V., Marchetti, B., Ashfold, M. N. R. & Domcke, W. *Ab Initio* study of potential ultrafast internal conversion routes in oxybenzone, caffeic acid, and ferulic acid: Implications for sunscreens. *The Journal of Physical Chemistry A* **118**, 11999–12010 (2014).

[15] Baker, L. A. *et al.* Probing the ultrafast energy dissipation mechanism of the sunscreen oxybenzone after UVA irradiation. *The Journal of Physical Chemistry Letters* **6**, 1363–1368 (2015).

[16] Peperstraete, Y. *et al.* Bottom-up excited state dynamics of two cinnamate-based sunscreen filter molecules. *Physical Chemistry Chemical Physics* **18**, 28140–28149 (2016).

[17] Worth, G. A. Beyond Born-Oppenheimer: molecular dynamics through a conical intersection. *Annual Review of Physical Chemistry* **55**, 127–158 (2004).

[18] Tan, E. M. M., Hilbers, M. & Buma, W. J. Excited-state dynamics of isolated and microsolvated cinnamate-based UV-B sunscreens. *The Journal of Physical Chemistry Letters* **5**, 2464–2468 (2014).

[19] Miyazaki, Y. *et al.* Experimental and theoretical study on the excited-state dynamics of *ortho-*, *meta-*, and *para-*methoxy methylcinnamate. *The Journal of Chemical Physics* **141**, 244313.1–244313.12 (2015).

[20] Imanbaew, D., Gelin, M. F. & Riehn, C. Rotational and vibrational dynamics in the excited electronic state of deprotonated and protonated fluorescein studied by time-resolved photofragmentation in an ion trap. *Structural Dynamics*, **3**, 043211.1–043211.12 (2016).

[21] Eppink, A. T. J. B. & Parker, D. H. Velocity map imaging of ions and electrons using electrostatic lenses: Application in photoelectron and photofragment ion imaging of molecular oxygen. *Review of Scientific Instruments* **68**, 3477–3484 (1997).

[22] Roberts, G. M., Nixon, J. L., Lecointre, J., Wrede, E. & Verlet, J. R. R. Toward real-time charged-particle image reconstruction using polar onion-peeling. *Review of Scientific Instruments* **80**, 1–17 (2009).

[23] Regan, P. M., Langford, S. R., Orr-Ewing, A. J. & Ashfold, M. N. R. The ultraviolet photodissociation dynamics of hydrogen bromide. *The Journal of Chemical Physics* **110**, 281–288 (1999).

[24] Snellenburg, J. J., Laptenok, S., Seger, R., Mullen, K. M. & van Stokkum, I. H. M. Glotaran: A Java-based graphical user interface for the R package TIMP. *Journal of Statistical Software* **49**, 1–22 (2012).

[25] Werner, H.-J. *et al.* MOLPRO, version 2010.1, a package of *ab initio* programs (2010).

[26] Werner, H.-J. A quadratically convergent MCSCF method for the simultaneous optimization of several states. *The Journal of Chemical Physics* **74**, 5794–5801 (1981).

[27] Szalay, P. G., Müller, T., Gidofalvi, G., Lischka, H. & Shepard, R. Multiconfiguration self-consistent field and multireference configuration interaction methods and applications. *Chemical Reviews* **112**, 108–181 (2012).

[28] Dunning, T. H. Gaussian basis sets for use in correlated molecular calculations. I. The atoms boron through neon and hydrogen. *The Journal of Chemical Physics* **90**, 1007–1023 (1989).

[29] Frisch, M. J. *et al.* Gaussian 09, Revision E.01 (2009).

[30] Jones, A. E. *A spectroscopic study of sunscreens.* Ph.D. thesis, Durham University (2000). Available at Durham E-Theses Online: http://etheses.dur.ac.uk/4261/.

[31] Roberts, G. M. *et al.* Unraveling ultrafast dynamics in photoexcited aniline. *Journal of the Americal Chemical Society* **134**, 12578–12589 (2012).

[32] King, G. A., Oliver, T. A. A. & Ashfold, M. N. R. Dynamical insights into $^1\pi\sigma^*$ state mediated photodissociation of aniline. *The Journal of Chemical Physics* **132**, 1–12 (2010).

[33] Marchetti, B., Karsili, T. N. V., Ashfold, M. N. R. & Domcke, W. A 'bottom up', *ab*

initio computational approach to understanding fundamental photophysical processes in nitrogen containing heterocycles, DNA bases and base pairs. *Physical Chemistry Chemical Physics* **18**, 19979–20832 (2016).

[34] Tuna, D., Nађa Došlić, Momir Mališ, Sobolewski, A. L. & Domcke, W. Mechanisms of photostability in kynurenines: A joint electronic structure and dynamics study. *The Journal of Physical Chemistry B* **119**, 2112–2124 (2015).

[35] Omidyan, R. & Iravani, M. Excited state proton transfer and deactivation mechanism of 2-(4-amino-2-hydroxyphenyl)-1h-imidazo-[4,5-c]pyridine and its analogues: A theoretical study. *The Journal of Physical Chemistry A* **120**, 1012–1019 (2016).

[36] Sobolewski, A. L. & Domcke, W. Photophysics of intramolecularly hydrogen-bonded aromatic systems: *ab initio* exploration of the excited-state deactivation mechanisms of salicylic acid. *Physical Chemistry Chemical Physics* **8**, 3410–3417 (2006).

[37] Raeker, T. & Hartke, B. Full-dimensional excited-state intramolecular proton transfer dynamics of salicylic acid. *The Journal of Physical Chemistry A* **121**, 5967–5977 (2017).

[38] Zhao, J., Ji, S., Chen, Y., Guo, H. & Yanga, P. Excited state intramolecular proton transfer (ESIPT): from principal photophysics to the development of new chromophores and applications in fluorescent molecular probes and luminescent materials. *Physical Chemistry Chemical Physics* **14**, 8803–8817 (2012).

[39] Lim, S.-J., Seo, J. & Park, S. Y. Photochromic switching of excited-state intramolecular proton-transfer (ESIPT) fluorescence: a unique route to high-contrast memory switching and nondestructive readout. *Journal of the American Chemical Society* **128**, 14542–14547 (2006).

[40] Kwon, J. E. & Park, S. Y. Advanced organic optoelectronic materials: Harnessing excited-state intramolecular proton transfer (ESIPT) process. *Advanced Materials* **23**, 3615–3642 (2011).

[41] Rodembusch, F. S., Leusin, F. P., Campo, L. F. & Stefani, V. Excited state intramolecular proton transfer in amino 2-(2-hydroxyphenyl)benzazole derivatives: Effects of the solvent and the amino group position. *Journal of Luminescence* **126**, 728–734 (2007).

[42] Southern, C. A. & Levy, D. H. Electronic and infrared spectroscopy of anthranilic acid in a supersonic jet. *The Journal of Physical Chemistry A* **107**, 4032–4040 (2003).

[43] Stolow, A. Femtosecond time-resolved photoelectron spectroscopy of polyatomic molecules. *Annual Review of Physical Chemistry* **54**, 89–119 (2003).

[44] Westheimer, F. H. The magnitude of the primary kinetic isotope effect for compounds of hydrogen and deuterium. *Chemical Reviews* **61**, 265–273 (1961).

[45] Bell, R. P. Liversidge Lecture. Recent advances in the study of kinetic hydrogen isotope effects. *Chemical Society Reviews* **3**, 513–544 (1974).

[46] Calegari, F. *et al.* Charge migration induced by attosecond pulses in bio-relevant molecules. *Journal of Physics B: Atomic, Molecular and Optical Physics* **49**, 142001.1–142001.25 (2016).

[47] El-Sayed, M. A. Triplet state. Its radiative and nonradiative properties. *Accounts of Chemical Research* **1**, 8–16 (1968).

[48] Bakker, H. J. Effect of intermolecular interactions on vibrational energy transfer in the liquid phase. *The Journal of Chemical Physics* **98**, 8496–8506 (1993).

[49] Matsumoto, S., Kumasaka, R., Yagi, M. & Kikuchi, A. Triplet-triplet energy transfer between UV absorbers in solutions at room temperature. *Journal of Photochemistry and Photobiology A: Chemistry* **346**, 396–400 (2017).

[50] Stolow, A., Bragg, A. E. & Neumark, D. M. Femtosecond time-resolved photoelectron spectroscopy. *Chemical Reviews* **104**, 1719–1757 (2004).

[51] Stolow, A. & Underwood, J. G. Timeresolved photoelectron spectroscopy of nonadiabatic dynamics in polyatomic molecules. In Rice, S. A. (ed.) *Advances in Chemical Physics*, chap. 6, 1–84 (John Wiley & Sons, Inc., Hoboken, NJ, USA, 2008).

[52] Bitto, H. & Huber, J. R. Molecular quantum beat spectroscopy. *Optics Communications* **80**, 184–198 (1990).

[53] Khalil, M., Demirdöven, N. & Tokmakoff, A. Vibrational coherence transfer characterized with Fourier-transform 2D IR spectroscopy. *The Journal of Chemical Physics* **121**, 362–373 (2004).

[54] Cina, J. A. & Fleming, G. R. Vibrational coherence transfer and trapping as sources

for long-lived quantum beats in polarized emission from energy transfer complexes. *The Journal of Physical Chemistry A* **108**, 11196–11208 (2004).

[55] Young, J., Staniforth, M., Paterson, M. & Stavros, V. Torsional motion of the chromophore catechol following the absorption of ultraviolet light. *Physical Review Letters* **114**, 233001 (2015).

[56] Ling, F. *et al.* Femtosecond time-resolved observation of butterfly vibration in electronically excited *o*-fluorophenol. *Scientific Reports* **7**, 1–8 (2017).

[57] Pillsbury, N. R., Mller, C. W., Meerts, W. L., Plusquellic, D. F. & Zwier, T. S. Conformational effects on excitonic interactions in a prototypical H-bonded bichromophore: Bis(2-hydroxyphenyl)methane. *The Journal of Physical Chemistry A* **113**, 5000–5012 (2009).

[58] Even, U., Jortner, J., Noy, D. & Lavie, N. Cooling of large molecules below 1 K and He clusters formation. *The Journal of Chemical Physics* **112**, 8068–8071 (2000).

[59] Even, U. The Even-Lavie valve as a source for high intensity supersonic beam. *EPJ Techniques and Instrumentation* **2**, 1–22 (2015).

[60] Compton, R. N., Miller, J. C., Carter, A. E. & Kruit, P. Resonantly enhanced multiphoton ionization of xenon: photoelectron enrgy analysis. *Chemical Physics Letters* **71**, 87–90 (1980).

[61] Knutson, J. R., Walbridge, D. G. & Brand, L. Decay-associated fluorescence spectra and the heterogeneous emission of alcohol dehydrogenase. *Biochemistry* **21**, 4671–4679 (1982).

[62] van Stokkum, I. H. M., Larsen, D. S. & van Grondelle, R. Global and target analysis of time-resolved spectra. *Biochimica et Biophysica Acta (BBA) - Bioenergetics* **1657**, 82–104 (2004).

[63] Schmidt, M. W. *et al.* General atomic and molecular electronic structure system. *Journal of Computational Chemistry* **14**, 1347–1363 (1993).

[64] Gordon, M. S. & Schmidt, M. W. Advances in electronic structure theory: GAMESS a decade later. In Dykstra, C., Frenking, G., Kim, K. & Scuseria, G. (eds.) *Theory and Applications of Computational Chemistry: The First Forty Years*, chap. 41, 1167–1189 (Elsevier Science, 2005).

[65] Kendall, R. A. & Dunning, T. H. Electron affinities of the first row atoms revisited. Systematic basis sets and wave functions. *The Journal of Chemical Physics* **96**, 6796–6806 (1992).

[66] Yanai, T., Tew, D. P. & Handy, N. C. A new hybrid exchange-correlation functional using the Coulomb-attenuating method (CAM-B3LYP). *Chemical Physics Letters* **393**, 51–57 (2004).

[67] Bode, B. M. & Gordon, M. S. Macmolplt: a graphical user interface for GAMESS. *Journal of Molecular Graphics and Modelling* **16**, 133–138 (1998).

[68] Pirowska, K., Kolek, P., Goclon, J. & J.Najbar. Geometry changes upon $S_0 \rightarrow S_1$ electronic excitation of aniline derivatives. *Chemical Physics Letters* **387**, 165–175 (2004).

[69] Nesbitt, D. J. & Field, R. W. Vibrational energy flow in highly excited molecules: role of intramolecular vibrational redistribution. *The Journal of Physical Chemistry* **100**, 12735–12756 (1996).

[70] Davies, J. A. & Reid, K. L. Intramolecular vibrational dynamics in S_1 *p*-fluorotoluene. I. Direct observation of doorway states. *The Journal of Chemical Physics* **135**, 124305.1– 124305.13 (2011).

[71] Fujii, M. *et al.* Mode-dependent intramolecular vibrational redistribution in the S_1 state of jet-cooled *p*-difluorobenzene. *The Journal of Physical Chemistry* **88**, 2937–2940 (1984).

[72] Brif, C., Rabitz, H., Wallentowitz, S. & Walmsley, I. A. Decoherence of molecular vibrational wave packets: Observable manifestations and control criteria. *Physical Review A* **63**, 063404 (1984).

[73] Avouris, P., Gelbart, W. M. & El-Sayed, M. A. Nonradiative electronic relaxation under collision free conditions. *Chemical Reviews* **77**, 793–833 (1977).

[74] Felker, P. M. & Zewail, A. H. Dynamics of intramolecular vibrationalenergy redistribution (IVR). I. Coherence effects. *The Journal of Chemical Physics* **82**, 2961–2974 (1985).

[75] Quack, M. Molecular quantum dynamics from high resolution spectroscopy and laser chemistry. *Journal of Molecular Structure* **292**, 171–195 (1993).

5 Structure-Dynamics-Function:

From fundamental science to product

'A ship in port is safe, but that is not what ships are for.'

Grace Hopper (1906–1992)

5.1 Overview

The ensuing discussion will place the studies presented in Chapters 3 and 4 in the wider context of recent advances in the field of ultrafast photodynamics of sunscreens, which we will review in an attempt to identify and analyse any trends emerging from the current literature on the subject. The following discussion relies strongly on a *bottom-up approach* to developing a rationale for molecular design, for which the molecular complexity of the system under study is incrementally increased; we employed the same approach to the studies presented in Chapters 3 and 4. Such an approach involves studying sunscreen molecules first in isolation (in vacuum) so that their intrinsic properties are understood and the effects of substituent position and/or functional group are evaluated. In order to understand the closer to real-life behaviour of the active ingredients in a sunscreen formulation, solvent effects on sunscreen photodynamics then need to be explored. Pushing the current boundaries of knowledge in this field will involve studying sunscreen mixtures in different solvents, thin films, and, ultimately, *in vivo*. While the emphasis of this chapter will be on time-resolved ultrafast spectroscopic techniques, in line with the remainder of this thesis, this chapter also focuses mainly on studies in solution, *i.e.* closer to the conditions in which sunscreens are used. In addition, results from other types of experiment and/or computational studies may also be evoked to inform the discussion and prompt future work.

5.2   Photophysical Mechanisms

As discussed in detail in Chapter 1, the photophysics of an ideal sunscreen molecule should allow for fast dissipation of excess energy as harmless heat, with no detriment to molecular integrity. In other words, a sunscreen molecule should efficiently transition from a given electronic excited to the electronic ground (S_0) state. As we have discussed and exemplified in previous chapters, such transitions between electronic states are commonly facilitated by conical intersections (CIs) at particular molecular geometries. Certain molecular motions undergone by photoexcited sunscreen molecules may drive them towards a CI with the S_0 state, thus allowing for fast relaxation to take place. In the next section we will review two such motions: *trans-cis* isomerisation and excited-state intramolecular proton transfer. These processes have been identified in the studies presented in Chapters 3 and 4 of this thesis and have also been observed in a series of other sunscreen molecules studied by other authors, indicating that these are key photoprotection mechanisms.

5.2.1   *Trans/Cis* isomerisation

Photoisomerisation has been found to be the preferred relaxation mechanism for a family of sunscreens used in commercial formulations, the cinnamates, an example of which (ethyl ferulate, EF, Figure 5.1) we have explored in Chapter 3. In our studies, we found that photoexcitation of EF to its first singlet excited state (S_1) was found to prompt an initial geometry relaxation followed by an evolution along the photoisomerisation coordinate. The *cis*-isomer, the presence of which we confirmed by ^{1}H NMR, was observed to appear approximately 2 ps after photoexcitation and to persist for several nanoseconds, as summarised in Table 5.1. However, our results were insufficient to unambiguously determine how many CIs were involved in the relaxation mechanism of EF; two possible mechanisms were suggested, as shown diagrammatically in Figure 5.2.

The photoisomerisation trend carries on for other cinnamates that are popular choices for commercial sunscreen formulations. Early gas-phase studies by Buma and co-workers on one of the most common UVB filters currently on the market, 2-ethylhexyl-E-4-methoxycinnamate (*E*-EHMC, where *E* refers to the isomer, see figure 5.1), had already found that clustering this molecule with a solvent resulted in efficient energy dissipation[1] — we shall explore how this differs from the case of the isolated molecule later on in

trans-cis Photoisomerisation

Ethyl Ferulate (EF)
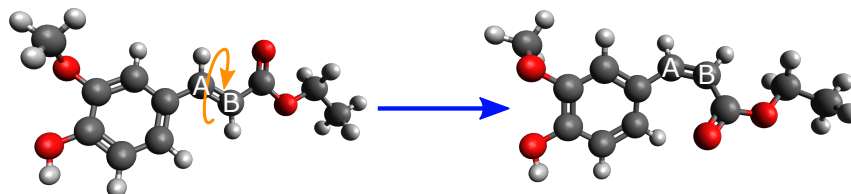
Ethylhexyl Methoxycinnamate (EHMC)
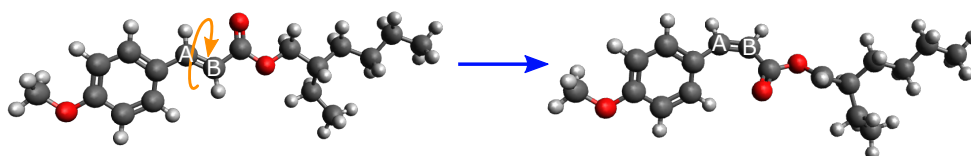
Sinapoyl Malate (SM)
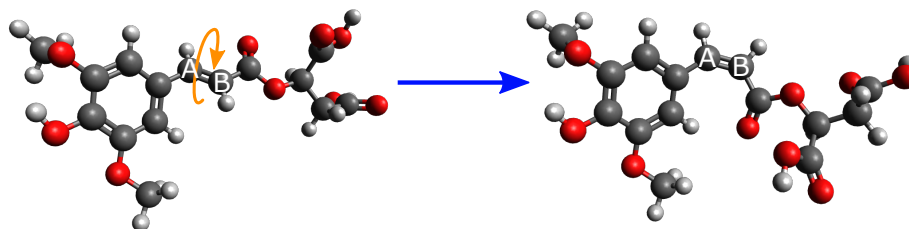
Figure 5.1: Representation of the isomerisation undergone by cinnamates and sinapoyl malate upon photoexcitation with UV radiation. It is this molecular motion that facilitates IC to the ground energy state in these molecules, ultimately affording them their photoprotective capabilities. It is desirable, however, that the resulting isomers retain such photoprotective capabilities and, importantly, that they are non-toxic.

this chapter. These gas-phase studies were expanded on by Peperstraete *et al.*, who also explored the excited state dynamics of *E*-EHMC in solution.[2] Peperstraete *et al.* photoexcited *E*-EHMC at its absorption peak (in the UV region) in both cyclohexane and methanol and found that, similarly to the other cinnamates discussed above, the resulting photodynamics are generally appropriately described by three time constants: $\tau_1 \sim 0.2$ – 0.6 ps, assigned to energy redistribution to the solvent (often accompanied by solvent rearrangement and molecular geometry relaxation), $\tau_2 \sim 0.7$ – 2 ps, assigned to photoisomerisation *via* a S_1/S_0 CI and, finally, $\tau_3 > 2$ ns, which reflects the persistence of the long-lived Z (*cis-*) isomer. As for the case of our studies on EF, the presence of the Z photoproduct was confirmed by comparison of the long-time TAS with the ΔUV/Vis and ^{1}H NMR spectra.[2]

There is further evidence suggesting that photoisomerisation may be one of nature's
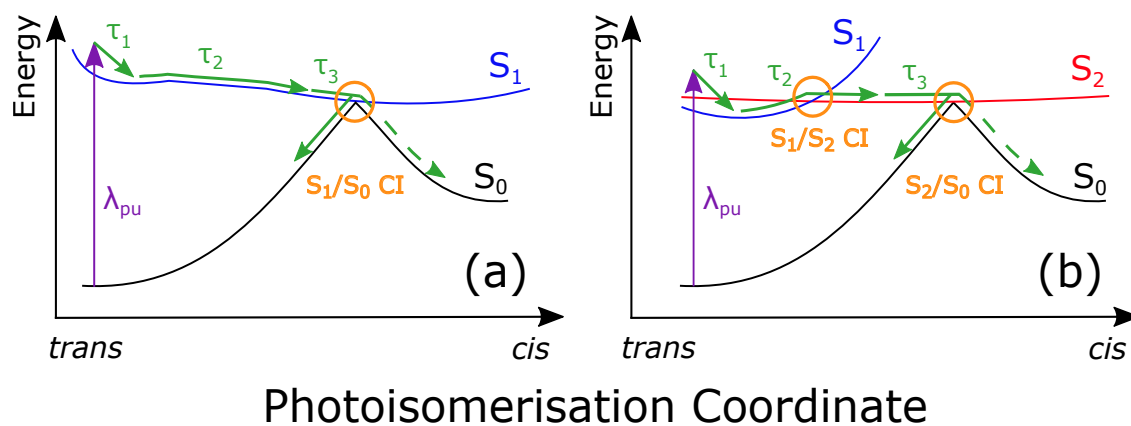
Figure 5.2: Representative schematic of the two relaxation mechanisms suggested to be responsible for the photodynamics of EF (in our studies) and in EHMC and SM in references 2 and 3, respectively. In mechanism (a) photoisomerisation occurs *via* an S_1/S_0 CI, while mechanism (b) proposes that an additional S_1/S_2 CI is involved in the photoisomerisation pathway.

preferred mechanism for dissipating excess energy resulting from absorption of UV radiation. Frequency resolved studies by Zwier and co-workers on sinapoyl malate (SM), the primary UVB filter in the leaves of *Brassicaceae* plants, had already identified the possibility for photoexcited SM to dissipate excess energy and return to its ground state *via* an efficient relaxation mechanism that would avoid undesirable side photochemistry.[4] At the time of Zwier's studies, however, there was no experimental or computational time-resolved information on the photochemical and/or photophysical processes occurring in SM.

Subsequent work by Baker *et al.* employed TEAS to explore the photophysical processes that follow photoexcitation of SM and thus unveiled the relaxation mechanisms that afford this natural molecule its photoprotective capabilities.[3] Photoexcitation of SM to its first singlet excited state (S_1) was found to initially be followed by geometry relaxation occurring within $\tau_1 \sim 50 – 600$ fs, depending on solvent. Both solvent rearrangement and internal conversion (IC) to a second electronic state, S_2, then occur ($\tau_2 \sim 1 – 5$ ps) *via* a S_1/S_2 CI.[3] Once on the S_2 state, SM undergoes photoisomerisation to its *cis*-isomer *via* a S_2/S_0 CI within $\sim 20 – 30$ ps.[3] The S_2/S_0 CI may also allow for the ground state *trans*-isomer of SM to be reformed. However, as was the case for our studies on EF, Baker *et al.* highlighted that they could not rule out the possibility that photoisomerisation would be facilitated by a single S_1/S_0 CI, as shown in Figure 5.2. It is interesting to note here that Baker *et al.* also studied the biological precursor to SM, sinapic acid (SA), having found

Table 5.1: Summary of the time constants extracted from TEAS measurements (parallel studies by different authors) along with their assigned process within the relaxation mechanisms of these molecules.

Molecule (author)[ref]	τ_1 / fs *Geometry relaxation/solvent rearrangement/energy redistribution*	τ_2 / ps *IC/evolution along photoisomerisation coordinate*	τ_3 / ps *Appearance of the cis-isomer*	τ_4 *Persistence of the cis-isomer*
EF (our studies)	$50 - 500$	$1 - 3$	$5 - 15$	$\gg$ ns
EHMC (Peperstraete)[2]	$200 - 600$	—	$0.7 - 2$	$\gg$ ns
SM (Baker)[3]	$50 - 600$	$1 - 5$	$20 - 30$	$\gg$ ns

no significant differences between their excited state dynamics.[3] It would seem counter-intuitive for a biological system to undergo a more energetically demanding process to produce a more complex molecule that would ultimately afford the same photoprotection. As discussed later in this chapter, in section 5.4.1, nature's choice of SM over SA may be related to the natural pH of plant leaves.

These examples highlight the importance of photoisomerisation as a mechanism by which sunscreen molecules dissipate the excess energy resulting from absorption of UV radiation. In fact, as we will see in the next section, even when sunscreen photodynamics are initially facilitated by other photophysical processes, photoisomerisation still plays a vital role in their ability to safely and effectively dissipate excess energy. However, it is important that the isomeric photoproduct is itself a safe and efficient UV absorber, and hence the photodynamics of the isomeric species should also be evaluated; it is also crucial that the final isomer is non-toxic — something that has recently been questioned for EHMC.[5] Moreover, evaluating how structural and environmental effects affect photoisomerisation in sunscreens — as we will discuss in subsequent sections — is of the utmost importance if a comprehensive understanding of the ultrafast mechanisms that afford photoprotection is to be achieved.

5.2.2 Excited State Intramolecular Proton Transfer (ESIPT) and *keto-enol* tautomerisation

Sunscreen molecules with an intramolecular hydrogen bond along which excited state proton transfer and/or tautomerisation processes may occur, such as the anthranilates discussed in Chapter 4 and salicylates, are usually referred to in sunscreen literature as "stable" and "safe" compounds.[6,7] While the enhanced excited state stability provided by intramolecular proton transfer (ESIPT) and *keto-enol* tautomerisation may hinder photofragmentation, the resulting (potentially) long-lived excited states are undesirable: the longer the excited state lifetimes, the higher the probability of energy transfer, from both singlet or triplet states, that may initiate harmful side photochemistry.[8–10] Nevertheless, there are currently marketed UV absorbers whose relaxation mechanisms are facilitated by these proton transfer processes.

One such example is avobenzone, shown in Figure 5.3(a), one of the most widely used UVA absorbers currently available on the market.[11] Avobenzone is known to exchange between its *enol* and *diketo* forms (*via* an *enol-keto* tautomerisation mechanism), which is thought to be the source of its undesirable photoinstability. Dunkelberger *et al.*[12] performed TEAS studies on avobenzone and modelled the resulting TAS with two time constants. The first, $\tau_1 \sim 0.5 - 1$ ps, reflects the decay of the S_1 state of avobenzone into a vibrationally hot *enol* and three non-chelated *enol* (NCE) isomers of avobenzone (see Figure 5.3(a)).[12] Following the decay of the S_1 state, Dunkelberger *et al.* were also able to observe the vibrational relaxation of hot *enol* avobenzone occurring within ~ 6 ps.[12] In addition, the authors found evidence for three further distinct relaxation processes, which they assigned to the appearance and subsequent relaxation of the three NCE isomers of avobenzone. The yield of *diketo* avobenzone, known to generate triplet states and subsequently lead to photodegradation and reactive oxygen species (ROS),[13] was found to be negligible, in accordance with previous parallel studies.[12,14]

Another example of a sunscreen molecule that undergoes *enol-keto* tautomerisation is oxybenzone, which was studied in solution by Baker *et al.*[15] In this case, migration of the intramolecularly bound hydrogen is accompanied by necessary rotational motion along the central C—C bond (see Figure 5.3(b)) leading to a CI with S_0; a twisted chelated *keto*-isomer is thus formed within a few hundred femtoseconds. However, the unstable chelated *keto*-isomer (on the S_0 potential energy surface) quickly decays into a vibrationally hot

Figure 5.3: Different relaxation mechanisms facilitated by ESIPT/*keto-enol* tautomerisation: the examples of (a) avobenzone, (b) oxybenzone and (c) meradimate (MenA) are presented. Figures adapted, respectively, from references (a) 12, (b) 15; figure (c) is based on the results presented in Chapter 4.

form of the chelated *enol*, which is then observed to cool by energy transfer to the solvent within $\sim 5 - 8$ ps.[15] Baker *et al.* also found evidence of a photoproduct being formed upon photoexcitation of oxybenzone which, by comparison of experimental data with computational studies, the authors identified as the long-lived (> 1.3 ns) *trans-keto*-isomer of oxybenzone, resulting from the photoisomerisation of the vibrationally hot chelated *keto*-isomer (see Figure 5.3(b)).[15] The authors suggested a quantum yield of formation for the *trans-keto*-isomer of approximately 10%, which could be significant if this isomer was found to have harmful effects on the skin. However, to the best of our knowledge,

the effects of *trans-keto* oxybenzone on the skin, specifically, remain unexplored, even though oxybenzone has been found to pose a risk for the development of photocontact allergic reactions.[16,17] Given the results of the study by Baker *et al.*, oxybenzone seems a close-to-ideal sunscreen: a strong UVA/UVB absorber which dissipates energy within a few picoseconds, almost completely regenerating to its ground energetic state. However, oxybenzone is a known endocrine disruptor and, therefore, there are concerns regarding its use in commercial sunscreen formulations.[18] Oxybenzone has also been found to have adverse effects on marine environments, particularly coral bleaching,[19] further hindering its suitability for use in commercial sunscreen formulations.

It is interesting to note that both the cases of avobenzone and oxybenzone show significant differences to the case of MenA (or *meradimate* as it is commercially known, shown in Figure 5.3(c)), which we have discussed in Chapter 4 along with its precursor MA. Having studied MenA both in vacuum and in solution, we found that photoexciting this sunscreen both in the UVA (330 nm) and UVB (315 nm) regions of the electromagnetic spectrum accesses an excited state (S_1) which persists for several nanoseconds, with no significant ultrafast photophysics taking place; we then proposed that the excited population of MenA is trapped in an electronic state in which H-atom dislocation, akin to an incomplete *keto-enol* isomerisation, occurs between the amino and carbonyl groups. This is in stark contrast with the case of oxybenzone, as discussed above, for which the *keto-enol* isomerisation, followed by a rotation motion, allows for quick dissipation of energy. While we have found evidence (from computational studies) for a nearby S_1/S_0 CI along a twisting motion around the C—C bond connecting the phenyl ring and the ester substituent, akin to the relaxation mechanism of oxybenzone, we have also established that the energy barrier for this twisting motion is outside the UVA/UVB range in MenA and thus would not be accessed in the context of normal sunscreen usage. Moreover, our quantum beat studies on MA (see Chapter 4, section 4.2) have also identified mechanisms which may facilitate highly efficient intramolecular energy redistribution mechanisms and thus enhance excited state population trapping on the S_1 state. Nevertheless, our studies suggest that if the energy barrier for this motion could be lowered by careful molecular design, then an effective relaxation pathway may be opened (akin to oxybenzone) and potentially optimum photoprotection capabilities could be achieved.

This section highlights the marked discrepancies in photochemical and photophysical behaviour between the anthranilates we have studied and similar systems, namely avoben-

zone and oxybenzone, despite the common ESIPT/*keto-enol* tautomerisation mechanism. Moreover, these observations are also in contrast with the cinnamates, for which the same *trans-cis* photoisomerisation process across a range of different cinnamates results in virtually the same photodynamics; ESIPT/*keto-enol* tautomerisation thus appears to be more sensitive to the overall molecular structure (but not necessarily environment since, as we have discussed in Chapter 4, MA and MenA present similar photodynamics both in vacuum and in solution). The case studies presented in this section highlight the importance of evaluating the effects of molecular structure on the photodynamics of sunscreen molecules, as is explored in the next section.

5.3   Molecular Structure Effects

It has long been known that substitution of aromatic rings alters their electronic structure and that both the nature and position of substituents influences the molecule's photodynamics.[20–25] In addition, time-resolved techniques have previously been successfully applied to evaluate how substituent effects alter molecular relaxation dynamics of aromatic systems.[24–26] Gathering a comprehensive understanding of how substituent nature (functional group) and position may affect the relaxation mechanisms of sunscreen molecules — a discussion we aim to initiate in the following sections — may inform future design of advanced sunscreens tailor-made for optimum photoprotection.

5.3.1   Functional Groups

Some molecular structural changes, despite increasing the molecular complexity quite significantly, do not alter the photo-induced ultrafast dynamics of the molecule. One such example would be the cases of the anthranilates discussed in Chapter 4: both the absorption spectra and the photodynamics of either molecule are virtually unchanged despite the addition of the large ($C_{10}H_{19}$) menthyl unit in MenA when compared to MA. Another example of similar photodynamics despite increased molecular complexity would be the precursor/sunscreen pair methyl-4-methoxycinnamate (MMC)/EHMC, as studied by Peperstraete *et al.*[2] MMC differs from EHMC in that, in place of the more complex ethylhexyl chain (in EHMC, see Figure 5.1), there is only a methyl group. This difference was found to have negligible impact on the observed photodynamics, as could perhaps be expected given the non-perturbative character of the molecular units in question (alkyl

chains).[2] Similarly, substituting the ester group in EF by a carboxylic acid — yielding the natural compound ferulic acid (FA) — was also found to have no impact on the observed photodynamics in studies by Horbury *et al.*, who found photoisomerisation still is the dominant relaxation pathway for the case of FA.[27] Moreover, as for EF, the intramolecularly bound phenolic OH group in FA does not dissociate (see the discussion in Chapter 3) and, while radical species (not observed for EF) were observed in FA by Horbury *et al.*, these were found to be an artefact of high laser powers and, therefore, not relevant in the context of normal sunscreen use under solar-like conditions.[27] The main relaxation pathway for FA is, therefore, virtually unchanged from the case of EF, *i.e. trans-cis* photoisomerisation.[27]

On the other hand, we have shown on our comparison studies between EF and its non-carbonyl compound precursors MVP and ConA, described in Chapter 3, that a carbonyl moiety may have a drastic effect on the observed photodynamics. We have established that photoexcited MVP and ConA both have long-lived excited states (> 1.2 ns), with the addition of the alcohol unit (MVP *vs.* ConA) thus appearing not to have any significant impact on the observed photodynamics. However, when an ester group is added in EF, the photodynamics are accelerated and we then proposed the corresponding relaxation mechanism to involve triplet states and fluorescence (in vacuum, see Chapter 3). Triplet state photochemistry becoming relevant upon addition of the ester functionality is in line with previous observations for carbonyl compounds, whose photochemistry is currently known to involve triplet staes.[28,29] The ester group was thus shown to alter the electronic structure of the molecule in such a way that it accelerated the relaxation of photoexcited EF, suggesting that the ester group plays an important role in the photoprotective capabilities of cinnamates.

Finally, we explore how different substituents affect photodynamics which are mediated by *keto-enol* tautomerisations, discussed previously. It is interesting to note that, in the case of oxybenzone, tautomerisation occurs, with the H-atom being transferred to the nearby oxygen and rotation around the central C—C bond then occurring as a result.[15] In *ortho*-hydroxybenzaldehyde, studied in the gas-phase with TR-PES by Stolow and co-workers, tautomerisation was also found to occur completely, with the *keto* and *enol*-isomers having well defined potential energy minima.[30] In MenA, the H-atom is exchanged between a nitrogen and an oxygen, as opposed to two oxygens in the former examples. Moreover, as discussed in previous sections of this chapter and in greater de-

tail in Chapter 4, MenA undergoes only an H-atom dislocation, rather than a complete transfer, ultimately resulting in a long-lived excited state. Using gas-phase frequency resolved techniques, Zwier and co-workers found that an H-atom dislocation mechanism (as opposed to complete transfer) also takes place for the carboxylic acid version of MenA, anthranilic acid.[31] Should chelated *enol* sunscreen molecules (such as oxybenzone), then, be preferred over their amino counterparts (*e.g.* long-lived excited state MenA)? Could MenA be a better sunscreen if the amino group was substituted by a hydroxy group? This change would yield a compound of the salicylate family, another category of sunscreen molecules currently used in the market. Some salicylates commonly found in commercial sunscreen formulations have been shown to generate triplet states,[32] while salicylic acid has been found to be toxic when used in relatively high concentrations.[33] To the best of our knowledge, however, the ultrafast photodynamics of salicylates remains largely unreported, particularly in the context of sunscreen development.

The examples of the cinnamates and anthranilates discussed here touch only the surface of the question of the effects of different functional groups on sunscreen photodynamics. With few studies having been carried out to date, there is not enough information to establish any behavioural trends and thus answer questions such as: are carbonyl compounds always good sunscreens? Do amino groups in tautomerising compounds always result in long-lived excited states? Given that each molecule has a specific electronic structure, which different functional groups will affect differently, establishing said trends presents itself as a monumental task. Nevertheless, being able to rationalise what functional groups tend to facilitate optimum relaxation mechanisms may prove crucial for effective sunscreen design and, therefore, further work on this topic is of the utmost importance.

5.3.2   Substituent Positioning

While the effects of substituent positioning (*ortho*, *meta*, *para*, see Figure 5.4) on the electronic structure of benzene rings and thus their overall chemical behaviour is well documented,[23,24] a comprehensive understanding of how these effects alter the ultrafast photodynamics of these molecules — particularly, of the sunscreen molecules we are here discussing — remains inadequate. An example of the approach required for such an understanding to be garnered is that of the studies by Promkatkaew *et al.*[34] These authors systematically studied a series of cinnamates and cinnamic acids using steady state spectroscopy — *i.e.* by measuring UV/Vis absorbance and emission spectra — accompanied by
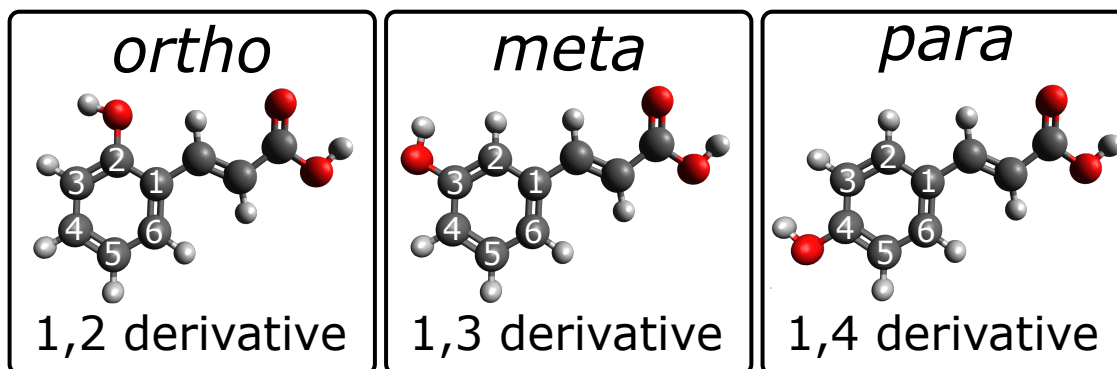
Figure 5.4: The *ortho*, *meta* and *para* substituent positions illustrated by the examples of some of the cinnamic acid derivatives studied by Promkatkaew *et al.*[34] These substituent positions can also be referred to in terms of numerical ordering of substituents, *i.e. ortho* compounds are substituted in positions 1 and 2, *meta* compounds are substituted in positions 1 and 3 and *para* compounds are substituted in positions 1 and 4.

theoretical studies. While the study by Promkatkaew *et al.* did not involve time-resolved spectroscopy, it constitutes a good example of how a systematic bottom-up approach may be used in exploring substituent position effects in sunscreen molecules and thus deserves a brief mention here.

Promkatkaew *et al.* studied eighteen different cinnamates and cinnamic acids and systematically explored the effects of hydroxy, nitro and fluoro substitutions at *ortho*, *meta* and *para* positions on their photophysical properties, with particular interest in the resulting photoprotective capabilities of these molecules.[34] These authors first report on the effects of substituent position on the shapes of absorption spectra: for hydroxy derivatives, for example, *ortho*-cinnamates show two distinct absorption bands, while the analogous *meta* compounds have a single absorption band with asymmetric shoulders and the *para* compounds present single broad absorption bands.[34] The same authors also found that the nature and positions of substituents could influence relaxation pathways. It was established in their work that electron-withdrawing (nitro and fluoro) groups tend to encourage relaxation mechanisms *via* triplet states, while compounds with electron-donating (hydroxy) groups tend to decay *via* singlet excited states.[34] Promkatkaew *et al.* point out, however, that this trend is highly dependent on substituent position. For example, these authors found that *meta*-hydroxy cinnamate derivatives show significantly more emission than their *para* counterparts, suggesting that the *para* substituent position promotes nonradiative decay pathways. In addition, the authors evaluated the photostability of the species under study by measuring their absorption spectra before and after irradiation (at

several time intervals) — Promkatkaew *et al.* then considered the molecule to be photo-stable if the absorption spectra are unchanged upon irradiation. It is worth noting here that this definition of "photostability", unlike the one we have thus far employed, does not take into consideration ultrafast mechanisms by which a sunscreen molecule dissipates energy, nor does it take into account species that may be released upon photoexcitation but not readily observed in steady-state spectra (radicals, isomers with similar UV ab-sorption spectra, *etc.*). Nevertheless, based on absorption and emission spectra and on the results from their photostability analysis, Promkatkaew *et al.* conclude that *para*-hydroxy cinnamate derivatives (a category within which, interestingly, EF is included) are the best sunscreen candidates.[34]

Following the systematic appproach of the studies by Promkatkaew *et al.*, we have attempted to evaluate the impact on substituent positioning on the photodynamics of anthranilates. We initiated these studies by obtaining preliminary TR-IY transients (in vacuum) for *meta-* and *para*-MA photoexcited to their respective S_1 states (note that MA is, in itself, an *ortho*-compound). The energy of the S_1 state of *meta*-MA was estimated from its steady-state UV/Vis absorption spectrum in cyclohexane, shown in Figure 5.5. In the case of *para*-MA, the S_1 state energy was instead estimated from gas-phase absorption spectra reported in the literature.[35] While the data obtained requires further analysis, some key points become immediately clear with these initial results. Firstly, the UV/Vis spectrum of *meta*-MA maintains the broad absorption peak observed for *ortho*-MA in the $\sim 310 - 320$ nm region, despite a considerable blue shift and decrease in absorption strength. Neverthless, the UV/Vis absorption spectra of *ortho-* and *meta*-MA are similar. The absorption spectrum is drastically changed when substitution of MA is done in the *para-* position, however: *para*-MA shows strong absorption at ~ 270 nm, with a slight shoulder at ~ 280 nm which likely corresponds to the S_1 state; the corresponding absorp-tion in vapour has been reported to be located at 288 nm.[35] It is interesting to note that a change in substituent position, even between the similar *ortho-* and *meta-* derivatives, has a more significant impact on the absorption spectra of MA than the addition of the menthyl unit, to create MenA, as discussed earlier and in Chapter 4.

With respect to the impact of substituent position on the photodynamics of the dif-ferent MA derivatives, we have found that the relative changes observed in the absorption spectra are not the same as observed for TR-IY transients, shown in Figure 5.6. That is, while the most significant differences observed in the absorption spectra are between *or-*
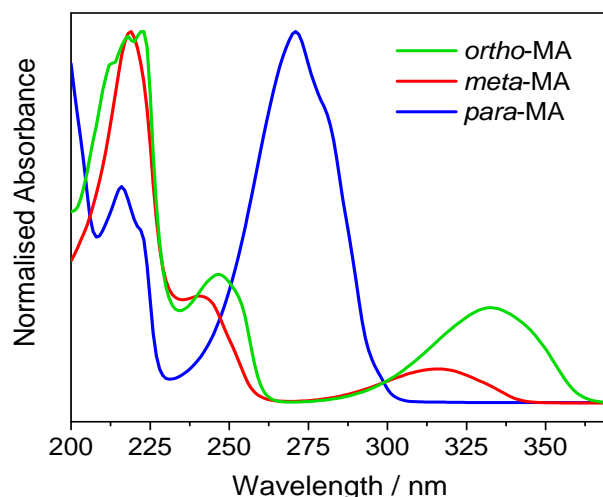
Figure 5.5: UV/Vis absorption spectra for dilute ($\sim 10^{-6}$ M) solutions of *ortho*- (green line), *meta*- (red line) and *para*-MA (blue line) in cyclohexane. Spectra were normalised to their respective absorption maxima.

tho-/*meta*- and *para*-MA, in terms of TR-IY transients, *meta*-MA is the derivative whose behaviour is most distinct from the other two compounds. We have presented results in Chapter 4 which demonstrate that the S_1 state of *ortho*-MA is long-lived (> 1.2 ns), and we have explained these observations in light of the intramolecular hydrogen bond which stabilises the first electronic excited state of MA; we have also elucidated the mechanisms by which excited state population becomes trapped on the S_1 surface of MA, unable to acccess a nearby CI along a rotation motion (see Chapter 4). Regardless of the absence of an intramolecular hydrogen bond in *para*-MA (*c.f.* *ortho*-MA), an equally long-lived state is observed for *para*-MA upon photoexcitation to its S_1 state, as shown in Figure 5.6(b). While the interpretation of these results is thus far preliminary and awaits further insights from computational studies, it is likely that the stabilisation of the first electronic excited state of *para*-MA is due to a twisted-intramolecular-charge-transfer (TICT) state; such states have been extensively reported for similar *para*-substituted compounds.[36–39] If a TICT state is indeed responsible for the observed photodynamics in *para*-MA, it will be important to evaluate solvent effects for this molecules, since such states have been found to be significantly affected by interactions with solvents.[40]

On the other hand, the TR-IY transients for *meta*-MA, shown in Figure 5.6(a), reveal a significantly shorter lifetime for its S_1 state, of approximately 1.7 ns (just outside the temporal probe window of our TR-IY experiments, see Chapter 2 for more details). Presumably, the stabilisation afforded to the excited states of *ortho*- and *para*- MA due to an intramolecular hydrogen bond or TICT state, respectively, is lost in the case of
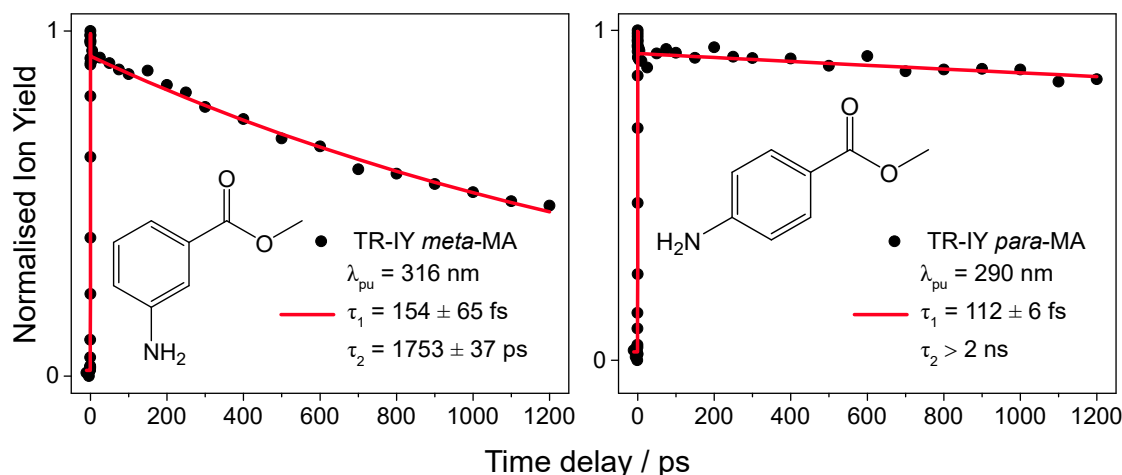
Figure 5.6: TR-IY transients for *meta*- and *para*-MA, obtained according to the methodology described in Chapter 2, section 2.2.1.1 and fit as described in section 2.4.3. The insets correspond to the molecular structures of *meta*- and *para*-MA. The extracted constants are also shown and are as follows: *meta*-MA ($\lambda_{pu} = 316$ nm), $\tau_1 = 154 \pm 65$ fs and $\tau_2 = 1753 \pm 37$ ps; *para*-MA ($\lambda_{pu} = 290$ nm), $\tau_1 = 112 \pm 6$ fs and $\tau_2 > 2$ ns.

meta-MA and a faster relaxation pathway is now accessible. The focus of our studies in the near future will be, apart from evaluating the impact of solvents on these gas-phase photodynamics, to unveil the mechanism by which *meta*-MA dissipates excess energy. While the low absorption of *meta*-MA accross the UVA/UVB wavelength range is likely to hinder its use in sunscreen formulations, it may serve as a case study to reveal an alternative relaxation pathway and potentially inform the molecular design of other sunscreen molecules.

The aforementioned studies provide valuable insight into substituent effects on the photodynamics of sunscreen molecules and their derivatives. In their publication, Promkatkaew *et al.* highlight the need for time-resolved measurements corresponding to their studies on cinnamates and cinnamic acids to be carried out in order to understand the relaxation mechanisms of these molecules, and thus better understand substituent effects on photodynamics.[34] Indeed, systematically studying the same eighteen species (or other such series of related molecules) with time-resolved laser spectroscopy techniques could reveal key trends in the photodynamics of differently substituted sunscreens; while we have made initial efforts towards such systematic studies on anthranilates, further work is necessary for any significant trends to be established. Such insight would expedite the molecular design of sunscreen molecules which are tailor made for optimised photoprotection.

5.4   Environmental Effects

It is intuitive that the surroundings of a molecule would have an effect on its electronic structure. The importance of solvent effects on the photochemical behaviour of sunscreens has long been recognised, and reports on the effect of solvent on their UV/Vis and Raman spectra, for example, are readily available in the literature.[6,41,42] However, a similarly extensive understanding of how solvent interactions affect the ultrafast photodynamics of sunscreen molecules remains elusive. Moreover, several aspects of the surroundings of a molecule affect its chemistry, such as solvent polarity, pH and viscosity, all of which are, therefore, worthy of attention when considering solvent effects on sunscreen active ingredients. In what follows, we will not only explore how solvent factors affect the ultrafast photodynamics of sunscreen molecules, but we will take a step forward in complexity and explore studies that have been carried out on sunscreen molecules within mixtures that more closely resemble real-life sunscreen formulations.

5.4.1   Solvent (vacuum *vs.* solution)

In comparison with a molecule in isolation (in vacuum), a solvated molecule (in solution) has a solvent "bath" into which it may dissipate excess energy. The presence of solvent can thus have a drastic impact on the observed photodynamics. In the specific case of EHMC, TR-IY (vacuum) studies by Peperstraete *et al.* revealed a long lifetime upon photoexcitation within the UVA/UVB range, assigned to a long-lived $^1n\pi^*$ state.[2] Tan *et al.* had already observed that clustering EHMC with water resulted in this long-lived behaviour being altered.[1] Peperstraete *et al.* expanded on these studies to reveal that even a non-polar (thus minimally perturbing) solvent such as cyclohexane caused sufficient re-ordering of the excited states of EHMC so as to facilitate ultrafast photoisomerisation to occur (as discussed in section 5.2.1).[1,2] Similar observations and conclusions can be drawn from our studies on EF (see Chapter 3), for which gas-phase TR-IY transients revealed a tri-exponential decay involving long-lived, potentially reactive triplet states (which may prompt singlet oxygen sensitising or fragmentation[43,44]). However, as for EHMC, we have found that solvent effects — even those of the weakly perturbing cyclohexane — allow for photoisomerisation relaxation pathways to become accessible in EF, justifying its use in sunscreen formulations. The solvent effects in these cases are evident, playing a crucial role in the suitability of EHMC and EF for use as efficient sunscreens. These experimental

observations are also in line with computational studies by Chang *et al.* which predicted significant changes in the energy barrier towards photoisomerisation in solution *vs.* in vacuum.[45]

It is not always the case, however, that solvents will significantly alter the gas-phase photodynamics of sunscreen molecules, as we have shown with our studies on MA and MenA, presented in Chapter 4. Both in vacuum and solution, MA and MenA are long-lived (> 1.2 ns) and photoexcitation of these molecules to their S_1 state is suggested to result in trapping of the excited state population, with no accessible CIs from this state at the pump energies used (330 nm $\leq \lambda_{pu} \leq$ 300 nm). Thus, radiative decay pathways (fluorescence and phosphorescence) were suggested for MA and MenA both in vacuum and solution. Therefore, solvent effects (at least those of cyclohexane and methanol) have been shown to not greatly affect the ultrafast photodynamics of the anthranilates we have studied, in contrast to what has been observed for the cinnamates.

The case study of how cinnamates react to solvent interactions *vs.* anthranilates, and only for single-solvent solutions in cyclohexane and/or methanol, is of course not a significant sample to allow for behavioural trends to be established in terms of the response of sunscreen photodynamics to different solvents. Nevertheless, our studies have highlighted the complexity of the effects of solvation on ultrafast photodynamics which, since they can vary significantly across different sunscreen molecules, remain poorly understood. Comprehensive studies focusing solely on such effects are required if the development of photophysically ideal sunscreen molecules, designed for optimum photoprotection, is to be pursued, as this will have an impact on sunscreen performance in real-life formulations. Computational studies on such sunscreen-solvent interactions could prove to be extremely useful in guiding and informing experimental observations, as they have thus far for other aspects of sunscreen photodynamics; the difficulty of modelling solute-solvent interactions computationally may be one of the reasons progress has been slow in this area of research.

5.4.2   pH

Parallel studies by Luo *et al.*[46] and Wang *et al.*[47] have recently explored the effects of environment pH on the photodynamics of sinapic acid/sinapoyl malate and ferulic acid, respectively. Wang *et al.* performed both absorption and emission time-resolved spectroscopy studies on *trans* and *cis* ferulic acid (FA) in their neutral, anionic and dianionic

forms.[47] With the aid of complementary computational studies, Wang *et al.* confirmed a photoisomerisation relaxation pathway for all species studied at all pH values. These authors were also able to gather evidence for photoisomerisation occurring *via* two CIs, *i.e.* S_1/S_2 and S_2/S_0 (as shown in Figure 5.2(b)) in all systems studied.[47] The lifetimes were found to be comparable in all cases but one, the di-ionic form of *cis* ferulic acid (cFA^{2-}), for which photoisomerisation was found to take place within 1.4 ps (*c.f.* ~ 20 ps in all other cases). Wang *et al.* thus concluded that, for the case of cFA^{2-}, environment pH induced a change in electronic states such that photoisomerisation became barrierless, accelerating the overall decay.[47]

Luo *et al.*, on the other hand, explored the effects of pH on the photodynamics of sinapic acid (SA) and sinapoyl malate (SM), in an attempt to justify nature's choice of SM as a plant sunscreen.[46] As discussed in section 5.2.1, from the results of studies by Baker *et al.* it had transpired that the photodynamics of SA and SM were similar and no evidence had been found to suggest SM, found in plant leaves, is a better sunscreen.[3] In recognising that the pH within a plant leaf ranges between pH = 6– 8, Luo *et al.* studied the ionic forms of SA and SM, SA^- and SM^{2-}, as they occur at physiological pH.[46] Luo *et al.* confirmed photoisomerisation (both $trans \rightarrow cis$ and $cis \rightarrow trans$) relaxation pathways for SA, SA^- and SM^{2-}, *i.e.* even when pH is taken into account, the photodynamics of these species seem to be comparable.[46] However, as Luo *et al.* concluded from steady state irradiation measurements, the photoisomerisation process for SM^{2-} (as for SA) yields a *cis*-isomer which retains the absorption spectrum characteristics of the *trans*-isomer, both in terms of shape and intensity. For SA^-, on the other hand, the peak of absorption of the *cis*-isomer is blue-shifted and decreased in intensity when compared to *trans* SA^-.[46] The fact that the *cis*-isomer resulting from photoisomerisation of the naturally occurring SM^{2-} retains good sunscreen capabilities, while that of SA^- does not, could explain nature's choice of SM for a plant sunscreen.[46]

These studies serve as examples of how pH may influence sunscreen photodynamics. Importantly, they also highlight the need to consider the pH of the environment in which sunscreens are employed, as this may alter their photophysical behaviour.

5.4.3   Viscosity

Early studies by Espagne *et al.* explored the influence of solvent viscosity on the absorption and emission spectra of *para*-hydroxycinnamates, and found the timescales for photoisomerisation in these compounds to be largely unaffected by solvent viscosity.[48] If photoisomerisation was facilitated by an out-of-plane rotation around the C=C bond, the large amplitude nuclear motion would have been expected to be affected by solvent viscosity. The authors suggest, therefore, that the photoisomerisation of *para*-hydroxycinnamates occurs instead along a lower amplitude in-plane twisting motion,[48] which has been separately confirmed in recent studies.[49]

On the other hand, TEAS measurements by Horbury *et al.* on SM have found that the time constant assigned by these authors to evolution of the excited state population along the *trans-cis* photoisomerisation increases significantly with increasing viscosity.[50] Specifically, photoisomerisation of SM dissolved in ethanol, ethylene glycol and glycerol (in order of increasing viscosity) takes 47 ps, 188 ps and 560 ps, respectively.[50] Horbury *et al.* therefore conclude that photoisomerisation of SM likely involves out-of-plane rotation about the C=C bond justifying the large effect of solvent viscosity on its photodynamics.[50]

The studies by Espagne *et al.* and Horbury *et al.* are not only the first steps towards understanding how viscosity affects sunscreen photodynamics, but they also provided more detail on the molecular motions involved in photoisomerisation relaxation pathways. The effects of viscosity on the photodynamics of sunscreen molecules remain, nevertheless, largely unexplored.

5.4.4   Mixtures

So far, we have considered the photodynamics of sunscreen molecules either in vacuum or in contact with a single solvent. In reality, however, commercial sunscreens do not consist of single molecules dissolved in one solvent: sunscreen formulations are complex mixtures of several sunscreens, emollients, stabilisers, solvents, *etc.* Therefore, it is necessary to expand on the aforementioned studies and consider how sunscreen molecules affect each other's photodynamics.

An example of one such study is the work by Baker *et al.* on a mixture of oxybenzone and titanium dioxide (TiO$_2$), spanning a range of solute ratios, including those observed

in commercial sunscreen lotions.[51] The authors evaluated the photodynamics of each component individually: oxybenzone, as had been observed previously (see section 5.2.2), undergoes *enol-keto* tautomerisation followed by rotation around the aliphatic C—C bond which either facilitates IC to the ground state or results in isomerisation to a *trans-keto* conformation of oxybenzone.[15,51] Despite being used in sunscreens mainly to scatter UV radiation, TiO_2 was found in the studies by Baker *et al.* to undergo ultrafast (femtosecond, within instrument response) photodynamics when in low concentrations; at higher concentrations TiO_2 is long-lived.[51] The TEAS measurements for the mixture of these two sunscreen molecules in different solvents is simply the addition of individual spectra, with the time constants extracted matching those from the individual photodynamics.[51] Given this observation, Baker *et al.* concluded that there is minimal interaction between oxybenzone and TiO_2, and that the presence of either of them in a solvated mixture does not affect the photodynamics of the other.[51]

When the mixture is composed of two or more chemical sunscreens, however, long-lived triplet states may facilitate energy transfer between two molecules. Matsumoto *et al.* explored this possibility by evaluating the ability of EHMC and octocrylene to quench the triplet states of MenA.[9,52] By comparing the lifetimes of an energy donor (in this case, MenA) as the concentration of an energy acceptor (EHMC or octocrylene) is changed in the sunscreen mixture, the authors determined the rate of triplet-triplet energy transfer between each pair of molecules, *i.e.* MenA-EHMC or MenA-octocrylene.[52] Matsumoto *et al.* found that the triplet-triplet energy transfer between these molecules is an extremely efficient, diffusion controlled process. In fact, these authors found that both EHMC and octocrylene quench the triplet states of MenA at much higher rates than those observed for quenching of MenA by oxygen.[52] While these results may suggest that EHMC and octocrylene could act as MenA stabilisers in sunscreen formulations, it is important to evaluate if, for these and other combinations of sunscreens, energy transfer processes promote harmful chemical reactions which lead to undesirable by-products. Continued efforts towards understanding interactions between sunscreen molecules, and their impact on the resulting photodynamics, are necessary.

5.5   Conclusions

With the development of ultrafast laser spectroscopic techniques, many exciting avenues of research became possible, with the understanding of the photodynamics of a plethora of systems — such as sunscreen molecules — now being within reach. While the field of ultrafast photodynamics of sunscreen molecules is relatively new, the promising results achieved in early studies have sparked the interest of the scientific community and, in fact, of the sunscreen industry. Therefore, research into the ultrafast mechanisms that allow sunscreen molecules to dissipate excess absorbed energy into harmless heat is currently receiving significant attention. Common behaviours and trends are starting to emerge, as described in this chapter, such as the photoisomerisation of the cinnamates, the excited state proton transfer mechanisms taking place in sunscreens with an intramolecular hydrogen bond, and the solvent factors that have an impact on photodynamics. However, much more work needs to be done in order to systematically evaluate the impact of changing molecular structures and of the environment surrounding sunscreen molecules on their photodynamics.

In gaining such comprehensive understanding, a bottom-up approach has proved (and will continue to prove) crucial: studying molecules in isolation, changing substituent nature and position, increasing molecular complexity, then introducing solvents of different polarities, pH, viscosity, and, eventually, studying sunscreen molecules as part of increasingly more complex mixtures, in thin films (higher interaction between molecules) and, finally, *in vivo* (exploring how the skin environment may alter sunscreen photodynamics). Undergoing such extensive studies on the many different sunscreen molecules currently on the market, and all the others that may thus come to light, presents itself as a promisingly prolific and exciting avenue of research which ultimately aims to unveil the key to photoprotection and hence develop the targeted molecular design of a new generation of sunscreens, tailor made for optimum photoprotection.

5.6   References

[1] Tan, E. M. M., Hilbers, M. & Buma, W. J. Excited-state dynamics of isolated and microsolvated cinnamate-based UV-B sunscreens. *The Journal of Physical Chemistry Letters* **5**, 2464–2468 (2014).

[2] Peperstraete, Y. *et al.* Bottom-up excited state dynamics of two cinnamate-based sunscreen filter molecules. *Physical Chemistry Chemical Physics* **18**, 28140–28149 (2016).

[3] Baker, L. A. *et al.* Ultrafast photoprotecting sunscreens in natural plants. *The Journal of Physical Chemistry Letters* **7**, 56–61 (2016).

[4] Dean, J. C., Kusaka, R., Walsh, P. S., Allais, F. & Zwier, T. S. Plant sunscreens in the UV-B: Ultraviolet spectroscopy of jet-cooled sinapoyl malate, sinapic acid, and sinapate ester derivatives. *Journal of the American Chemical Society* **136**, 14780–14795 (2014).

[5] Nečasová, A., Bányiová, K., Literák, J. & Čupr, P. New probabilistic risk assessment of ethylhexyl methoxycinnamate: Comparing the genotoxic effects of *trans*–and *cis*–EHMC. *Environmental Toxicology* **32**, 569–580 (2017).

[6] Lowe, N. J. & Shaath, N. A. *Sunscreens: Development, Evaluation and Regulatory Aspects* (Marcel Dekker Inc., New York, 1990).

[7] Gasparro, F. P. *Sunscreen Photobiology* (Springer, New York, 1997).

[8] Wondrak, G. T. In Alberts, D. S. & Hess, L. M. (eds.) *Fundamentals of Cancer Prevention*, chap. 11, 301–320 (Springer, Berlin, 2014).

[9] Kikuchi, A., OguchiFujiyama, N., Miyazawa, K. & Yagi, M. Triplet-triplet energy transfer from a UV-A absorber butylmethoxydibenzoylmethane to UV-B absorbers. *Photochemistry and Photobiology* **90**, 511–516 (2014).

[10] Forestier, S. Rationale for sunscreen development. *Journal of the American Academy of Dermatology* **58**, 133–138 (2008).

[11] Wang, S. Q. & Lim, H. W. *Principles and Practice of Photoprotection* (ADIS, Switzerland, 2016).

[12] Dunkelberger, A. D., Kieda, R. D., Marsh, B. M. & Crim, F. F. Picosecond dynamics of avobenzone in solution. *The Journal of Physical Chemistry A* **119**, 6155–6161 (2015).

[13] Kockler, J., Oelgemöller, M., Robertson, S. & Glass, B. D. Photostability of sunscreens. *Journal of Photochemistry and Photobiology C: Photochemistry Reviews* **13**, 91–110 (2012).

[14] Yamaji, M. & Kida, M. Photothermal tautomerization of a UV sunscreen (4-tert-butyl-4-methoxydibenzoylmethane) in acetonitrile studied by steady-state and laser flash photolysis. *The Journal of Physical Chemistry A* **117**, 1946–1951 (2013).

[15] Baker, L. A. *et al.* Probing the ultrafast energy dissipation mechanism of the sunscreen oxybenzone after UVA irradiation. *The Journal of Physical Chemistry Letters* **6**, 1363–1368 (2015).

[16] Szczurko, C., Dompmartin, A., Michel, M., Moreau, A. & Leroy, D. Photocontact allergy to oxybenzone: ten years of experience. *Photodermatology, Photoimmunology & Photomedicine* **10**, 144–147 (1994).

[17] Collins, P. & Ferguson, J. Photoallergic contact dermatitis to oxybenzone. *British Journal of Dermatology* **131**, 124–129 (1994).

[18] Kinnberg, K. L. *et al.* Endocrine-disrupting effect of the ultraviolet filter benzophenone-3 in zebrafish, *danio rerio*. *Environmental Toxicology and Chemistry* **34**, 2833–2840 (2015).

[19] Downs, C. A. *et al.* Oxybenzone (Benzophenone-3), on coral *Planulae* and cultured primary cells and its environmental contamination in Hawaii and the U.S. Virgin Islands. *Archives of Environmental Contamination and Toxicology* **70**, 265–288 (2016).

[20] Porter, G. & Suppan, P. Primary photochemical processes in aromatic molecules. Part 12. — Excited states of benzophenone derivatives. *Transactions of the Faraday Society* **61**, 1664–1673 (1965).

[21] Jones, R. N. Some factors influencing the ultraviolet absorption spectra of polynuclear aromatic compounds. I. A general survey. *Journal of the American Chemical Society* **67**, 2127–2150 (1945).

[22] Stevenson, P. E. Effects of chemical substitution on the electronic spectra of aromatic compounds: Part IV. A general theory of substituent effects and its application to the spectra of the flower pigments. *Journal of Molecular Spectroscopy* **18**, 51–58 (1965).

[23] Karsili, T. N. V. *et al.* O—H bond fission in 4-substituted phenols: S_1 state predissociation viewed in a Hammett-like framework. *Chemical Science* **4**, 2434–2446 (2013).

[24] Pino, G. A. *et al.* Excited state hydrogen transfer dynamics in substituted phenols

and their complexes with ammonia: $\pi\pi^* - \pi\sigma^*$ energy gap propensity and *ortho*-substitution effect. *The Journal of Chemical Physics* **133**, 124313.1–124313.12 (2010).

[25] Hermann, R., Mahalaxmi, G. R., Jochum, T., Naumov, S. & Brede, O. Balance of the deactivation channels of the first excited singlet state of phenols: effect of alkyl substitution, sterical hindrance, and solvent polarity. *The Journal of Physical Chemistry A* **106**, 2379–2389 (2002).

[26] Lee, S.-H. *et al.* Substituent effects in molecular electronic relaxation dynamics *via* time-resolved photoelectron spectroscopy: $\pi\pi^*$ states in benzenes. *The Journal of Physical Chemistry A* **106**, 8979–8991 (2002).

[27] Horbury, M. D., Baker, L. A., Quan, W.-D., Greenough, S. E. & Stavros, V. G. Photodynamics of potent antioxidants: ferulic and caffeic acids. *Physical Chemistry Chemical Physics* **18**, 17691–17697 (2016).

[28] Coyle, J. D. & Carless, H. A. J. Selected aspects of photochemistry: I Photochemistry of carbonyl compounds. *Chemical Society Reviews* **1**, 465–480 (1972).

[29] Fang, W.-H. & Phillips, D. L. The crucial role of the $S_1/T_2/T_1$ intersection in the relaxation dynamics of aromatic carbonyl compounds upon $n \to \pi^*$ excitation. *ChemPhysChem* **3**, 889–892 (2002).

[30] Lochbrunner, S. *et al.* Dynamics of excited-state proton transfer systems *via* time-resolved photoelectron spectroscopy. *The Journal of Chemical Physics* **114**, 2519–2522 (2001).

[31] Southern, C. A. & Levy, D. H. Electronic and infrared spectroscopy of anthranilic acid in a supersonic jet. *The Journal of Physical Chemistry A* **107**, 4032–4040 (2003).

[32] Sugiyama, K., Tsuchiya, T., Kikuchi, A. & Yagi, M. Optical and electron paramagnetic resonance studies of the excited triplet states of UV-B absorbers: 2-ethylhexyl salicylate and homomenthyl salicylate. *Photochemical & Photobiological Sciences* **14**, 1651–1659 (2015).

[33] Madan, R. K. & Levitt, J. A review of toxicity from topical salicylic acid preparations. *Journal of the American Academy of Dermatology* **70**, 788–792 (2014).

[34] Promkatkaew, M. *et al.* Photophysical properties and photochemistry of substituted cinnamates and cinnamic acids for UVB blocking: effect of hydroxy, nitro, and fluoro

substitutions at *ortho*, *meta*, and *para* positions. *Photochemical & Photobiological Sciences* **13**, 583–594 (2014).

[35] Józefowicz, M. & Heldt, J. Experimental and theoretical studies of electronic transition dipole moments of methyl benzoate derivatives. *Journal of Luminescence* **132**, 755–764 (2012).

[36] Grabowski, Z. R. & Dobkowski, J. Twisted intramolecular charge transfer (TICT) excited states: energy and molecular structure. *Pure and Applied Chemistry* **55**, 245–252 (1983).

[37] L.Sobolewski, A. & Domcke, W. Promotion of intramolecular charge transfer in dimethylamino derivatives: twisting versus acceptor-group rehybridization. *Chemical Physics Letters* **259**, 119–127 (1996).

[38] L.Sobolewski, A., Sudholt, W. & Domcke, W. *Ab Initio* investigation of reaction pathways for intramolecular charge transfer in dimethylanilino derivatives. *The Journal of Physical Chemistry A* **102**, 2716–2722 (1998).

[39] Grabowski, Z. R., Rotkiewicz, K. & Rettig, W. Structural changes accompanying intramolecular electron transfer: Focus on twisted intramolecular charge-transfer states and structures. *Chemical Reviews* **103**, 3899–4032 (2003).

[40] Sudholt, W., Staib, A., Sobolewskib, A. L. & Domcke, W. Molecular-dynamics simulations of solvent effects in the intramolecular charge transfer of 4-(N,N-dimethylamino)benzonitrile. *Physical Chemistry Chemical Physics* **2**, 4341–4353 (2000).

[41] Agrapidis-Paloympis, L. E. & Nash, R. A. The effect of solvents on the ultraviolet absorbance of sunscreens. *Journal of the Society of Cosmetic Chemists* **38**, 209–221 (1987).

[42] Beyere, L., Yarasi, S. & Loppnow, G. R. Solvent effects on sunscreen active ingredients using Raman spectroscopy. *Journal of Raman Spectroscopy* **34**, 743–750 (2003).

[43] Cai, X. *et al.* α-Carbonyl substituent effect on the lifetimes of triplet 1,4-biradicals from Norrish-Type-II reactions. *Chemistry: A European Journal* **12**, 4662–4667 (2006).

[44] Scaiano, J. C., Lissi, E. A. & Encina, M. V. Chemistry of the biradicals produced in the Norrish-Type-II reaction. *Reviews of Chemical Intermediates* **2**, 139–196 (1978).

[45] Chang, X.-P., Li, C.-X., Xie, B.-B. & Cui, G. Photoprotection mechanism of *p*-methoxy methylcinnamate: A CASPT2 study. *The Journal of Physical Chemistry A* **119**, 11488–11497 (2015).

[46] Luo, J. *et al.* Ultrafast barrierless photoisomerization and strong ultraviolet absorption of photoproducts in plant sunscreens. *The Journal of Physical Chemistry Letters* **8**, 1025–1030 (2017).

[47] Wang, S. *et al.* Ultrafast dynamics of UV-excited *trans*- and *cis*-ferulic acid in aqueous solutions. *Physical Chemistry Chemical Physics* **19**, 30683–30694 (2017).

[48] Espagne, A., Paik, D. H., ChangenetBarret, P., Martin, M. M. & Zewail, A. H. Ultrafast photoisomerization of photoactive yellow protein chromophore analogues in solution: Influence of the protonation state. *ChemPhysChem* **7**, 1717–1726 (2006).

[49] Kuramochi, H., Takeuchi, S. & Tahara, T. Ultrafast structural evolution of photoactive yellow protein chromophore revealed by ultraviolet resonance femtosecond stimulated Raman spectroscopy. *The Journal of Physical Chemistry Letters* **3**, 2025–2029 (2012).

[50] Horbury, M. D., Quan, W.-D., Flourat, A. L., Allais, F. & Stavros, V. G. Elucidating nuclear motions in a plant sunscreen during photoisomerization through solvent viscosity effects. *Physical Chemistry Chemical Physics* **19**, 21127–21131 (2017).

[51] Baker, L. A., Grosvenor, L. C., Ashfold, M. N. R. & G.Stavros, V. Ultrafast photophysical studies of a multicomponent sunscreen: Oxybenzone-titanium dioxide mixtures. *Chemical Physics Letters* **664**, 39–43 (2016).

[52] Matsumoto, S., Kumasaka, R., Yagi, M. & Kikuchi, A. Triplet-triplet energy transfer between UV absorbers in solutions at room temperature. *Journal of Photochemistry and Photobiology A: Chemistry* **346**, 396–400 (2017).

6 Conclusion and Outlook

'For a research worker, the unforgotten moments of their life are those rare ones which come after years of plodding work, when the veil over nature's secret seems suddenly to lift and when what was dark and chaotic appears in a clear and beautiful light pattern.'

Gerty Theresa Cori (1896–1957)

It is currently well-established that exposure to UV radiation triggers several cutaneous responses in humans, including the production of vitamin D, but also erythema (skin reddening commonly referred to as sunburn) and DNA damage. UV radiation-induced DNA damage is now known to be the main cause of skin cancer, the incidence of which has increased in recent decades. While the most effective methods of photoprotection are seeking shade at times of strongest solar intensity and covering the skin with appropriate clothing when exposure cannot be avoided, the societal urge to seek solar exposure and thus tanned skin results in sunscreens being, in fact, the most popular source of photoprotection. Therefore, the performance of sunscreen lotions in protecting human skin from UV-induced damage plays a crucial role in tackling the increasing rates of skin cancer incidence. In this thesis we explore innovative ways in which the field of ultrafast laser spectroscopy may inform the molecular design of sunscreen molecules which are tailor-made for optimum photoprotection.

Chapter 1 of this thesis is essentially divided in two main parts. Firstly, in section 1.1 "Sun, Skin and Sunscreens", we explored the underlying discussion regarding the interactions between UV radiation and the skin and the role of sunscreens in photoprotection, which ultimately motivates the research presented in following chapters. Given the nature of the studies undergone in preparation of this thesis, it was also important to provide an overview of the fundamental principles which describe the interactions between light and matter, as well as of the terminology commonly used to describe them — this was the topic of section 1.2 "Fundamentals of Quantum Mechanics and Spectroscopy". In finishing Chapter 1, it was intended that the reader would be familiar with the challenges we aimed to address with this line of research, as well as having a strong understanding of the background concepts which guide the science discussed in later chapters.

Having explored the "why" and "what" of the topic under discussion, Chapter 2 serves as an introduction to the "how". In particular, it covers the basic reasoning behind laser femtochemistry, which allows for ultrafast processes to be studied, as well as the technology necessary for the generation of ultrashort laser pulses and the theoretical and practical considerations of the experiments reported in chapters 3, 4 and 5.

The research presented in this thesis focused mainly on two of the seven categories of sunscreen molecules (presented in Chapter 1): the cinnamates and anthranilates. The cinnamates, and in particular ethyl ferulate (EF) were discussed in Chapter 3, from which three main points can be gathered: *i)* as for other cinnamates, the photodynamics of EF in solution involve ultrafast *trans-cis* photoisomerisation; *ii)* the addition of a carbonyl moiety to a molecular structure can have a drastic effect on the observed ultrafast photodynamics, potentially due to the resulting accessibility of triplet states; *iii)* solvent effects can be very significant for a sunscreen molecule, potentially altering the observed photodynamics observed in vacuum completely. Our studies on EF serve as an important addition to a series of studies which allow for a trend in the behaviour of cinnamates to be established. However, the discussion becomes particularly interesting when comparing the cinnamates with our observations for the anthranilates, the latter having been discussed in Chapter 4. In studying methyl and menthyl anthranilate (MA and MenA) we have not only found that the addition of the menthyl unit (in MenA *vs.* MA) does not produce any significant differences in the observed photodynamics, but also that, in stark contrast to the observations on cinnamates, solvent interactions do not have any significant impact on the vacuum photodynamics of the anthranilates we have studied. We have also concluded that the intramolecular hydrogen bond facilitated by the *ortho* configuration of both MA and MenA stabilises their respective excited states and thus plays a pivotal role in determining their photophysical behaviour which is non-ideal for a sunscreen molecule. Moreover, we have identified highly efficient intramolecular energy redistribution processes in the anthranilates which may enhance trapping of excited state population and thus hinder efficient relaxation to the ground electronic state. Work is currently underway to assess the influence of *meta* and *para* substitution on the photodynamics observed for *ortho*-MA.

It can be said that the studies presented in this thesis, rather than answering questions regarding the ultrafast photodynamics of sunscreen molecules, highlight the complexity and lack of knowledge about the energy dissipation mechanisms responsible for photoprotection. We have observed profound differences across only two of the sunscreen families

(extensive time-resolved studies on the remaining five categories are still lacking), not only in terms of the observed photodynamics but also their responses to the environment. Despite the fact that, on their own, our studies are insufficient to allow for any significant trends in sunscreen molecule behaviour to be established, our efforts towards elucidating the ultrafast photodynamics of sunscreen molecules did not take place in isolation: other authors have concurrently investigated similar systems in an attempt to understand their photodynamics and the implications of these to the context of sunscreen usage and development. A comprehensive picture of the current progress in the field could not, therefore, be complete without an overview of the parallel work on sunscreen photodynamics that has been carried out by other authors, which we have provided in Chapter 5, while also demonstrating how our own studies fit into this wider perspective. Importantly, this chapter served to highlight the main findings in the field of sunscreen photodynamics and to identify and analyse any trends emerging from the current literature on the subject. The discussion in Chapter 5 emphasises the novelty of this field of research. Inevitably, this novelty implies there is still limited understanding regarding ultrafast photoprotection mechanisms: the energy dissipation mechanisms of many families of sunscreens remain elusive, as do the extent of the impact of environment on such mechanisms, especially for more complex mixtures (including several sunscreen molecules but also emollients, for example) and *in vivo* conditions. Nevertheless, these currently uninvestigated issues constitute exciting opportunities for further research, as the field evolves from fundamental science to product optimisation.

This thesis demonstrates the potential of ultrafast laser femtochemistry techniques to elucidate the ultrafast photodynamics of sunscreen molecules. Moreover, it illustrates how employing a bottom-up approach to this subject — studying sunscreen molecules of incrementally increased molecular and environmental complexity, from vacuum to *in vivo* — may provide a rationale for molecular design of advanced sunscreens which are tailor-made for optimum photoprotection. In reaching its full potential, this innovative approach to sunscreen development has the potential to create a new generation of sunscreens to address current challenges to the skin and healthcare industry sectors. These novel, optimised sunscreen active ingredients may then be used in high-performance photoprotective lotions in an attempt to disrupt the rise in skin cancer incidence.

A "Particle in a Box" Solution

The particle in a box problem, for which a particle is considered to be trapped in an infinite potential well, is an hypothetical scenario often used to illustrate quantum mechanical principles, in particular, the quantisation of energy. It also illustrates the use of differential equations and boundary conditions to solve the Schrödinger equation for the wavefunction of the particle, Ψ.

The "box" in which the translational motion of the particle is trapped (U_2 in Figure A.1) is a region of space, from $x = 0$ to $x = L$, where the particle has no potential energy ($V = 0$), with the potential energy being infinite everywhere else, *i.e.* $V = \infty$ for $x < 0$ (U_1) and for $x > L$ (U_3). Under these conditions, it is impossible to provide enough energy to the particle to allow it to leave the region of space $0 \leq x \leq L$.

Let's recall the form of the time-independent Schrödinger equation, presented in Equation 1.6 in Chapter 1, which consists of the sum of the kinetic and potential energies of the particle:

$$-\frac{\hbar^2}{2m}\frac{\mathrm{d}^2\Psi(x)}{\mathrm{d}x^2} + \hat{V}(x)\Psi(x) = E\Psi(x) \tag{A.1}$$

In the equation above, the first term refers to the kinetic energy of the particle, the second term to its potential energy, with $\hat{V}$ being the potential energy operator; E is the total energy of the system and Ψ the wavefunction which describes it. For the regions of space U_1 and U_3, since the potential energy is so large the particle cannot occupy these regions of space, hence we can approximate the wavefunction to be zero in these regions, *i.e.* $\Psi_1 = 0$ and $\Psi_3 = 0$ (for regions of space U_1 and U_3, respectively). In the case of U_2, the potential energy of the particle is zero according to the constraints of our hypothetical scenario. Hence, the Schrödinger equation simplifies to:

$$-\frac{\hbar^2}{2m}\frac{\mathrm{d}^2\Psi(x)}{\mathrm{d}x^2} = E\Psi(x). \tag{A.2}$$

From the known solutions to differential equations, such as the one presented above, we can find a solution for the wavefunction in region U_2, Ψ_2:

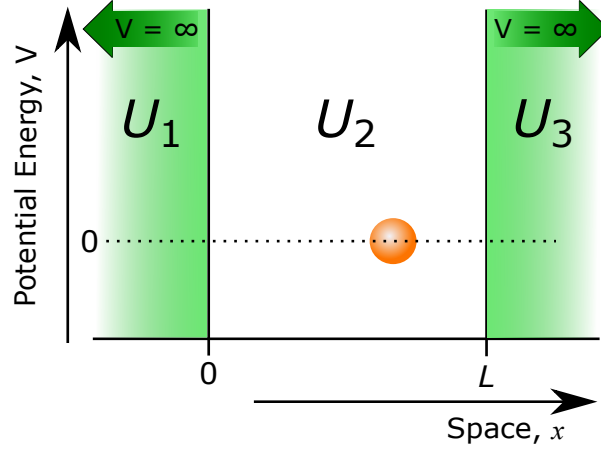$$\Psi_2(x) = A\sin(kx) + B\cos(kx) \tag{A.3}$$

Figure A.1: The "particle in a box" scenario: translational motion of the particle (in orange) is restricted to the region between $x = 0$ and $x = L$, U_2, where $V = 0$. The particle is sided by regions U_1 and U_3, where $V = \infty$, *i.e.* $\Psi_n = 0$ (in green). These boundaries essentially trap the particle in this "box": it cannot exist anywhere else as it is impossible to provide it with enough energy for it to be able to leave this region of space.

where A, B and k are constants. Substituting into Equation A.2, we have, therefore:

$$
\begin{aligned}
E\Psi_2(x) &= -\frac{\hbar^2}{2m}\left(-Ak^2\sin(kx) - Bk^2\cos(kx)\right) \\[2mm]
&= \frac{\hbar^2 k^2}{2m}\left(A\sin(kx) + B\cos(kx)\right) \\[2mm]
&= \frac{\hbar^2 k^2}{2m}\Psi_2(x)
\end{aligned}
\tag{A.4}
$$

$$
\Rightarrow E = \frac{\hbar^2 k^2}{2m} \quad \Leftrightarrow \quad \boxed{k = \sqrt{\frac{2mE}{\hbar^2}}}
$$

While we have now established the relationship between the parameter k and the energy of the system, the latter remains unknown. However, we can obtain more information on the value of k based on the restrictions that can be applied to the solutions for a given wavefunction in light of Born's interpretations of its meaning (see Chapter 1 for more details). In particular, since the wavefunction should be continuous, we know that at the U_1/U_2 and U_2/U_3 boundaries the values of the wavefunctions must match, *i.e.*:

$$
\begin{aligned}
\text{at } x = 0: \quad &\Psi_1(0) = \Psi_2(0) \\
\text{at } x = L: \quad &\Psi_2(L) = \Psi_3(L).
\end{aligned}
\tag{A.5}
$$

We can find solutions for Ψ_2 at both $x = 0$ and $x = L$:

$$\Psi_2(0) = A\sin(k \times 0) + B\cos(k \times 0) = B$$
$$\Psi_2(L) = A\sin(k \times L) + B\cos(k \times L). \tag{A.6}$$

Moreover, as we have established earlier, $\Psi_1 = 0$ and $\Psi_3 = 0$, hence we can extract the values of A and B, as follows:

$$\Psi_2(0) = \Psi_1(0) \Leftrightarrow \boxed{B = 0}$$

If $B = 0$, then: $\tag{A.7}$

$$\Psi_2(L) = \Psi_1(0) \Leftrightarrow A\sin(kL) + 0 = 0 \Leftrightarrow \boxed{A\sin(kL) = 0}$$

The latter of the relationships above would hold valid for either $A = 0$ or $\sin(kL) = 0$. However, if $A = 0$ the overall solution would reduce to zero, which would imply $\Psi_2(L) = 0$. Assuming the particle *must* exist within the "box", Ψ_2 must be non-zero, hence $\sin(kL)$ must be zero. This is only true if:

$$\sin(kL) = 0 \quad \therefore \quad \boxed{kL = n\pi} \qquad n = 0, \pm 1, \pm 2, \ldots \tag{A.8}$$

This is perhaps the crucial result of the particle in a box problem, since it demonstrates how the corresponding solution to the Schrödinger equation results in quantised energy, with n being the principal quantum number. Moreover, from Equation A.8 and the expression for k, boxed in Equation A.4, we can obtain the expression for the energy of the particle in a box:
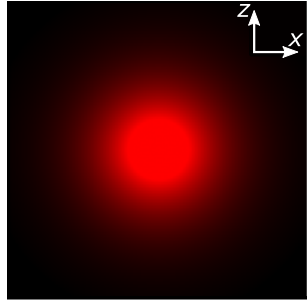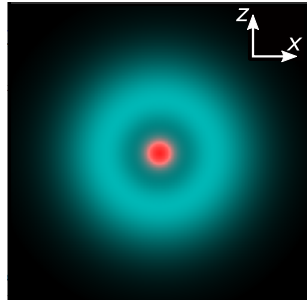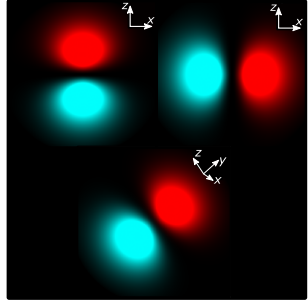
$$\sqrt{\frac{2mE}{\hbar^2}}L = n\pi \quad \Leftrightarrow \quad \frac{2mE}{\hbar^2} = \frac{n^2\pi^2}{L^2} \quad \Leftrightarrow \quad \boxed{E = \frac{n^2\pi^2\hbar^2}{2mL^2}} \tag{A.9}$$
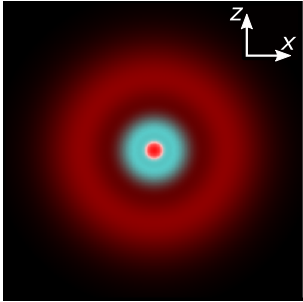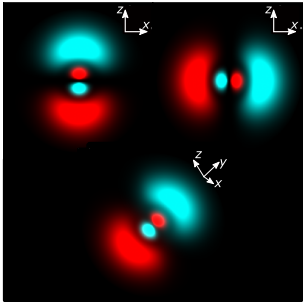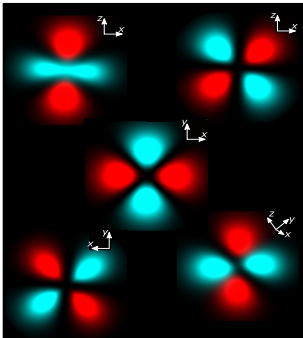
The approach shown here for a 1D "box" can be extended to more dimensions. The boundary conditions can also be set up so that the particle is confined to a circular plane, to a two dimensional ring or even a sphere; these examples, which will not be explored here (see, instead, reference 42 in Chapter), demonstrate quantisation of rotational motion and angular momentum and thus give rise to the orbital angular momentum and magnetic quantum numbers.

B Solutions to the Schrödinger Equation for the Hydrogen atom

Table B.1: The solutions to the Schrödinger equation for the hydrogen atom for different combinations of quantum numbers. The wavefunction solutions were taken from A. Beiser, *Perspectives of Modern Physics*, McGraw-Hill, 1969; the corresponding visual representations were obtained from an online hydrogen atom orbital generator, available from http://www.falstad.com/qmatom/. In this table, a_0 is defined as $\hbar^2/m_e^2 = 0.529$ nm. This quantity is also known as the Bohr radius.

Quantum numbers

n	l	m_l	Wavefunction	Orbital
1	0	0	$\frac{1}{\sqrt{\pi}a_0^{3/2}}e^{-r/a_0}$	
2	0	0	$\frac{1}{4\sqrt{2\pi}a_0^{3/2}}\left(2-\frac{r}{a_0}\right)e^{-r/a_0}$	
	1	0	$\frac{1}{4\sqrt{2\pi}a_0^{3/2}}\ \frac{r}{a_0}\ e^{-r/a_0}\ cos\ \theta$	
	1	± 1	$\frac{1}{4\sqrt{2\pi}a_0^{3/2}}\ \frac{r}{a_0}\ e^{-r/a_0}\ cos\ \theta$	

| | 0 | 0 | $\frac{1}{81\sqrt{3\pi}a_0^{3/2}} \left(27 - 18\frac{r}{a_0} + 2\frac{r^2}{a_0^2}\right) e^{-r/3a_0}$ |

| 3 | 1 | 0 | $\frac{\sqrt{2}}{81\sqrt{\pi}a_0^{3/2}} \left(6 - \frac{r}{a_0}\right) \frac{r}{a_0} e^{-r/3a_0} \cos\theta$ |
| | 1 | ± 1 | $\frac{\sqrt{2}}{81\sqrt{\pi}a_0^{3/2}} \left(6 - \frac{r}{a_0}\right) \frac{r}{a_0} e^{-r/3a_0} \sin\theta\ e^{\pm i\phi}$ |

	2	0	$\frac{1}{81\sqrt{6\pi}a_0^{3/2}} \frac{r^2}{a_0^2} e^{-r/3a_0} (3\cos^2\theta - 1)$
	2	± 1	$\frac{1}{81\sqrt{\pi}a_0^{3/2}} \frac{r^2}{a_0^2} e^{-r/3a_0} \sin\theta\ \cos\theta\ e^{\pm i\phi}$
	2	± 2	$\frac{1}{162\sqrt{\pi}a_0^{3/2}} \frac{r^2}{a_0^2} e^{-r/3a_0} \sin^2\theta\ e^{\pm i2\phi}$

C Teaching Statement

From my experiences in higher education, as both a student and a teacher, it has become clear to me that some the most important skills one can develop during a university degree are those which create excellent professionals: problem solvers who can go out into the world to help tackle the many critical challenges our society faces at any one given time. As a scientist and a teacher, I regard critical thinking as one of the most valuable of these skills. I interpret critical thinking as the ability to question one's assumptions and to persist in finding answers to difficult problems, as well as the ability to connect acquired knowledge to other areas of enquiry and be willing to risk finding collaborative solutions outside one's disciplinary zone of comfort. However, critical thinking is not an easy skill to develop nor to teach; it is a long journey that must be nourished by other academic achievements and continuously encouraged.

In order to facilitate a teaching and learning environment which fosters critical thinking, I make use of different teaching methods and tools based on educational research and proven pedagogy. One of the most fundamental principles which guides my teaching practice is Vygotsky's concept of the zone of proximal development (ZPD), in which students are faced with a problem for which they have no immediate solution; instead, they are required to build on previous knowledge and, with access to new relevant information, guidance and encouragement, complete the task at hand. This approach is also commonly referred to as a "instructional scaffolding". Moreover, I believe Kolb's theory of experiential learning is incredibly valuable to teaching, particularly with regards to demonstrating how theoretical or abstract concepts manifest physically, and how these in turn relate to "real-life" and "day-to-day" applications. In this context, science is a privileged subject, since practical activities are traditionally a significant part of teaching in the sciences. I believe these practical activities are golden opportunities for the development of experiential learning opportunities, and in developing laboratory activities for undergraduate students I aim to connect the practical experience with lecture material, thus giving physical meaning to academic content, and relating these to students' everyday reality. The main objective is to provide students with a transformative experience that allows them to experience their own day-to-day lives in light of what they have learnt from my teaching

activities. In this sense, I truly set out to deliver life-changing teaching.

There are other underlying principles that encompass all aspects of my teaching. First of all, I consider having open communication channels between me and my students of great importance, allowing feedback to flow freely from me to students and *vice-versa*. I believe that students who take responsibility for their learning, who actively engage with the teaching and learning process and, importantly, who feel their perspectives are taken into account, are more motivated and thus tend to be higher academic achievers. In addition, I believe that feedback from students is one of the most valuable tools at the disposal of any teacher and it can have a transformative impact in the teaching and learning process. Therefore, I actively seek student feedback and I am proactive in adapting my teaching practice to my students' expressed needs. However, open communication channels which allow for the free, bi-directional flow of feedback can only exist within an inclusive and open classroom, where each and every student feels confident to share their thoughts, ideas and concerns. Creating an inclusive environment is not limited to issues of gender, race, religion, ability, *etc.*: it extends to other student learning needs which can range from dyslexia to preferred learning media (*e.g.* a student who prefers learning from visual aids as opposed to a student who prefers large amounts of reading). As such, creating an inclusive environment may not always be easy, particularly for large cohorts of students whose needs I may not be aware of (if students' decide not to disclose them, for example). Therefore, inclusivity is a wide-reaching issue and addressing it is a continuous process that needs to be taken into account throughout the teaching process. The open communication channels mentioned earlier may also help with making students feel comfortable discussing their learning needs in more detail.

Last, but most certainly not least, I am passionate about teaching and about my subject area and I think this is essential for my success as a teacher. I am a true believer that my enthusiasm is key to keeping students engaged and motivated. Ultimately, the goal is to leave students with an inspiring "buzz" that will accompany them beyond the lecture room and drive them to want to know more, explore on their own, pursue their own curiosity, ask and answer their own questions. In conclusion, I am dedicated to more than simply delivering information or ideas: my passion for teaching stems from my heartfelt dedication to guiding students in their journey to achieve their full potential.

D Science Communication

How do sunscreens work?

My thesis to a non-expert audience

There is no denying that often all it takes is a bit of sunshine to lift your mood, especially if it is the first warm Spring day after a long, harsh Winter. As you enjoy those delightful rays of warm light, however, perhaps you remember the warning regarding the risks of being out in the sun too long (if you have ever experienced a painful sunburn, maybe you won't need further warning!). The widespread advice regarding staying safe in the sun is clear: stay in the shade when the sun is strongest (which in the UK, according to the NHS, 'is between 11am and 3pm from March to October'), cover your skin with appropriate clothing and your eyes with sunglasses when out in the sun, and make sure you never burn. While these are the safest and most reliable methods to avoid sun damage to your skin, sometimes it is simply too tempting, and indeed irresistible, to stay in the sun for just a little bit longer — so where did I leave my sunscreen bottle from last year? Particularly if you are planning a holiday to a sunny part of the world, you may find yourself packing plenty of sunscreen and planning to use it as your main source of protection against the sun. But what do these protective lotions, on which we rely so much, actually do?

Sunscreens are designed to protect us from the ultraviolet (UV) radiation we receive from the sun, which is usually classified as UVA and UVB. While UVB radiation is more aggressive to the skin and causes direct DNA damage, much higher levels of UVA actually reach our skin; UVA is also generates free radicals which cause skin ageing and indirect damage to DNA in skin cells. The bottom-line is, however, that both UVA and UVB have the ability to prompt a cascade of processes that may ultimately lead to skin cancer. In fact, UV radiation (both UVA and UVB) is the primary origin of skin cancer, the incidence of which has risen in recent years. It is also important to remember that there isn't such a thing as a "healthy tan" — the darkening of our skin as a result of sun exposure, even if

it was just a nice day out in the mild Spring sun, occurs as a response to damage caused by UV radiation. Therefore, if you are even mildly tanned, your skin has already suffered some level of damage. So you can imagine what tanning beds do to you!

The way sunscreens protect us from the destructive effects of UV radiation is, quite simply, by absorbing the harmful UV radiation from the sun before our skin has the chance to. Which means: yes, wearing sunscreen will hinder tanning, at least if you are using it right, which means re-applying every few hours and especially after you've been in the sea or the pool. When the minuscule components of any material, which we call *molecules*, absorb radiation, such as sunscreen molecules which absorb UV radiation from the sun to protect the skin against it, they get excited. I know what you are thinking — 'to be fair, I also get excited when I'm out in the sun' — but that's not quite what it means here. Excited molecules have extra energy, which they get from absorbing the radiation from the sun. This extra energy, in turn, needs to *go* somewhere, it can not simply disappear (if you are ever asked about it in a pub quiz, this is called the *law of conservation of energy*). So where does the extra energy go? Different molecules deal with extra energy in different ways: some release it by emitting light (ever play with glow sticks?), others quite simply break apart and generate secondary chemicals (that can either be harmless or deadly), and others will simply shake it off (the molecule gets rid of the energy by shaking all over until it's "tired"). What about sunscreen molecules, in particular? What do those molecules do?

The answers to those questions have only recently started to emerge, despite modern sunscreen having been on the market since the 1930's, when Eugene Schueller, the founder of L'Oreal, released the first version of Ambre Solaire. We have known for a while that some sunscreen molecules are *photoallergenic*, that is, they don't cause any harmful or unpleasant reactions on the skin when first applied, but when the skin (and, therefore, the sunscreen molecule) is exposed to the sun a rash may develop. This was the case for the famous sunscreen PABA (the chemists call it *para*-aminobenzoic acid), which a significant number of sunscreen users found to be photoallergenic and PABA was, therefore, removed from commercial sunscreen formulations. Nevertheless, the case of PABA demonstrates the issue with sunscreens rather well: there may be sunscreen molecules that absorb the radiation as they are supposed to, but then the extra energy has some effect that ultimately results in the sunscreen molecule being harmful to human skin.

What the scientific community is now starting to come to understand is that if the

extra energy that molecules receive from absorbing UV radiation hangs around for too long, it increases the chances of harmful chemistry taking place (the kind that results in photoallergy). In essence, if the sunscreen molecule does not find a quick sink for the excess energy, it may not have another option but to break apart. As mentioned before, molecules could potentially start to glow to release the extra energy, but glowing is a process that happens over several minutes, which is not ideal if we are trying to get rid of energy quickly. It is a shame, really, because if sunscreens did glow when exposed to the sun, going to the beach would be like an immense colourful glowing party.

The remaining option is for sunscreen molecules to shake the energy away. And, as it turns out, they can shake it away quite quickly, on a timescale of femto to picoseconds. That is approximately 0.000000000000001 to 0.000000000001 seconds — *very* fast. The way in which sunscreen molecules shake, however, can be quite particular. Sometimes they shake so much their overall structure changes. Importantly, they sometimes shake differently depending on what liquid they are dissolved in. This can be quite significant, considering sunscreen formulations can be either water- or oil-based, for example. Do sunscreen work better in water? Oil? What kind of oil? Are there other liquids we may use? And how do other components of the sunscreen (fragrances, for example) affect how the sunscreens release the harmful extra energy? These are all questions that remain unanswered, and that the field of ultrafast sunscreen photodynamics — the study of how

Figure D.1: "UV-B-Gone": can we develop a new generation of sunscreens which are targetted for the most effective level of protection against radiation from the sun? Can we achive that while also creating screens that are more environmentally friendly?

sunscreen molecules use fast shaking to get rid of extra energy — is currently trying to answer.

Once we understand how the current sunscreen molecules work their magic, we may be able to alter them at a molecular level to enhance their performance. Importantly, we may use the new knowledge provided by the field of ultrafast sunscreen photodynamics to address some of the challenges currently facing the sunscreen industry. One of these challenges is to provide appropriate protection which covers both the UVA and UVB radiation ranges: there are few UVA sunscreen molecules, for example, and some of them tend to be unstable within commercial formulations, *i.e.* they degrade and lower the sunscreen's protective performance. In addition, some studies now reveal a negative impact of sunscreen molecules on the environment. When we apply sunscreens and go into the sea, the sunscreen molecules eventually end up having an effect on plant and animal sea life. Oxybenzone, for example, which is used in many commercial sunscreen formulations, has been linked to coral bleaching. In fact, this is the reason why Hawaii has recently banned sunscreen which contain oxybenzone on their beaches!

The sunscreen molecules currently used in commercial sunscreen formulations have been consistently shown to provide important and safe protection against UV radiation from the sun by absorbing it before the skin has the chance to. However, currently we don't fully understand the mechanisms by which sunscreen molecules get rid of the extra energy they receive from solar radiation and, importantly, we don't know how the components of a commercial sunscreen formulation may affect these mechanisms. The field of ultrafast sunscreen photodynamics is unveiling these mysteries in the hope of guiding the development of a new generation of sunscreens targeted for optimum UV protection. In the future, these innovative sunscreens may be incorporated in high performance commercial sunscreen formulations which absorb more UV radiation and dissipate the extra energy quicker, making them more effective against sunburn. The optimised protection provided by these innovative high performance sunscreens may also help curb the rising numbers of skin cancer incidence. Finally, the development of new sunscreens is also an environmental concern, since current sunscreen molecules have been shown to have a negative impact on the environment, and in particular on sea life.

'Pressure is a privilege.'

Lizzy Yarnold, Skeleton Racer and Olympic Gold Medalist